SISSA
Scuola
Internazionale
Superiore di
Studi Avanzati

Neuroscience Area – PhD course in

<Neurobiology>

Construction of carbon-based three-dimensional neural scaffolds and their structural regulation

Candidate:

Miao Xiao

Advisor:

Prof. Vincent Torre

Academic Year 2019-2020

Contents

List of publications

Peer reviewed publications:

1) **Xiao, M.**[#]; Li, X.[#]; Song, Q.; Zhang, Q.; Lazzarino, M.; Cheng, G.[*]; Ulloa Severino, F. P.[*]; Torre, V.[*], A Fully 3D Interconnected Graphene-Carbon Nanotube Web Allows the Study of Glioma Infiltration in Bioengineered 3D Cortex-Like Networks. *Advanced materials* **2018,** *30* (52), 1806132. **(IF: 25.8) (Inside Cover)**
2) Ma, X.; **Xiao, M.**; Hao, Y.; Cheng, G.[*], Precisely controllable hybrid graphene scaffold reveals size effects on differentiation of neural progenitor cells in mimicking neural network. *Carbon* **2019,** *145*, 90-99. **(IF: 7.4)**
3) Guo, R.[#]; Zhang, S.[#]; **Xiao, M.**[#]; Qian, F.; He, Z.; Li, D.; Zhang, X.; Li, H.; Yang, X.; Wang, M.; Chai, R.[*]; Tang, M.[*], Accelerating bioelectric functional development of neural stem cells by graphene coupling: Implications for neural interfacing with conductive materials. *Biomaterials* **2016,** *106*, 193-204. **(*contributed equally as first author*) (IF: 10.2)**

Papers in preparation:

1) Guo, R.[#]; Li, J.[#]; Chen, C.[#]; **Xiao, M.**[#]; Liao, M.; Hu, Y.; Liu, Y.; Li, D.; Zou, J.; Sun, D.; Torre, V.; Zhang, Q.[*]; Chai, R.[*]; Tang, M.[*], Biomimetic three-dimensional bacterial cellulose-graphene foam materials regulate neural stem cell proliferation and differentiation. (**contributed equally as first author**) (**submitted**)
2) **Xiao, M.**; Ulloa Severino, F. P.; Iseppon, F.; Cheng, G.[*]; Torre, V.[*], 3D free-standing ordered graphene network geometrically regulates neuronal growth and network formation. (**ready to submit**)
3) **Xiao, M.**; Pifferi, S.; Pastore, B.; Liu, Y.; Chai, R.; Torre, V.[*]; Tang, M.[*], MXene-based interfaces do not alter directly targeted neurons. (In preparation)

Abstract

Motivation

The brain is formed by an intricate assembly of cellular networks, where neurons are embedded in an extracellular matrix (ECM) consisting of an intricate three-dimensional (3D) mesh of proteins that provides complex chemical, electrical and mechanical signalling.[1] Given this complexity as well as the limitations of *in vivo* studies,[2] it is important to develop *in vitro* models able to recapitulate the brain connectivity at various levels and ultimately, provide a mimic of the human brain suitable for preclinical applications.[3] By reproducing cell to cell and cell to ECM interactions so to mimic the *in vivo* microenvironment, 3D tissue engineering promotes more physiological responses than conventional 2D cultures.[4] Toward this goal, several 3D supporting materials or scaffolds have been developed, tested and applied.[5] Among them, emerging carbon-based materials, such as carbon nanotubes (CNTs) [6], graphene oxide [7] and graphene foam (GF) [8] have high mechanical stability, high porosity and dense interconnectivity, providing a 3D microenvironment beneficial for cell growth and interaction.[9]

My Work

In my Ph.D., I aimed to construct 3D neural scaffolds based on carbon materials especially graphene and carbon nanotubes (CNTs) and explore the regulation of these scaffolds for specific application in neural cultures. To achieve these goals, I combined chemical vapor deposition (CVD) and nano-fabrication for the preparation of different kinds of scaffolds and then used these scaffolds for the neural cultures. In the characterization of neural culture part, I mainly used optical imaging methods, particularly immunochemistry and calcium imaging, to investigate the neuronal network morphology and electrical dynamics of reconstructed 3D primary cultures from rats. These are my main results:

1) By using Fe nanoparticles confined to the interlamination of graphite as catalyst, we have obtained a fully 3D interconnected CNT web through the pores of graphene foam (GCNT web) by *in situ* chemical vapor deposition. This 3D GCNT web has a thickness up to 1.5 mm and a completely geometric, mechanical and electrical interconnectivity. Dissociated cortical cells cultured inside the GCNT web form a functional 3D cortex-like network exhibiting a spontaneous electrical activity that is closer to what is observed *in vivo*.

Moreover, we have explored the application of this functional 3D cortex-like network:

2) By co-culturing and fluorescently labelling glioma and healthy cortical cells with different colours, a new *in vitro* model is obtained to investigate malignant glioma infiltration. This model allows reconstruction of the 3D trajectories and velocity distribution of individual infiltrating glioma with an unprecedented precision. The model is cost-effective and allows a quantitative and rigorous screening of anti-cancer drugs.

3) We have fabricated a 3D free-standing ordered graphene (3D-OG) network with the pore size of 20 μm, the skeleton width of 20 μm and an exact 90° orientation angle between the building blocks. Extensive interconnectivity of graphene sheets allows 3D-OG scaffolds to be free-standing and to be easily manipulated. When primary cortical cells are cultured on 3D-OG scaffolds, the cells form well-defined 3D connections with a cellular density similar to that observed when cells were cultured on 2D coverslip. In contrast to the 2D coverslips culture, astrocytes cultured on 3D-OG scaffolds did not have a flat morphology but had a more ramified shape similar to that seen in vivo conditions. Moreover, neurons on 3D-OG scaffolds had axons and dendrites aligned along the graphene skeleton allowing the formation of neuronal networks with highly controlled connections. Neuronal networks grown on 3D-OG scaffolds had a higher electrical activity with functional signaling over a long distance.

4) We have constructed a novel scaffold of three-dimensional bacterial cellulose-

graphene foam (3D-BC/G) for neural stem cells (NSCs) *in vitro*, which was prepared via *in situ* bacterial cellulose interfacial polymerization on the skeleton surface of porous graphene foam. We found that 3D-BC/G can not only support NSCs growth and adhesion, but also keep NSCs stemness and enhanced its proliferative capacity. Further phenotypic analysis indicated that 3D-BC/G can induce NSCs selectively to differentiate into neurons, forming a neural network in short time. It was also meanwhile demonstrated to have good biocompatibility for primary cortical neurons and enhanced neuronal network activities by measuring calcium transient.

Introduction

The brain, spinal cord, and retina constitute the central nervous system (CNS) that is responsible for integrating sensory information from the entire body and coordinating movement accordingly.[10] The CNS is a highly specialized network of billions of neurons and neuroglia cells. Neurons are electrically excitable cells which transmit information through electrical and chemical signals through synaptic transmission. Neurons in the nervous system represent a fundamental element that consist of soma (cell body), axons, and dendrites. The soma contains a prominent nucleus and nucleolus therein. Axons convey impulses away from the soma via microtubules and neurofilaments. Dendrites receive and transmit electrical signals to the neuron cell body and the axons conduct action potentials to dendrites of nearby cells.[11] Glial cells are non-neuronal cells that constitute a supportive element of the nervous system. They maintain homeostasis, form myelin, and provide support and protection of neurons in both the peripheral nervous system (PNS) and the CNS.[12] Both neurons and glial cells are embedded in an extracellular matrix (ECM) consisting of an intricate three-dimensional (3D) mesh of proteins, for example, collagens, aggrecan, laminin and so on, to form the microenvironment that serves not only as a structural foundation for neurons and glial cells but also as a source of 3D biochemical and biophysical cues that trigger and regulate the physiological and pathological processes in the CNS.[13]

To construct a more physiologically relevant microenvironment *in vitro*, 3D culture systems, especially material-based 3D assemblies of neurons, have been developed for overcoming the limitations of 2D cell culture. Material-based 3D assemblies of neurons usually use porous substrates that can support cell growth and network organization in a manner that is analogous to how the brain works.[14] In contrast to 2D culture systems, 3D culture systems not only preserve the natural 3D ECM structure, but also more accurately represent the actual microenvironment that leads to differences in cell morphology, viability, migration, proliferation, and gene expression.[15] Thus, 3D cell culture has become a necessary method for *in vitro* researches. Currently, numerous

materials in different formats are being used as scaffolds to support the 3D culture of neurons or even tissues from never system. To improve biocompatibility or for special uses, scaffolds can be structural modified, mechanically tuned, or biochemically functionalized, all of which are intended to provide different cues for promoting the attachment, neuron network complexity, and specific neuronal regulation,[16] and a variety of fabrication processes have been developed or adapted to enhance these properties.[17]

2.1 The History of 3D Culture

To develop 3D cell culture systems, scientists in the field of tissue engineering and regenerative medicine all around the world have studied biochemical factors and artificial 3D matrices through a combination of cell biology, materials science, and engineering methods.[18] Such work began in the 1980s when the encapsulation of de-differentiated chondrocytes in a 3D culture system was found to restore their *in vivo* phenotype, including their shape and their expression of cartilaginous markers.[19] Similarly, mammary gland epithelial cells grown in a 3D environment were found to stop dividing uncontrollably and to assemble into acinar structures, as well as to establish a *de novo* basement membrane.[20]

These observations demonstrated that the dimensional aspect of a cell culture system is a crucial fate determinant and that culturing cells in a monolayer drives abnormal cell function or de-differentiation, whereas culturing in 3D systems leads to a more physiologically relevant state.[21] In a 3D cell culture, cells are usually grown in a cell-cell or cell-scaffold arrangement that provides a microenvironment that is closer to the *in vivo* microenvironment than that of a 2D surface culture system and that is more conducive to cell growth, migration, proliferation, and differentiation.[22] Over the last three decades, tremendous efforts have been put into the development of a variety of 3D culture systems, and three main types have emerged.[23] The first is material-free 3D cell spheroids, which can be generated in cell suspensions by the application of external physical forces. The hanging drop method, the forced floating method, and agitation-

based approaches are the most commonly used methods to culture 3D cell spheroids.[24] These approaches are advantageous as it uses the natural tendency of cells to aggregate, the cell guided assembly of 3D environment and the possibility to obtain induced neurons in different ways.[25] However, cells cultured in these system usually tend to suffer from high variability, due to the stem cell clone-ability, and size limitation and formation of necrotic cores due to the insufficient oxygen and nutrient diffusion. **Figure 1a** shows that human induced pluripotent stem cells (hiPSCs) encapsulated in Matrigel, result in spontaneous development of cerebral organoids that can model and recapitulate the distinct characteristics of microcephaly, a disorder that has been difficult to obtain with in vivo rodent models.[26]

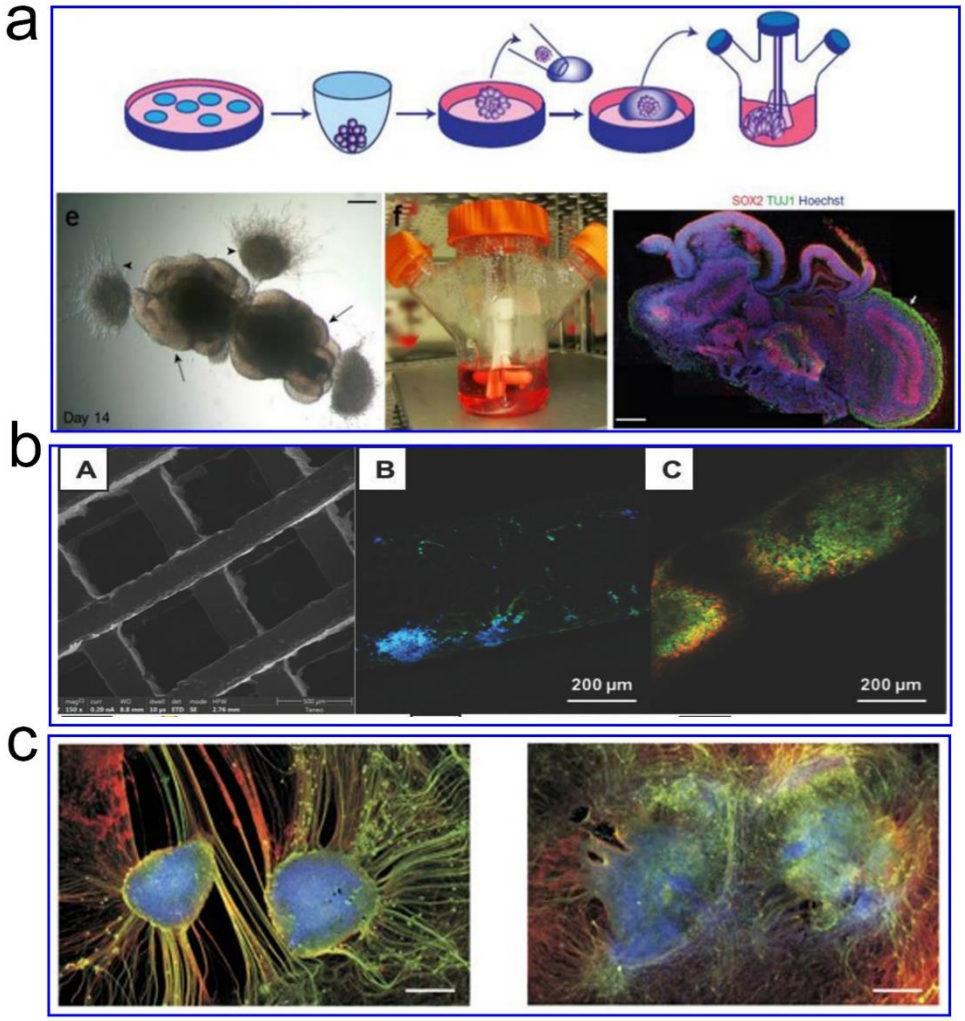

Figure 1. Representative three types of 3D culture systems. a) a human pluripotent

stem cell-derived three-dimensional organoid culture system, termed cerebral organoids, that develop various discrete, although interdependent, brain regions was developed.[26] b) MWCNTs were homogeneously distributed inside the 3D bio-printed scaffolds to support primary cortical neurons growth and neural stem cell differentiation.[27] c) Segregated spinal explants were cultured to study the functional reconnection.[28] See the details from the references.

The second is material-based 3D assemblies of cells that can be fabricated by seeding cells on an acellular 3D porous scaffold. The scaffold support the growth of cells thus providing a 3D microenvironment that mimics the structure of the ECM for the growth of engineered cells, tissues, and organs, and these scaffolds provide excellent *in vitro* models for studying cellular responses in a setting that mimics *in vivo* environments.[29] **Figure 1b** shows that multi-wall carbon nanotubes (MWCNTs) were homogeneously distributed inside the 3D printed scaffolds. 0.1% MWCNT-incorporated scaffolds greatly promoted outgrowth of primary cortical neurons and NSC-differentiated cortical neurons in the presence of electrical stimulation.[27]

The third kind of 3D culture is explanted cultures which can be obtained through techniques that allow growing of intact tissues *in vitro*. Slices of tissues dissected from the animal body can be freshly used for experimental purposes that need cells which cannot be harvested. Otherwise they can be cultured using supporting membrane insert (organotypic cultures). These approaches aim to retain the complex 3D organization of tissues *in vitro*. However, usually the slices lost the *in vivo* function after removal from the body.[30] In addition, the ability to rebuild their connections *in vitro* has been applied in tissue engineering to study the reconnection of segregated spinal explants through the application of biocompatible materials as neuronal prostheses for possible *in vivo* application and injury repair (**Figure 1c**).[28] Taken together, cells, in 3D culture systems, can communicate well with each other, the ECM, and their microenvironment in a spatial environment that has significant effects on a variety of cellular functions such as proliferation, differentiation, morphological changes, gene and protein expression.[31]

2.2 The Advantages of 3D Culture

In traditional 2D culture systems, cells attach on a flat surface which provides all cells with the same concentrations of nutrients and growth factors from the culture medium during the cell growth.[32] In terms of morphology, cells attached on 2D surfaces often show spindle or flat and round shapes. Abnormal cell morphology in a homogenous culture system will influence many cellular functions such as cell proliferation, differentiation, gene expression, and protein expression.[33] As a result, cells cultured as 2D monolayers might not behave as they would *in vivo* because 2D cultures cannot accurately recapitulate the in *vivo* 3D growth structure.[23c] In order to improve cellular function and behavior in 2D cell culture, a lot of new technologies have been developed to build topographical features onto 2D substrates, including patterned polydimethylsiloxane (PDMS) *via* micro-contact printing,[34] designed silicon surfaces,[35] and patterning of nano-roughness on glass surfaces by micro-fabrication.[36] Many new materials, such as graphene[37] and graphene oxide,[38] are also used to culture different kinds of cells. However, whether or not, these endeavors to improve cell function better mimick *in vivo* behaviors still needs further investigation.

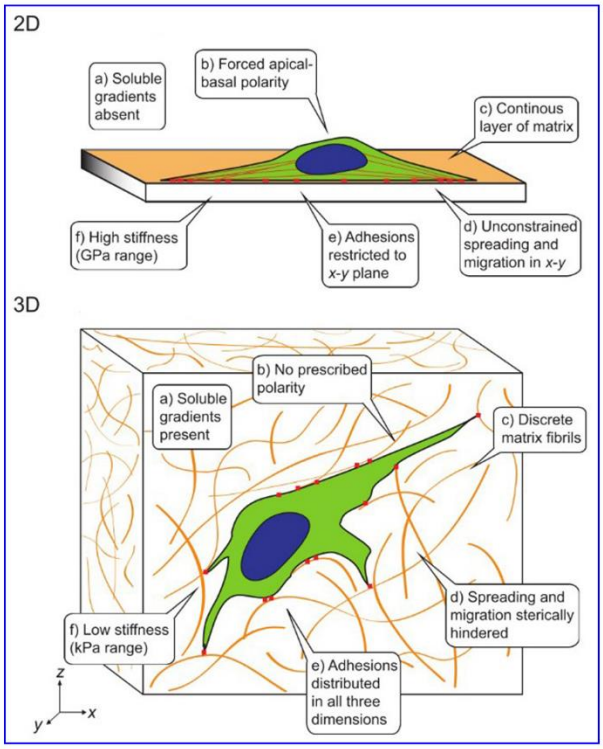

Figure 2. Adhesive, topographical mechanical and soluble cues in 2D and 3D culture systems, which are summarized in table 1.[21]

Table 1. Comparison of 2D and 3D culture system.

2D culture system	3D culture system
High stiffness surfaces provide supraphysiological mechanical signals.	Tunable, relatively low stiffness environment closer to that of tissues.
Continuous, flat surface available for unencumbered adhesion, spreading, and migration.	Nano- and micro-scale 3D surfaces provided by ECM fibers and matrix porosity guide and hinder cell motility.
Soluble gradients absent without microfluidics.	Gradients of soluble factors, nutrients, and oxygen based on diffusion through gel or cell aggregates.
2D geometry constrains morphogenesis and cell-substrate interactions dominate.	Free to self-organize in 3D. In multicellular structures, cell-cell interactions dominate.
Automatic apical-basal polarization.	Embedded cells generate apical-basal polarity on their own.

(https://mimetas.com/article/3d-cell-culture-vs-traditional-2d-cell-culture)

In contrast, when embedded in 3D culture systems, cells generally form spheroids within or on a scaffold or in a suspension medium. In cell spheroids, cells can interact with the ECM and with each other in 3D space, which more closely mimics the *in vivo* microenvironment. Thus, cell morphology in such systems tends to mimic the morphology of the cells in the body (**Figure 2**). In addition, 3D spheroids consist of proliferating, quiescent, apoptotic, and necrotic cells.[39] Thus the morphology and the communication among cells cultured in 3D systems is closer to what occurs *in vivo*, and the resulting 3D model usually simulates the *in vivo* microenvironment better than

2D systems.[40] Furthermore, cells in 3D cultures differ significantly from cells in 2D cultures in terms of gene and protein expression.[19, 41] 3D culture systems promote the expression of ECM proteins like fibrinogen, fibronectin, and laminin-1,[41] and it has been demonstrated that collagen I hydrogels can facilitate the development of 3D *in vitro* bioengineered tumors that significantly upregulate the expression of vascular endothelial growth factor-A and hypoxia-inducible factor-1α genes.[42] Christina and colleagues found that the expressions of hormone receptors and differentiation markers in growth plate chondrocytes and articular chondrocytes are highly influenced by culture conditions.[43]

2.3 Biomimetic scaffolds for 3D cell culture

2.3.1 Functional and biomimetic scaffolds design

Tissue engineering and regeneration based on biomimetic scaffolds aim to construct *in vitro* models able to replicate the *in vivo* microenvironment or supply organs or tissues for injury repair by combining material scaffolds, biochemical signals, and cells. The greatest challenge entails the creation of a suitable, biocompatible 3D support and interface to allow for *ex vivo* or *in vivo* cell-induced tissue formation.[44] Scaffolds used for cell culture usually have porous structures that can serve as a 3D microenvironment for cell growth and the regulation of growth factors and can provide communication between cells and between cells and the ECM. Thus the scaffold supports the attachment, proliferation, and differentiation of cells in a manner similar to the *in vivo* environment.[45] In this case, when researchers design the scaffold, they should first think about biocompatibility with specific cell types and with the various factors that will be used to control the cells and modulate their activities. Scaffolds must have the appropriate mechanical and chemical properties to support the necessary cell functions, while at the same time it is critical that the scaffold materials do not induce inflammatory responses.[46] Large numbers of studies over the past decades have generated material systems that enabled the development of our understanding of how biochemical (e.g., cell adhesion ligands, soluble factor immobilization, and chemical

functional groups) and biophysical (e.g., structural properties, mechanical properties, degradability, and electrical conductivity) cues affect cells (**Figure 3**).[13] In particular, selection of suitable biomaterials as the scaffolding medium in neural tissue engineering is critical, considering the complex and intricate nature of the human nervous system.[47] In general, neural scaffold design should exhibit three key characteristics. Firstly, neuro-compatibility that allows adherence and growth of surrounding nerve cells; secondly, elastic properties that can mimic the mechanical aspects of native nerve tissues; thirdly, hierarchical microarchitecture that displays biomimetic features as well as physiochemical properties of human neural tissue extracellular matrices. In addition to the above three principal criteria, the capacity for electroconductivity within the scaffold is also desirable.[10, 48] There are currently two major types of 3D scaffold materials, including natural and artificial materials. Synthetic organic and inorganic porous materials are the two main kinds of artificial materials. Biomaterials from natural components [49], such as collagen hyaluronic acid and Matrigel, have been widely used for 3D cultures; however, scaffolds made of synthetic materials, such as poly(lactic-co-glycolic acid) and others, exhibit better long-term performance [50]. Emerging carbon-based materials, such as carbon nanotubes (CNTs) [6], graphene oxide [7] and graphene foam (GF) [8] have high mechanical stability, high porosity and dense interconnectivity, providing a 3D microenvironment beneficial for cell growth and interaction [9].

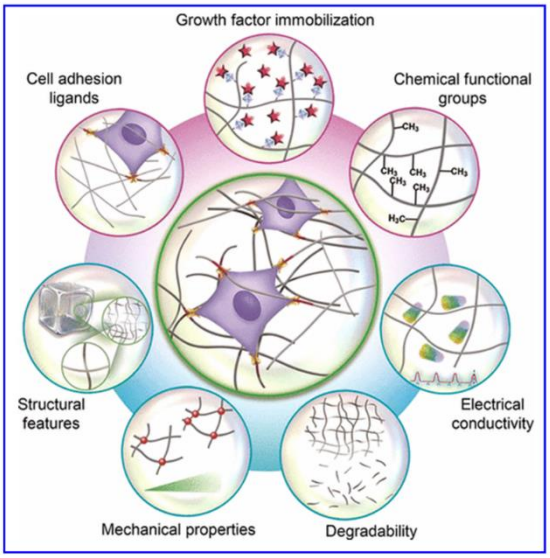

Figure 3. Biomimetic material design considerations for bio-engineering 3D cell microenvironment. The design considerations can be generally divided into two classes, which are biochemical (e.g., cell adhesion ligands, soluble factor immobilization, and chemical functional groups) and biophysical design considerations (e.g., structural features, mechanical properties, degradability, and electrical conductivity).[13]

2.3.2 Natural materials

Materials such as gelatin, laminin, collagen, alginate, and hyaluronic acid are natural products from the body or plants and thus possess biological properties, such as bioactive motifs and cell-binding domains for communication between the cell and the ECM, that are critical for the maintenance of the natural tissue phenotype and function. Collagen type-I is the most popular natural organic material used for 3D culture systems. It is the major component of the ECM and allows for proper cell adhesion and migration,[51] and it has been widely used in 3D culture systems due to its excellent biocompatibility, mechanical strength, degradability, and limited immunogenicity.[52] Collagen hydrogel tubes with 180 μm diameters were used as scaffolds to create aligned astrocyte bundles, which were shown to guide the alignment of neurites and thus mimic the glial tubes that direct the migration of neural progenitor cells (NPCs) *in vivo*.[53] Matrigel™ is a bio-matrix hydrogel that is derived from the Engelbreth–Holm–Swarm (EHS) tumor,[54] and it is particularly useful because it contains collagen, laminin, entactin, and other important growth factors that mimic the ECM. Self-organized neural structures that resemble those present in an early developing cerebral organoid were created using human induced pluripotent stem cells (hiPSCs) grown on Matrigel™ scaffolds.[55] Matrigel™ has high biocompatibility and high telomerase activity, which can promote stem cell proliferation. **Figure 4a** shows that neural stem cells encapsulated into a 2 mm thick peptide nanofiber hydrogel scaffolds differentiated into progenitor neural cells, neurons, astrocytes and oligodendrocytes when cultured in serum-free medium. Moreover, cell survival studies showed that neural cells in peptide

hydrogels thrive for at least 5 months.[56] In **Figure 4b**, Xiaowei Li and coworkers developed a novel peptide sequence with only 12 amino acids , similar to tissue-derived full laminin molecules, supported human neural stem cells (hNSCs) to attach and proliferate to confluence for continuous passage and subculture. This short peptide also directed hNSCs to differentiate into neurons.[57] Maria Teresa Tedesco and coworkers investigated the use of a widely popular polysaccharide, chitosan (CHI), for the fabrication of a microbead based 3D scaffold to be coupled to primary neuronal cells (**Figure 4c**).[58]

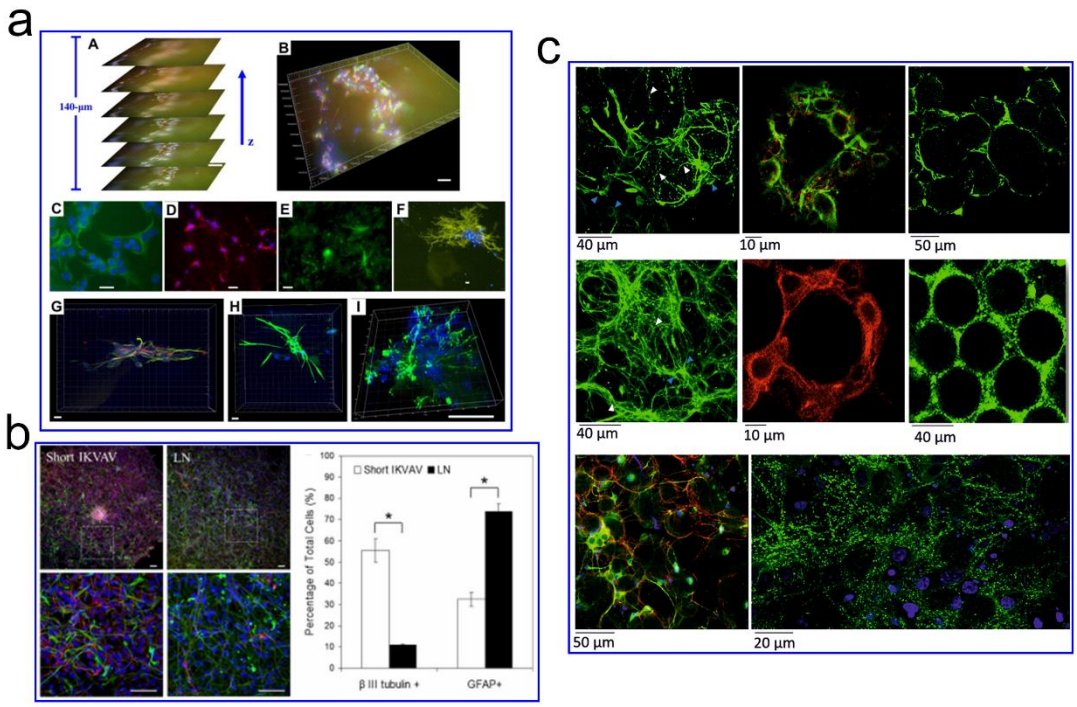

Figure 4. Examples of natural materials used in neural tissue engineering. a) Neural stem cells encapsulated into a 2 mm thick peptide nanofiber hydrogel scaffolds differentiated into progenitor neural cells, neurons, astrocytes and oligodendrocytes. Neural progenitors were stained with anti-nestin (green), neurons were stained with anti-Tuj1 (red) in subtitle C, D, G. Astrocytes were stained with anti-GFAP (green) in subtitle E, H. Oligodendrocytes were stained with anti-GalC (green) in subtitle F, I. Cells nuclei were stained with DAPI (blue).[56] b) Differentiation of human neural stem/progenitor cells cultured on substrates coated with short IKVAV peptides and whole Laminin at the day 14. Short IKVAV peptide induced

significantly higher rate of differentiation into neurons and lower rate to glial cells compared with Laminin.[57] c) A widely popular polysaccharide, chitosan (CHI), for the fabrication of a microbead based 3D scaffold to be coupled to primary neuronal cells. MAP-2 (green) and Synapsin (red).[58] See the details from the references.

However, although natural materials can maintain many of their biological functions *in vitro*, they suffer from poor mechanical properties and poorly defined compositions under such conditions and they are usually difficult to modify biochemically because they cannot be designed from the bottom up like synthetic materials.[59] Natural materials might also be limited in their clinical application due to the risk of immune rejection and disease transfer.[60] To improve the usefulness of these natural ingredients, it is necessary to improve their mechanical properties and stability, for example, through with organic polymers.

2.3.3 Synthetic organic scaffolds

Synthetic organic materials are often made from polymers like polycaprolactone (PCL), polyethylene glycol (PEG), polyvinyl alcohol (PLA), and poly(hydroxyethyl methacrylate) (PHEMA).[61] These scaffolds can be synthesized with controlled physical and chemical properties to meet specific applications and are typically highly reproducible and simple to manufacture.[62] There are two important features of synthetic organic materials. First, they are usually inert but biodegradable. The scaffolds degrade during cell growth to make space for the cells to synthesize their own ECM and to create their own scaffold.[63] Second, they can be decorated with immobilized biological components to encourage natural cell-matrix interactions. For example, PLC nanofibers were used to promote neural stem cell (NSC) adhesion and to support differentiation and neurite outgrowth,[64] and 3D polyhydroxylalkanoate nanofibers displayed suitability for NSC attachment, synaptic outgrowth, and synaptogenesis.[65] Zhenning Zhang and coworkers developed a soft 3D hydrogel from methacrylate-modified hyaluronic acid to mimic the brain environment and accelerates maturation of neurons from human induced pluripotent stem cell (iPSC)-derived neural progenitor cells

(NPCs), yielding electrophysiologically active neurons within just 3 weeks (**Figure 5a**).[66]

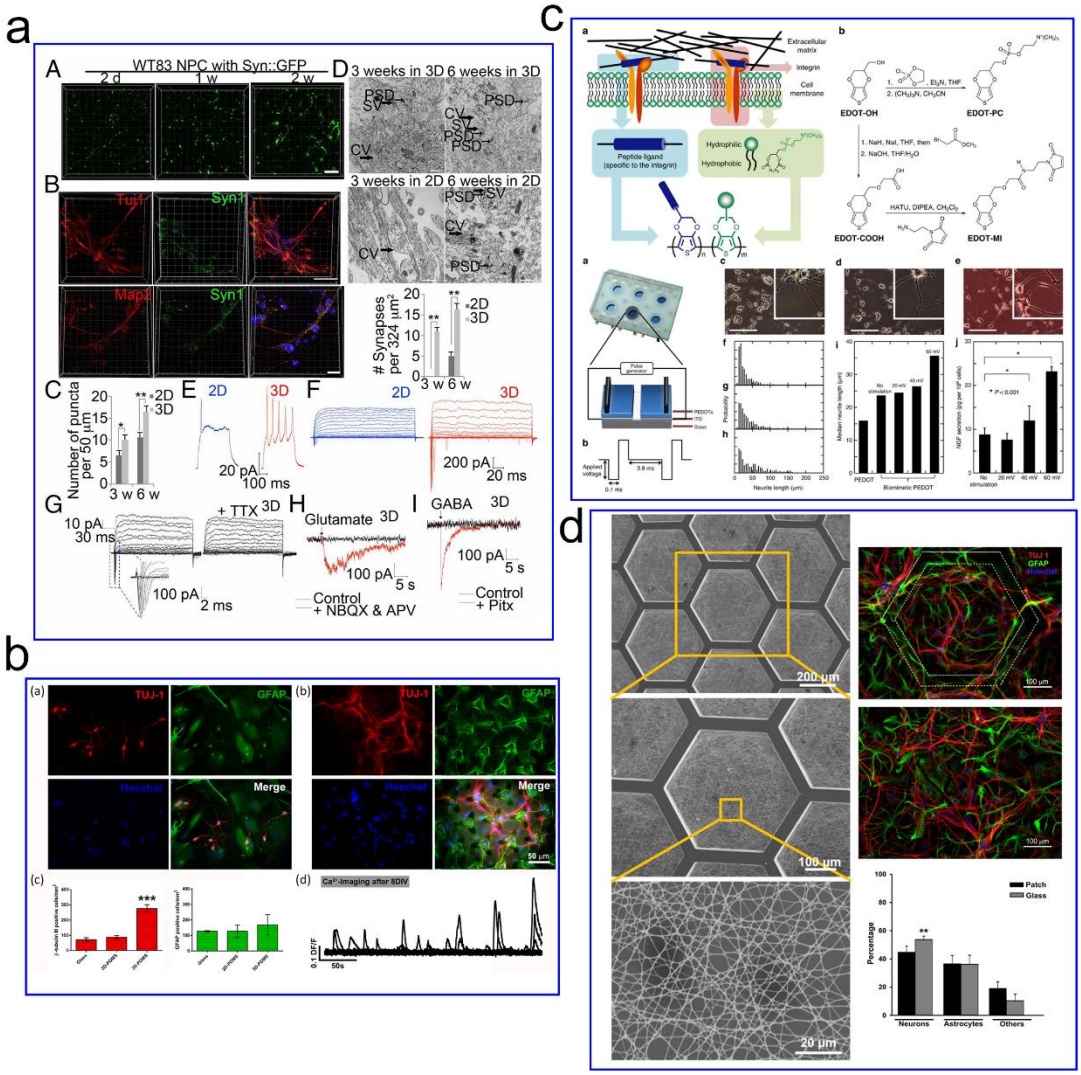

Figure 5. Examples of synthetic organic scaffolds used in neural tissue engineering. a) Rapid maturation of human iPSC-derived neurons in 3D layered polymer-hydrogels from methacrylate-modified hyaluronic acid. (A) Representative images of human iPSC-derived NPCs infected with Syn::GFP lentivirus after neural differentiation for the indicated times in 3D hydrogels. (B) Representative images of human iPSC-derived neurons stained for Tuj1 or Map2 (red), Syn1 (green), and DAPI (blue) in a 3D hydrogel. (C) Quantification of Syn1 puncta on Map2-positive neurites, showing that the density of Syn1-positive puncta in 3D culture was significantly higher after 3 weeks of culture and was even more significant after 6 weeks of

culture compared to 2D culture. (D) Representative images of an ultrastructural investigation of synaptogenesis by transmission electron microscopy (TEM) in control NPCs differentiated in 3D or 2D systems at the indicated times. CV, large clear vesicle; SV, synaptic vesicle. Quantification of the numbers of synapses in control NPCs differentiated in 3D or 2D systems at the indicated times. The density of synapses was significantly higher in 3D culture compared with 2D culture after both 3 weeks and 6 weeks of differentiation. (E) Representative whole-cell current clamp recordings of human iPSC-derived neurons after 3 weeks of differentiation in 3D or 2D systems. Spikes in activity were observed following current injection. In response to steps of depolarizing current, only neurons in 3D culture, and not in 2D culture, for 3 weeks showed firing trains of action potentials (F) Representative voltage clamp recording of a 3D or 2D cultured neuron held at −75 mV and then stepped through a series of voltages (−80 to +20 mV) in 5 mV increments. (G) Representative voltage clamp recording of a 3D cultured neuron before and after application of 1 μM tetrodotoxin (TTX), showing the rapid maturation of 3D cultured cells. (H) Response to glutamate in the presence and absence of the glutamate receptor blockers 20 μM NBQX and 50 μM APV. (I) Response to γ-aminobutyric acid GABA in the presence and absence of 50 μM picrotoxin (Pitx), indicating the presence of functional GABA receptors, as these events were blocked by 50 μM picrotoxin.[66] b) Morphological differences of primary hippocampal neurons cultured 2D (a) and 3D (b) PDMS substrates. Number of neurons and astrocytes (c) for mm2 after 8 DIV were calculated. Example traces of calcium activity from neuron growth on the 3D PDMS lattice (d).[67] c) Ethylenedioxythiophene (EDOT)—based polymers was designed and used for electrical stimulation on cell behavior. Neurite outgrowth is enhanced greatly on this new conducting polymer with electrical stimulation.[68] d) After electrospinning and crosslinking, the gelatin nanofibers on PEGDA microframe formed a high porosity nanonet with pore sizes smaller than 8 μm and hippocampal neurons after 8–10 DIV in astrocyte conditioned medium on culture patch were different from that on 2D glass.[69] See the details from the references.

Figure 5b shows that an elastomer polydimethylsiloxane (PDMS) producing lattice-type scaffolds from a photolithography-defined template, which can be used as primary neuron culture. As expected, a much higher cell number was found in the 3D PDMS lattices compared to the 2D culture. It was also found that there was a higher neuron-to-astrocyte ratio and a higher degree of cell ramification in the 3D culture compared to the 2D culture due to the change of scaffold topography and the elastic properties of the PDMS micro-lattices.[67] In **Figure 5c**, Bo Zhu and coworkers developed a cell membrane-mimicking conducting polymer possessing several attractive features. This polymer displays high resistance towards nonspecific enzyme/cell binding and recognizes targeted cells specifically to allow intimate electrical communication over long periods of time. This material is capable of integrating biochemical and electrical stimulation to promote neural cellular behavior. Neurite outgrowth is enhanced greatly on this new conducting polymer.[68] A patch method was developed for culture of primary neurons on a monolayer of gelatin nanofibers electrospun and crosslinked on a honeycomb microframe of poly (ethylene glycol) diacrylate (PEGDA). This method allows us to minimize exogenous material contact of cells and largely increase the exposure area of cells to the culture medium (**Figure 5d**).[69]

2.3.3 Carbon-based scaffolds

Besides natural and synthetic polymers, many inorganic porous 3D structures have been utilized to fabricate cell culture scaffolds, Almost all of these solid materials have very high mechanical stability, and this along with their high porosity and tight interconnectivity make them ideal for highly interactive 3D cell culture.[9] The high porosity of these scaffolds allows for deeper and more uniform nutrient transport, while at the same time cells can freely migrate along the structure without significant resistance.[70] Therefore, the 3D porous structure should allow the migration of cells but not limit the communication between cells and cells with microenvironment. Carbon-based materials, especially carbon nanotubes (CNTs) and graphene have made over the past few decades huge contributions in *in vitro* tissue model constructions and tissue

regeneration.[71] Because of their unique one dimensional nanotube structures, CNTs support an intensive interaction with and among cells, which boosts electrical signalling (**Figure 6a**) [72], modulates neuronal growth [73] and guides the functional reconnection of segregated spinal cord slices [5c]. Bosi and collaborators were able to fabricate 3D PDMS scaffolds with pores layered by an irregular CNT carpet stably entrapped in the PDMS matrix. These mixed 3D scaffolds were applied to study the activity of primary hippocampal neurons *in vitro* (**Figure 6b**).[74] In the same group, CNTs were directly grown on a supporting silicon surface by a chemical vapor deposition (CVD)–assisted technique. When primary neurons were cultured on the substrates, they developed neuronal networks showing increased electrical activity when compared to a similar network developed on a control glass surface.[75] Hanein and co-workers used CNT electrodes as conduits for retinal prosthetics. Specifically, a semiconductor nanorod CNT (NR-CNT) platform was prepared for wire-free, light induced retina stimulation.[76] CdSe/CdS NRs were covalently attached onto neuro-adhesive, three-dimensional CNT surfaces using polymerized acrylic acid. The interface provided highly efficient photosensitivity and enabled binding between the tissue and the optoelectronic device. The NR-CNT electrodes exhibited good efficiency (i.e., lower threshold for evoking action potentials), durability, flexibility, and demonstrated generation of localized stimulation. In particular, the capacitive charge transfer mechanism and low impedance of CNTs underlined the construction of an effective platform for efficient neuronal light induced stimulation.[76] In another study, the same group used CNT electrodes to stimulate retinal ganglion cells (RGCs) in a mouse model for outer retinal degeneration.[77] Besides on CNTs, graphene, graphene oxide (GO), reduced graphene oxide (rGO), and their composites further containing metals or polymers) offer exciting opportunities to stimulate cells in artificial scaffolds, primarily due to their tunable surface properties. In particular, the physicochemical properties of graphene-based materials intimately influence surface interactions of individual cells and cell populations.[78] Several studies explored applications of graphene or GO as scaffolds for neural tissue engineering (**Figure 6d, e**).[7, 79] Graphene foams (GFs) have high

mechanical rigidity, can reach one millimetre in height, and are biocompatible, promoting the differentiation of neural stem cells in neurons (**Figure 6e**)[7] and the synchronization of neuronal network activity (**Figure 6d**).[80]

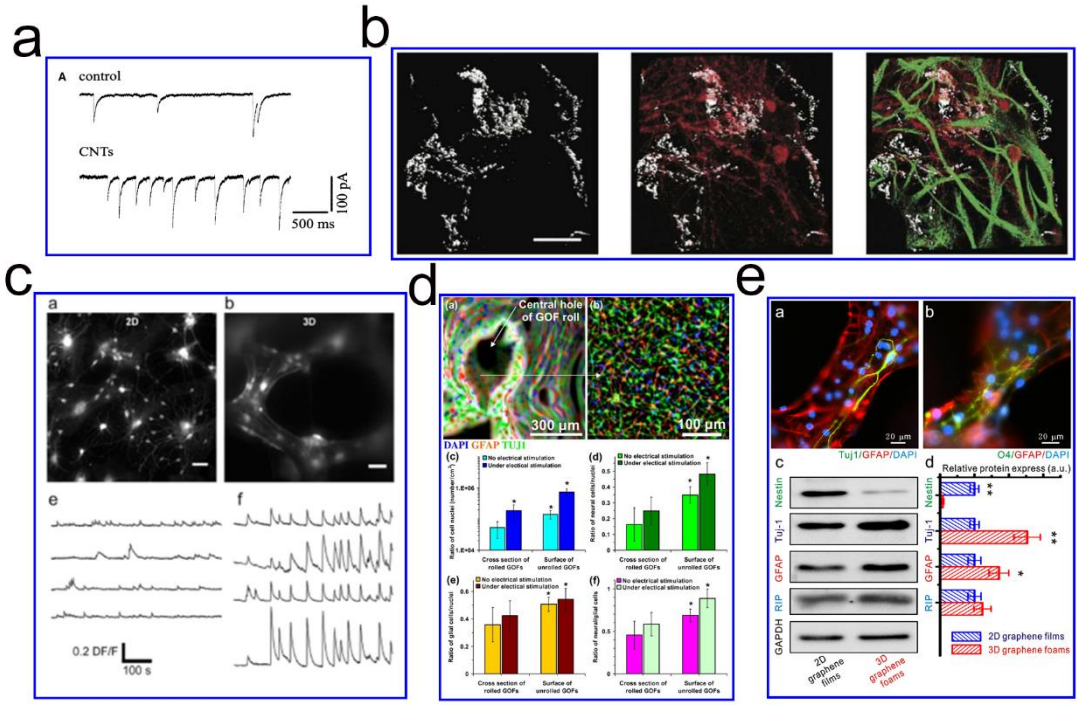

Figure 6. Carbon-based materials have been widely used for 3D cell culture scaffold preparations. a) Neurons grown on a CNT substrate displayed increased spontaneous activity and firing.[72] b) 3D hippocampal culture growth on a PDMSMWCNT scaffold. The carbon nanotubes are reported in grey and acquired using the reflection mode of a confocal microscope; in red there are the neurons and in green the astrocytes.[74] c) 3D hippocampal neuronal networks developed on 3D GF showed higher activities and synchronization compared to the neuronal networks on 2D glass.[80] d) Fluorescence images of differentiated human NSCs on a cross section and the interior surface of a rolled graphene oxide foam (GOF) scaffold after 2 weeks of electrical stimulation. The nuclei, glial cells, and neural cells of the differentiated cells were stained by DAPI (blue) and with antibodies against GFAP (red) and Tuj1 (green), respectively.[76] e) Dfferentiation of NSCs on a 3D graphene foam scaffold. Representative fluorescence images of differentiated NSCs under differentiation conditions. The cells were immunostained with Tuj-1 for neurons

(green), O4 for oligodendrocytes (green), GFAP for astrocytes (red), and DAPI for nuclei (blue).[7] See the details from the references.

As mentioned before, hierarchical microarchitecture that displays biomimetic features as well as physiochemical properties of neural tissue extracellular matrices is essential for 3D neuronal scaffold designs. Nevertheless, although 2D CNT-based bricks such as forests of vertically aligned CNTs,[81] films of CNT building blocks[82] and extended 2D meshes of CNT[28] have been deposited on different substrates to form dense blocks useful for several applications, cells could not migrate into the deep layers of these CNT assemblies. On the other hand, CNTs embedded in hydrogel or porous organic structures[83] can host 3D cellular assemblies but do not have well-defined mechanical or electrical connections. Genuine 3D networks of CNTs have been produced by chemical infiltrating aqueous CNT dispersion into porous ceramic.[84] However, there is no additional crosslinking existing between the individual CNTs so that the electrical and mechanical connectivity is random and not fully controlled. Therefore, the first motivation of my PhD researches is the development of a 3D web of CNTs with a fully geometric, electrical and mechanical interconnectivity allowing the reconstruction of *in vitro* neuronal networks mimicking the *in vivo* brain connectivity which could be used for the screening of drugs against a variety of diseases,[85] such as malignant glioma infiltration. In particular, hierarchical 3D graphene-carbon nanotubes (GCNT) web was prepared where graphene foam supported the 3D growth of cells and CNTs served as the nano-interface with cells.

Results

This section is the sum of the published papers and papers in preparation during my PhD. They were finished by me and my collaborators under the supervision of Prof. Vincent Torre and his collaborators. In detail:

- In the first article published in Advanced Materials, I fabricated and characterized the GCNT web and prepared the primary cortical cell cultures. We chose cortical neurons in this work for the construction of glioma infiltration model afterwards. Then I performed the calcium imaging and the analysis of the data. I performed the immunofluorescence and living cell imaging with my collaborators and analyzed the data. I prepared the figures and wrote the manuscript with all the authors.
- In the second article ready to submit, I fabricated and characterized the 3D free-standing ordered graphene network and prepared the primary cortical cell cultures, carried out the calcium imaging and analyzed the data of calcium imaging and immunofluorescence. I prepared the figures and wrote the manuscript with all the authors.
- In the third article submitted, I set the culture protocol and performed calcium imaging experiments. I carried out data analysis, figure preparation and manuscript writing with all the authors.
- In the fourth article published in Carbon, I supervised and fabricated the 3D hybrid graphene (3D-HG) consisting of 3D controllable graphene skeletons and 2D graphene film with my collaborator. I participated in the writing of the manuscript.

I actively participated in designing all these works.

3.1 A Fully 3D Interconnected Graphene–Carbon Nanotube Web Allows the Study of Glioma Infiltration in Bioengineered 3D Cortex-Like Networks

Miao Xiao[#], Xiaoyun Li[#], Qin Song, Qi Zhang, Marco Lazzarino, Guosheng Cheng,[*] Francesco Paolo Ulloa Severino,[*] and Vincent Torre[*]

Advanced Materials

Vol. 30 • No. 52 • December 27 • 2018

www.advmat.de

ADVANCED MATERIALS

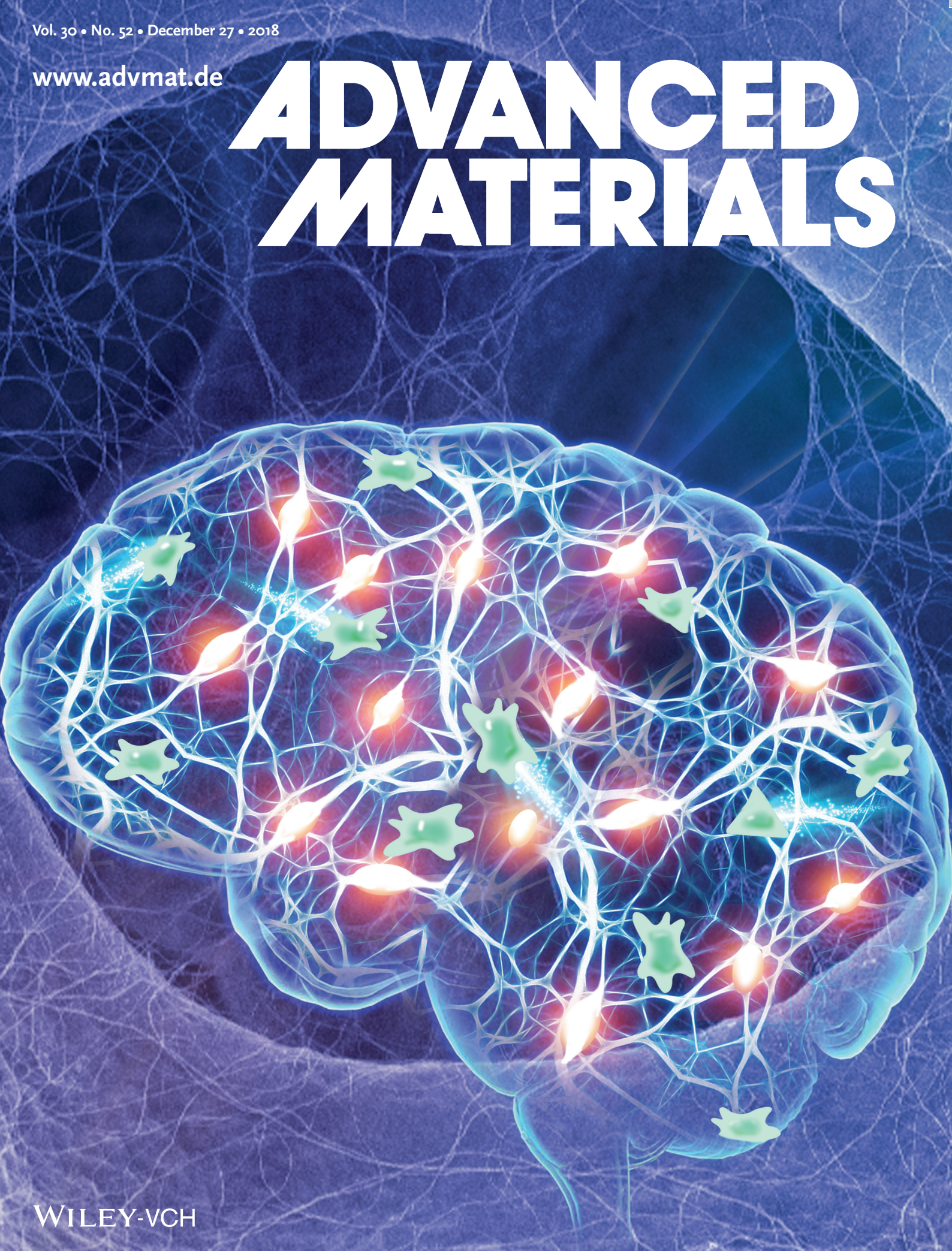

WILEY-VCH

ADVANCED MATERIALS
www.advmat.de

A Fully 3D Interconnected Graphene–Carbon Nanotube Web Allows the Study of Glioma Infiltration in Bioengineered 3D Cortex-Like Networks

Miao Xiao, Xiaoyun Li, Qin Song, Qi Zhang, Marco Lazzarino, Guosheng Cheng, Francesco Paolo Ulloa Severino,* and Vincent Torre**

Currently available 3D assemblies based on carbon nanotubes (CNTs) lag far behind their 2D CNT-based bricks and require major improvements for biological applications. By using Fe nanoparticles confined to the interlamination of graphite as catalyst, a fully 3D interconnected CNT web is obtained through the pores of graphene foam (GCNT web) by in situ chemical vapor deposition. This 3D GCNT web has a thickness up to 1.5 mm and a completely geometric, mechanical and electrical interconnectivity. Dissociated cortical cells cultured inside the GCNT web form a functional 3D cortex-like network exhibiting a spontaneous electrical activity that is closer to what is observed in vivo. By coculturing and fluorescently labeling glioma and healthy cortical cells with different colors, a new in vitro model is obtained to investigate malignant glioma infiltration. This model allows the 3D trajectories and velocity distribution of individual infiltrating glioma to be reconstructed with an unprecedented precision. The model is cost effective and allows a quantitative and rigorous screening of anticancer drugs. The fully 3D interconnected GCNT web is biocompatible and is an ideal tool to study 3D biological processes in vitro representing a pivotal step toward precise and personalized medicine.

The brain is formed by an intricate assembly of cellular networks, where neurons are embedded in an extracellular matrix (ECM) consisting of a dense 3D mesh of proteins that provides complex chemical, electrical, and mechanical signaling.[1] Given this complexity as well as the limitations of in vivo studies,[2] it is important to develop in vitro models able to recapitulate the brain connectivity at various levels and, ultimately, provide a mimic of the human brain suitable for preclinical applications.[3] Toward this goal, several 3D supporting materials or scaffolds have been developed, tested, and applied.[4] But further progress is needed: the combination of new materials with biotechnology can provide 3D tissue engineering with the tools to make a major step toward precise and personalized medicine.[5] Biomaterials from natural components,[6] such as collagen hyaluronic acid and Matrigel, have been widely used for 3D cultures. However, scaffolds made of synthetic materials, such as poly(lactic-*co*-glycolic acid) and others, exhibit better long-term performance.[7] Emerging carbon-based materials, especially carbon nanotubes (CNTs)[8] have been widely utilized to produce scaffolds with improved mechanical strength and conductivity.[9] CNTs with their 1D hollow structure and good

Dr. M. Xiao, Dr. X. Li, Dr. Q. Song, Prof. V. Torre
International School for Advanced Studies (SISSA)
via Bonomea 265, Trieste 34136, Italy
E-mail: torre@sissa.it
Dr. M. Xiao, Prof. V. Torre
Joint Laboratory of Biophysics and Translational Medicine
ISM-SISSA
Suzhou Industrial Park, Jiangsu 215123, China
Dr. Q. Song, Prof. V. Torre
Cixi Institute of Biomedical Engineering
Ningbo Institute of Materials Technology and Engineering
Chinese Academy of Sciences
Zhejiang 315201, China
Dr. Q. Song
School of Pharmaceutical Engineering
Zhejiang Pharmaceutical College
Ningbo, Zhejiang 315100, China
The ORCID identification number(s) for the author(s) of this article can be found under https://doi.org/10.1002/adma.201806132.

DOI: 10.1002/adma.201806132

Prof. Q. Zhang
School for Radiological and Interdisciplinary Sciences (RAD-X)
and Collaborative Innovation Center of Radiation Medicine of Jiangsu
Higher Education Institutions
Medical College of Soochow University
Suzhou Industrial Park, Suzhou, Jiangsu 215123, China
Dr. M. Lazzarino
IOM-CNR
Area Science Park, Basovizza, Trieste 34149, Italy
Prof. G. Cheng
CAS Key Laboratory of Nano-Bio Interface
Suzhou Institute of Nano-Tech and Nano-Bionics
Chinese Academy of Sciences
398 Ruoshui Road, Suzhou Industrial Park, Jiangsu 215123, China
E-mail: gscheng2006@sinano.ac.cn
Dr. F. P. Ulloa Severino
Cell Biology Department
Duke University Medical Center
335 Nanaline Duke Building Duke University Medical Center
Durham, NC 27710, USA
E-mail: francesco.ulloa@duke.edu

electrical properties allow intensive interactions with and among cells, which boost electrical signaling,[10] modulate neuronal growth,[11] and guide the functional reconnection of segregated spinal cord slices.[4c] Different kinds of assemblies based on CNTs have been realized for a variety of applications (Figure S1a–c, Supporting Information). In terms of biological applications, 2D CNT-based bricks such as forests of vertically aligned CNTs,[12] films of CNT building blocks,[9b] and extended 2D meshes of CNT[13] have been deposited on different substrates to form dense blocks useful for several applications, but cells could not migrate into the deep layers of these CNT assemblies. On the other hand, CNTs embedded in hydrogel or porous organic structures[14] can host 3D cellular assemblies but do not have well-defined mechanical or electrical connections. Genuine 3D networks of CNTs have been produced by chemical infiltrating aqueous CNT dispersion into porous ceramic.[15] However, there is no additional crosslinking existing between the individual CNTs so that the electrical and mechanical connectivity is random and not fully controlled. Therefore, the first motivation of the present work is the development of a 3D web of CNTs with a fully geometric, electrical, and mechanical interconnectivity allowing the reconstruction of in vitro neuronal networks mimicking the in vivo brain connectivity which could be used for the screening of drugs against a variety of diseases,[16] such as malignant glioma infiltration.

Malignant glioma is composed of mutated glia cells that generate brain tumors.[17] The motility and ability of malignant glioma to migrate is at the basis of metastases in healthy brain regions. In terms of malignancy, malignant glioma kills 94.5% of patients within 5 years after diagnosis.[18] Malignant glioma uses different roots to infiltrate the brain,[17,19] and its malignancy also stems from its ability to recover from surgical resection and its resistance to chemo and radio therapies.[20] At the moment, orthotopic models based on xenografts of malignant glioma cells on the whole brain of rats or mice are thought to be the best way to quantify malignant glioma infiltration. However, orthotopic models suffer from the use of immune-compromised animals and the obtained results could be affected also by species-differences.[21] Therefore, the second motivation of the present work is the development of in vitro models able to recapitulate the complex biology of malignant glioma infiltration.[22]

Graphene foams (GFs) have high mechanical rigidity, can reach more than one millimeter in height, and are biocompatible, promoting the differentiation of neural stem cells in neurons[23] and the synchronization of neuronal network activity.[4b] However, GFs have large pores ranging from 100 to 300 µm in diameter.[24] Consequently, the cellular assemblies that grow inside them are not dense.[24] To combine the advantages of both GF and CNTs, we constructed a hybrid scaffold made by graphene foam in situ growing carbon nanotubes to fill the pores.

A summary of the process for the fabrication of 3D CNT web through the pores of graphene foam (GCNT web) is illustrated in **Figure 1**a. Commercial 3D porous nickel foam[25] was used to prepare 3D GFs with a chemical vapor deposition (CVD) system. CH_4 molecules was heated to 950 °C diffused into the Ni lattice and released carbon atoms that subsequently precipitated as graphene on the Ni surface during the cooling process.[26] Then, the 3D graphene/nickel foam was used to support the in situ growth of CNTs. Iron nanoparticles were confined to the interlamination of graphite using the intercalated $FeCl_3$–graphite compound[27] as a catalyst during CNT growth. The catalyst was loaded upstream of the vapor flow, beside the graphene/nickel foam (Figure 1a, left panel). The CVD chamber was first heated to 1050 °C and was protected with a stream of Ar so that $FeCl_3$ evaporated and the Fe atoms were captured by the GF. Afterward, the CNTs grew in situ on

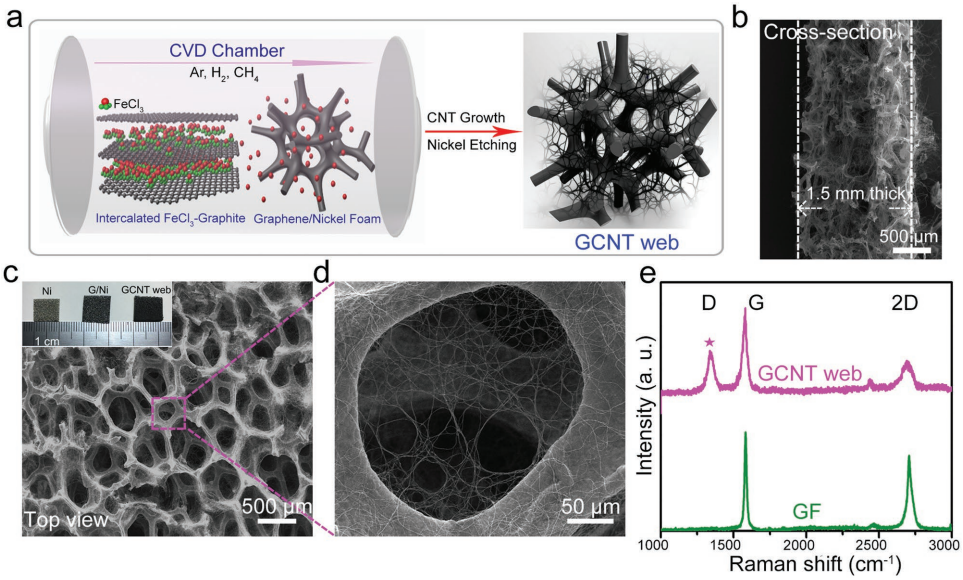

Figure 1. The fabrication and physical properties of GCNT web. a) Schematic illustration of the procedure for the in situ growth of CNTs inside GF scaffold. b) Representative SEM image of the GCNT web from the cross-section. c,d) Representative SEM images of the GCNT web with low- and high-magnification of the CNT web from the top view (inset: the optical images of porous nickel, graphene/nickel foam, and GCNT web). e) Typical Raman spectra acquired on the GF (green) and the GCNT web (magenta).

the surface of the graphene skeleton under an appropriate ratio of CH_4 and H_2, which formed a monolithic graphene–CNT hybrid with microscale graphene skeletons and a 3D nanoscale CNT web inside. The GCNT web was finally obtained after wet etching of the Ni template (Figure 1a, right). The CNTs adhered well onto the GF even after having been exposed to ultrasound at 150 W for 30 min. The optical images of porous nickel, graphene/nickel foam, and GCNT web (Figure 1c, inset) indicated highly functional structures. Scanning electron microscopy (SEM) images showed that the GCNT web presented a fully interconnected structure, where the CNTs filled up the pores of the GF, creating a web (Figure 1c) with a variable pore size distribution, ranging from hundreds of nanometers to tens of micrometers (Figure 1d). Moreover, the SEM image from the cross-section of the GCNT web presented a genuine 3D CNT interconnectivity along the *z*-direction and the GCNT web thickness could reach 1.5 mm according to the Ni template (Figure 1b). Compared to the previous GF scaffolds, these new GCNT web have a higher modulus of elasticity and conductivity (Figure S2a,b, Supporting Information), which are beneficial for neuronal proliferation, migration, and differentiation.[28] Raman spectra (Figure 1e) acquired on GF (green trace) and GCNT web (magenta trace) presented few-layer graphene and CNTs features identified as three characteristic peaks.[29] Besides, the spectrum of GF showed a strongly suppressed defect-related D band, indicating an overall high quality of graphene. The D peak (≈1348 cm^{-1}) associated with sp^3-hybridized carbon atoms showed disordered carbon atoms and was attributed to the presence of CNTs.[30] To the best of our knowledge, this is the first time that GFs with CNTs filling the pores have been successfully realized. Reported graphene–CNT hybrids either have a dense CNT mesh grown coaxially around the GF skeleton[31] or have thin nanoneedles on the surface of the GF skeleton.[32] These processes improve the surface area-to-volume ratio and enrich the skeleton surface topology, but they do not provide a strong interconnectivity between CNTs. If compared to the previous assemblies based on CNTs (Figure S1a–c, Supporting Information), the GCNT web represents for the first time a genuine 3D monolithic CNT web with a fully interconnected structure leaving inner spaces between CNTs from hundreds of nanometers to tens of micrometers, which match the biological dimensions. The productive growth of CNTs allows highly crosslinked nanotubes to form fully geometric and mechanical interconnectivity. Because of the interconnected graphene skeleton and the in situ growth of CNTs, the CNT web also has a strong electrical connectivity.

The 3D GCNT web offers neuronal culture compatibility, where the dense CNT web provides the physical support to guide neuronal growth in a genuine 3D manner that is not restricted to a 2D flat culture. Confocal images of cortical cultures stained with phalloidin, an actin marker, and Hoechst, a nuclear marker, show that neurons grew primarily on the skeleton of GF (Figure S3c, Supporting Information) and developed in 3D following the skeleton's topology. In contrast, neurons grown inside the GCNT web formed a denser network (**Figure 2**b), extending along the CNT web and filling the GF pores. SEM imaging of these cultures show that neurons pervaded the CNTs and that neurite outgrowth was guided by the overall CNT orientation (Figure 2c). The staining of neuronal axons and dendrites using SMI_312 and MAP2 as markers shows that neurons extended both axons and dendrites in all directions, developing a dense 3D network reminiscent of a native neural tissue (Figure 2a and Movie S1, Supporting Information).

The staining of axons with SMI_312 from a cross-section of the GCNT web shows the formation of a neuronal network (Figure 2f) extending up to 635 micrometers indicating that neurons penetrate through the entire 3D GCNT web. In addition, the almost uniform staining along the *z*-axis for several hundred of micrometers (Figure 2g) proves that we have a 3D neuronal network with a homogeneous density and there is no major difference between shallow and deeper layers. The same conclusion is obtained by SEM cross-section views of GCNT web (Figure 2h) showing cortical cells embedded over the entire *z*-axis. More interesting, the cortical cells could not only grow along the CNTs but also twine around the CNTs (Figure 2h, inset). The lower porosity of the GCNT web enables the retention of a larger number of neurons and glia inside the GCNT web, better mimicking the in vivo situation. After 8 d in culture (DIV 8), the nuclei count showed a fourfold increase in cell density in GCNT web compared to GFs (Figure 2d). A morphometric analysis using confocal microscopy indicated that the average volume occupied by every single cell on the GCNT web was 50% higher than that observed on GFs (Figure 2e).

Calcium plays a critical role in regulating neuronal network activities by participating in the synaptic transmission between neurons, controlling vesicle release.[33] To investigate whether neurons grown in the 3D GCNT web are alive and functionally active, we performed calcium imaging experiments using the calcium indicator Fluo-4 AM as previously described.[4b] Fluorescent images showed clear bright spots associated with the cell body of neurons and glia (Figure S4a, Supporting Information), which were located on the graphene skeleton but were also seen as suspended inside CNT web pores. Spontaneous calcium transients (DF/F) associated with the electrical firing of neurons were obtained by acquiring images at 3–5 Hz for 10–20 min (Movie S2, Supporting Information). At DIV 8, synchronous calcium transients with an amplitude of up to 1.5 DF/F were observed (Figure 2i); they had a sharp rising phase and a relatively slower decline, similar to the transients obtained from spiking neurons but not those from glial cell bodies (Figure S4b, Supporting Information). At DIV 15 (Figure 2j), calcium transients had a lower degree of synchrony, as shown by the raster plots (Figure 2m) and crosscorrelation matrices (Figure 2n). Similar results were also observed on GF scaffolds[4] (Figure S5, Supporting Information). During the early stages of development, specifically from DIV 2 to 4, the neuronal networks had a very low level of activity on both the GF and GCNT web. At DIV 6, the frequency and mean correlation coefficient (Figure S5f,g, Supporting Information) had a threefold increase and further increased over time. The bursting rate of neuronal growth inside the GCNT web was always higher than that of the growth on GF (Figure S5f, Supporting Information), even after DIV 15. A significant increase in burst frequency could be seen after DIV 15 inside the GCNT web (Figure 2k). Cortical networks grown inside the GCNT web at DIV 8 also showed a higher degree of synchrony than those grown inside the GF. As expected from the dynamics of the cortical network in vivo,[34]

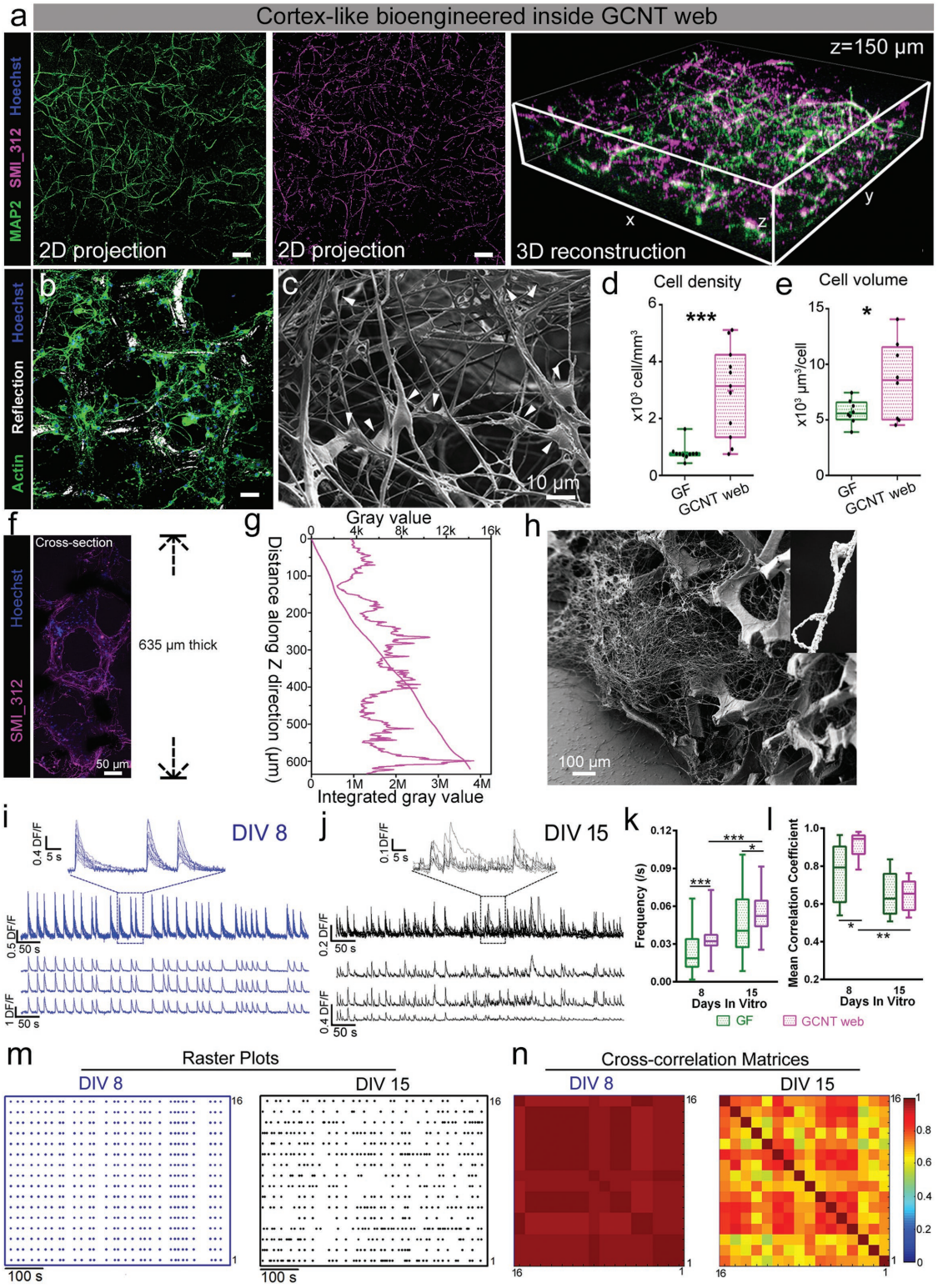

Figure 2. 3D functional cortex-like network is bioengineered inside 3D GCNT web. a) Representative staining for neurites (with MAP2, left) and axons (with SMI_312, middle) inside GCNT web after 8 d of culture and 3D reconstruction of the neuronal network (right). b) Actin staining of cortical cells after 8 d of culture inside the GCNT web. c) SEM images of cortical cells (white arrow heads) trapped into CNTs web. d) Box plot of cell density for cortical cultures grown inside the GCNT web and GF scaffolds (Unpaired t-test; $n = 10$ and $n = 11$, respectively). e) Box plot of occupied volume by cortical cells grown inside the GCNT web and GF scaffolds (Unpaired t-test; $n = 8$ for both the GF and GCNT web). f) Staining of axons (with SMI_312) acquired from a cross-section of the GCNT web along the *z*-direction. Scale bar = 50 µm. g) The overall intensity distribution of the axon staining along the *z*-axis. h) SEM image of the GCNT web embedded with cortical cells acquired from the cross-section (inset: a cortical cell twined around a CNT).

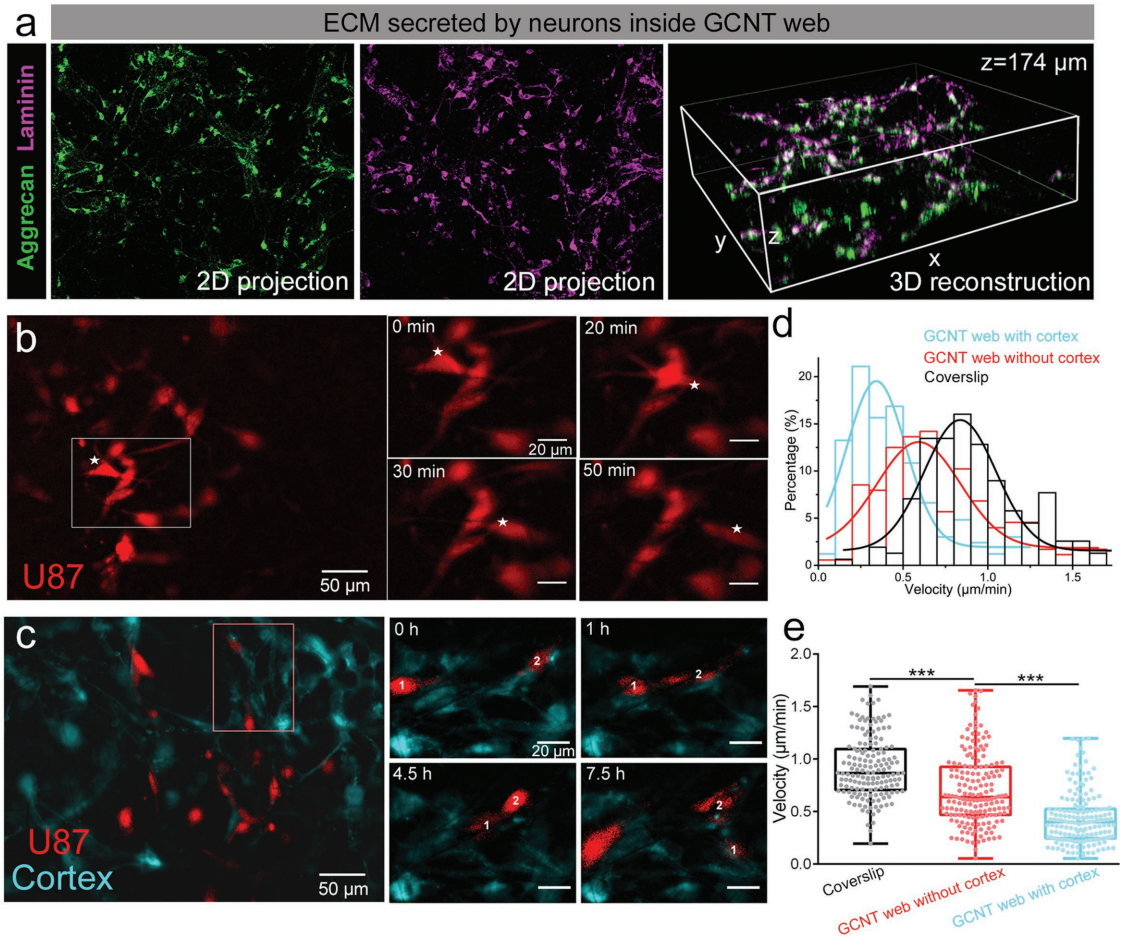

Figure 3. a) Staining for aggrecan and laminin proteins secreted by neurons cultured inside 3D GCNT web. b) An example of fluorescently labeled U87MG cells seeded inside the GCNT web. c) A representative live cell imaging experiment with fluorescently labeled U87MG cells (in red) and cortical cells (in cyan) obtained at different times. d,e) Cell velocity distribution and average velocities of malignant glioma cultured on coverslip ($n = 156$ cells), the GCNT web ($n = 176$ cells), and the cortex-like network ($n = 171$ cells, unpaired t-test).

after 15 DIV, the degree of synchrony decreased in networks cultured inside the GF and GCNT web (Figure 2l). Therefore, cortical cells inside the GCNT web grow in all directions to form through-space connectivity and functional properties that resemble the synchronized dynamical activity of in vivo networks.[34] In contrast to conventional GF and CNT scaffolds, the 3D GCNT web provides an appropriate microenvironment for neuronal network formation, such as neuron anchoring, cellular compartments, and cortical mechanical properties. Considering the brain complexity, our fully 3D interconnected GCNT web presents a major improvement for the study of the physiological and pathological processes in the brain.

An essential component of all 3D cellular assemblies is the ECM, which has the role of orchestrating the interactions between individual cells and the surrounding microenvironment.[35] The ECM is formed by different kinds of secreted molecules arranged in a 3D mesh and is not easily revealed in in vitro investigations with typical flat dishes. ECM proteins are important for retaining the network connectivity of a mature neuronal network[36] and constitute the matrix through which brain tumors, such as malignant glioma, travel to invade brain regions.[37] To verify whether cortical cells cultured on GCNT web secrete and produce the proteins forming the ECM, we stained the 3D coculture with standard markers for aggrecan and laminin. Aggrecan is an important protein specifically secreted by neurons that forms the perineuronal net,[38] whereas laminin is a key component of the basal lamina, which influences adhesion, migration, differentiation and survival.[39] Confocal images of neurons stained with specific antibodies against aggrecan and laminin (**Figure 3**a and Figure S6a, Supporting Information)

i,j) Superimposed optical traces (three of them are shown separately at the bottom) obtained from neuronal cultures grown inside the GCNT web at DIV 8 and 15. k) Comparison of the frequency inside the GF and GCNT web at DIV 8 and 15 ($n = 8$ for GF, $n = 10$ for GCNT web at DIV 8; $n = 6$ for GF, $n = 6$ for GCNT web at DIV 15). l) Comparison of the crosscorrelation at DIV 8 and 15 ($n = 8$ for GF and GCNT web at DIV 8; $n = 6$ for GF and $n = 5$ for GCNT web at DIV 15; two-way analysis of variance (ANOVA), Sidak's test). m) Representative raster plot of the peaks of calcium transients from cortical cultures grown inside the GCNT web at DIV 8 obtained from 16 different neurons. n) Representative crosscorrelation matrices of calcium transients from neuronal networks cultured inside the GCNT web at DIV 8 and 15.

show a rich presence of the two proteins inside the GF and GCNT web, but the ratio between aggrecan and laminin on the GCNT web (73.5 ± 4.2%) is lower than that on GF (97.0 ± 5.5%) (Figure S6c, Supporting Information). A 3D reconstruction from serial images taken with confocal microscope allows us to visualize the 3D organization of the ECM (Figure 3a and Figure S6b, Supporting Information). We found that the degree of colocalization of aggrecan and laminin was higher inside the GCNT web than inside the GF (Figure S6d, Supporting Information), indicating that colocalization in 2D and 3D is different. The 3D GCNT web can provide an exact 3D visualization of the ECM secreted by different cells, particularly by brain cancer cells, and can resolve the fine mechanical details of cell motility. In this way, it will be possible to link the mechanical and chemical abnormalities of the ECM to brain cancer invasion.

The basic mechanisms of cell motion on 2D flat culture are generally understood, and several methods have been developed to visualize and analyze cell migration in 2D. Nevertheless, in vivo cells grown in a 3D environment can follow different migration strategies, and 2D cultures cannot adequately replicate the complex in vivo tumor microenvironment; therefore, 2D cultures are poor predictors of tumor cell behavior in vivo.[40] To gain detailed insights into glioma cells infiltration in an intact brain, experimental models that recapitulate the highly complex 3D in vivo environment are needed, and therefore, we cultured U87MG cells inside the GCNT web. U87MG cells were genetically labeled with the red fluorophore mCherry, and their 3D motion was investigated with 3D time-lapse imaging. In these experiments, we acquired a stack of 20 images with z-steps of 3 µm every 3 min. Glioma grown inside the GCNT web (Figure 3b and Movie S3, Supporting Information) moved rapidly, and in a time window of just 10 min, they could move over several micrometers. During their motion, they squeezed, modifying their shape (see the U87MG cells indicated by asterisks). From the acquired stack of images, we recovered the 3D trajectories (**Figure 4**a, left panel, and Figure S7a, Supporting Information) using the Fiji plugin TrackMate as previously described[41] over periods of time of up to 6–24 h. From these trajectories, the velocity of the movements along the x-, y-, and z-axes distribution and the velocity of the cells during this period were computed. A comparison of the velocity of glioma in 2D and in 3D (Figure 3d,e) showed that glioma moved with a lower velocity inside the GCNT web than on 2D flat dishes. Our 3D trajectories are very similar to those obtained with a recently proposed method based on label-free 3D single cell tracking.[42] Similarly to what we observed in human primary macrophages in 3D biometric matrices,[42] the migration velocity of U87MG cells along the z-axis is lower than the lateral velocity along the x and y-axes (Figure 4b,c).

Brain cancer infiltration occurs in a 3D environment composed of healthy cortical tissue, i.e., neurons, glia cells, blood vessels, and the ECM. Therefore, U87MG cells were cocultured with rat cortical cells, comprising both neurons and glia cells. Having verified that cortical cells grown inside the GCNT web produce ECM proteins, we compared glioma motility in the GCNT web and the GCNT-web-based cortex-like network. Before seeding inside the GCNT web, cortical cells were labeled with the fluorescent probe DiD, which intercalates in the lipid membranes. In this way, it was possible to distinguish red fluorescent U87MG cells from healthy cyan cortical cells (Figure 3c). Their motions were investigated by 3D time-lapse imaging, lasting from several hours up to 2 d. U87MG infiltrated the 3D network formed by neurons and glia cells, often sliding along the thin CNTs in a way reminiscent of what they do along blood vessels[17] in the intact brain (Movie S4, Supporting Information). U87MG moved much more than neurons and glia cells, which appeared to be stable. The presence of cortical cells significantly slows down the motion of glioma (Figure 3d,e).

Our data show that the migration velocity of malignant glioma cells depends on the environment where they are cultured; this velocity decreases inside the GCNT web, and it decreases even more when glioma cells are cocultured with cortical cells. The obvious question, therefore, is how different is the action of drugs on glioma migration inside the GCNT web and in the presence of cortical cells? We compared the effect of the metabolic inhibitor blebbistatin on the migration of glioma cells in these three environments. Blebbistatin is a small molecule that inhibits both nonmuscle myosin II and smooth muscle myosin II,[43] and it has already been used as a blocker for brain cancer infiltration.[44] The effect of blebbistatin on the migration of fluorescently labeled U87MG on the flat 2D dish was observed with conventional live cell imaging (Figure 4f and Figure S7b, Supporting Information). The 3D trajectories of U87MG (Figure 4a) were obtained over a 4 h period before the application of 50×10^{-6} M blebbistatin and over another 4 h period after the addition of the drug. From the 3D trajectories, we derived the mean velocity (averaged on time and among all cells) before and after the addition of 50×10^{-6} M blebbistatin (Figure 4f). Upon application of 50×10^{-6} M blebbistatin, the mean velocity of U87MG decreased by almost 34% inside the GCNT web and to a lower extent (approximately 23%) in our cortex-like network.

From the 3D trajectories, we also computed the velocity of the movement along the three axes (x, y, and z) with the aim of determining the existence of differences in the velocity in the lateral (x- and y-axes) and axial direction (z-axis). In the absence of coculture with cortical cells, the addition of blebbistatin decreased the velocity in all three directions (Figure 4b). On the other hand, when U87MG cells were cocultured inside the GCNT web with cortical cells (Figure 4c), we observed a significant difference in the velocity only along the x- and y-axes ($p < 0.001$, Kolmogorov–Smirnov test) but not on the z-axis ($p = 0.9467$, Kolmogorov–Smirnov test), indicating that blebbistatin reduces primarily the lateral velocity. Therefore, our results suggest an involvement of the extracellular environment in malignant glioma motility, and in turn, a reduced effect of blebbistatin in the presence of cortical cells compared to the GCNT web alone (Figure 4d,e).

The recent advances in in vitro 3D culture technologies including organoids, spheroid cultures and primary cells grafted directly into biologically relevant matrix preparations and appropriate cortical slices[45] have opened new avenues for the development of more physiological cancer models.[46] The ability of these models to accurately replicate the complex microenvironmental and extracellular conditions prevailing in the brain allows us to visualize brain cancer infiltration, such as in an arthotopic xenograph of malignant glioma in the mouse brain.[47] Nevertheless, none of these approaches allow

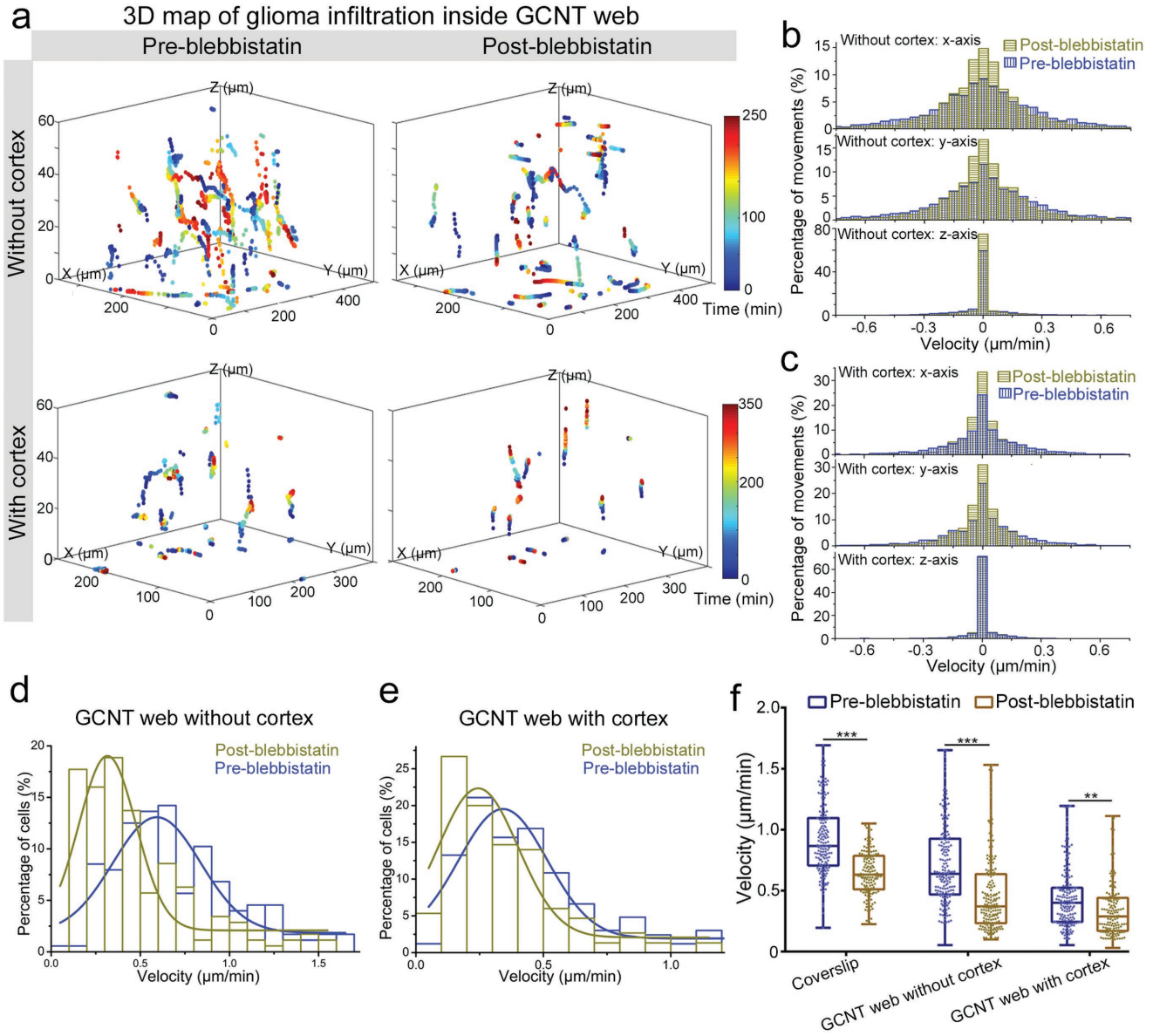

Figure 4. Blebbistatin performed properly on the glioma infiltration model constructed by the cortex-like network. a) 3D map for reconstructing trajectories of glioma infiltration during almost 6 h of live cell imaging pre- and postblebbistatin inside the single GCNT web and the cortex-like network. b,c) Cell movement velocity distribution along *x*, *y*, and *z* inside the single GCNT web and the cortex-like network preblebbistatin (blue) and postblebbistatin (yellow). d) Distribution of absolute cell velocities of glioma preblebbistatin (blue) and postblebbistatin (yellow). e) The same as in (d) but inside the cortex-like network. f) Comparison of the effect of blebbistatin on the absolute glioma velocity grown on a flat coverslip, GCNT web and the cortex-like network (preblebbistatin: coverslip $n = 156$ cells; GCNT web without cortex $n = 176$; with cortex $n = 171$ cells, postblebbistatin: coverslip $n = 144$ cells; GCNT web without cortex $n = 179$ cells; with cortex $n = 149$ cells, two-way ANOVA, Sidak's test).

the recovery of the 3D motion of individual glioma which could provide a 3D map of overall invasion. The combination of our 3D GCNT web with live cell imaging of fluorescently labeled glioma cells and cortical cells allows exact recovery of the 3D trajectories of individual malignant glioma infiltration and quantification of the effect of drugs.

In summary, we have fabricated a 3D monolithic porous GCNT web with fully geometric, mechanical and electrical interconnectivity by in situ CVD growth of interconnected CNT web into the GF pores. The 3D GCNT web provides a novel biomaterial to construct a 3D cortex-like network which responds to dense neuronal network and functional activity closer to the in vivo conditions. The cortex-like network allows to study brain connectivity and neuronal dysfunction and, further, to construct an ideal glioma infiltration model to map the 3D overall invasion, which could be an additional and more visible technology for preclinical therapeutic approaches screening. Future developments already in process include the analysis of the 3D motion of malignant glioma from patients in our model and the comparison of ECM secreted by different kinds of malignant glioma cells. The application of 3D GCNT web in cancer model construction also represents an important step

toward precise and personalized medicine. Indeed, it is possible to derive cortical cells from the stem cells of a patient and to screen drugs that can block the infiltration of brain cancer cells obtained from the same patient. Therefore, our system is not only a novel platform for live cell imaging achievement but also a new route toward the findings of improved methods to eradicate tumors without affecting the host's cells.

Supporting Information

Supporting Information is available from the Wiley Online Library or from the author.

Acknowledgements

M.X. and X.L. contributed equally to this work. This work was supported by the funds from National Key Basic Research Program of China (973 Program Grant No. 2014CB965003), Key Research and Development Program of Jiangsu Province (BE2017665), Regione friuli–venezia giulia (FVG) (Italy) for the project "GLIOBLASTOMA—Infiltrazione nei gliomi: nuovo target terapeutico," the 3315 Innovative Teams Program of Ningbo—China, Zhejiang Provincial Natural Science Foundation of China under Grant No. LQ17C100001, Natural Science Foundation of Ningbo City under Grant No. 2017A610256. The authors thank Beatrice Pastore for technical assistance, Jing Xu and Jiaxin Wang for useful discussions, and Manuela Schipizza Lough for carefully reading the paper. M.X. and G.C. fabricated and characterized the GCNT web. M.X. and F.P.U.S. prepared the cultures and M.L. performed the SEM experiment. M.X. performed calcium imaging experiments with F.P.U.S. and analyzed the data. F.P.U.S., Q.S., and M.X. performed immunofluorescence experiments. V.T. performed the ECM analysis. X.L. performed living cell imaging and analyzed the data with F.P.U.S. and M.X. M.X, F.P.U.S., and X.L. made the figures. V.T. designed the experiments and wrote the paper with M.X., F.P.U.S., X.L., and Q.Z. All the authors read and revised the paper. The authors thank Beatrice Pastore for technical assistance, Jing Xu and Jiaxin Wang for useful discussions and Manuela Schipizza Lough for carefully reading the manuscript. Cortical neurons from Wistar rats (P1–P3) were prepared in accordance with the guidelines of the Italian Animal Welfare Act, and their use was approved by the Local Veterinary Service, the SISSA Ethics Committee board and the National Ministry of Health (Permit Number: 630-III/14) in accordance with the European Union guidelines for animal care (d.1.116/92; 86/609/C.E.).

Conflict of Interest

The authors declare no conflict of interest.

Keywords

3D GCNT web, cancer models, cortex-like, malignant glioma infiltration, neuronal networks

Received: September 20, 2018
Published online: November 2, 2018

[1] K. Watanabe, D. Kamiya, A. Nishiyama, T. Katayama, S. Nozaki, H. Kawasaki, Y. Watanabe, K. Mizuseki, Y. Sasai, *Nat. Neurosci.* **2005**, *8*, 288.
[2] B. Derby, *Science* **2012**, *338*, 921.
[3] B. B. Biswal, M. Mennes, X. N. Zuo, S. Gohel, C. Kelly, S. M. Smith, C. F. Beckmann, J. S. Adelstein, R. L. Buckner, S. Colcombe, A. M. Dogonowski, M. Ernst, D. Fair, M. Hampson, M. J. Hoptman, J. S. Hyde, V. J. Kiviniemi, R. Kotter, S. J. Li, C. P. Lin, M. J. Lowe, C. Mackay, D. J. Madden, K. H. Madsen, D. S. Margulies, H. S. Mayberg, K. McMahon, C. S. Monk, S. H. Mostofsky, B. J. Nagel, J. J. Pekar, S. J. Peltier, S. E. Petersen, V. Riedl, S. A. R. B. Rombouts, B. Rypma, B. L. Schlaggar, S. Schmidt, R. D. Seidler, G. J. Siegle, C. Sorg, G. J. Teng, J. Veijola, A. Villringer, M. Walter, L. H. Wang, X. C. Weng, S. Whitfield-Gabrieli, P. Williamson, C. Windischberger, Y. F. Zang, H. Y. Zhang, F. X. Castellanos, M. P. Milham, *Proc. Natl. Acad. Sci. USA* **2010**, *107*, 4734.
[4] a) M. D. Tang-Schomer, J. D. White, L. W. Tien, L. I. Schmitt, T. M. Valentin, D. J. Graziano, A. M. Hopkins, F. G. Omenetto, P. G. Haydon, D. L. Kaplan, *Proc. Natl. Acad. Sci. USA* **2014**, *111*, 13811; b) F. P. Ulloa Severino, J. Ban, Q. Song, M. Tang, G. Bianconi, G. Cheng, V. Torre, *Sci. Rep.* **2016**, *6*, 29640; c) S. Usmani, E. R. Aurand, M. Medelin, A. Fabbro, D. Scaini, J. Laishram, F. B. Rosselli, A. Ansuini, D. Zoccolan, M. Scarselli, *Sci. Adv.* **2016**, *2*, e1600087; d) P. Soman, J. A. Kelber, J. W. Lee, T. N. Wright, K. S. Vecchio, R. L. Klemke, S. Chen, *Biomaterials* **2012**, *33*, 7064.
[5] L. G. Griffith, M. A. Swartz, *Nat. Rev. Mol. Cell Biol.* **2006**, *7*, 211.
[6] A. Ray, Z. M. Slama, R. K. Morford, S. A. Madden, P. P. Provenzano, *Biophys. J.* **2017**, *112*, 1023.
[7] Y. Mu, F. Wu, Y. R. Lu, L. M. Wei, W. E. Yuan, *Nanomedicine* **2014**, *9*, 1869.
[8] M. C. Serrano, S. Nardecchia, C. Garcia-Rama, M. L. Ferrer, J. E. Collazos-Castro, F. del Monte, M. C. Gutierrez, *Biomaterials* **2014**, *35*, 1543.
[9] a) S. R. Shin, R. Farzad, A. Tamayol, V. Manoharan, P. Mostafalu, Y. S. Zhang, M. Akbari, S. M. Jung, D. Kim, M. Comotto, N. Annabi, F. E. Al-Hazmi, M. R. Dokmeci, A. Khademhosseini, *Adv. Mater.* **2016**, *28*, 3280; b) J. Ren, Q. Xu, X. Chen, W. Li, K. Guo, Y. Zhao, Q. Wang, Z. Zhang, H. Peng, Y. G. Li, *Adv. Mater.* **2017**, *29*, 1702713.
[10] V. Lovat, D. Pantarotto, L. Lagostena, B. Cacciari, M. Grandolfo, M. Righi, G. Spalluto, M. Prato, L. Ballerini, *Nano Lett.* **2005**, *5*, 1107.
[11] E. B. Malarkey, K. A. Fisher, E. Bekyarova, W. Liu, R. C. Haddon, V. Parpura, *Nano Lett.* **2009**, *9*, 264.
[12] S. R. Shin, C. Shin, A. Memic, S. Shadmehr, M. Miscuglio, H. Y. Jung, S. M. Jung, H. Bae, A. Khademhosseini, X. S. Tang, M. R. Dokmeci, *Adv. Funct. Mater.* **2015**, *25*, 4486.
[13] S. Usmani, E. R. Aurand, M. Medelin, A. Fabbro, D. Scaini, J. Laishram, F. B. Rosselli, A. Ansuini, D. Zoccolan, M. Scarselli, M. De Crescenzi, S. Bosi, M. Prato, L. Ballerini, *Sci. Adv.* **2016**, *2*, e1600087.
[14] a) S. R. Shin, S. M. Jung, M. Zalabany, K. Kim, P. Zorlutuna, S. B. Kim, M. Nikkhah, M. Khabiry, M. Azize, J. Kong, K. T. Wan, T. Palacios, M. R. Dokmeci, H. Bae, X. W. Tang, A. Khademhosseini, *ACS Nano* **2013**, *7*, 2369; b) E. R. Aurand, S. Usmani, M. Medelin, D. Scaini, S. Bosi, F. B. Rosselli, S. Donato, G. Tromba, M. Prato, L. Ballerini, *Adv. Funct. Mater.* **2018**, *28*, 1700550.
[15] F. Schutt, S. Signetti, H. Kruger, S. Roder, D. Smazna, S. Kaps, S. N. Gorb, Y. K. Mishra, N. M. Pugno, R. Adelung, *Nat. Commun.* **2017**, *8*, 1215.
[16] M. Kato-Negishi, H. Onoe, A. Ito, S. Takeuchi, *Adv. Healthcare Mater.* **2017**, *6*, 1700143.
[17] V. A. Cuddapah, S. Robel, S. Watkins, H. Sontheimer, *Nat. Rev. Neurosci.* **2014**, *15*, 455.
[18] Q. T. Ostrom, H. Gittleman, P. Liao, T. Vecchione-Koval, Y. Wolinsky, C. Kruchko, J. S. Barnholtz-Sloan, *Neuro-Oncology* **2017**, *19*, v1.
[19] R. Poincloux, O. Collin, F. Lizarraga, M. Romao, M. Debray, M. Piel, P. Chavrier, *Proc. Natl. Acad. Sci. USA* **2011**, *108*, 1943.
[20] B. Auffinger, D. Spencer, P. Pytel, A. U. Ahmed, M. S. Lesniak, *Expert Rev. Neurother.* **2015**, *15*, 741.

[21] D. Hanahan, R. A. Weinberg, *Cell* **2011**, *144*, 646.
[22] L. Gu, D. J. Mooney, *Nat. Rev. Cancer* **2016**, *16*, 56.
[23] X. Zhou, M. Nowicki, H. T. Cui, W. Zhu, X. Q. Fang, S. D. Miao, S. J. Lee, M. Keidar, L. J. G. Zhang, *Carbon* **2017**, *116*, 615.
[24] N. Li, Q. Zhang, S. Gao, Q. Song, R. Huang, L. Wang, L. W. Liu, J. W. Dai, M. L. Tang, G. S. Cheng, *Sci. Rep.* **2013**, *3*, 1604.
[25] Z. P. Chen, W. C. Ren, L. B. Gao, B. L. Liu, S. F. Pei, H. M. Cheng, *Nat. Mater.* **2011**, *10*, 424.
[26] Q. K. Yu, J. Lian, S. Siriponglert, H. Li, Y. P. Chen, S. S. Pei, *Appl. Phys. Lett.* **2008**, *93*, 113103.
[27] X. M. Geng, Y. F. Guo, D. F. Li, W. W. Li, C. Zhu, X. F. Wei, M. L. Chen, S. Gao, S. Q. Qiu, Y. P. Gong, L. Q. Wu, M. S. Long, M. T. Sun, G. B. Pan, L. W. Liu, *Sci. Rep.* **2013**, *3*, 1134.
[28] a) G. C. Reilly, A. J. Engler, *J. Biomech.* **2010**, *43*, 55; b) G. Cellot, E. Cilia, S. Cipollone, V. Rancic, A. Sucapane, S. Giordani, L. Gambazzi, H. Markram, M. Grandolfo, D. Scaini, F. Gelain, L. Casalis, M. Prato, M. Giugliano, L. Ballerini, *Nat. Nanotechnol.* **2009**, *4*, 126.
[29] A. C. Ferrari, J. C. Meyer, V. Scardaci, C. Casiraghi, M. Lazzeri, F. Mauri, S. Piscanec, D. Jiang, K. S. Novoselov, S. Roth, A. K. Geim, *Phys. Rev. Lett.* **2006**, *97*, 187401.
[30] G. Y. Zhu, Z. He, J. Chen, J. Zhao, X. M. Feng, Y. W. Ma, Q. L. Fan, L. H. Wang, W. Huang, *Nanoscale* **2014**, *6*, 1079.
[31] W. Liu, C. Lu, X. Wang, K. Liang, B. K. Tay, *J. Mater. Chem. A* **2015**, *3*, 624.
[32] a) D. Kim, S. M. Kim, S. Lee, M. H. Yoon, *Sci. Rep.* **2017**, *7*, 7716; b) J. L. Liu, L. L. Zhang, H. B. Wu, J. Y. Lin, Z. X. Shen, X. W. Lou, *Energy Environ. Sci.* **2014**, *7*, 3709.
[33] T. Bacaj, D. Wu, X. F. Yang, W. Morishita, P. Zhou, W. Xu, R. C. Malenka, T. C. Sudhof, *Neuron* **2013**, *80*, 947.
[34] P. Golshani, J. T. Goncalves, S. Khoshkhoo, R. Mostany, S. Smirnakis, C. Portera-Cailliau, *J. Neurosci.* **2009**, *29*, 10890.
[35] a) C. A. Whittaker, K. F. Bergeron, J. Whittle, B. P. Brandhorst, R. D. Burke, R. O. Hynes, *Dev. Biol.* **2006**, *300*, 252; b) S. Ozbek, P. G. Balasubramanian, R. Chiquet-Ehrismann, R. P. Tucker, J. C. Adams, *Mol. Biol. Cell* **2010**, *21*, 4300; c) P. F. Lu, V. M. Weaver, Z. Werb, *J. Cell Biol.* **2012**, *196*, 395.
[36] A. Bikbaev, R. Frischknecht, M. Heine, *Sci. Rep.* **2015**, *5*, 14527.
[37] a) S. P. Koh, A. C. Wickremesekera, H. D. Brasch, R. Marsh, S. T. Tan, T. Itinteang, *Front. Surg.* **2017**, *4*, 28; b) J. S. Rao, *Nat. Rev. Cancer* **2003**, *3*, 489.
[38] a) K. A. Giamanco, M. Morawski, R. T. Matthews, *Neuroscience* **2010**, *170*, 1314; b) M. Morawski, G. Bruckner, T. Arendt, R. T. Matthews, *Int. J. Biochem. Cell Biol.* **2012**, *44*, 690.
[39] M. Aumailley, *Cell Adhes. Migr.* **2013**, *7*, 48.
[40] a) A. D. Doyle, F. W. Wang, K. Matsumoto, K. M. Yamada, *J. Cell Biol.* **2009**, *184*, 481; b) F. Sabeh, R. Shimizu-Hirota, S. J. Weiss, *J. Cell Biol.* **2009**, *185*, 11.
[41] J. Y. Tinevez, N. Perry, J. Schindelin, G. M. Hoopes, G. D. Reynolds, E. Laplantine, S. Y. Bednarek, S. L. Shorte, K. W. Eliceiri, *Methods* **2017**, *115*, 80.
[42] J. Sapudom, J. Waschke, K. Franke, M. Hlawitschka, T. Pompe, *Sci. Rep.* **2017**, *7*, 14135.
[43] a) J. H. Huang, J. X. Zhang, A. Pathak, J. X. Li, G. A. Stouffer, *J. Pharmacol. Exp. Ther.* **2011**, *336*, 116; b) M. Shutova, C. S. Yang, J. M. Vasiliev, T. Svitkina, *PLoS One* **2012**, *7*, e40814.
[44] S. Ivkovic, C. Beadle, S. Noticewala, S. C. Massey, K. R. Swanson, L. N. Toro, A. R. Bresnick, P. Canoll, S. S. Rosenfeld, *Mol. Biol. Cell* **2012**, *23*, 533.
[45] B. M. Baker, C. S. Chen, *J. Cell Sci.* **2012**, *125*, 3015.
[46] J. Drost, H. Clevers, *Nat. Rev. Cancer* **2018**, *18*, 407.
[47] J. G. Valadez, A. Sarangi, C. J. Lundberg, M. K. Cooper, *JoVE* **2014**, *83*, e50865.

ADVANCED MATERIALS

Supporting Information

for *Adv. Mater.*, DOI: 10.1002/adma.201806132

A Fully 3D Interconnected Graphene–Carbon Nanotube Web Allows the Study of Glioma Infiltration in Bioengineered 3D Cortex-Like Networks

Miao Xiao, Xiaoyun Li, Qin Song, Qi Zhang, Marco Lazzarino, Guosheng Cheng, Francesco Paolo Ulloa Severino,* and Vincent Torre**

Supporting Information

A Fully 3D Interconnected Graphene–Carbon Nanotube Web Allows the Study of Glioma Infiltration in Bioengineered 3D Cortex-Like Networks

Miao Xiao, Xiaoyun Li, Qin Song, Qi Zhang, Marco Lazzarino, Guosheng Cheng, Francesco Paolo Ulloa Severinoe,* and Vincent Torre**

Materials and Methods

Synthesis processes of intercalated $FeCl_3$-graphite. Intercalated $FeCl_3$-graphite was synthesized using a reported two-zone vapour transport method[24]. Graphite flakes (1 g, 99.8%, ABCR Karlsruhe, Germany) and anhydrous $FeCl_3$ powder (5.6 g, Alfa Aesar) were mixed in a two-zone reactive container. Then, the container was heated at 380℃ for 24 hours in a muffle furnace (TM-0912P, China). After having naturally cooled down to room temperature, the as-synthesized compound was used as the catalyst in CNT growth.

Synthesis processes of GCNT web. The GCNT web were fabricated by a two-step chemical vapour deposition (CVD) process in a horizontal tube furnace (Thermcraft, USA), including the growth of GF and GCNT web. The pre-cleaned porous Ni foam (PPI 100±10, Alantum Advanced Technology Materials, China) was placed in a 1-inch-diameter quartz tube that was pre-mounted in the furnace. During the preparation of GF, the Ni foam was first annealed at 950℃ for 10 minutes under H_2 (100 sccm) and Ar (100 sccm) atmosphere to clean their surfaces and eliminate surface oxidation layers. Next, 50 sccm of H_2 and CH_4 was introduced into the CVD system for 30 minutes, following by cooling to room temperature to allow graphene to grow on the Ni scaffold surfaces. The prepared GFs were cut at a width of 1 cm to be the carrier of CNTs. During the growth of CNTs, the as-synthesized intercalated $FeCl_3$-graphite powder was loaded upstream and next to the GF in a rail boat, which was then transferred into the middle of a quartz tube. Approximately 160 sccm of H_2 and 40 sccm of CH_4 was introduced into the CVD system for 15 minutes after the furnace was heated to 1050

℃ under the protection of Ar (200 sccm). The samples were then submerged into a $FeCl_3$ (1 M) solution for 48 hours to chemically etch Ni from the Ni foam. Then, the samples were immersed into hot HNO_3 at 80 ℃ for 2 hours. After complete etching, the GCNT web were washed with deionized water until the pH was 7. The GCNT web samples were finally dried at 60 ℃ in air.

Morphological, structural and physical property characterizations of GCNT web. Morphological and structural characterizations of the 3D-CG samples were investigated by field-emission scanning electron microscopy (SEM) equipped with an energy dispersive spectrometer (EDS) (Quanta 400 FEG, FEI, USA). The crystallinity and number of the layer presented within graphene were examined by a Raman spectrometer (LabRAMHR800, HORIBA, France). In the mechanical property characterization, a compression test was carried out by a high-precision mechanical testing system (Instron 3365, USA). Conductivity was performed using an Agilent B1500A semi-conductor device analyser (Agilent Technologies Inc., USA).

Neuronal network preparation and culture. Cortical neurons from Wistar rats (P1-P3) were prepared in accordance with the guidelines of the Italian Animal Welfare Act, and their use was approved by the Local Veterinary Service, the SISSA Ethics Committee board and the National Ministry of Health (Permit Number: 630-III/14) in accordance with the European Union guidelines for animal care (d.1.116/92; 86/609/C.E.). To minimize the suffering of animals, the rats were anaesthetized with CO_2 and sacrificed by decapitation quickly. During the culture process, substrates, including 3D GFs and 3D GCNT web, were first cleaned with O_2 plasma and sterilized with ultraviolet rays (UV). Then, they were coated with 50 μg mL^{-1} poly-L-ornithine (Sigma-Aldrich, St. Louis, MO, USA) overnight, immersed in culture medium overnight and coated with Matrigel just before cell seeding (Corning, Tewksbury MA, USA). The samples for ECM protein immunocytochemical staining were not coated with Matrigel. Dissociated cells were plated at a concentration of 2.4×10^6 cells Ml^{-1} on 3D

GF and 3D GCNT web in a drop of minimum essential medium (MEM) with GlutaMAXTM supplemented with 10% foetal bovine serum (FBS, all from Invitrogen, Life Technologies, Gaithersburg, MD, USA), 0.6% D-glucose, 15 mM Hepes, 0.1 mg ml^{-1} apo-transferrin, 30 μg ml^{-1} insulin, 0.1 μg ml^{-1} D-biotin, 1 μM vitamin B12 (all from Sigma-Aldrich), and 2.5 μg ml^{-1} gentamycin (Life Technologies). After 1 hour Neurobasal supplemented with 2% of B-27, 10 mM Glutamax (all from ThermoFisher) and 0.5 μM Gentamycin (Sigma) was added as a culture medium. Half of the medium was changed every week. Neuronal cultures were maintained in an incubator at 37 °C, 5% CO_2 and 95% relative humidity.

Morphological and immunocytochemical analysis. Cells were fixed in 4% paraformaldehyde containing 0.15% picric acid in phosphate-buffered saline (PBS), saturated with 0.1 M glycine, permeabilized with 0.1% Triton X-100, saturated with 0.5% BSA (all from Sigma-Aldrich) in PBS and then incubated with phalloidin Alexa Fluor® 488 (Life Technologies) for 30 minutes or o.n. at 4°C with primary antibodies: rabbit polyclonal against MAP2, rabbit polyclonal against aggrecan and mouse monoclonal against laminin (all from Sigma-Aldrich) and SMI 312 mouse monoclonal antibodies (Covance, Berkeley, CA). The secondary antibodies were goat anti-rabbit Alexa Fluor® 488, goat anti-mouse Alexa Fluor® 488, (all from Life Technologies), biotin conjugated goat anti-mouse and goat anti-rabbit (Sigma); the incubation time was 3 hours at room temperature (20–22 °C). When a biotin conjugated secondary antibody was used, another incubation of 1 hour with streptavidin Alexa Fluor® 647 (Life Technology) was performed. Nuclei were stained with 2 μg ml^{-1} PBS Hoechst 33342 (Sigma-Aldrich) for 5 minutes. Samples were mounted in Vectashield (Vector Laboratories) on 1-mm thick coverslips with a homemade adaptor of PDMS to host the 3D samples. The cells were examined using a Nikon C2 confocal microscope to acquire higher quality images. The fluorescence images were collected with a 20X magnification and 0.5 NA objective. Each image was acquired with z-steps of 2 μm. Analysis and 3D reconstruction of

the image stack were accomplished using NIS-Elements AR software (Nikon), Volocity (PerkinElmer), and the open source image-processing package Fiji (http://fiji.sc/Fiji).

Calcium imaging acquisition procedures. The cultured cells at 2, 3, 4, 6, 8, and 15 days *in vitro* (DIV 2, 3, 4, 6, 8, and 15, respectively) were loaded with a membrane-permeable calcium dye Fluo4-AM (Life Technologies) by incubating them with 4 μM Fluo4-AM (dissolved in anhydrous DMSO (Sigma-Aldrich), stock solution 4 mM) and Pluronic F-127 20% solution in DMSO (Life Technologies) at a ratio of 1:1 in Ringer's solution (145 mM NaCl, 3 mM KCl, 1.5 mM $CaCl_2$, 1 mM $MgCl_2$, 10 mM glucose and 10 mM Hepes, pH 7.4) at 37°C for 1 hour. After incubation, the cultures were washed with Ringer's solution for 30 minutes and then transferred to the stage of a Nikon Eclipse Ti-U inverted microscope equipped with a piezoelectric table (Nano-ZI Series 500 μm range, Mad City Labs), an HBO 103 W/2 mercury short arc lamp (Osram, Munich, Germany), a mirror unit (exciter filter BP 465–495 nm, dichroic 505 nm, emission filter BP 515–555) and an Electron Multiplier CCD Camera C9100-13 (Hamamatsu Photonics, Japan). The calcium imaging recordings were performed at RT, and images were acquired using the NIS Element software (Nikon, Japan) with an S-Fluor 20x/0.75 NA objective at a sampling rate of 3–5 Hz with a spatial resolution of 256×256 pixels for 10 minutes. To avoid saturation of the signals, excitation light intensity was attenuated by ND4 and ND8 neutral density filters (Nikon).

Calcium imaging processing and analysis. The initial video was processed with ImageJ (U. S. National Institutes of Health, Bethesda, MA) software. The image sequences were then analysed as previously described. Briefly, neurons were localized, and an appropriate region of interest (ROI) was selected to subtract the background. Appropriate ROIs around the cells bodies were then selected. The time course of the fluorescence intensity, $I_f(t)$, in this ROI was displayed, and any decay, which is a consequence of dye bleaching, was evaluated. The Ca^{2+} transients of each cell signal were extracted in a semi-automatic manner by selecting a threshold for the smallest detectable peak that was equal to three times the standard deviation

of the baseline. Subsequently, the decay of $I_f(t)$ was fitted to a cubic spline (Y(t)) interpolating $I_f(t)$ at 10 or 20 points. Y(t) was then added to the original optical signal to compensate for dye bleaching, and the fractional optical signal was calculated as follows:

$$\Delta F/F = (Y(t) + If(t))/ If(0) \quad (1)$$

where $I_f(0)$ is the fluorescence intensity at the beginning of the recording.

Computation of raster plot and correlation coefficient of Calcium transient occurrence. The times, t_i, at which transient peaks occurred are presented in a conventional raster plot. To isolate the smaller transients from the larger ones, single traces were considered independently. The amplitude distribution of peaks was calculated to separate the two different classes of events. Based on this distribution, a threshold was set to approximately 30% of the maximum amplitude. All peaks under the threshold were considered small transients, whereas all other peaks were considered to be large calcium transients.

The correlation coefficient of the calcium transients for neuron *i* and neuron *j* (σ_{CTij}) was computed as follows. The total recording time, T_{tot}, was divided into *N* intervals (1..,n,…,N) of a duration Δt. Thus, if f_{in} and f_{jn} are the numbers of calcium transients of neuron *i* and neuron *j* in the time interval Δt_n, then we have the following equation:

$$\sigma_{CT_{ij}} = \frac{\Sigma_n f_{in} f_{jn}}{\sqrt{(\Sigma_n f_{in}^2)(\Sigma_n f_{jn}^2)}} \quad (2)$$

where σ_{CTij} depends on Δt and varies between 0 and 1. The range of explored values of Δt was 20 s.

Live cell imaging of U87MG culture and co-culture system. U87MG purchased from SIGMA (#89081402) were cultured in Dulbecco's Modified Eagle Medium (DMEM) supplemented with 10% foetal bovine serum (FBS, all from Invitrogen, Life Technologies, Gaithersburg, MD, USA), 1% PenStrep (100 U mL^{-1} penicillium and 100 µg mL^{-1} streptomycin, Invitrogen) and passaged every 3 days. The mCherry-labelled U87MG cells were kindly provided by the laboratory of Prof. Antonello Mallamaci from the International

School of Advanced Studies. U87MG cells were acutely infected at a concentration of 500 cells μL^{-1} by a mix containing a lentiviral vector, LV_Pgk1p-mCherry, at a multiplicity of infection (m.o.i.)=6. This m.o.i. is sufficient to infect almost all U87MG cells in these conditions.

When required, U87MG cells were treated with 1Xtrypsin-EDTA (0.05% trypsin and 0.02% EDTA, Sigma) and suspended in the culture medium. Approximately $2.0x10^4$ U87MG cells were plated on a flat coverslip, 3D GCNT web and 3D GCNT web with cortex cells that had been cultured for 5 days, and then, the co-culture system was cultured in the incubator at 37°C, 5% CO_2 and 95% relative humidity for two days, and the recording experiments were started. Before seeding U87MG cells, the cortex cells were stained with Vybrant™ DiD Cell-Labeling Solution (5 µL mL^{-1}, Thermo Fisher) for 20 minutes and then washed with a warm medium. During the imaging experiment, blebbistatin (Sigma) was administered to the cells at a final concentration of 50 µM in the culture medium.

Living cell imaging acquisition procedures and analysis. Live cell imaging experiments were performed on an epi-fluorescence microscope (Olympus IX-83, Olympus) equipped with an imaging chamber incubator (Okolab, Pozzuoli, Italy) and LED illumination (λ=590 nm for mCherry, λ=660 nm for Vybrant DiD). During all imaging experiments, cells were kept at 37°C, 5.0% CO_2 and 95% humidity. Time-lapse images were taken with 500 ms of exposure time. When Z-stack images were acquired for 3D motion tracking, we recorded a stack of 20 images with z-steps of 3 µm every 3 minutes. All acquisitions were done with a CCD sensor at 12-bit depth (ORCA-D2, Hamamatsu) and operated with a 20X air objective (Olympus, NA=0.75).

The videos were analysed using the Fiji plugin TrackMate[50], which allows the selection of regions of interest (ROIs) for every cell in 3D. It also allows us to follow the centroid of the 3D ROI over time and obtain the average velocities and 3D coordinates. Once the cell ID, xyz positions and time points were extracted, the trajectories and velocities on the three axes (x, y,

and z) were visualized by plotting the coordinates using Matlab 2015. To calculate and plot the velocities on every single axis (x, y, and z), we established a 5-point numerical differentiation formula (see Matlab code) as follows:

$$f'[x_0] = \frac{f[x_0-2h]-8f[x_0-h]+8f[x_0+h]-f[x_0+2h]}{12h} \quad (4)$$

Using this approach, we could evaluate the different velocities of U87MG cells in the presence and absence of cortical cells and before and after the administration of the drug blebbistatin.

Statistical analysis. Data are shown as the mean ± s.e.m. from at least three neuronal culture preparations from different animals. For the morphological analysis of immunofluorescence images, n refers to the number of images analysed. The quantified activity (IEI and cross-correlation) and morphological data were analysed with the ANOVA test followed by post-hoc comparisons using the software Sygma Plot 10.0. Differences between two groups were evaluated with an unpaired t-test (Statistica 6.0 – StatSoft Italy). The number of replicas and statistical tests used for each experiment is mentioned in the respective figure legends or in the Results section. Significance was set to *$p < 0.05$, **$p < 0.01$ and ***$p < 0.001$.

Supporting Figures

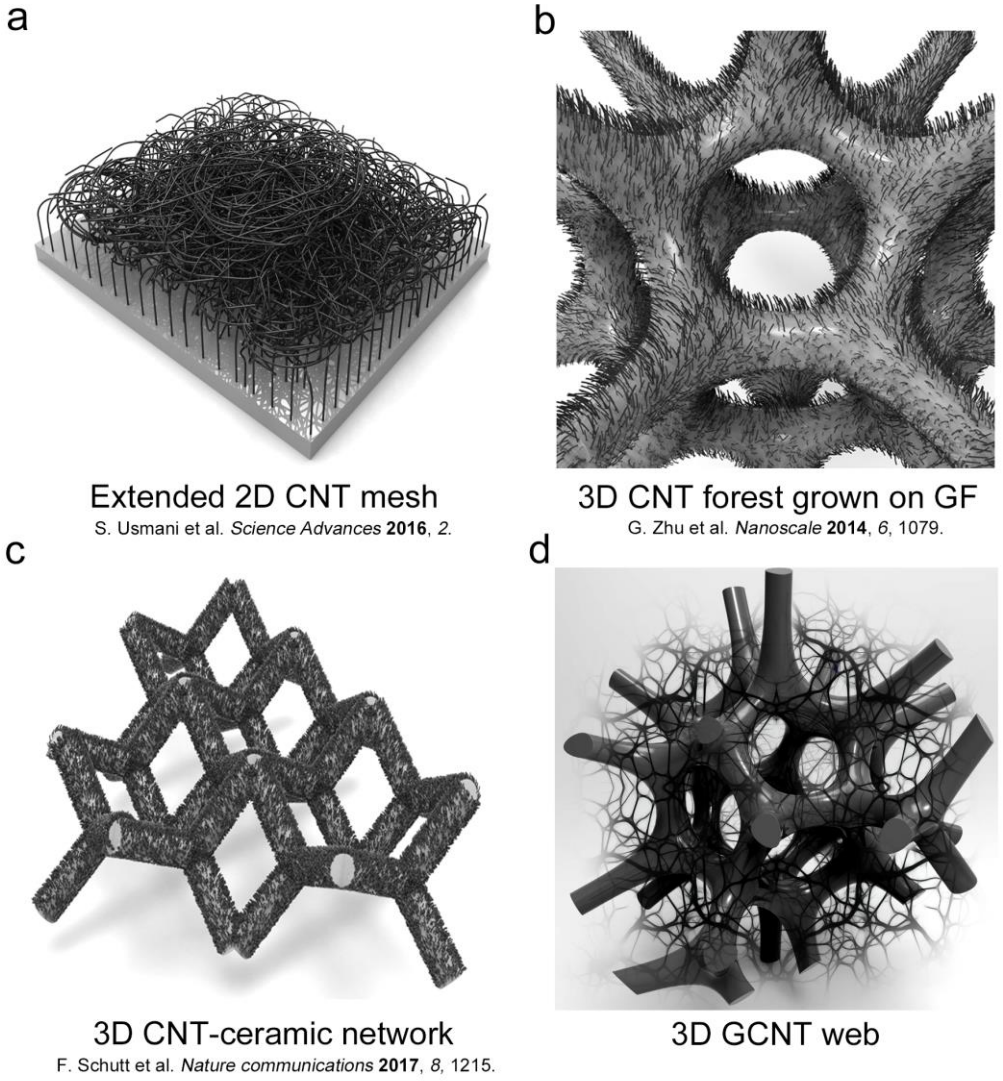

Figure S1. Representative CNT structures reported in the literature.

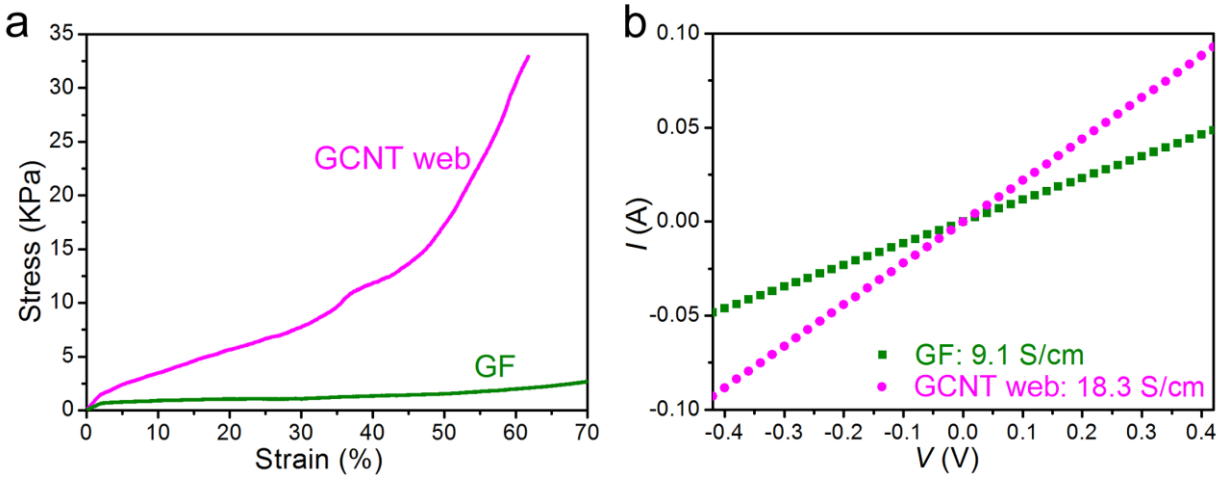

Figure S2. Physical properties of GCNT web. a) Strain-stress curves acquired from compressed test on GCNT web and GF. b) *I-V* curves acquired from four points electrical test on GCNT web and GF.

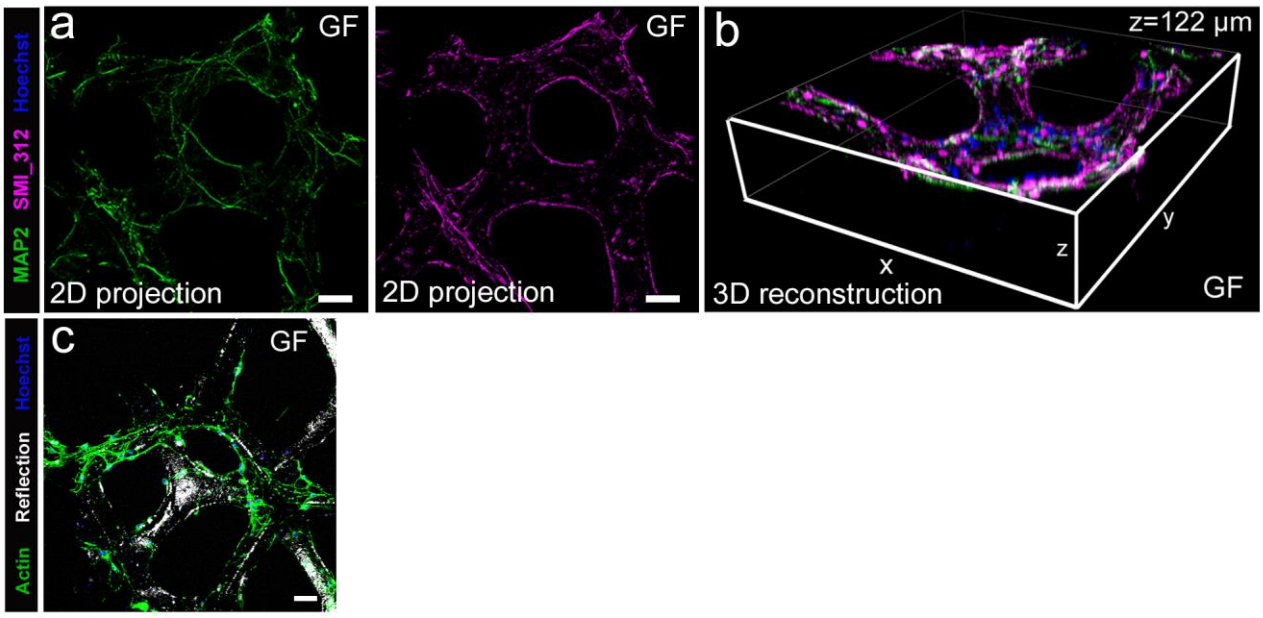

Figure S3. 3D cortical culture embedded into GF scaffolds. a-b) Staining for axons (with SMI_312) and neurites (with MAP2) on GF c) Actin staining of cortical cells after 8 days of culture on GF scaffold. The intricate mesh made by neuronal processes inside the GCNT web is more extended than the network formed on GF.

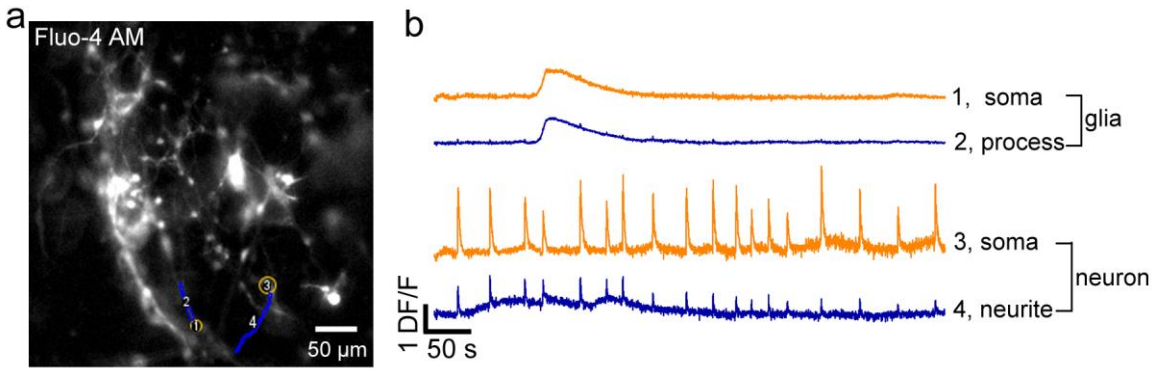

Figure S4. Typical calcium transients from glial cells and neurons. a) Representative fluorescence image of a neuronal culture loaded with Fluo-4 AM grown on a GCNT web. Orange (blue) circles indicate selected regions corresponding to the soma (neurite/process) of both neuron and glia cell. b) Optical transients from glia have a slow time course (upper portion of the panel) and those from neurons (lower portion) have a faster rising phase. Occasionally the neuronal fast transients can be contaminated from slow signals coming from glia cells often positioned below the neurons.

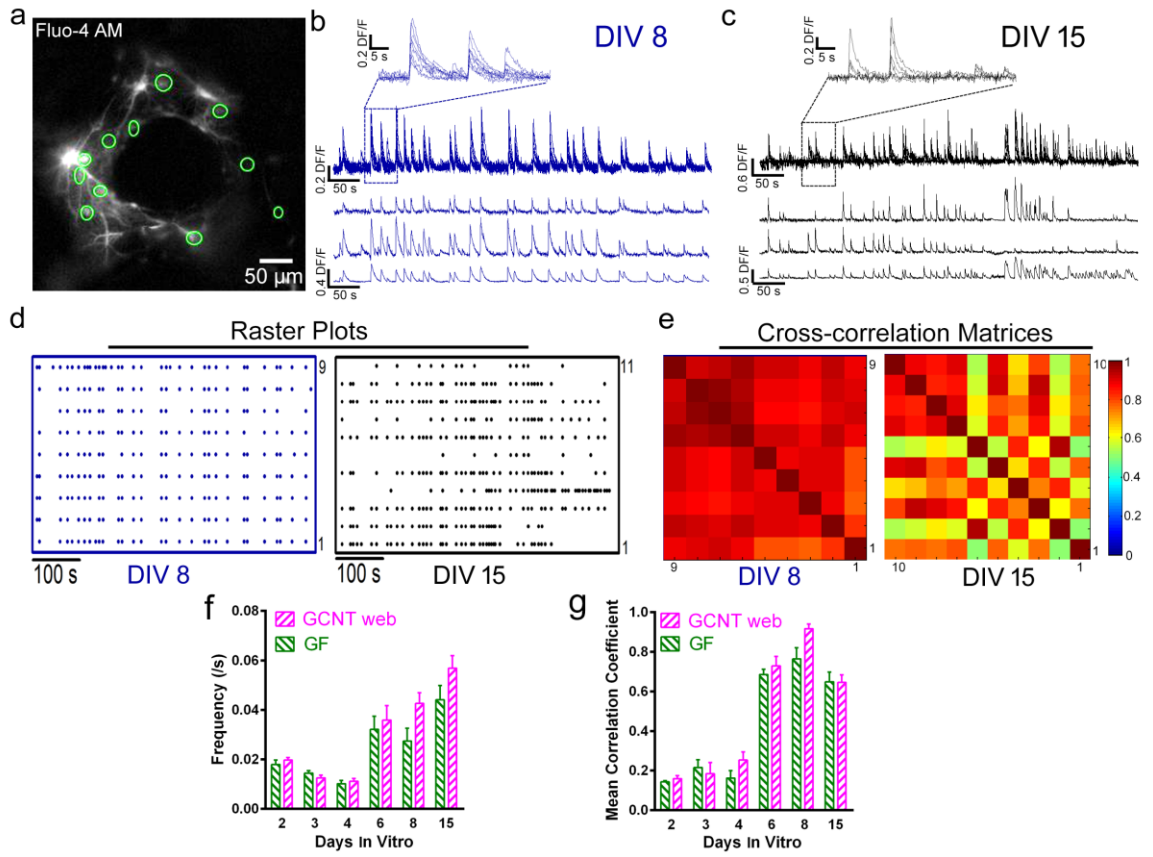

Figure S5. Spontaneous activity dynamics of 3D cortical cultures. a) Representative fluorescent image of a neuronal culture loaded with Fluo-4 AM grown in a GF scaffold. Olive circles indicate regions selected for the recovery of calcium transients. b-c) Representative superimposed optical traces (3 of them are shown separately in the bottom) obtained from the 3D neuronal network cultured on GF at DIV 8 and 15 respectively. The insets in the top portion of both panels show on an expanded time scale the synchronized calcium transients. d) Raster plot of the peaks of optical transients at DIV 8 and 15 for 9 and 11 different neurons respectively. e) Cross-correlation matrices of calcium transients from neuronal networks cultured on GF at DIV 8 and 15 respectively. f) Frequency of calcium transients from cortical cultures grown on GF and GCNT web at different developmental stages. g) Mean correlation coefficient of calcium transients from cortical cultures grown on GF and GCNT web at different developmental stages.

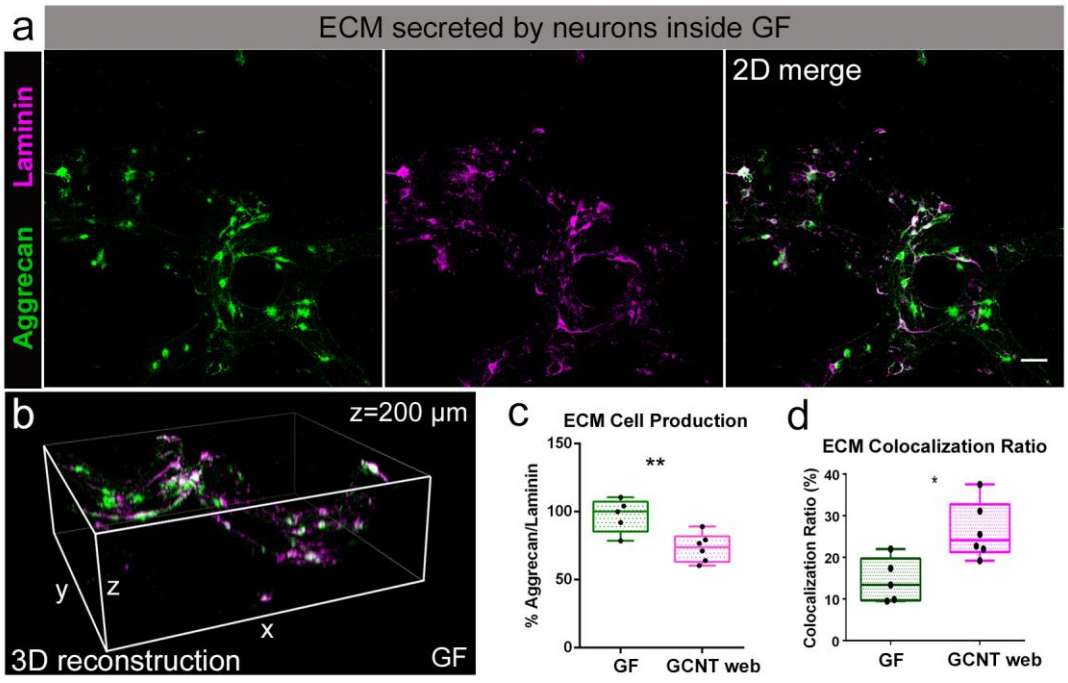

Figure S6. The 3D ECM secreted by cortical cells grown on GF scaffolds. a) Representative staining of aggrecan (left panel) and laminin (middle panel) secreted by cortical cells cultured in 3D GF scaffold. b) 3D reconstruction of laminin and aggrecan, which form the ECM secreted by cortical cells grown on GF. c) Ratio of production of aggrecan versus laminin on

GF and GCNT web. Collected data from 4 and 6 different stains in GF and GCNT web, respectively. d) Colocalization ratio between aggrecan and laminin on GF and GCNT web.

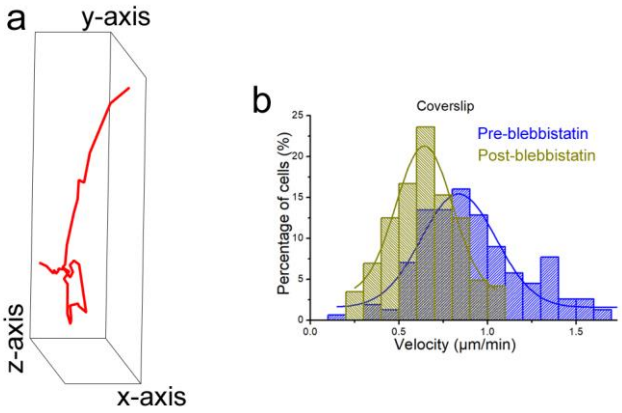

Figure S7. a) Representative trajectory of a U87MG infiltration inside GCNT web. b) Velocity distribution of glioma cultured on coverslip under the treatment of blebbistatin. n=156 cells for pre-blebbistatin and n=144 cells for post-blebbistatin.

Supporting Movies

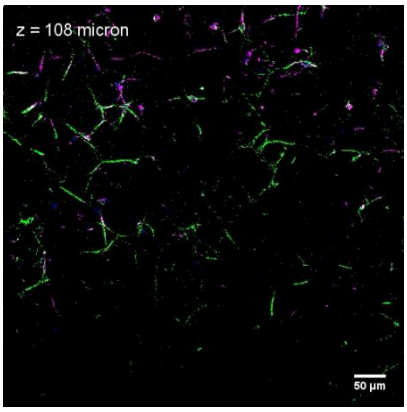

Movie S1. 3D reconstruction of cortical neuronal network embedded in GCNT web at DIV 8. Images were acquired by Nikon C2 confocal microscope with a 20X magnification and 0.5 NA objective. Each image was acquired with z-steps of 2 µm.

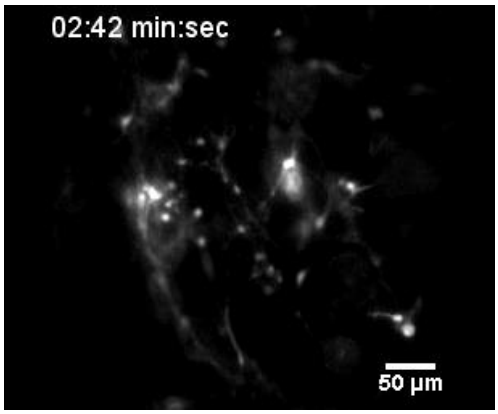

Movie S2. Calcium imaging from neuronal culture loaded with 4 µM Fluo-4-AM calcium indicator in 3D GCNT web at DIV 8. Images were acquired with 20X and 0.75 NA objective, 5 Hz, a spatial resolution of 256 × 256 pixels and for 10 min. The movie reproduction has been made using 100 frames per second.

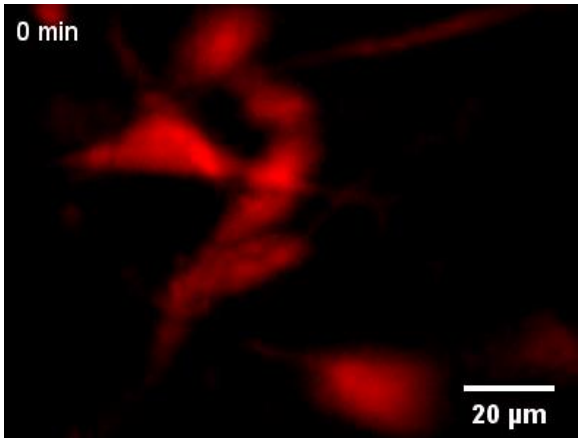

Movie S3. Living cell imaging from U87 GBM cells labeled with the red fluorophore mCherry by infecting with LV_Pgk1p-mCherry cultured in 3D GCNT web. Images were taken with a 20X and 0.75 NA air objective, 2 Hz. Stack of 20 images with z-steps of 3 µm every 3 minutes.

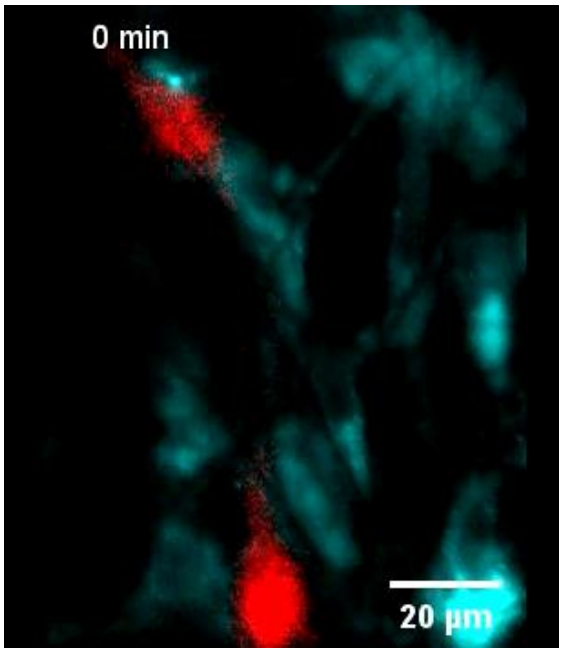

Movie S4. Living cell imaging from U87 GBM cells labeled with the red fluorophore mCherry by infecting with LV_Pgk1p-mCherry and cortical cells labeled with the fluorescent probe DiD co-cultured in 3D GCNT web. Images were taken with a 20X and 0.75 NA air objective, 2 Hz. Stack of 20 images with z-steps of 3 µm every 3 minutes.

3.2 3D free-standing ordered graphene network geometrically regulates neuronal growth and network formation

Miao Xiao, Francesco Paolo Ulloa Severino, Federico Iseppon, Guosheng Cheng*, Mingliang Tang*, Vincent Torre*

3D free-standing ordered graphene network geometrically regulates neuronal growth and network formation

Miao Xiao[1], Francesco Paolo Ulloa Severino[4], Federico Iseppon[5], Guosheng Cheng[6,*], Mingliang Tang[7,*], Vincent Torre[1,2,3,*]

[1]Neurobiology Sector, International School for Advanced Studies (SISSA), via Bonomea 265, Trieste 34136, Italy.

[2]Laboratory of Translational Medicine, Suzhou Institute of Systems Medicine, Center for Systems Medicine, Chinese Academy of Medical Sciences, Suzhou Industrial Park, Jiangsu 215123, China.

[3]Cixi Institute of Biomedical Engineering, Ningbo Institute of Materials Technology and Engineering, Chinese Academy of Sciences, Zhejiang 315201, China.

[4]Cell Biology Department, Duke University Medical Center, 335 Nanaline Duke Building Duke University Medical Center, Durham, NC 27710, USA.

[5]Molecular Nociception Group, Wolfson Institute for Biomedical Research, University College London, Gower Street, London, WC1E 6BT.

[6]CAS Key Laboratory of Nano-Bio Interface, Suzhou Institute of Nano-tech and Nano-bionics, Chinese Academy of Sciences, 398 Ruoshui Road, Suzhou Industrial Park, Jiangsu 215123, China.

[7]Jiangsu Province High-Tech Key Laboratory for Bio-Medical Research, Southeast University, Nanjing 211189, China

Email: mingliangtang@seu.edu.cn, gscheng2006@sinano.ac.cn, torre@sissa.it.

Abstract

The control of cell–microenvironment interactions plays a pivotal role in constructing tissue specific functional scaffolds for tissue engineering. Here, we fabricated a 3D free-standing ordered graphene (3D-OG) network with the pore size of 20 μm, the skeleton width of 20 μm and an exact 90° orientation angle between the building blocks. Extensive interconnectivity of graphene sheets allows 3D-OG scaffolds to be free-standing and easily to manipulate. When primary cortical cells are cultured on 3D-OG scaffolds, the cells form well-defined 3D connections with a cellular density similar to that observed when cells were cultured on 2D coverslip. In contrast to the 2D coverslips culture, astrocytes cultured on 3D-OG scaffolds did not have a flat morphology but had a more ramified shape similar to that seen i*n vivo* conditions. Moreover, neurons on 3D-OG scaffolds had axons and dendrites aligned along the graphene skeleton allowing the formation of neuronal networks with highly controlled connections. Neuronal networks

grown on 3D-OG scaffolds had a higher electrical activity with functional signaling over a long distance. Our study firstly investigated the geometrical cues on ordered neuronal growth and alignment of neuronal network formation on the support of graphene in 3D, will therefore advance the development of customized scaffolds for brain–machine interfaces or neuro-prosthetic devices.

Introduction

Highly organized assembly of neurons with defined pathways in the nervous system suggests that neurite branching and orientation are critical for functional neuronal network formation during all the development stages of central and peripheral nervous systems (CNS and PNS). For example, the dorsal column provides tracks for guiding the dorsal root ganglion to enter into the spinal cord.[1] Furthermore, neuronal alignment and patterning is also essential in nerve regeneration. Axons directionally regenerate along their preinjury path to the original branch points, which is the key point for the repair of spinal cord injury.[2] Therefore, revealing the underlying mechanism and adequate regulation of neural directionality not only contributes to the understanding of physiological and pathological processes in nervous system but also can be used for various of disease-relevant preclinical applications.

Tissue-engineered platforms provide specialized chemical and physical cues *in vitro* to mimic the microenvironment for cells to grow, expand, and differentiate in conditions resembling *in vivo* settings. In particular, geometrical cues including surface roughness, pores, and orientation has been proven to play an essential role in neuronal growth and circuit formation.[3] Emerging biomaterials and advanced fabrication techniques have advanced geometrical regulation on artificial substrates to guide neuronal cell adhesion, migration, proliferation and differentiation.[4-6] To pattern neurons, numerous of nano-, micro- and macro-fabrication techniques haven been applied for creating substrates with varying degrees of topology, including photolithography, soft lithography, ion-beam lithography, microcontact printing, electrospinning, three-dimensional printing and so on.[7-10] Although these studies investigated neurite orientation and pathfinding

preferences in micro/nanopatterned surface, most of them are based on 2D or 2.5D substrates that neurons can't form strict 3D networks.[11] However, the neurons are embedded in an extracellular matrix (ECM) that forms a complex 3D network of proteins that provide complex mechanical, biochemical and physical signals.[12]

To construct a more physiologically relevant microenvironment *in vitro* to better mimic *in vivo* microenvironment, 3D culture systems, especially scaffold-based 3D assemblies of never cells, have been widely developed for overcoming the limitations of 2D culture.[13] In terms of the regulation of neuronal guidance on 3D platforms, 3D patterned structures, such as well aligned gel and hydrogel constructs has also been used to direct axonal growth, thus mimicking the topography and orientation of structures that naturally occur in the mature nervous system.[14, 15] However, currently available methods for 3D patterning of neural networks are usually not easily reproducible nor sufficiently stable to allow for easy manipulation.[16] Besides natural and synthetic polymers, carbon materials, especially graphene, has been widely used in 3D neural tissue engineering.[12, 17] Because of its unique structure, graphene possesses tremendous electron mobility[18], remarkable thermal conductivity[19], high surface area[20] and excellent mechanical strength[21]. In the past ten years, biomedical applications of graphene have attracted an ever-increasing interest, including neuro-electrodes, bioimaging, drug/gene delivery, stem cell study and tissue engineering based scaffold.[22-24] Recently, a controllable fabrication of highly conductive interconnected graphene networks with precise pattern and dimension has been developed. [25] The pore and skeleton sizes, orientation angles of building blocks can be customized. It has been proven to have significant impact on the differentiation behaviors of neural progenitor cells (NPCs).[26]

In this work, we extended the 3D free-standing ordered graphene (3D-OG) network's application in guidance of neuronal growth and network formation for the first time. These 3D-OG scaffolds have an 3D ordered architecture with the pore size of 20 μm and the skeleton width of 20 μm which match the size of cortical cells. Cortical co-culture networks were analyzed not only morphologically, using immune-fluorescent approach, but also functionally through calcium imaging.

Experimental Section

Fabrication processes of 3D free-standing ordered graphene network (3D-OG). The fabrication processes have been reported as reported.[25] Briefly, the ordered Ni templated with the pore size of 20 μm and the skeleton width of 20 μm were prepared follows a typical top-down micro-fabrication strategy firstly, where 150 nm thick Au film was deposited on 200 nm thick PMMA layer via magnetron sputtering(FHR Anlagenbau GmbH, Germany) as active electrode for electroplating. After desired pattern of AZ 4620 photoresist (AZ Electronic Materials, USA) was formed under photolithography and etching, the substrate was immersed into an electroplating bath for Ni deposition. The as-fabricated monolayer of Ni skeletons was then peeled off from the substrate and aligned with 5 monolayers. Afterwards, Ni templates with specific angles were annealed at 700℃ for 3 min in a muffle furnace (TM-0912P, China) to bond the monolayers together. The as-prepared 3D Ni scaffolds were placed into a chemical vapor deposition (CVD) system. The scaffolds were first annealed at 950℃ for 10 min under H_2 and Ar atmosphere to clean their surface and eliminate surface oxidation layers. Next, H_2 and CH_4 were introduced into the CVD system for 60 min, followed by cooled down to room temperature to allow graphene growth on the Ni scaffold surfaces. The 3D-OG was finally obtained by sequentially rinsed with 1 M, 0.1 M and 0.01 M HCl solutions, followed by rinsing with deionized water for 48 hours to remove residual etching agents.

Morphological and micro-structural characterizations of 3D free-standing ordered graphene network (3D-OG). Field-emission scanning electron microscopy (SEM) equipped with energy dispersive spectrometer (EDS) (Quanta 400 FEG, FEI, USA), Raman spectrometer (LabRAMHR800, HORIBA, France) and transmission electron microscopy (TEM, Tecnai G2 F20 S-TWIN) were utilized to characterize the morphology and micro-structure. For TEM observations, 3D-OG sheets were ultrasonically dispersed in ethanol for 45 min and then dropped onto a copper grid.

Neuronal network preparation and culture. Cortical neurons from Wistar rats (P1-P3) were prepared in accordance with the guidelines of the Italian Animal Welfare Act,

and their use was approved by the Local Veterinary Service, the SISSA Ethics Committee board and the National Ministry of Health (Permit Number: 630-III/14) in accordance with the European Union guidelines for animal care (d.1.116/92; 86/609/C.E.). To minimize the suffering of animals, the rats were anaesthetized with CO_2 and sacrificed by decapitation quickly. During the culture process, OG scaffolds were first cleaned with O_2 plasma and sterilized with ultraviolet rays (UV). Then, they were coated with 50 μg mL^{-1} poly-L-ornithine (Sigma-Aldrich, St. Louis, MO, USA) overnight, immersed in culture medium overnight and coated with Matrigel just before cell seeding (Corning, Tewksbury MA, USA). Dissociated cells were plated at a concentration of 2.4 × 10^6 cells mL^{-1} on 3D-OG scaffolds in a drop of minimum essential medium (MEM) with GlutaMAXTM supplemented with 10% foetal bovine serum (FBS, all from Invitrogen, Life Technologies, Gaithersburg, MD, USA), 0.6% D-glucose, 15 mM Hepes, 0.1 mg ml^{-1} apo-transferrin, 30 μg ml^{-1} insulin, 0.1 μg ml^{-1} D-biotin, 1 μM vitamin B12 (all from Sigma-Aldrich), and 2.5 μg ml^{-1} gentamycin (Life Technologies). After 1hour, Neurobasal supplemented with 2% of B-27, 10 mM Glutamax (all from ThermoFisher) and 0.5 μM Gentamycin (Sigma) was added as a culture medium. Half of the medium was changed every week. Neuronal cultures were maintained in an incubator at 37 °C, 5% CO_2 and 95% relative humidity.

Morphological and immunocytochemical analysis. Cells were fixed in 4% paraformaldehyde in phosphate-buffered saline (PBS), saturated with 0.1 M glycine, permeabilized with 0.1% Triton X-100, saturated with 0.5% BSA (all from Sigma-Aldrich) in PBS and then incubated over night at 4°C with primary antibodies: mouse monoclonal glial fibrillary acidic protein (GFAP)(Sigma-Aldrich) and anti-β-tubulin III (TUJ1) mouse monoclonal antibody (Covance, Berkeley, CA). The secondary antibodies were goat anti-mouse immunoglobulin (Ig) G1 Alexa Fluor® 488, goat anti-mouse IgG2a Alexa Fluor® 594 (all from Life Technologies). the incubation time was 3 hours at room temperature (20–22 °C). Nuclei were stained with 2 μg ml^{-1} PBS Hoechst 33342 (Sigma-Aldrich) for 5 minutes. Samples were mounted in Vectashield (Vector Laboratories) on 1-mm thick coverslips with a homemade adaptor of PDMS to host the 3D samples. The cells were examined using a Nikon C2 confocal microscope

to acquire higher quality images. The fluorescence images were collected with a 20X magnification and 0.5 NA objective. Each image was acquired with z-steps of 2 µm. Analysis of the image stack were accomplished using NIS-Elements AR software (Nikon), Volocity (PerkinElmer), and the open source image-processing package Fiji (http://fiji.sc/Fiji). Neurite preferential alignments in networks were performed on the traces of fluorescent immunostaining images and the resultant polar plots were obtained using Neurolucida 360 (MBF Bioscience, VT, United States).

Calcium imaging acquisition procedures. The cultured cells at 8 days *in vitro* (DIV 8) were loaded with a membrane-permeable calcium dye Fluo4-AM (Life Technologies) by incubating them with 4 µM Fluo4-AM (dissolved in anhydrous DMSO (Sigma-Aldrich), stock solution 4 mM) and Pluronic F-127 20% solution in DMSO (Life Technologies) at a ratio of 1:1 in Ringer's solution (145 mM NaCl, 3 mM KCl, 1.5 mM $CaCl_2$, 1 mM $MgCl_2$, 10 mM glucose and 10 mM Hepes, pH 7.4) at 37°C for 1 hour. After incubation, the cultures were washed with Ringer's solution for 30 minutes and then transferred to the stage of a Nikon Eclipse Ti-U inverted microscope equipped with a piezoelectric table (Nano-ZI Series 500 µm range, Mad City Labs), an HBO 103 W/2 mercury short arc lamp (Osram, Munich, Germany), a mirror unit (exciter filter BP 465–495 nm, dichroic 505 nm, emission filter BP 515–555) and an Electron Multiplier CCD Camera C9100-13 (Hamamatsu Photonics, Japan). The calcium imaging recordings were performed at RT, and images were acquired using the NIS Element software (Nikon, Japan) with an S-Fluor 20x/0.75 NA objective at a sampling rate of 3–5 Hz with a spatial resolution of 256×256 pixels for 10 minutes. To avoid saturation of the signals, excitation light intensity was attenuated by ND4 and ND8 neutral density filters (Nikon).

Calcium imaging processing and analysis. The initial video was processed with ImageJ (U. S. National Institutes of Health, Bethesda, MA) software. The image sequences were then analysed as previously described. Briefly, neurons were localized, and an appropriate region of interest (ROI) was selected to subtract the background. Appropriate ROIs around the cells bodies were then selected. The time course of the fluorescence intensity, $I_f(t)$, in this ROI was displayed, and any decay, which is a

consequence of dye bleaching, was evaluated. The Ca^{2+} transients of each cell signal were extracted in a semi-automatic manner by selecting a threshold for the smallest detectable peak that was equal to three times the standard deviation of the baseline. Subsequently, the decay of $I_f(t)$ was fitted to a cubic spline (Y(t)) interpolating $I_f(t)$ at 10 or 20 points. Y(t) was then added to the original optical signal to compensate for dye bleaching, and the fractional optical signal was calculated as follows: DF/F= (Y(t)+ $I_f(t)$)/$I_f(0)$, where $I_f(0)$ is the fluorescence intensity at the beginning of the recording.

Computation of raster plot and correlation coefficient of Calcium transient occurrence. The times, t_i, at which transient peaks occurred are presented in a conventional raster plot. To isolate the smaller transients from the larger ones, single traces were considered independently. The amplitude distribution of peaks was calculated to separate the two different classes of events. Based on this distribution, a threshold was set to approximately 30% of the maximum amplitude. All peaks under the threshold were considered small transients, whereas all other peaks were considered to be large calcium transients.

The correlation coefficient of the calcium transients for neuron i and neuron j (σ_{CTij}) was computed as follows. The total recording time, T_{tot}, was divided into N intervals (1..,n,…,N) of a duration Δt. Thus, if f_{in} and f_{jn} are the numbers of calcium transients of neuron i and neuron j in the time interval Δt_n, then we have the following equation:

$$\sigma_{CT_{ij}} = \frac{\sum_n f_{in} f_{jn}}{\sqrt{(\sum_n f_{in}^2)(\sum_n f_{jn}^2)}}$$

where σ_{CTij} depends on Δt and varies between 0 and 1. The range of explored values of Δt was 20 s.

Statistical analysis. Data are shown as the mean ± SD from at least three neuronal culture preparations from different animals. The quantified activity (IEI and cross-correlation) and morphological data were analysed with the ANOVA test followed by post-hoc comparisons using the software Sygma Plot 10.0. Differences between two groups were evaluated with an unpaired t-test (Statistica 6.0 – StatSoft Italy). Significance was set to *p < 0.05, **p < 0.01 and ***p < 0.001.

Results and discussion

3D assembly of graphene architectures not only preserves the intrinsic properties inherited from graphene sheets, but also provides a high surface area, porous structure, and strong operability for practical system.[27] We have already reported the fabrication of macroscopic and conductive interconnected graphene networks with controllable patterns, pore, and skeleton sizes via chemical vapor deposition,[25] To extend the further application of this ordered graphene network and study the geometrical cues of 3D free-standing scaffold on neuronal growth and network formation, we fabricated a 3D ordered graphene (3D-OG) scaffold with the pore size of 20 μm and the skeleton width of 20 μm. The orientation angles of building blocks were 90°. SEM image of **Figure 1**A indicated the sheet comprises hollow 3D-OG in a large-area, uniform, and well interconnected structure. The 3D-OG preserved the interconnected structure of the Ni template and all the graphene sheets in the 3D-OG are strongly connected to each other with no significant breaks and agglomeration. Successful etching of Ni template with no residual was confirmed by energy dispersive spectrometer (EDS) analysis after the etching (**Figure 1** D). Meanwhile, very tiny quantity of oxygen is probably induced during Ni wet etching.[28] Because of different thermal expansion coefficients of polycrystalline nickel, ripples and wrinkles were commonly exhibited on the graphene skeleton surface[29] (**Figure 1**B). The enriched nano-topography has been proven to enhance the communication in neuronal network.[30] Raman spectrum (**Figure 1** E) acquired on 3D-OG showed a strongly suppressed defect-related D band, indicating an overall high quality of graphene.[31, 32] Usually, the layer numbers of graphene sheets is different in different domains, which is attributed to the polycrystalline nature of the nickel scaffold,[33] which can be further confirmed by TEM analysis (**Figure 1** C). Moreover, a hexagonal pattern of the carbon atoms arrangement was acquired from selected area electron diffraction (SAED) on 3D-OG (**Figure 1** F), implying the nature of high-quality crystallinity of 3D-OG. Overall, the morphological and micro-structural characterizations of 3D-OG indicated that the 3D-OG scaffolds were constructed by pure graphene sheets with high quality. Intense interconnectivity allows 3D-OG scaffolds to be free-standing and easily manipulative. Moreover, the top-down micro-fabrication strategy ensures the

reproducible produce of customized structures.

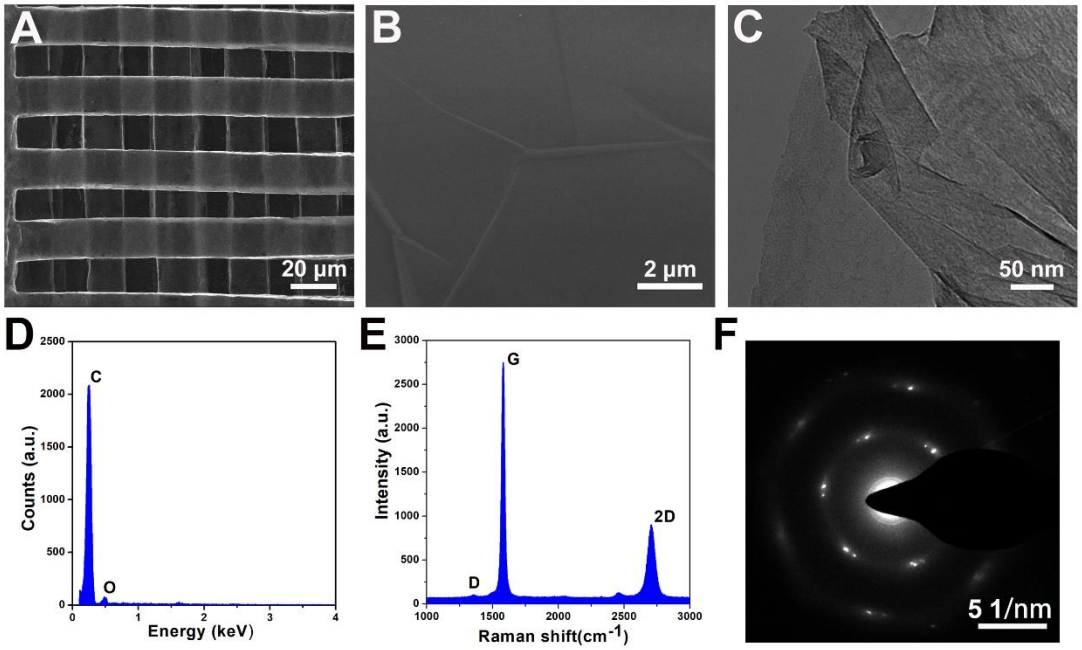

Figure 1. Morphological and structural characterizations of 3D-OG scaffolds. A) Representative SEM image of the 3D-OG with the pore size of 20 μm and the skeleton width of 20 μm. The orientation angles of building blocks were 90°. B) Enlarged higher-magnification SEM image of the 3D-OG showed the graphene skeleton surface and corresponding EDS spectrum was shown in (D). C) HRTEM image on the wall edges of the 3D-OG and selected area electron diffraction pattern was presented in (F). E) Representative Raman spectrum acquired on the 3D-OG surface.

The manufactured 3D-OG scaffolds have a well-defined structure in which the graphene skeletons are organized in an ordered array. There is an optimal size range for the skeleton diameter for neurite guidance during *in vitro* model mimicking *in vivo* microenvironment or never regeneration. Previous reports demonstrated that filaments with diameters in the range of cellular size and below were most prominent for highly directional and robust neuronal growth.[34] Considering the typical size of neurons and glial cells, 3D-OG scaffolds with the pore size of 20 μm, the skeleton width of 20 μm and the 90° orientation angles of building blocks were chosen for the following experiments.

Cortical cells were isolated from postnatal wistar rats (P1-P3) and seeded on both Matrigel/poly-L-ornithin coated 3D-OG scaffolds and coverslip as control. In order to

examine the relative abundance of neurons and glial cells grown on 3D-OG scaffolds and control, cultures after 8 – 10 DIV were immunofluorescence stained with antibodies for neurons with β-tubulin III (TUJ1, in red) and for glial cells with glial fibrillary acidic protein (GFAP, in green) (**Figure 2** A for 3D-OG and B for control). In both images, nuclei were pointed out by Hoechst 33342 (Sigma-Aldrich) (Hoechst, in blue). Neuron and astrocyte staining indicated that the cells were homogeneously distributed on the 3D-OG structure with globular healthy shapes extending numerous neurites Remarkably, 3D-OG structure didn't affect the relative abundance of neurons and glial cells (**Figure 2** C). We then investigated the morphology of glial cells. GFAP is the main component of astrocyte intermediate filament cytoskeleton.[35]. Glia cells and in particular astrocytes have a flat and not ramified morphology when grown on glass 2D coverslip, rather different from what seen in *in vivo* conditions[36]. Glia cells, in contrast, cultured on our 3D-OG scaffolds have a completely different morphology with a small cell body from which several process emerge more reminiscent of what observed *in vivo*[36]. As interactions between astrocytes and neurons are essential for the maintenance of neuronal networks in healthy conditions, our 3D-OG scaffolds allow the development of cellular networks with a better biocompatibility.

To further measure the regulation of 3D-OG structure on neuronal growth, we further show another immunofluorescence staining of neurons and glial cells in **Figure 3** A in which we also acquired the reflection of 3D-OG structure. The supported skeleton was exhibited to better order the neurite growth compared the flat patterns. To further compare the two patterns, we outlined the neurite morphology in **Figure 3** B, which showed that neurons developed on 3D-OGs were straighter but growth on glass 2D coverslip were random. Moreover, ten representative neurite curvatures were presented in **Figure 3** C respectively**.** The neurite curvatures on 3D-OG were uniform and much less than that on glass 2D coverslip, indicating that neurons aligned with the support of ordered graphene structures. Polar histogram in **Figure 3** D further confirmed that both neurons and glial cells preferred to grow along the graphene skeleton. Thus, the ordered structure of 3D-OG successfully regulated the neuronal growth.

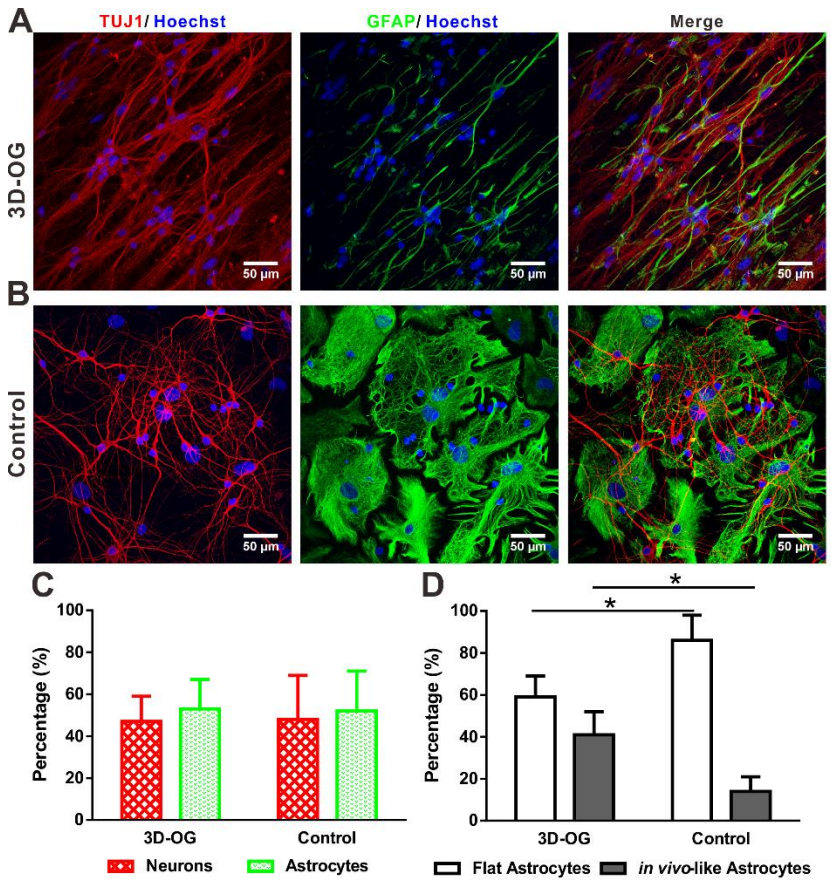

Figure 2. 3D-OG scaffolds are biocompatible for primary cortical cells growth and maturation. Immunofluorescence images of cortical cells after 8-10 DIV culture on 3D-OG scaffolds (A) and coverslip control (B), stained with β-tubulin III (TUJ1, red), GFAP (green) and Hoechst (blue). C) Proportion of neurons (β-tubulin III-positive) and astrocytes (GFAP-positive) on 3D-OG scaffolds and coverslip control respectively. D) Percentage of astrocytes with flattened and *in vivo* like morphology on 3D-OG scaffolds and coverslip control respectively. *$p < 0.05$, two-way analysis of variance (ANOVA), Sidak's test.

Spontaneous calcium transients occur extensively during the whole development of the nervous system, where it operates over a wide temporal range to influence many important cellular processes, including proliferation, migration, and differentiation.[37] On the other hand, the spike synchronization of calcium transients underlies information processing and storage in the brain.[38] To investigate how the ordered structure of 3D-OG impact neuronal network performance, we monitored the spontaneous network activity by means of fluorescence calcium imaging. Fluo-4 AM fluorescent images showed clear bright spots associated with the cell body of neurons

and glia (**Figure 4**A). Neural activity was evaluated by recording their calcium transients (DF/F) in fluorescence images at 3 – 5 Hz for 10 min (**Movie S1, Supporting Information**). At DIV 8, synchronous calcium transients with an amplitude of up to 1.5 DF/F were observed. Neurons and glial cells formed well-defined connections in 3D due to the support of 3D-OG. In **Figure 4**B, examples of calcium transients from three representative neurons grown on 3D-OG scaffolds in normal extracellular saline solution and in bicuculline (a competitive antagonist of inhibitory $GABA_A$ receptors) were depicted.

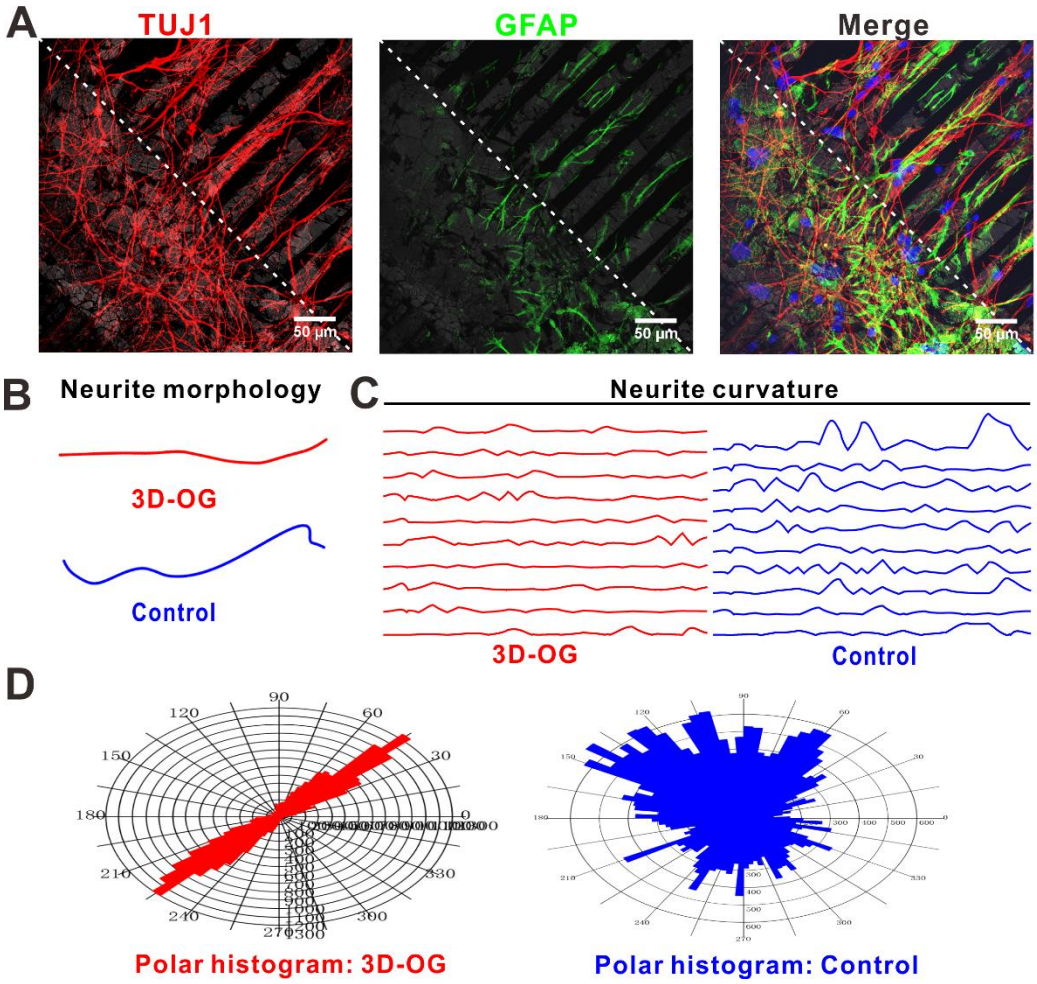

Figure 3. 3D-OG scaffolds geometrically regulated neuronal growth. A) Immunofluorescence images of cortical cells after 8-10 DIV culture on 3D-OG scaffolds, stained with β-tubulin III (TUJ1, red), GFAP (green) and DAPI (blue). 3D-OG structure was reflected with gray. B) Representative neurite morphology on 3D-OG scaffolds and coverslip control respectively. C) Representative neurite curvature distributions on 3D-OG scaffolds and coverslip control respectively. D) Representative polar histogram of neurite growth on 3D-OG scaffolds and coverslip control

respectively.

In our recordings, spontaneous calcium activity was detected in 38.9 % of cells present in each field visualized on coverslips. Notably, more than 53 % of the visualized cells were active and generate spontaneous calcium episodes (**Figure 4**C). The Δt interval between two successive calcium transients was computed to obtain an average inter events interval (IEI) for each neuron. We found that IEI was significant shorter on 3D-OG scaffolds (47.3 ± 8.6 s) when compared to controls (74.8 ± 12.1 s) (**Figure 4**D), thus suggesting that 3D-OGs promote and enhance electrical activity. The synchronization of activity could be measured by the mean correlation coefficient of the calcium transients. However, the synchrony of neural activity did not show obvious difference on 3D-OG scaffolds and on control (**Figure 4**E). Additionally, we pharmacologically blocked $GABA_A$ receptors by bicuculline (20×10^{-6} M; 10 min) application, which was known to alter network activity patterns.[39] Because of bicuculline addition, IEI decreasing was found on control and synchrony increasing was identified on both groups. From an electrophysiological point of view, 3D-OG increased the overall number of active cells as well the efficacy of neural signaling by boosting the frequency of network electrical activity. Furthermore, the impact of 3D-OG on network activity was preserved in the presence of bicuculline, highlighting a change in the excitation/inhibition ratio

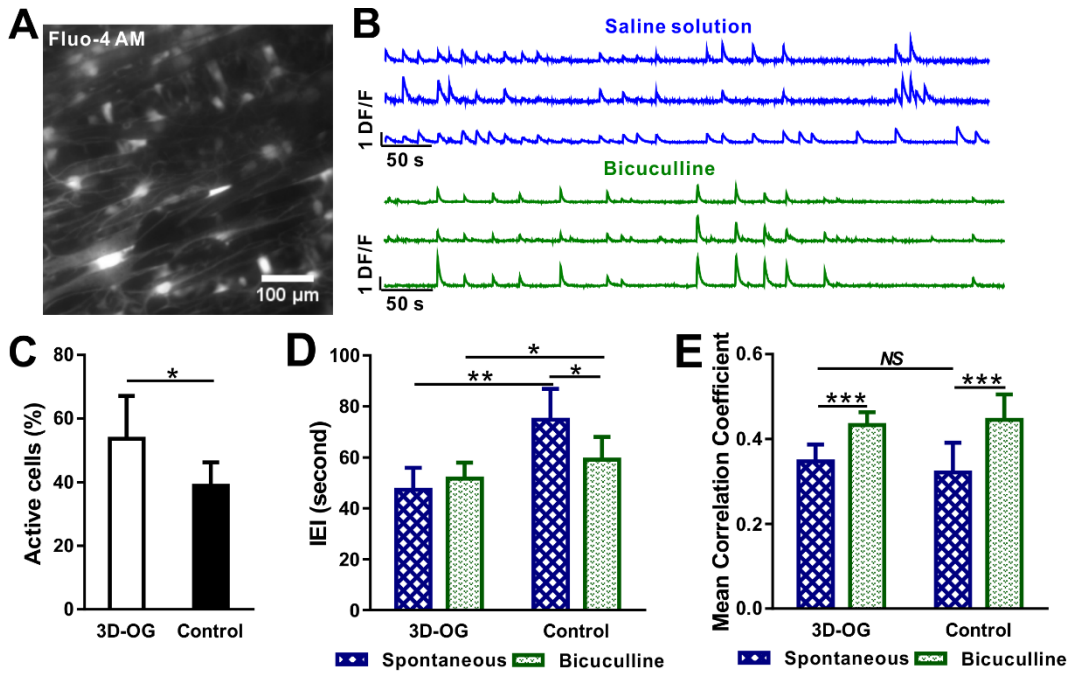

Figure 4. 3D-OG scaffolds promoted neuronal network activity *in vitro*. A) Representative fluorescent image of a neuronal culture grown on a 3D-OG scaffold loaded with the membrane-permeable calcium fluorescent dye Fluo-4 AM at 8 DIV. B) Representative calcium transients spontaneously (up) or bicuculline-induced (down) recorded from 3 selected neurons at 8 DIV. C) A histogram of the percentage of spontaneous active cells cultured on 3D-OG scaffold and coverslip control at 8 DIV. D) Average of interevent interval (IEI) values of neurons cultured on 3D-OG scaffold and coverslip control in normal saline solution and in disinhibiting bicuculline solution at 8 DIV. E) Comparison of the mean correlation coefficient of neurons cultured on 3D-OG scaffold and coverslip control in normal saline solution and in disinhibiting bicuculline solution at 8 DIV. *p < 0.05, **p < 0.01, ***p < 0,001, NS means no significant difference, two-way analysis of variance (ANOVA), Sidak's test.

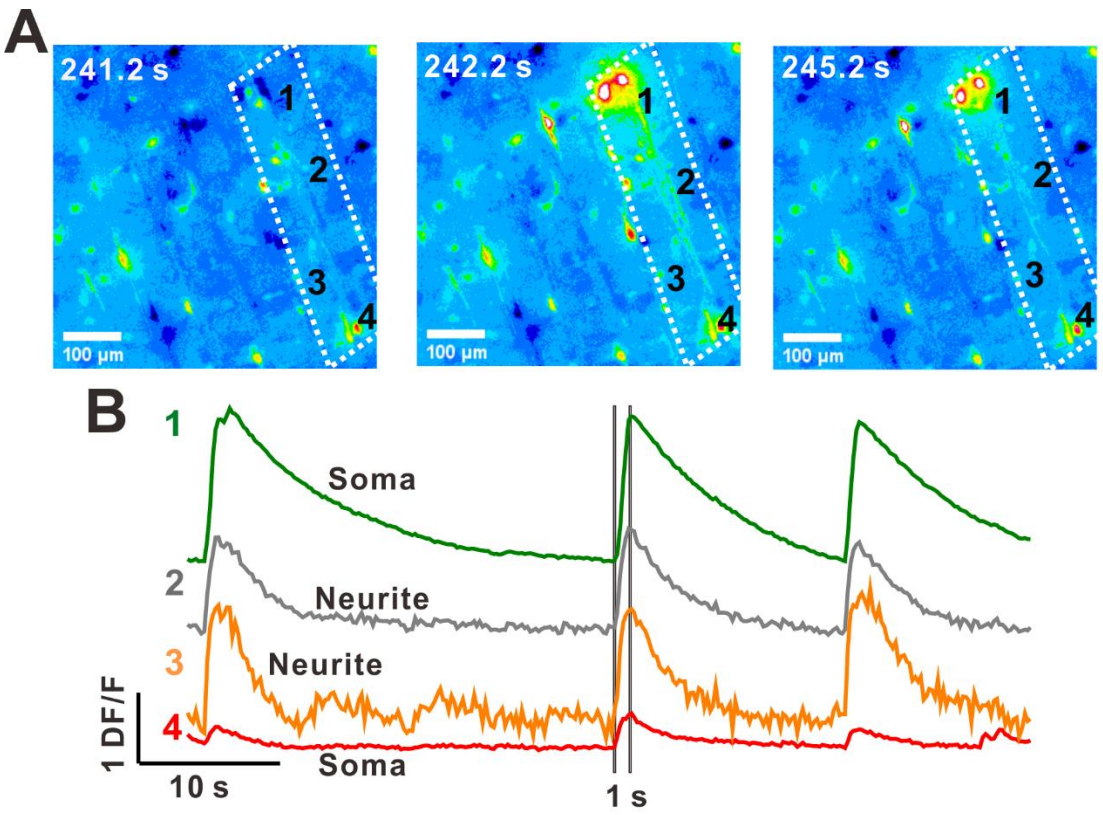

Figure5. 3D-OG scaffolds patterned the formation of neuronal network. A) Representative DF/F fluorescent images in a time series of neuronal network formed on a 3D-OG scaffold loaded with the membrane-permeable calcium fluorescent dye Fluo-4 AM at 8 DIV. 1 and 4 are marked for two different soma, 2 and 3 are marked for the neurites. B) Synchronous calcium transients acquired from four points located on a same graphene skeleton.

Furthermore, we analyzed the signaling between soma and neurites along the same graphene skeleton. We provided three DF/F fluorescent images in a time series below one independent spike period (**Figure 5**A). Along the graphene skeleton, soma and neurites had synchronous calcium transients (trace number 1, 2 and 3, **Figure 5**B) in a long distance over 600 μm, Moreover, different neurons also presented synchronous calcium activity, indicating that the ordered structure of 3D-OG guide the neuronal network functional formation. Overall, the 3D-OG scaffolds patterned the formation of neuronal network and enhanced firing rates of network activity.

Conclusion

One of the primary goals of neural tissue engineering is to guide neurite growth in a desired direction, therefore, to pattern the alignment of the neuronal growth and

network formation is highly valued.[40] In this study, we show the ordered growth of neurons and alignment of neuronal network formation on the support of graphene in 3D for the first time. The fabricated 3D-OG with the pore size of 20 μm, the skeleton width of 20 μm and the 90° orientation angles of building blocks presented high neuronal culture compatibility, where neurons and glia grew along the skeleton geometry and formed functional network. Compared to standard neuronal culture on coverslip, 3D-OG structure didn't affect the relative abundance of neurons and glial cells but induced astrocytes exhibiting much more in vivo like morphologies. Moreover, much more bipolar neurons were found on 3D-OG scaffolds because of the ordered graphene skeleton. We also found that neurons were more active on 3D-OG scaffolds and cellular communication occurred along the graphene skeleton over a long distance. Our results imply that 3D ordered graphene structures provided geometrical cues in neurons, leading to directional neurite outgrowth and consequently increasing neuronal network connections, which leads to significant process in designing scaffold−tissue interfaces and ultimately the development of customized neuro-prosthetics in tissue engineering and regenerative medicine.

References

[1] Sun F, Park KK, Belin S, Wang D, Lu T, Chen G, et al. Sustained axon regeneration induced by co-deletion of PTEN and SOCS3. Nature 2011;480:372-5.

[2] Nguyen QT, Sanes JR, Lichtman JW. Pre-existing pathways promote precise projection patterns. Nature Neuroscience 2002;5:861.

[3] Basso JMV, Yurchenko I, Simon M, Rizzo DJ, Staii C. Role of geometrical cues in neuronal growth. Physical Review E 2019;99.

[4] Gilbert PM, Havenstrite KL, Magnusson KEG, Sacco A, ., Leonardi NA, Kraft P, ., et al. Substrate elasticity regulates skeletal muscle stem cell self-renewal in culture. Science 2010;329:1078-81.

[5] Wang LS, Du C, Chung JE, Kurisawa M. Enzymatically cross-linked gelatin-phenol hydrogels with a broader stiffness range for osteogenic differentiation of human mesenchymal stem cells. Acta Biomater 2012;8:1826-37.

[6] Guicai L, Xueying Z, Weixin Z, Luzhong Z, Caiping W, Maorong J, et al. Porous chitosan scaffolds with surface micropatterning and inner porosity and their effects on Schwann cells. Biomaterials 2014;35:8503-13.

[7] Kane RS, Takayama S, Ostuni E, Ingber DE, Whitesides GM. Patterning proteins and cells using soft lithography. Biomaterials 1999;20:2363-76.

[8] Poudel I, Lee JS, Tan L, Lim JY. Micropatterning-retinoic acid co-control of neuronal cell morphology and neurite outgrowth. Acta Biomater 2013;9:4592-8.
[9] Pardo-Figuerez M, Martin NRW, Player DJ, Roach P, Christie SDR, Capel AJ, et al. Controlled Arrangement of Neuronal Cells on Surfaces Functionalized with Micropatterned Polymer Brushes. Acs Omega 2018;3:12383-91.
[10] Xie C, Gao Q, Wang P, Shao L, Yuan H, Fu J, et al. Structure-induced cell growth by 3D printing of heterogeneous scaffolds with ultrafine fibers. Materials & Design 2019;181:108092.
[11] Kuddannaya S, Tong CS, Fan YT, Zhang YL. Geometrically Mediated Topographic Steering of Neurite Behaviors and Network Formation. Advanced Materials Interfaces 2018;5.
[12] Xiao M, Li X, Song Q, Zhang Q, Lazzarino M, Cheng G, et al. A Fully 3D Interconnected Graphene-Carbon Nanotube Web Allows the Study of Glioma Infiltration in Bioengineered 3D Cortex-Like Networks. Advanced Materials 2018;30:1806132.
[13] Liu Z, Tang M, Zhao J, Chai R, Kang J. Looking into the Future: Toward Advanced 3D Biomaterials for Stem-Cell-Based Regenerative Medicine. Adv Mater 2018.
[14] Moncal KK, Ozbolat V, Datta P, Heo DN, Ozbolat IT. Thermally-controlled extrusion-based bioprinting of collagen. Journal of Materials Science: Materials in Medicine 2019;30:55.
[15] Lee SJ, Esworthy T, Stake S, Miao S, Zuo YY, Harris BT, et al. Advances in 3D Bioprinting for Neural Tissue Engineering. Adv Biosyst 2018;2:18.
[16] Georgiou M, Bunting SCJ, Davies HA, Loughlin AJ, Golding JP, Phillips JB. Engineered neural tissue for peripheral nerve repair. Biomaterials 2013;34:7335-43.
[17] Guo R, Zhang S, Xiao M, Qian F, He Z, Li D, et al. Accelerating bioelectric functional development of neural stem cells by graphene coupling: Implications for neural interfacing with conductive materials. Biomaterials 2016;106:193-204.
[18] Novoselov KS, Geim AK, Morozov SV, Jiang D, Katsnelson MI, Grigorieva IV, et al. Two-dimensional gas of massless Dirac fermions in graphene. Nature 2005;438:197-200.
[19] Balandin AA, Ghosh S, Bao W, Calizo I, Teweldebrhan D, Miao F, et al. Superior Thermal Conductivity of Single-Layer Graphene. Nano Letters 2008;8:902-7.
[20] Stankovich S, Dikin DA, Dommett GHB, Kohlhaas KM, Zimney EJ, Stach EA, et al. Graphene-based composite materials. Nature 2006;442:282-6.
[21] Ponomarenko LA, Schedin F, Katsnelson MI, Yang R, Hill EW, Novoselov KS, et al. Chaotic Dirac Billiard in Graphene Quantum Dots. Science 2008;320:356-8.
[22] Bramini M, Alberini G, Colombo E, Chiacchiaretta M, DiFrancesco ML, Maya-Vetencourt JF, et al. Interfacing graphene-based materials with neural cells. Frontiers in systems neuroscience 2018;12:12.
[23] Schouteden K, Galvanetto N, Wang CD, Li Z, Van Haesendonck C. Scanning probe microscopy study of chemical vapor deposition grown graphene transferred to Au(111). Carbon 2015;95:318-22.
[24] Ma Q, Yang L, Jiang Z, Song Q, Xiao M, Zhang D, et al. Three-Dimensional Stiff Graphene Scaffold on Neural Stem Cells Behavior. ACS Appl Mater Interfaces 2016;8:34227-33.
[25] Xiao M, Kong T, Wang W, Song Q, Zhang D, Ma Q, et al. Interconnected Graphene Networks with Uniform Geometry for Flexible Conductors. Adv Funct Mater 2015;25:6165-72.
[26] Ma X, Xiao M, Hao Y, Cheng G. Precisely controllable hybrid graphene scaffold reveals size effects on differentiation of neural progenitor cells in mimicking neural network. Carbon 2019;145:90-9.
[27] Lv W, Zhang C, Li ZJ, Yang QH. Self-Assembled 3D Graphene Monolith from Solution. J Phys Chem Lett 2015;6:658-68.
[28] Nguyen DD, Suzuki S, Kato S, To BD, Hsu CC, Murata H, et al. Macroscopic, Freestanding, and

Tubular Graphene Architectures Fabricated via Thermal Annealing. ACS Nano 2015;9:3206-14.
[29] Chae SJ, Guenes F, Kim KK, Kim ES, Han GH, Kim SM, et al. Synthesis of Large-Area Graphene Layers on Poly-Nickel Substrate by Chemical Vapor Deposition: Wrinkle Formation. Advanced Materials 2009;21:2328-+.
[30] Onesto V, Cancedda L, Coluccio ML, Nanni M, Pesce M, Malara N, et al. Nano-topography Enhances Communication in Neural Cells Networks. Sci Rep 2017;7:13.
[31] Malard LM, Pimenta MA, Dresselhaus G, Dresselhaus MS. Raman spectroscopy in graphene. Physics Reports-Review Section of Physics Letters 2009;473:51-87.
[32] Ferrari AC, Meyer JC, Scardaci V, Casiraghi C, Lazzeri M, Mauri F, et al. Raman Spectrum of Graphene and Graphene Layers. Physical Review Letters 2006;97.
[33] Reina A, Jia X, Ho J, Nezich D, Son H, Bulovic V, et al. Large Area, Few-Layer Graphene Films on Arbitrary Substrates by Chemical Vapor Deposition. Nano Letters 2009;9:30-5.
[34] Wen X, Tresco PA. Effect of filament diameter and extracellular matrix molecule precoating on neurite outgrowth and Schwann cell behavior on multifilament entubulation bridging device In vitro. Journal of Biomedical Materials Research Part A 2010;76A:626-37.
[35] Rago I, Rauti R, Bevilacqua M, Calaresu I, Pozzato A, Cibinel M, et al. Carbon Nanotubes, Directly Grown on Supporting Surfaces, Improve Neuronal Activity in Hippocampal Neuronal Networks. Adv Biosyst 2019;3:13.
[36] Tang Y, Ulloa Severino FP, Iseppon F, Torre V, Chen Y. Patch method for culture of primary hippocampal neurons. Microelectronic Engineering 2017;175:61-6.
[37] Uhlen P, Fritz N, Smedler E, Malmersjo S, Kanatani S. Calcium Signaling in Neocortical Development. Developmental Neurobiology 2015;75:360-8.
[38] Takahashi N, Sasaki T, Matsumoto W, Matsuki N, Ikegaya Y. Circuit topology for synchronizing neurons in spontaneously active networks. Proceedings of the National Academy of Sciences 2010;107:10244-9.
[39] Tibau E, Valencia M, Soriano J. Identification of neuronal network properties from the spectral analysis of calcium imaging signals in neuronal cultures. Frontiers in Neural Circuits 2013;7:199.
[40] Marcus M, Baranes K, Park M, Choi IS, Kang K, Shefi O. Interactions of Neurons with Physical Environments. Adv Healthc Mater 2017;6:19.

3.3 Biomimetic three-dimensional bacterial cellulose-graphene foam materials regulate neural stem cell proliferation and differentiation

Rongrong Guo[#], Jian Li[#], Chuntao Chen[#], Miao Xiao[#], Menghui Liao, Yangnan Hu, Yun Liu, Dan Li, Jun Zou, Dongping Sun, Vincent Torre, Qi Zhang[*], Mingliang Tang[*], Renjie Chai[*]

Biomimetic three-dimensional bacterial cellulose-graphene foam materials regulate neural stem cell proliferation and differentiation

Rongrong Guo[1,2,3,4,#], Jian Li[2,4,#], Chuntao Chen[5,#], Miao Xiao[6,#], Menghui Liao[2,3,4], Yangnan Hu[2,3,4], Yun Liu[2,3,4], Dan Li[2,3,4], Jun Zou[7], Dongping Sun[5], Vincent Torre[6], Qi Zhang[1*], Mingliang Tang[2,3,4]*, Renjie Chai[2,3,4,8]*

[#]these authors contributed equally to this paper.

[1]School of Radiation Medicine and Protection and School for Radiological and Interdisciplinary Sciences (RAD-X), Collaborative Innovation Center of Radiation Medicine of Jiangsu Higher Education Institutions, Medical College of Soochow University, Suzhou, Jiangsu 215123, China

[2]Key Laboratory for Developmental Genes and Human Disease, Ministry of Education, Institute of Life Sciences, Southeast University, Nanjing 210096, China

[3]Co-innovation Center of Neuroregeneration, Nantong University, Nantong 226001, China

[4]Joint Research Institute of Southeast University and Monash University, Suzhou 215123, China

[5]Institute of Chemicobiology and Functional Materials, Key Laboratory for Soft Chemistry and Functional Materials of Ministry Education, School of Chemical Engineering, Nanjing University of Science and Technology, 200 Xiao Ling Wei Street, Nanjing, 210094, Jiangsu Province, China

[6]International School for Advanced Studies (SISSA), via Bonomea 265, Trieste 34136, Italy.

[7]Department of Orthopaedic Surgery, The First Affiliated Hospital of Soochow University, 188 Shizi Street, Suzhou, Jiangsu 215006, China

[8]Institute for Stem Cell and Regeneration, Chinese Academy of Science, Beijing, China.

***Correspondence:**

Dr. Qi Zhang,
School of Radiation Medicine and Protection and School for Radiological and Interdisciplinary Sciences (RAD-X), Collaborative Innovation Center of Radiation Medicine of Jiangsu Higher Education Institutions, Medical College of Soochow University, Suzhou, Jiangsu 215123, China
Email: qzhang2012@suda.edu.cn

Dr. and Prof. Mingliang Tang,
Key Laboratory for Developmental Genes and Human Disease, Ministry of Education, Institute of Life Sciences, Southeast University, Nanjing 210096, China; Co-innovation Center of Neuroregeneration, Nantong University, Nantong 226001, China; Joint Research Institute of Southeast University and Monash University, Suzhou 215123, China
Email: mingliangtang@seu.edu.cn

Dr. and Prof. Renjie Chai,
Key Laboratory for Developmental Genes and Human Disease, Ministry of Education, Institute of Life Sciences, Southeast University, Nanjing 210096, China; Co-innovation Center of Neuroregeneration, Nantong University, Nantong 226001, China; Joint Research Institute of Southeast University and Monash University, Suzhou 215123, China
Email: renjiec@seu.edu.cn

Abstract

Neural stem cell (NSC)-based therapy is a promising candidate for treating neurodegenerative diseases, but its transition from the lab to the clinic is hampered by many obstacles. This suggests an urgent need for research into the factors that can be manipulated in order to regulate the growth and differentiation of such cells in different in vivo environments. The recognition that three-dimensional culture has the potential to be a biologically significant system has stimulated an extraordinary impetus for scientific research in all fields of tissue engineering and regenerative medicine. Here, we report a novel scaffold for culturing NSCs *in vitro*, three-dimensional bacterial cellulose-graphene foam (3D-BC/G), which was prepared via in situ bacterial cellulose interfacial polymerization on the skeleton surface of porous graphene foam. We found that 3D-BC/G not only supports NSC growth and adhesion, but also maintains NSC stemness and enhances their proliferative capacity. Further phenotypic analysis indicated that 3D-BC/G induces NSCs to selectively differentiate into neurons, forming a neural network in a short amount of time. We also found that the material has good biocompatibility with primary cortical neurons and that it enhances the neuronal network activities of these cells as indicated by measurements of calcium transients. To explore the underlying mechanisms behind these effects, we performed RNA-Seq analysis to identify genes and signaling pathways that are important for NSC development and maintenance. Our findings suggest that graphene foam embedded with bacterial cellulose offers a more promising three-dimensional conductive substrate for NSC research and neural tissue engineering, and the repertoire of gene expression that we present serves as a basis for further studies to better understand NSC biology.

Keywords: graphene foam, bacterial cellulose, three-dimensional culture, neural stem cell, proliferation, differentiation

Introduction

An increasing number of studies have shown that neural stem cells (NSCs) have the potential for wide use in cell-based therapy to both protect and restore damaged neurons in neurodegenerative diseases such cervical spinal cord injury [1], Parkinson's disease (PD) [2] and Alzheimer's disease [3]. However, NSC transplantation faces many obstacles in its transition from the lab to the clinic, especially issues related to the uncontrolled differentiation and functional engraftment of implanted tissues [4]. By further developing our knowledge of the molecular, cellular, and developmental biology of NSCs, we can better understand the organization and function of the complex brain. Under normal physiological conditions, NSCs reside in neurogenic niches, and neurogenesis occurs in a spatially and temporally regulated fashion through many physiological stimuli, including culture media, co-culture with other cells, physicochemical conditions, surface biochemistry, surface topography, mechanical signals, and 3D culture scaffolds [5]. Consequently, significant efforts have been made to develop tunable three-dimensional NSC microenvironments that can regulate and control NSC fate in the desired direction, and such porous scaffolds show great promise for manipulating cell behavior in the areas of tissue engineering and regenerative medicine.

Electrically conductive scaffolds have found applications in neural regeneration through their ability to guide NSCs to differentiate into neural lineages, and graphene film has been shown to induce stem cells to preferentially differentiate into specific lineages [6]. Of clinical interest, three-dimensional graphene foam (3D-G) has been widely accepted as a good scaffold material in the field of tissue engineering by virtue of its excellent biocompatibility and electrical properties along with its porous structure and precisely tunable properties [7]. Previous research by our group has shown that 3D-G is a biocompatible and conductive scaffold for use with NSCs [8] and that the material improves skin wound healing by promoting the growth and proliferation of mesenchymal stem cells [9].

Taken together, many of the properties of three-dimensional graphene make it a highly favorable microenvironment for neural cells to reside in and respond to.

However, these materials have pore sizes of 100–300 μm such that cells seeded into them typically attach, proliferate, and differentiate along the walls of the pores rather than filling the entire space [8]. This observation has motivated us to develop a method to functionalize these unoccupied cavities in order to simulate a more realistic and suitable three-dimensional microenvironment.

Three-dimensional bacterial cellulose (3D-BC), which is an unbranched polymer of β-1, 4-linked glucopyranose residues [10], has long been used as an effective biomaterial for use in full-thickness skin tissue repair [11], blood vessel grafts [12], bone tissue engineering [13], and meniscus replacement [14] with the advantage of easy purification and manipulation, good biocompatibility, high tensile strength and elastic modulus, high hydrophilicity, efficient biodegeneration, and similar morphological characteristics to collagenous fibers [10b, 15]. It has thus been extensively researched as a suitable substrate material for tissue engineering and biomedical applications [16]. Several studies have shown that 3D-BC alone or with specific surface modifications can maintain the biological activity of cultured cells and can direct the morphology and differentiation of various cells, including adipose-derived stem cells [17], glial cells, neurons, and skeletal muscle cells [18].

These unique properties of bacterial cellulose have opened up new perspectives for developing nanofiber scaffolds for tissue engineering. However, bacterial cellulose fermented directly by *Acetobacter xylinum* forms a dense network of nanofibers with pore sizes of 0.02–10μm [19], which are smaller than the dimensions of mammalian cells such that these cells cannot penetrate into the pore and form three-dimensional structures [20]. The preparation methods of scaffold structures with bacterial cellulose or natural nanofiber materials have been reported to form nanofibrous structures [21]. To address this issue, we fermented *A. xylinum* on 3D-G to create a novel microporous, nanofiber-based, and electrically conductive scaffold (3D-BC/G) that integrates the advantages of graphene foam and bacterial cellulose, and this method enhances the topographic properties and decreases the pore diameter of 3D-G in order to increase its usefulness in tissue engineering [22]. We show that this material possesses good biocompatibility and is a suitable neural tissue-engineering scaffold

that can regulate the biological behaviors of NSCs, including survival, adhesion, spreading, proliferation, and differentiation.

Results and discussion

Fabrication and characterization of 3D-BC/G for NSC culture

Multilayer 3D-G foams were fabricated by chemical vapor deposition using 3D-Ni scaffolds as both catalysts and templates. Nickel was subsequently removed by $FeCl_3$ etching. The 3D-BC/G was obtained by culturing *A. xylinum*on the 3D-G surface. As shown in Figure 1A, the 3D-BC nanofibers were bunched together on the surface of the graphene skeleton. The scanning electron microscopy (SEM) images (Figure 1B, a–d) showed a robust, porous, and nanofiber-embedded 3D-BC/G foam. The inclusion of BC did not compromise the structural integrity of the graphene foams, and this is important for future applications because it is critical that the three-dimensional microstructures provide sufficient physical support in order for NSCs to homogenously distribute and expand. Moreover, the BC nanofibers on the surface of the graphene skeleton significantly improve the nano-sized topological structures, leading to enhanced cell-scaffold interaction [23].

Figure 1C shows the Raman spectra of the 3D-BC, 3D-G, and 3D-BC/G materials. The prominent 2D band located at ~2700 cm^{-1} and the G band centered at ~1580 cm^{-1} were observed in the spectrum of 3D-G, indicating the overall high quality of the graphene. These two peaks were also observed in the spectrum of 3D-BC/G but were weakened because of the presence of BC on the surface of the graphene skeleton. Similar to BC, a Raman band located at ~1090 $cm^{-1}$for 3D-BC/G was assigned to C-O stretching ring modes. The bands at 1337 cm^{-1} and 1377 cm^{-1} were assigned to C–H deformation and O–H deformation, respectively, which were also seen in the spectrum of 3D-BC/G. X-ray powder diffraction (XRD) and Raman spectroscopy were used to verify the construction of the 3D-BC/G scaffold. The intrinsic peaks of 3D-G ($2\theta = 27.5°$ and 55.2°), corresponding to its diffraction planes (002) and (004), were seen in the XRD patterns (Figure 1D). Three major peaks of BC located at 14.5°, 16.8°, and 22.7°, corresponding to the $(1\bar{1}0)$, (110), and (200) diffraction planes of

cellulose I, respectively, were also observed. The characteristic peaks of both BC (2θ = 14.5°) and G (2θ = 27.5°) were inherited in the 3D-BC/G composite material, but with weakened intensities. Furthermore, the incorporation of nanofibrous BC on the surface of the graphene skeleton increased its surface area, reduced its pore size, and provided a broad array of oxygen groups. All of these features suggest that this novel 3D-BC/G material has the ability to enhance cell-cell and cell-matrix interactions.

Biocompatibility of 3D-BC/G

For the successful clinical application of scaffold biomaterials, biocompatibility is a critical issue. We first evaluated the biocompatibility of 3D-BC/G using a live/dead assay. We found that NSCs cultured on 3D-BC/G for 3 days had a viability of more than 99%, which was comparable to that of NSCs grown on 3D-G (Figure 2A). SEM images showed that NSCs on these two scaffolds had normal morphology and normal extensions and protrusions (Figure 2B). SEM analysis of the cultures also allowed investigation of the interactions of such protrusions with the three-dimensional materials. As shown in the high-magnification images, the fibers appeared tightly anchored to the surface of scaffolds with evident development of membrane-substrate junctions and growth cones. These findings suggest the biocompatibility of 3D-BC/G *in vitro*.

Maintaining the stemness of NSCs on 3D-BC/G

Neurogenesis consists of several developmental stages, including proliferation, differentiation, maturation, migration, and integration. The foundation of all of these processes is the maintenance of NSC stemness on the scaffold biomaterials because NSCs themselves are key determinates of neurogenesis. To test whether 3D-BC/G maintains NSC stemness, the expression of nestin, a protein that is essential for maintaining the stemness of NSCs, was evaluated by immunofluorescence staining (Supplementary Figure S1). Almost all of the cells cultured on 3D-BC/G were nestin-positive (green), with no obvious differences compared to those cultured on 3D-G and 3D-BC, indicating that NSCs cultured on 3D-BC/G maintained physiological levels of stemness.

Focal adhesion of NSCs on 3D-BC/G

It has been demonstrated that spatiotemporal and topographical cues can regulate multiple cellular behaviors, including survival, proliferation, differentiation, and migration, by modulating integrin-based focal adhesion and subsequent changes in cytoskeletal organization and mechanosensitive signaling cascades [24]. The interactions between cells and scaffold biomaterials are very complex multi-step processes, but these can be studied in vitro by studying the adsorption of extracellular matrix (ECM) proteins, such as laminin, collagen, and fibronectin, onto the surfaces of the materials. The recognition of cell-binding domains of the ECM by cell surface receptors focuses primarily on the integrin superfamily, and the collection of focal adhesion proteins, including vinculin, FAK, and paxillin, is followed by cytoskeletal rearrangements that lead to changes in cell behavior [25]. In this study, qPCR showed that NSCs cultured on 3D-G had greater expression levels of the focal adhesion proteins vinculin, FAK, and paxillin than NSCs cultured on 3D-BC/G (Figure 3B and C), which indicated that 3D-G was more effective than 3D-BC/Gin facilitating focal adhesion development of NSCs, likely by providing more focal adhesion points.

NSC proliferation on 3D-BC/G

To evaluate the structural and topographical effects of 3D-BC/G on the proliferation of NSCs, NSC proliferation on 3D-BC/G was determined by measuring the percentage of EdU-positive cells, which indicate early S-phase cells. We found that NSCs cultured on 3D-BC/G had greater proportions of EdU-positive cells compared to 3D-G (Figure 4A and B) suggesting that NSCs cultured on 3D-BC/G have greater proliferative ability compared to cells cultured on 3D-G. To further verify this phenotype, an alamarBlue assay was carried out to measure NSC proliferation (Figure 4C). The NSCs cultured on 3D-BC/G had a greater reduction in alamarBlue than those cultured on 3D-G, which was similar to the EdU assay. qPCR experiments also supported this result by showing that the gene expression levels of *Ki67*, *MCM2*, and *PCNA*, which are all markers of proliferation, were higher in NSCs cultured on 3D-BC/G compared to those cultured on 3D-G (Figure 4D).Together these observations indicate that the addition of bacterial cellulose onto a graphene skeleton can significantly increase the proliferative ability of NSCs.

The proliferative potential of NSCs is tightly regulated by extrinsic signals – such as growth factors, ECM components, neurotransmitters, and cellular focal adhesion molecules – in order to maintain the homeostasis of the stem cell pool. The deletion or decrease in cellular focal adhesion proteins enhances NSC proliferation by integrin-β1-mediated signaling,[26] and this is consistent with our results (Figure 3A). We further speculate that this improvement is because the bacterial cellulose simulates the self-assembly process of protein fibrillogenesis in vivo, which leads to the formation of ECM [27].

NSC differentiation on 3D-BC/G

To further investigate the phenotypic differences of differentiated NSCs, we induced NSCs to differentiate for 7 days and visualized their offspring by immunofluorescence staining for Tuj-1(Figure 5).The images indicated that the differentiated neurons cultured on 3D-BC/G formed an obvious three-dimensional neural network, while the differentiated neurons on 3D-G had shorter neurite outgrowths. These images of cells grown on 3D-BC/G and 3D-G were all obtained by confocal microscopy, in which every picture is an optical slice. The resulting projections of several optical slices show that 3D-BC/G can quickly organize a three-dimensional neural network.

Mounting evidence suggests the importance of mechanosensitivity, in which biophysical signals are transduced into biochemical signals [28], for modulating the physiological functions of stem cells or neurons, including their adhesion, motility, differentiation, and neurite outgrowth [29]. The addition of BC to 3D-G compensates for many of the limitations of 3D-G's mechanical properties. For example, the Young's modulus of 3D-BC is about 80 GPa, while that of 3D-G is about 1,000–2,000 MPa, and thus 3D-BC/G shows a Young's modulus that is similar to soft-tissue membranes. At the same time, the micro- and nano-scale topography of biomaterials has been shown to be very important for determining neural differentiation and for influencing neurite outgrowth by mimicking the topography of native collagen films [30]. The 3D-BC/G scaffold showed more complicated nano-topography than 3D-G (Figure 1B), and therefore it is tempting to speculate that the neurites of newborn neurons adapt to the distinctive morphological and mechanical features of scaffold

materials and that this might explain why 3D-BC/G induced longer neurites to form a neural network.

Construction of functional 3D neural networks on 3D-BC/G and 3D-G

The novel 3D-BC/G scaffold was also found to be compatible with neuronal culture. Primary cortical neurons isolated from Wistar rats (postnatal day 1–3) were used to compare 3D neuronal network formation on both 3D-BC/G and 3D-G. After 8 days of culture, the cells were stained with antibodies against Tuj-1 to identify neurons and with antibodies against glial fibrillary acidic protein (GFAP) to identify glial cells. Confocal images of cortical neuronal networks grown on 3D-BC/G and 3D-G (Figure 6A) showed that the neurons grew primarily along the walls of the 3D-G scaffold and developed a 3D neural network that followed the scaffold's topology. In contrast, neurons grown on 3D-BC/G formed a denser network with the support of BC, which was confirmed by the cell density analysis (Figure 6B). After 8 days in culture, nucleus counting showed an almost 3-fold increase in cell density on 3D-BC/G compared to 3D-G. The decreased porosity of 3D-BC/G scaffolds compared to the porosity of the 3D-G scaffolds enabled the retention of a larger number of neurons and glia cells inside the 3D-BC/G scaffolds, thus better mimicking the in vivo situation.

Spontaneous calcium transients occur extensively throughout the development of the nervous system, and these transients operate over a wide temporal range to influence proliferation, migration, and differentiation [31]. To determine whether neurons grown on the 3D-BC/G scaffolds are alive and functionally active, we performed calcium imaging experiments using the calcium indicator Fluo-4 AM. The fluorescence images of Fluo-4-loaded cortical cells cultured on 3D-BC/G and 3D-G are shown in Figures 6C and D, respectively. Spontaneous calcium transients (DF/F) associated with the electrical firing of neurons were obtained by acquiring images at 3–5 Hz for 10–20 minutes (Figure 6E and F). After 8 days in culture, calcium transients with an amplitude of up to 1 DF/F were observed. The neuronal activity on 3D-BC/G scaffolds was ~50% more frequent than that on 3D-G scaffolds (Figure 6G), and the synchronization of neuronal activity could be represented by the mean

correlation coefficient of the calcium transients. However, the synchrony of neuronal activity did not show any obvious difference between the 3D-BC/G and 3D-G substrates. Considering the complex features of the brain, such highly-packed neurons and glial cell culture system with complex functional neuronal networks constructed on 3D-BC/G present a better model for studying the physiological and pathological processes in the brain.

Differential gene expression on the three-dimensional biomaterials

RNA-Seq was performed to identify differences in the gene expression profiles of NSCs cultured on 3D-G and 3D-BC/G substrates, and we explored the most abundantly expressed genes in NSCs cultured on these substrates. Figure 7 shows the expression levels of the top 200 most abundant genes in NSCs cultured on 3D-BC/G (red bar). For comparison, the expression levels for the same transcripts in NSCs cultured on 3D-G (green bar) and the abundance rankings for these transcripts are also illustrated. As shown in the figures, the majority of the transcripts that were richly expressed in one group were also abundantly expressed in the other. We compared the expression levels of all of the transcripts in these two groups and selected the top 40 differentially expressed genes (Figures 8A and B). The differentially expressed genes were categorized as those whose expression levels were above background and at least 2-fold different between the two groups ($p < 0.01$). Among these differentially expressed genes, *Nhlh1*, *Epcam*, *Cidea*, *Pdzph1*, *2310069G16Rik*, *Serpinf1*, *Emb*, *Cacng6*, *Vwc2*, *Flywch2*, *Ptgs1*, *Pgm5*, *Kcnip2*, *Fut4*, *Gjd2*, *Fhl2*, *Fam213a*, *Dbpht2*, *Krt1*, *Gal3st1*, *Ppp1r1b*, *Mroh3*, and *Insc* were preferably expressed in the NSCs cultured on 3D-BC/G.*Pkn3*, *BC030867*, *Tes*, *1700001L05Rik*, *Frmd3*, *Slc3a1*, *Arhgef3*, and *1700012D01Rik* were preferably expressed in NSCs cultured on 3D-G.

Cell cycle analysis

Our results showed that NSCs cultured on 3D-BC/G had significantly greater proliferative ability than NSCs cultured on 3D-G. However, the detailed mechanism behind this difference remains unknown. In order to identify the possible cell-cycling genes regulated by 3D-BC/G, we compared our differentially expressed genes with the KEGG pathway database and identified 31 differentially expressed genes related

to the cell cycle (Figure 9A). The genes that were highly expressed in NSCs cultured on 3D-G included *Stag1*, *Rad21*, *Mad1l1*, *Gsk3b*, *Smad3*, *Gadd45a*, *Mad2l1*, *Prkdc*, *Ep300*, *Cdk6*, *Atm*, *Smad2*, *Ccnd1*, *Crebbp*, *E2f1*, *Cdc20*, *Bub1b*, and *Plk1* (Figure 9A). Silencing of *Rad21* has been shown to induce cell cycle arrest and apoptosis in breast tumor cells [32], and *Smad2* and *Smad3* can create an appropriate chromatin landscape to allow enhancer transcription. *Smad2* and *Smad3* are also the effectors of TGFβ signaling, which is important for NSC proliferation and development [33]. The histone acetyltransferase gene *EP300* is critical for sustaining the proliferation of human leukemia and lymphoma cell lines [34]. Mad2l1 is an essential component of the spindle assembly checkpoint, and deletion of a single *Mad2l1* allele results in defective mitotic checkpoint activation in mouse embryonic fibroblasts and in human HCT116 cancer cells [35]. *Gadd45a* is involved in DNA repair and helps to maintain genomic stability.

The highly expressed genes in NSCs cultured on 3D-BC/G included *Cdkn1c*, *Ccne1*, *Cdc25b*, *Mcm2*, *Gadd45g*, *Anapc13*, *Mcm4*, *Ccnh*, *Rbx1*, *Cdkn2b*, and *Cdkn1a* (Figure 9A). Interestingly, we identified three cyclin-dependent kinase inhibitors – *Cdkn1c*, *Cdkn2b*, and *Cdkn1a*. Cdkn1c is a major regulator of cell cycle progression and inhibits cyclin/cyclin-dependent kinase complexes in the mid-G1 phase [36]. Cdkn1a can inhibit the progression from G1 to S phase by interacting with the N-terminal domain or by interfering with the phosphorylation of CDK1 and CDK2 [37], and similarly Cdkn2b induces G1 arrest. Mcm2 and Mcm4 are essential protein components of pre-replicative complexes and catalyze the unwinding of DNA duplexes, and their activation requires the actions of cyclin-dependent kinases.[38] Most of the remaining differentially expressed cell cycle-regulating genes we identified have not been characterized in-depth in NSCs and need to be further studied.

Transcription factor analysis

Transcription factors (TFs) are associated with neurogenesis, proliferation, differentiation, and epigenetic control in NSCs. We identified seven TF genes (*Bmp4*, *Id3*, *Id2*, *Id1*, *Map2k2*, *Id4*, and *Fzd2*) that were significantly highly expressed in NSCs cultured on 3D-BC/G and 25 TF genes (*Map2k1*, *Smad2*, *Jarid2*, *Wnt5a*, *Apc*,

Fzd10, *Skil*, *Fzd1*, *Jak3*, *Zfhx3*, etc.) that were significantly highly expressed in NSCs cultured on 3D-G (Figure 9B).What is striking is that *Jak3* was richly expressed in NSCs cultured on 3D-BC/G,but not in NSCs cultured on 3D-G. Jak3 inhibition has been shown to induce neuronal differentiation,[39] and the highly expressed TF genes *Rest* and *Skil* have the ability to promote the self-renewal of NSCs and other stem cells [40]. Thus we speculate that 3D-G has reduced ability to maintain the stemness of NSCs and thus results in low proliferation ability.

Signaling pathway analysis

Signaling pathways such as Notch, Wnt, and growth factor-mediated pathways have been shown to play important roles in stem cell biology. In the current study, we examined each of these pathways in greater depth. Figure 10 summarizes all of the different signaling pathways and the differential gene expression among these pathways. As shown in Figure 10A, we identified many significant signaling pathways that play important roles in regulating NSC homeostasis and neurogenesis, such as FoxO [41], insulin [42], HIF-1 [43], estrogen, cAMP [44], ErbB, Ras, Wnt [45], Notch [46], and TGF-β [47]. Remarkably, the FoxO signaling pathway, which dominates the stem cell fate decision by regulating critical cellular events such as apoptosis, cell-cycle progression, glucose metabolism, oxidative stress resistance, and longevity, was the leader in top rankings (Figure 7A) [48]. The FoxO family has four isoforms in mammals – FoxO1, Fox3a, Fox4, and the more distantly related FoxO6 [49] – and we found that FoxO4 was highly expressed in NSCs cultured on 3D-BC/G but FoxO3 and FoxO6 were highly expressed in NSCs cultured on 3D-G.Most importantly, the FoxO signaling pathway has been shown to cross talk with other signaling pathways such as the insulin, IGF, EGF, Akt, and Wnt signaling pathways [49-50]. Therefore, we speculate that the top position of the FoxO signaling pathway is the result of the cumulative effects of various signaling pathways.

Conclusion

The addition of bacterial cellulose to graphene foam significantly enhanced the biocompatibility, proliferation, differentiation, and formation of neural networks

differentiated from NSCs. Moreover, primary cortical neurons cultured on 3D-BC/G formed an intense neuronal network with greater network activity than that which was formed on 3D-G. We investigated the transcriptome differences between NSCs cultured on the 3D-BC/G and 3D-G scaffolds and found significantly differentially expressed genes that might regulate NSC differentiation and proliferation. This provides a better understanding of the regulatory patterns of NSCs. However, the clinical application of these materials needs further investigation. Our 3D-BC/G culture system is not restricted to NSCs and primary cortical neurons, and it has the potential to be optimized for use with different cells or in different areas of regenerative medicine.

Methods

Fabrication of the 3D-BC/G scaffold for NSC culture

We synthesized the 3D-G foam using the chemical vapor deposition method. After etching away the nickel skeleton with 1M $FeCl_3$ dissolved in HCl, we obtained a monolayer of continuous and interconnected graphene 3D networks. Modification of the 3D-G foam by O_2 plasma treatment was used to increase its surface hydrophilicity. The scaffolds were immersed in a solution of 75% ethanol and water (v/v) for 30 min and then exposed to ultraviolet radiation for 30 min before use.

*A. xylinum*NUST4.2 was grown in a static culture containing 20 g/L D-glucose, 21 g/L sucrose, 10 g/L yeast extract, 4 g/L $(NH_4)_2SO_4$, 2 g/L KH_2PO_4, and 0.4 g/L $MgSO_4$ dissolved in deionized water at 29°C. The pH of the medium was adjusted to 6.0–6.2by addition of 2.5 M NaOH. One day later, the prepared 3D-G foam was immersed in the bacterial culture medium and allowed to incubate for 24 h. The 3D-G foam scaffolds were then treated with 0.1 M sodium hydroxide solution at 80°C for 2 h in order to remove the bacteria, and they were brought to neutral pH by washing with distilled water several times.

Characterization of the 3D-BC/G material

The infrared spectra were obtained using a Nicolet iS10 FTIR instrument. Powder X-ray diffractometry in reflection mode was performed using a Bruker D8 Advance

diffractometer with Cu Kα radiation (5–50o, 40 kV, and 35 mA). The N_2 gas adsorption and desorption isotherms were obtained with an ASAP 2020 (Micromeritics, USA). The pore size distribution and the specific surface area were calculated according to the standard method of BET. SEM was performed using a Zeiss electron microscope (Supra 55, Carl Zeiss). XPS spectra were obtained using an RBD-upgraded PHI-5000C ESCA system (Perkin Elmer) with Mg K radiation (h = 1253.6 eV). Raman spectra were recorded from 250 $cm^{-1}$to 2,000 cm^{-1} on a Renishaw Invia Raman Microprobe using a 532 nm argon ion laser. The electrical conductivity of the BC/PEDOT nanofibers was measured using the four-probe method (MCP-T610, Mitsubishi Chemical Analytech). The water contact angle was measured using a contact angle goniometer (SL 200B, Solon Technology Co., Ltd, China) at room temperature with a water drop volume of 3 μL.

NSC dissociation and culture

NSCs were obtained from the brains of embryonic day 14 embryos from C57 wild type mice. Animals were prepared and sacrificed in accordance with a protocol approved by the Institutional Animal Care and Use Committee. The entire hippocampus was dissected out and digested in Accutase for 20–30 min at 37°C. To achieve a single-cell suspension, mechanical percussion and filtration through a 40μm strainer was carried out after removing the Accutase, and the cells were resuspended in NSC proliferation medium. The formation of free-floating neurospheres indicated that NSCs had been isolated successfully. NSCs were subsequently purified by subculturing through three passages, and all NSCs used in this study were between passages 4 and 7. For proliferation studies, the NSCs were seeded in proliferative medium containing DMEM-F12 with 1% B27 supplement (Life Technologies, USA), the proliferation-inducing factor EGF (20 ng/mL, R&D System, USA), and FGF-2 (10 ng/mL, R&D system). For the differentiation study, proliferative medium was exchanged for medium containing DMEM-F12 with 1% B27 supplement, the differentiation-inducing factor retinoic acid (1 mM, Sigma-Aldrich, USA), and 1% fetal bovine serum (Life Technologies, USA). For cell seeding, neurospheres were collected and digested enzymatically with Accutase to obtain single-cell suspensions.

Cell viability assay

NSCs were seeded into three-dimensional scaffolds for 5 days of culture, and the cell viability assay was preformed using the LIVE/DEADViability/Cytoxicity Kit for mammalian cells (Invitrogen, USA) according to the manufacturer's instructions. The working concentration of calcein-AM was 2μM, and the working concentration of EthD-1 was 0.5 μM

SEM observation of NSCs cultured on 3D scaffolds

After 5 days of culturing NSCs on the 3D scaffolds, the samples were rinsed with phosphate-buffered saline (PBS) once and fixed with 2.5% glutaraldehyde in PBS at 4°C overnight. The samples were then washed with deionized water three times. The samples were dehydrated in a gradient of 30%, 50%, 70%, 90%, 100%, 100%, and 100% ethanol at 4°C for 10min and freeze dried. Finally, samples were imaged using a Zeiss Ultra Plus scanning electron microscope after coating with gold.

Immunofluorescence staining of NSCs

For immunofluorescence staining, NSCs were washed with PBS once and fixed in 4% paraformaldehyde for 60 min at room temperature followed by blocking and permeabilization with 0.1% Triton X-100 and 0.5% BSA (Sigma-Aldrich) for another 60 min at room temperature. Primary antibodies were incubated overnight at 4°C. For further secondary antibody staining, AlexaFluor 546- and Cy5-conjugated antibodies (Life Technologies) and DAPI were incubated for 60 min simultaneously. The antibody panel used included primary antibodies against nestin, integrin β1, and Tuj-1. Samples were imaged with a Zeiss confocal microscope.

Cortical neuron culture

Cortical neurons from Wistar rats (postnatal day 1–3) were prepared in accordance with the guidelines of the Italian Animal Welfare Act, and their use was approved by the Local Veterinary Service, the SISSA Ethics Committee board, and the National Ministry of Health (Permit Number: 630-III/14) in accordance with the European Union guidelines for animal care (d.1.116/92; 86/609/C.E.). The rats were anaesthetized with CO_2 and sacrificed by decapitation. During the culture process, scaffolds were first cleaned with O_2 plasma and sterilized with ultraviolet light. The

scaffolds were then coated with 50 μg/mL poly-L-ornithine (Sigma-Aldrich, St. Louis, MO, USA) overnight, immersed in culture medium overnight, and coated with Matrigel (Corning, Tewksbury MA, USA) before seeding cells. Dissociated cortical cells were plated at a concentration of 2.4×10^6 cells/mL on 3D-BC/G and 3D-G in a drop of medium (Neurobasal-A supplemented with 2% B-27 and 10 mM Glutamax (all from ThermoFisher) and 0.5 μM gentamycin (Sigma)). The medium was added after 1h to give a final volume of 3mL in a 35 mm petri-dish. Neuronal cultures were maintained in an incubator at 37°C, 5% CO_2, and 95% relative humidity.

EdU staining

EdU staining was performed with the Click-It EdU imaging kit (Invitrogen) according to the manufacturer's protocol. Samples were washed twice with PBS, fixed with 4% paraformaldehyde, and then blocked for 1h with 3% bovine serum albumin followed by incubating with a cocktail solution containing 1× Click-It reaction buffer, $CuSO_4$, Alexa Fluor 647 Azide, reaction buffer additive, and DAPI for 45min. Samples were imaged with a confocal fluorescence microscope (Zeiss 700), and the percentage of EdU-positive cells was counted by ImageJ.

AlamarBlue assay

The alamarBlue assay (Invitrogen) wasused to quantify the proliferation of NSCs according to the manufacturer's protocol. After NSCs were cultured for 2 days on 3D-G, 3D-BC, and 3D-BC/G, fresh media was replaced for a further 24 hours of incubation. Fresh media containing no cells served as the negative control. At the end of the incubation, alamarBlue was added for 1 hour at 37°C and checked for color change using an Enzyme-labeled meter (Bio-Rad) at wavelengths of 570nm and 600nm. The percent reduction of alamarBlue was calculated according to the computational formula provided by the manufacturer.

RNA extraction and RT-qPCR

RNA was extracted from NSCs and purified using the RNeasy Micro Kit (Qiagen) according to the manufacturer's protocol. First-strand cDNA was synthesized using the Thermo Scientific RevertAid First Strand cDNA Synthesis Kit. Finally, the FastStart Universal SYBR Green Master (Roche) was used for real-time PCR on a

C1000 Touch Thermal Cycler (Bio-Rad). Expression levels of vinculin, FAK, paxillin, integrin β1, Ki67, MCM2, and PCNAwere normalized to GAPDH in the same samples. The primers were as follows:

Vinculin (F): AGGTGGATCAGCTCACCAATGACA, vinculin (R): TCAAGGTCAAGACGTGCCAGAGAA; FAK (F): CCTGGTTATCCTAGCCCGAGA, FAK (R): GTCCAAAGCTGCCGAATCCTC; paxillin (F): CCT GCC TGT CTC TCG TCC CT, paxillin (R): TCT GCC CTC CCA ATG ACC AC; integrin β1 (F): CTG GTC CCG ACA TCA TCC CAA, integrin β1 (R): CCA AAT CAG CAG CAA GGC AAG; Ki67 (F): AAA ACT GCC CAG CTC GTC T, Ki67 (R): TTT CCC CTG ATA TTT GTG GAT GC; MCM2 (F): ATC CAC CAC CGC TTC AAG AAC, MCM2 (R): TAC CAC CAA ACT CTC ACG GTT; PCNA (F): TTT GAG GCA CGC CTG ATC C, PCNA (R): GGA GAC GTG AGA CGA GTC CAT; GAPDH (F): AGG TCG GTG TGA ACG GAT TTG, GAPDH (R): TGT AGA CCA TGT AGT TGA GGT CA.

RNA-seq and analysis

Sequencing libraries for transcriptome analysis were prepared with the RNA-seq kit (Illumina, San Diego, CA) according to the manufacturer's standard protocol. In brief, purified polyA RNA from 2 μg total RNA was fragmented with fragmentation buffer at 94°C for 3min to cut the polyA RNA into fragments of 200–300 nt. The first-strand cDNA was synthesized with random hexamer primers, and second-strand synthesis was performed by incubation with RNase H and DNA polymerase followed by end-repair with Klenow polymerase, T4 DNA polymerase, and T4 polynucleotide kinase (to blunt-end the DNA fragments). A single 3' 'A' base was added to the cDNA using Klenowexo− and dATP. The Illumina PE adapters were ligated onto the 'A' base on repaired cDNA ends, and an agarose gel was run to recover the ligation products. The libraries were amplified by 15 cycles of PCR with Phusion polymerase and PCR primers with barcode sequences. The fragments were 320 bp long, and the libraries were sequenced with HiSeq (Illumina) using a standard paired-end 150 nt sequencing procedure.

RNA-Seq data processing was performed with STAR[51] for reads alignment and with Edge R [52] for identifying the expression levels of the transcripts. Estimation of the expression levels of the identified mRNAs was performed by calculating the value

of fragments per kilobase of exon per million fragments mapped (FPKM). Paired t-tests were performed to compare FPKM values for each transcript from the repeats between the graphene and control groups. A value of $p \leq 0.05$ was considered statistically significant. A fold change greater than 2 between the two groups for the expression of each transcript and a p-value less than 0.05 were regarded as significantly differentially expressed genes. The significantly differentially expressed genes between the groups that had a logFC larger than 1, logCPM larger than 2, and adjusted p-value less than 0.01 were used for GO enrichment analysis.

We used STRING [53] to analyze networks for the identified top significantly differentially expressed genes based on the functional association data, including protein and genetic interactions, pathways, co-expression, co-localization, and protein domain similarity. The differentially expressed genes with logFC larger than 1, logCPM larger than 2, and FDR less than 0.01 were analyzed with STRING.

Calcium imaging

The cultured cortical cells at 8 days were incubated with 4 μM Fluo4-AM dissolved in anhydrous DMSO (Sigma-Aldrich) and Pluronic F-127 20% solution in DMSO (Life Technologies) at a ratio of 1:1 in neuronal medium at 37°C for 1 hour. After incubation, the cultures were washed with Ringer's solution (145 mM NaCl, 3 mM KCl, 1.5 mM $CaCl_2$, 1 mM $MgCl_2$, 10 mM glucose, and 10 mM Hepes, pH 7.4) for 30 minutes and then transferred to the stage of a Nikon Eclipse Ti-U inverted microscope equipped with an HBO 103 W/2 mercury short arc lamp (Osram, Munich, Germany), a mirror unit (exciter filter BP 465–495 nm, dichroic 505 nm, emission filter BP 515–555), and an Electron Multiplier CCD Camera C9100-13 (Hamamatsu Photonics, Japan). The images were acquired using the NIS Element software (Nikon, Japan) with an S-Fluor 20x/0.75 NA objective at a sampling rate of 3–5 Hz with a spatial resolution of 256×256 pixels for 10 minutes. To avoid saturation of the signals, excitation light intensity was attenuated using ND4 and ND8 neutral density filters.

Calcium imaging analysis

The initial videos were processed with the ImageJ software, and the neurons were localized. Appropriate regions of interest around the cell bodies were then selected. The time course of the fluorescence intensity (If(t)) was displayed, and any decay,

which is a consequence of dye bleaching, was evaluated. The calcium transients of each cell signal were extracted in a semi-automatic manner by selecting a threshold for the smallest detectable peak that was equal to three times the standard deviation of the baseline. Subsequently, the decay of If(t) was fitted to a cubic spline (Y(t)) interpolating If(t) at 10 or 20 points. Y(t) was then added to the original optical signal to compensate for dye bleaching, and the fractional optical signal was calculated as follows: DF/F= (Y(t)+ If(t))/If(0),where If(0) is the fluorescence intensity at the beginning of the recording.

Computation of the correlation coefficient of Ca^{2+} transient occurrence

The times, t_i, at which transient peaks occurred were used to calculate the rate of activity. The correlation coefficient of the calcium transients for neuron i and neuron j (σCT_{ij}) was computed as follows. The total recording time, T_{tot}, was divided into N intervals (1..,n,…,N) of duration Δt. Thus, if f_{in} and f_{jn} are the numbers of calcium transients of neuron i and neuron j in the time interval Δt_n, then we have the following equation:

$$\sigma_{CT_{ij}} = \frac{\sum_n f_{in} f_{jn}}{\sqrt{\left(\sum_n f_{in}^2\right)\left(\sum_n f_{jn}^2\right)}} \sigma_{\mathrm{CT_{ij}}} = \frac{\sum_n f_{in} f_{jn}}{\sqrt{\left(\sum_n f_{in}^2\right)\left(\sum_n f_{jn}^2\right)}} \quad (2)$$

where σCT_{ij}depends on Δt and varies between 0 and 1. The range of explored values of Δt was 6 s.

Statistical analysis

The data are presented as means± standard errors. Two-group comparisons were tested by Student's t-test.

Conflict of interest

The authors declare no competing financial interests.

Acknowledgements

This work was supported by grants from the Major State Basic Research Development Program of China (2015CB965000), the National Natural Science Foundation of China (No. 81970883, 31571530, 81622013, 81470692, 31500852,

31871322), the Strategic Priority Research Program of the Chinese Academy of Science (XDA16010302), the Jiangsu Province Natural Science Foundation (BK20181435), Boehringer Ingelheim Pharma GmbH, the Yingdong Huo Education Foundation, the Fundamental Research Funds for the Central Universities (2242017K41042, 2242017K3DN23, 2242017K41041), the Scientific Research Foundation of the Graduate School of Southeast University (YBJJ1739), and "the Fundamental Research Funds for the Central Universities" and "Postgraduate Research & Practice Innovation Program of Jiangsu Province" (KYCX17_0050).

Reference

1. Rosenzweig, E. S.; Brock, J. H.; Lu, P.; Kumamaru, H.; Salegio, E. A.; Kadoya, K.; Weber, J. L.; Liang, J. J.; Moseanko, R.; Hawbecker, S.; Huie, J. R.; Havton, L. A.; Nout-Lomas, Y. S.; Ferguson, A. R.; Beattie, M. S.; Bresnahan, J. C.; Tuszynski, M. H. Restorative effects of human neural stem cell grafts on the primate spinal cord. *Nature medicine,* **2018**.

2. Kalia, L. V.; Lang, A. E. Parkinson's disease. *The Lancet,* **2015,** *386* (9996), 896-912.

3. Martino, G.; Pluchino, S.; Bonfanti, L.; Schwartz, M. Brain Regeneration in Physiology and Pathology: The Immune Signature Driving Therapeutic Plasticity of Neural Stem Cells. *Physiological Reviews,* **2011,** *91* (4), 1281-1304.

4. Ringe, J.; Kaps, C.; Burmester, G. R.; Sittinger, M. Stem cells for regenerative medicine: advances in the engineering of tissues and organs. *Die Naturwissenschaften,* **2002,** *89* (8), 338-351.

5. Dingal, P. C.; Discher, D. E. Combining insoluble and soluble factors to steer stem cell fate. *Nature materials,* **2014,** *13* (6), 532-537.

6. (a) Nayak, T. R.; Andersen, H.; Makam, V. S.; Khaw, C.; Bae, S.; Xu, X.; Ee, P. L.; Ahn, J. H.; Hong, B. H.; Pastorin, G.; Ozyilmaz, B. Graphene for controlled and accelerated osteogenic differentiation of human mesenchymal stem cells. *ACS nano,* **2011,** *5* (6), 4670-4678; (b) Wang, Y.; Lee, W. C.; Manga, K. K.; Ang, P. K.; Lu, J.; Liu, Y. P.; Lim, C. T.; Loh, K. P. Fluorinated graphene for promoting neuro-induction of stem cells. *Advanced materials,* **2012,** *24* (31), 4285-4290; (c) Park, S. Y.; Park, J.; Sim, S. H.; Sung, M. G.; Kim, K. S.; Hong, B. H.; Hong, S. Enhanced Differentiation of Human Neural Stem Cells into Neurons on Graphene. *Advanced materials,* **2011,** *23* (36), H263-+.

7. (a) Chen, Z.; Ren, W.; Gao, L.; Liu, B.; Pei, S.; Cheng, H. M. Three-dimensional flexible and conductive interconnected graphene networks grown by chemical vapour deposition. *Nature materials,* **2011,** *10* (6), 424-428; (b) Hu, X. B.; Liu, Y. L.; Wang, W. J.; Zhang, H. W.; Qin, Y.; Guo, S.; Zhang, X. W.; Fu, L.; Huang, W. H. Biomimetic Graphene-Based 3D Scaffold for Long-Term Cell Culture and Real-Time Electrochemical Monitoring. *Analytical chemistry,* **2018,** *90* (2), 1136-1141; (c) Ameri, S. K.; Singh, P. K.; D'Angelo, R.; Stoppel, W.; Black, L.; Sonkusale, S. R. Three dimensional graphene scaffold for cardiac tissue engineering and in-situ electrical recording. *Conference proceedings : ... Annual International Conference of the IEEE Engineering in Medicine and Biology Society. IEEE Engineering in Medicine and Biology Society. Annual Conference,* **2016,** *2016*, 4201-4203; (d) Krueger,

E.; Chang, A. N.; Brown, D.; Eixenberger, J.; Brown, R.; Rastegar, S.; Yocham, K. M.; Cantley, K. D.; Estrada, D. Graphene Foam as a Three-Dimensional Platform for Myotube Growth. *Acs Biomater Sci Eng,* **2016,** *2* (8), 1234-1241; (e) Xiao, M.; Li, X.; Song, Q.; Zhang, Q.; Lazzarino, M.; Cheng, G.; Ulloa Severino, F. P.; Torre, V. A Fully 3D Interconnected Graphene-Carbon Nanotube Web Allows the Study of Glioma Infiltration in Bioengineered 3D Cortex-Like Networks. *Advanced Materials,* **2018,** *30* (52), 1806132.

8. Li, N.; Zhang, Q.; Gao, S.; Song, Q.; Huang, R.; Wang, L.; Liu, L.; Dai, J.; Tang, M.; Cheng, G. Three-dimensional graphene foam as a biocompatible and conductive scaffold for neural stem cells. *Scientific reports,* **2013,** *3*, 1604.

9. Li, Z.; Wang, H.; Yang, B.; Sun, Y.; Huo, R. Three-dimensional graphene foams loaded with bone marrow derived mesenchymal stem cells promote skin wound healing with reduced scarring. *Materials science & engineering. C, Materials for biological applications,* **2015,** *57*, 181-188.

10. (a) Dugan, J. M.; Gough, J. E.; Eichhorn, S. J. Bacterial cellulose scaffolds and cellulose nanowhiskers for tissue engineering. *Nanomedicine (Lond),* **2013,** *8* (2), 287-298; (b) Prof. Dr. Eng. Stanislaw Bielecki, D. E. A. K., Prof. Dr. Marianna Turkiewicz, Dr. Eng. Halina Kalinowska. Bacterial cellulose.

11. (a) Fu, L.; Zhang, J.; Yang, G. Present status and applications of bacterial cellulose-based materials for skin tissue repair. *Carbohydrate polymers,* **2013,** *92* (2), 1432-1442; (b) Fu, L.; Zhang, Y.; Li, C.; Wu, Z.; Zhuo, Q.; Huang, X.; Qiu, G.; Zhou, P.; Yang, G. Skin tissue repair materials from bacterial cellulose by a multilayer fermentation method. *Journal of Materials Chemistry,* **2012,** *22* (24), 12349; (c) Li, Y.; Wang, S.; Huang, R.; Huang, Z.; Hu, B.; Zheng, W.; Yang, G.; Jiang, X. Evaluation of the effect of the structure of bacterial cellulose on full thickness skin wound repair on a microfluidic chip. *Biomacromolecules,* **2015,** *16* (3), 780-789.

12. Klemm, D.; Schumann, D.; Udhardt, U.; Marsch, S. Bacterial synthesized cellulose - artificial blood vessels for microsurgery. *Prog Polym Sci,* **2001,** *26* (9), 1561-1603.

13. (a) Zaborowska, M.; Bodin, A.; Backdahl, H.; Popp, J.; Goldstein, A.; Gatenholm, P. Microporous bacterial cellulose as a potential scaffold for bone regeneration. *Acta biomaterialia,* **2010,** *6* (7), 2540-2547; (b) Shi, Q.; Li, Y.; Sun, J.; Zhang, H.; Chen, L.; Chen, B.; Yang, H.; Wang, Z. The osteogenesis of bacterial cellulose scaffold loaded with bone morphogenetic protein-2. *Biomaterials,* **2012,** *33* (28), 6644-6649.

14. Bodin, A.; Concaro, S.; Brittberg, M.; Gatenholm, P. Bacterial cellulose as a potential meniscus implant. *J Tissue Eng Regen M,* **2007,** *1* (5), 406-408.

15. (a) Czaja, W.; Krystynowicz, A.; Bielecki, S.; Brown, R. M., Jr. Microbial cellulose--the natural power to heal wounds. *Biomaterials,* **2006,** *27* (2), 145-151; (b) Klemm, D.; Heublein, B.; Fink, H. P.; Bohn, A. Cellulose: fascinating biopolymer and sustainable raw material. *Angewandte Chemie,* **2005,** *44* (22), 3358-3393; (c) Jonas, R.; Farah, L. F. Production and application of microbial cellulose. *Polym Degrad Stabil,* **1998,** *59* (1-3), 101-106; (d) Miyamoto, T.; Takahashi, S.; Ito, H.; Inagaki, H.; Noishiki, Y. Tissue Biocompatibility of Cellulose and Its Derivatives. *J Biomed Mater Res,* **1989,** *23* (1), 125-133.

16. Czaja, W. K.; Young, D. J.; Kawecki, M.; Brown, R. M., Jr. The future prospects of microbial cellulose in biomedical applications. *Biomacromolecules,* **2007,** *8* (1), 1-12.

17. (a) Wang, P.; Shi, Y.; Jia, Y.; Zheng, J.; Wang, Z.; Chen, Y.; Zhou, Y. Study on the feasibility of bacterial cellulose as tissue engineering scaffold. In *Multi-Functional Materials and Structures Ii, Pts 1 and 2*, Yin, Y. S.; Wang, X., Eds. 2009; Vol. 79-82, pp 147-+; (b) Zang, S.; Zhuo, Q.; Chang, X.; Qiu, G.; Wu, Z.; Yang, G. Study of osteogenic differentiation of human adipose-derived stem cells (HASCs) on

bacterial cellulose. *Carbohydrate polymers,* **2014,** *104*, 158-165.
18. Dugan, J. M.; Gough, J. E.; Eichhorn, S. J. Directing the Morphology and Differentiation of Skeletal Muscle Cells Using Oriented Cellulose Nanowhiskers. *Biomacromolecules,* **2010,** *11* (9), 2498-2504.
19. Brown, R. M., Jr.; Willison, J. H.; Richardson, C. L. Cellulose biosynthesis in Acetobacter xylinum: visualization of the site of synthesis and direct measurement of the in vivo process. *Proceedings of the National Academy of Sciences of the United States of America,* **1976,** *73* (12), 4565-4569.
20. (a) Rnjak-Kovacina, J.; Weiss, A. S. Increasing the Pore Size of Electrospun Scaffolds. *Tissue Eng Part B-Re,* **2011,** *17* (5), 365-372; (b) Lotfi, M.; Bagherzadeh, R.; Naderi-Meshkin, H.; Mahdipour, E.; Mafinezhad, A.; Sadeghnia, H. R.; Esmaily, H.; Maleki, M.; Hasssanzadeh, H.; Ghayaour-Mobarhan, M.; Bidkhori, H. R.; Bahrami, A. R. Hybrid chitosan-ss-glycerol phosphate-gelatin nano-/micro fibrous scaffolds with suitable mechanical and biological properties for tissue engineering. *Biopolymers,* **2016,** *105* (3), 163-175; (c) Nelson, C.; Khan, Y.; Laurencin, C. T. Nanofiber-microsphere (nano-micro) matrices for bone regenerative engineering: a convergence approach toward matrix design. *Regenerative biomaterials,* **2014,** *1* (1), 3-9.
21. (a) Sun, L.; Jiang, S.; Tang, X.; Zhang, Y.; Qin, L.; Jiang, X.; Yu, A. C. The Nanoscale Observation of the Three-Dimensional Structures of Neurosynapses, Membranous Conjunctions Between Cultured Hippocampal Neurons and Their Significance in the Development of Epilepsy. *Molecular neurobiology,* **2016,** *53* (10), 7137-7157; (b) Martinez Avila, H.; Feldmann, E. M.; Pleumeekers, M. M.; Nimeskern, L.; Kuo, W.; de Jong, W. C.; Schwarz, S.; Muller, R.; Hendriks, J.; Rotter, N.; van Osch, G. J.; Stok, K. S.; Gatenholm, P. Novel bilayer bacterial nanocellulose scaffold supports neocartilage formation in vitro and in vivo. *Biomaterials,* **2015,** *44*, 122-133; (c) Yin, N.; Stilwell, M. D.; Santos, T. M.; Wang, H.; Weibel, D. B. Agarose particle-templated porous bacterial cellulose and its application in cartilage growth in vitro. *Acta biomaterialia,* **2015,** *12*, 129-138.
22. Franco, D.; Klingauf, M.; Cecchini, M.; Falk, V.; Starck, C.; Poulikakos, D.; Ferrari, A. On cell separation with topographically engineered surfaces. *Biointerphases,* **2013,** *8* (1), 34.
23. Chen, C. T.; Zhang, T.; Zhang, Q.; Chen, X.; Zhu, C. L.; Xu, Y. H.; Yang, J. Z.; Liu, J.; Sun, D. P. Biointerface by Cell Growth on Graphene Oxide Doped Bacterial Cellulose/Poly(3,4-ethylenedioxythiophene) Nanofibers. *ACS applied materials & interfaces,* **2016,** *8* (16), 10183-10192.
24. (a) Loulier, K.; Lathia, J. D.; Marthiens, V.; Relucio, J.; Mughal, M. R.; Tang, S. C.; Coksaygan, T.; Hall, P. E.; Chigurupati, S.; Patton, B.; Colognato, H.; Rao, M. S.; Mattson, M. P.; Haydar, T. F.; Ffrench-Constant, C. beta1 integrin maintains integrity of the embryonic neocortical stem cell niche. *PLoS biology,* **2009,** *7* (8), e1000176; (b) Yim, E. K.; Darling, E. M.; Kulangara, K.; Guilak, F.; Leong, K. W. Nanotopography-induced changes in focal adhesions, cytoskeletal organization, and mechanical properties of human mesenchymal stem cells. *Biomaterials,* **2010,** *31* (6), 1299-1306; (c) Tilghman, R. W.; Parsons, J. T. Focal adhesion kinase as a regulator of cell tension in the progression of cancer. *Semin Cancer Biol,* **2008,** *18* (1), 45-52.
25. <Corgel-BioHydrogel-Kit-Instructions.pdf>.
26. Porcheri, C.; Suter, U.; Jessberger, S. Dissecting integrin-dependent regulation of neural stem cell proliferation in the adult brain. *The Journal of neuroscience : the official journal of the Society for Neuroscience,* **2014,** *34* (15), 5222-5232.
27. (a) Ahn, S.; Deravi, L. F.; Park, S. J.; Dabiri, B. E.; Kim, J. S.; Parker, K. K.; Shin, K. Self-organizing large-scale extracellular-matrix protein networks. *Advanced materials,* **2015,** *27* (18), 2838-2845; (b)

Rozario, T.; DeSimone, D. W. The extracellular matrix in development and morphogenesis: A dynamic view. *Developmental biology,* **2010,** *341* (1), 126-140; (c) Frantz, C.; Stewart, K. M.; Weaver, V. M. The extracellular matrix at a glance. *J Cell Sci,* **2010,** *123* (24), 4195-4200.

28. (a) Bao, R.; Tan, B.; Liang, S.; Zhang, N.; Wang, W.; Liu, W. A pi-pi conjugation-containing soft and conductive injectable polymer hydrogel highly efficiently rebuilds cardiac function after myocardial infarction. *Biomaterials,* **2017,** *122*, 63-71; (b) Peng, C.; Yang, K.; Xiang, P.; Zhang, C.; Zou, L.; Wu, X.; Gao, Y.; Kang, Z.; He, K.; Liu, J.; Cheng, M.; Wang, J.; Chen, L. Effect of transplantation with autologous bone marrow stem cells on acute myocardial infarction. *International journal of cardiology,* **2013,** *162* (3), 158-165.

29. (a) Rosso, G.; Liashkovich, I.; Young, P.; Röhr, D.; Shahin, V. Schwann cells and neurite outgrowth from embryonic dorsal root ganglions are highly mechanosensitive. *Nanomedicine: Nanotechnology, Biology and Medicine,* **2017,** *13* (2), 493-501; (b) Spinal Cord Explants Use Carbon Nanotube Interfaces To Enhance Neurite Outgrowth and To Fortify Synaptic Inputs. *ACS nano,* **2012**.

30. Tijore, A.; Cai, P.; Nai, M. H.; Zhuyun, L.; Yu, W.; Tay, C. Y.; Lim, C. T.; Chen, X.; Tan, L. P. Role of Cytoskeletal Tension in the Induction of Cardiomyogenic Differentiation in Micropatterned Human Mesenchymal Stem Cell. *Advanced healthcare materials,* **2015,** *4* (9), 1399-1407.

31. Uhlen, P.; Fritz, N.; Smedler, E.; Malmersjo, S.; Kanatani, S. Calcium Signaling in Neocortical Development. *Dev Neurobiol,* **2015,** *75* (4), 360-368.

32. Mahmood, S. F.; Gruel, N.; Chapeaublanc, E.; Lescure, A.; Jones, T.; Reyal, F.; Vincent-Salomon, A.; Raynal, V.; Pierron, G.; Perez, F.; Camonis, J.; Del Nery, E.; Delattre, O.; Radvanyi, F.; Bernard-Pierrot, I. A siRNA screen identifies RAD21, EIF3H, CHRAC1 and TANC2 as driver genes within the 8q23, 8q24.3 and 17q23 amplicons in breast cancer with effects on cell growth, survival and transformation. *Carcinogenesis,* **2014,** *35* (3), 670-682.

33. (a) Zhang, Q. B.; Guo, W.; Di, C.; Lou, M. Q.; Li, H. M.; Zhao, Y. D. EFFECTS OF TRANSFORMING GROWTH FACTOR-beta INHIBITOR ON THE PROLIFERATION OF GLIOMA STEM/PROGENITOR CELL. *Pol J Pathol,* **2017,** *68* (4), 312-316; (b) Fueyo, R.; Iacobucci, S.; Pappa, S.; Estaras, C.; Lois, S.; Vicioso-Mantis, M.; Navarro, C.; Cruz-Molina, S.; Reyes, J. C.; Rada-Iglesias, A.; de la Cruz, X.; Martinez-Balbas, M. A. Lineage specific transcription factors and epigenetic regulators mediate TGF beta-dependent enhancer activation. *Nucleic acids research,* **2018,** *46* (7), 3351-3365.

34. Garcia-Carpizo, V.; Ruiz-Llorente, S.; Sarmentero, J.; Grana-Castro, O.; Pisano, D. G.; Barrero, M. J. CREBBP/EP300 bromodomains are critical to sustain the GATA1/MYC regulatory axis in proliferation. *Epigenetics & chromatin,* **2018,** *11* (1), 30.

35. Michel, L. S.; Liberal, V.; Chatterjee, A.; Kirchwegger, R.; Pasche, B.; Gerald, W.; Dobles, M.; Sorger, P. K.; Murty, V. V.; Benezra, R. MAD2 haplo-insufficiency causes premature anaphase and chromosome instability in mammalian cells. *Nature,* **2001,** *409* (6818), 355-359.

36. (a) Tury, A.; Mairet-Coello, G.; DiCicco-Bloom, E. The multiple roles of the cyclin-dependent kinase inhibitory protein p57KIP2 in cerebral cortical neurogenesis. *Developmental neurobiology,* **2012,** *72* (6), 821-842; (b) Hildebrand, J.; Sporl, F.; Korge, S.; Gallinat, S.; Wenck, H.; Deppert, W.; Knott, A.; Blatt, T. Cell cycle regulator Cdkn1c (p57/KIP2) shows distinct expression in epidermal differentiation. *Eur J Dermatol,* **2012,** *22* (5), 694-696.

37. Mandal, M.; Bandyopadhyay, D.; Goepfert, T. M.; Kumar, R. Interferon-induces expression of cyclin-dependent kinase-inhibitors p21WAF1 and p27Kip1 that prevent activation of cyclin-dependent kinase by CDK-activating kinase (CAK). *Oncogene,* **1998,** *16* (2), 217-225.

38. (a) Bell, S. P.; Dutta, A. DNA replication in eukaryotic cells. *Annu Rev Biochem,* **2002,** *71*, 333-

374; (b) Tye, B. K. MCM proteins in DNA replication. *Annu Rev Biochem,* **1999,** *68*, 649-686.
39. Kim, Y. H.; Chung, J. I.; Woo, H. G.; Jung, Y. S.; Lee, S. H.; Moon, C. H.; Suh-Kim, H.; Baik, E. J. Differential regulation of proliferation and differentiation in neural precursor cells by the Jak pathway. *Stem cells,* **2010,** *28* (10), 1816-1828.
40. (a) Covey, M. V.; Streb, J. W.; Spektor, R.; Ballas, N. REST regulates the pool size of the different neural lineages by restricting the generation of neurons and oligodendrocytes from neural stem/progenitor cells. *Development,* **2012,** *139* (16), 2878-2890; (b) Diomede, F.; Rajan, T. S.; Gatta, V.; D'Aurora, M.; Merciaro, I.; Marchisio, M.; Muttini, A.; Caputi, S.; Bramanti, P.; Mazzon, E.; Trubiani, O. Stemness Maintenance Properties in Human Oral Stem Cells after Long-Term Passage. *Stem cells international,* **2017,** *2017*, 5651287.
41. Ro, S. H.; Liu, D.; Yeo, H.; Paik, J. H. FoxOs in neural stem cell fate decision. *Archives of biochemistry and biophysics,* **2013,** *534* (1-2), 55-63.
42. Ziegler, A. N.; Levison, S. W.; Wood, T. L. Insulin and IGF receptor signalling in neural-stem-cell homeostasis. *Nat Rev Endocrinol,* **2015,** *11* (3), 161-170.
43. Li, L.; Candelario, K. M.; Thomas, K.; Wang, R.; Wright, K.; Messier, A.; Cunningham, L. A. Hypoxia Inducible Factor-1 alpha (HIF-1 alpha) Is Required for Neural Stem Cell Maintenance and Vascular Stability in the Adult Mouse SVZ. *Journal of Neuroscience,* **2014,** *34* (50), 16713-16719.
44. Su, C.; Wang, P.; Jiang, C.; Ballerini, P.; Caciagli, F.; Rathbone, M. P.; Jiang, S. Guanosine Promotes Proliferation of Neural Stem Cells through Camp-Creb Pathway. *J Biol Reg Homeos Ag,* **2013,** *27* (3), 673-680.
45. Bengoa-Vergniory, N.; Kypta, R. M. Canonical and noncanonical Wnt signaling in neural stem/progenitor cells. *Cellular and molecular life sciences : CMLS,* **2015,** *72* (21), 4157-4172.
46. Kageyama, R.; Ohtsuka, T.; Shimojo, H.; Imayoshi, I. Dynamic regulation of Notch signaling in neural progenitor cells. *Current opinion in cell biology,* **2009,** *21* (6), 733-740.
47. Golestaneh, N.; Mishra, B. TGF-beta, neuronal stem cells and glioblastoma. *Oncogene,* **2005,** *24* (37), 5722-5730.
48. Kim, D. Y.; Hwang, I.; Muller, F. L.; Paik, J. H. Functional regulation of FoxO1 in neural stem cell differentiation. *Cell Death Differ,* **2015,** *22* (12), 2034-2045.
49. Ro, S. H.; Liu, D.; Yeo, H.; Paik, J. H. FoxOs in neural stem cell fate decision. *Archives of biochemistry and biophysics,* **2013,** *534* (1-2), 55-63.
50. Luo, W.; Zhao, X.; Jin, H.; Tao, L.; Zhu, J.; Wang, H.; Hemmings, B. A.; Yang, Z. Akt1 signaling coordinates BMP signaling and beta-catenin activity to regulate second heart field progenitor development. *Development,* **2015,** *142* (4), 732-742.
51. Dobin, A.; Gingeras, T. R. Mapping RNA-seq Reads with STAR. *Curr Protoc Bioinformatics,* **2015,** *51*, 11 14 11-19.
52. Robinson, M. D.; McCarthy, D. J.; Smyth, G. K. edgeR: a Bioconductor package for differential expression analysis of digital gene expression data. *Bioinformatics,* **2010,** *26* (1), 139-140.
53. Szklarczyk, D.; Franceschini, A.; Wyder, S.; Forslund, K.; Heller, D.; Huerta-Cepas, J.; Simonovic, M.; Roth, A.; Santos, A.; Tsafou, K. P.; Kuhn, M.; Bork, P.; Jensen, L. J.; von Mering, C. STRING v10: protein-protein interaction networks, integrated over the tree of life. *Nucleic Acids Res,* **2015,** *43* (Database issue), D447-452.

Figure legends

Figure 1. (A) The schematic diagram for the preparation of 3D-BC/G. (B) The SEM images of 3D-BC (a),3D-G (b), and 3D-BC/G (c, d). (C) Raman images of 3D-BC, 3D-G, and 3D-BC/G. (D) XRD spectra of 3D-BC, 3D-G, and 3D-BC/G.

Figure 2. Biocompatibility of 3D-BC/G and the morphology of NSCs cultured on 3D-BC/G. (A) Cell viability assay of NSCs cultured on 3D-G and 3D-BC/G after 5 days of culture. Cell-permeating calcein-AM produced an intense green fluorescence within live cells. EthD-1, producing red fluorescence, entered into dead cells with damaged membranes. (B) Low-, medium-, and high-magnification SEM images of NSCs cultured on 3D-G and 3D-BC/G under proliferation conditions. The insets illustrate the interaction between the cell growth cone and the three-dimensional scaffold.

Figure 3. NSC adhesion on 3D-BC/G. (A) NSCs were immuno-stained with anti-integrin β1 (red), a transmembrane receptor that mediates the connection between cells and their microenvironment. DAPI (blue)was usedto stain nuclei. (B,C) The relative mRNA expression of the four adhesion-related molecules integrin β1, vinculin, FAK, and paxillin. The data are presented as the mean ± SEM, * $p < 0.05$, ** $p < 0.01$, *** $p < 0.001$.

Figure 4. NSC proliferation on 3D-BC/G. (A) Representative immunofluorescence images of NSCs labeled with EdU and DAPI. (B) The percentage of EdU-labeled NSCs. (C) The percent reduction of alamarBlueas measured by microplate reader. (D) Relative mRNA expression of the proliferation markers Ki67, MCM2, and PCNA.

Figure 5. NSC differentiation on 3D-BC/G. Representative immunofluorescence images of differentiated NSCs stained with Tuj-1 (red) and DAPI (blue).

Figure 6. Three-dimensional functional neuronal networks were constructed on 3D-

BC/G and 3D-G. (A) Representative immunofluorescence images of cortical cells after 8 days of culture on 3D-BC/G (left) and 3D-G (right) stained for neurons (with Tuj-1, red), astrocytes (with GFAP, green), and nuclei (with DAPI, blue). (B) Box plot of cell density for cortical cultures grown on 3D-BC/G and 3D-G (n=8, **$p < 0.01$ from the Mann–Whitney U-test). (C, D) Representative fluorescence images of cortical cultures after 8 days loaded with Fluo-4 AM and grown on 3D-BC/G (C) and 3D-G (D). (E, F) Spontaneous calcium transients on 3D-BC/G and 3D-G from three selected neurons after 8 days of culture. (G) Frequency of neuronal calcium spikes in NSCs cultured on 3D-BC/G and 3D-G (n = 121 neurons from five independent cultures for 3D-BC/G and n = 76 neurons from three independent cultures for 3D-G; *$p < 0.05$ from Mann-Whitney test). (H) Mean correlation coefficient of neuronal calcium spikes in NSCs cultured on 3D-BC/G and 3D-G (data are from five independent cultures for 3D-BC/G and three independent cultures for 3D-G; ns: no significant difference).

Figure 7. Top 200 genes highly expressed in NSCs cultured on 3D-BC/G ranked in descending order. The number in red on the right side of each panel represents the same gene ranking in the 3D-G group. The red solid bar represents the gene expression level in NSCs cultured on 3D-BC/G. The green hollow bar represents the gene expression level in NSCs cultured on 3D-G.

Figure 8. The differentially expressed genes in NSCs cultured on 3D-BC/G and 3D-G. (A) The top 40 highly differentially expressed genes in NSCs cultured on 3D-BC/G. The numbers on the right of each panel represent the fold difference in expression for NSCs cultured on 3D-BC/G versus NSCs cultured on 3D-G. (B) The top 40 highly differentially expressed genes of NSCs cultured on 3D-G. The numbers on the right of each panel represent the fold difference in expression for NSCs on 3D-G versus 3D-BC/G. The red bars represent the gene expression levels of NSCs cultured on 3D-BC/G. The green bars represent the gene expression levels of NSCs cultured on 3D-G.

Figure 9. Cell cycle gene and TF expression in NSCs cultured on 3D-BC/G 3D-G. (A) The expression of 31 genes involved in the cell cycle in NSCs cultured on 3D-BC/G and 3D-G. (B) The expression of TF genes in NSCs cultured on 3D-BC/G and 3D-G. The red hollow bars represent the gene expression levels of NSCs cultured on 3D-BC/G, and the solid green bars represent the gene expression levels of NSCs cultured on 3D-G. The numbers on the right show the value of log transformed based 2 fold change between 3D-BC/G and 3D-G.

Figure 10. Signaling pathway gene expression in NSCs cultured on 3D-BC/G and 3D-G. (A) The differential KEGG pathways in NSCs cultured on 3D-BC/G versus NSCs cultured on 3D-G. The differentially expressed genes in NSCs cultured on 3D-BC/G and 3D-G that are involved in the FoxO (B), Hippo (C), Wnt (D), PI3K-Akt (E), and TGF β(F) signaling pathways. The red hollow bars represent the gene expression levels of NSCs cultured on 3D-BC/G. The solid green bars represent the gene expression levels of NSCs cultured on 3D-G.

886 Figure 1

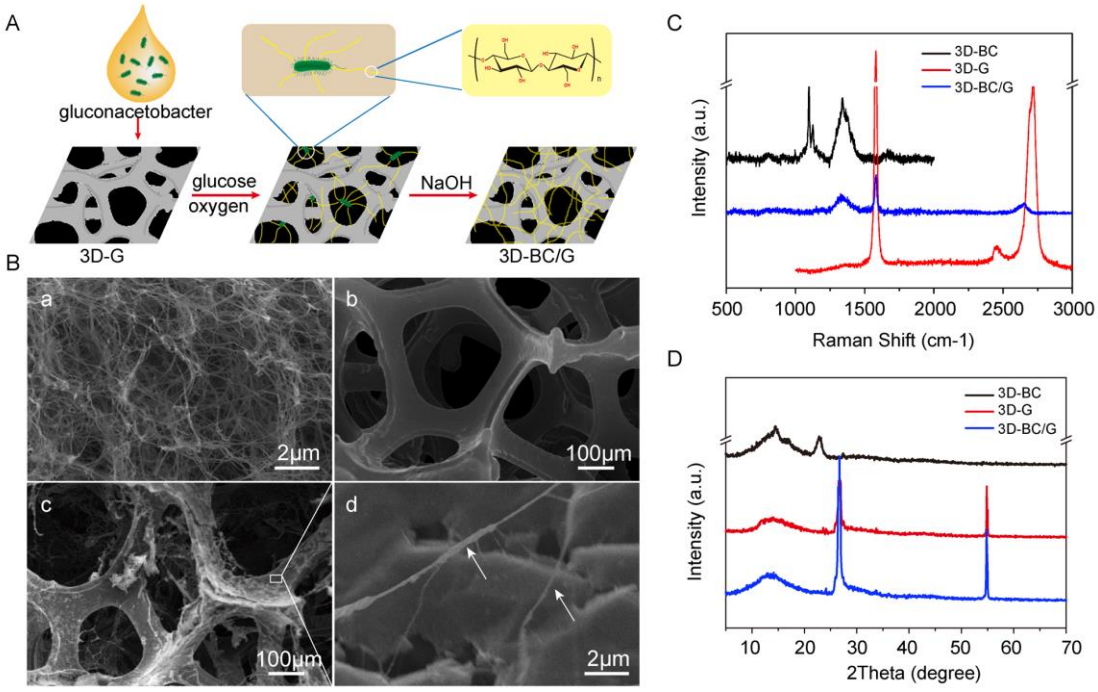

887

888

889

890 Figure 2

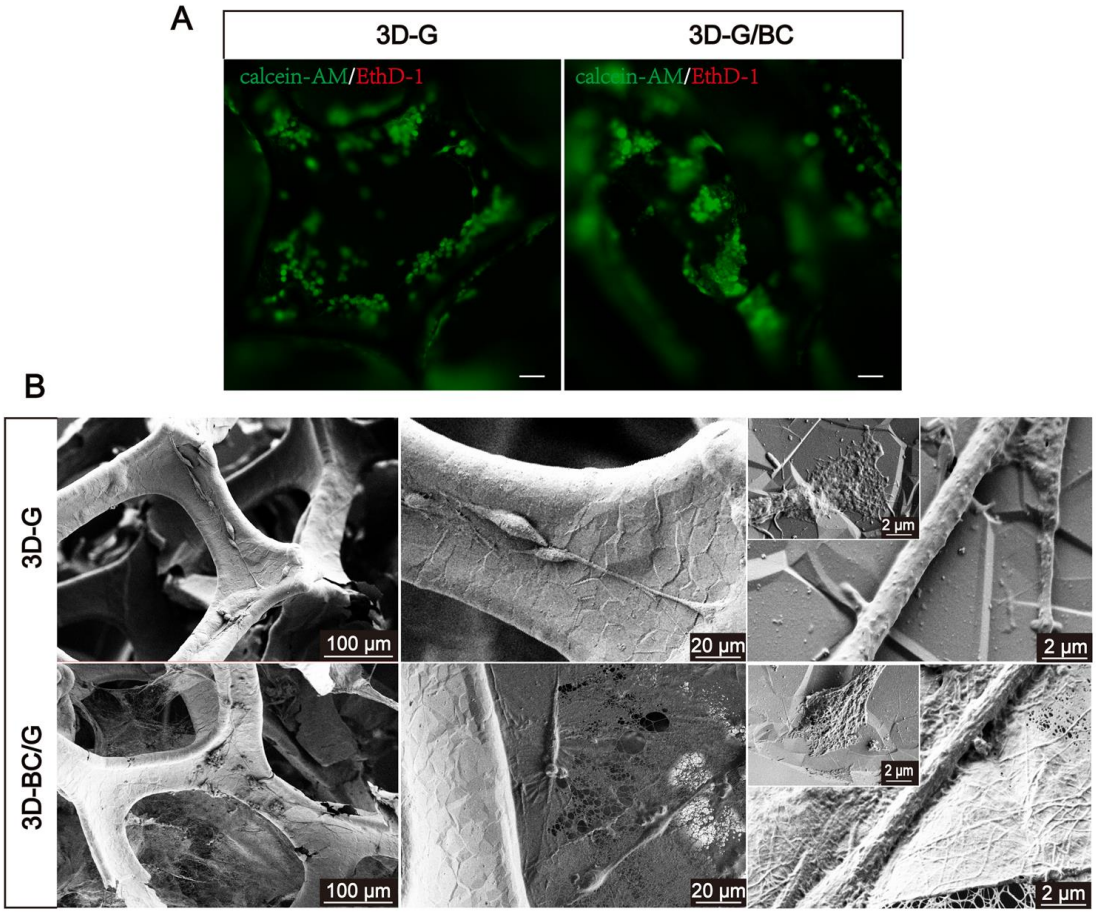

891

892

Figure 3

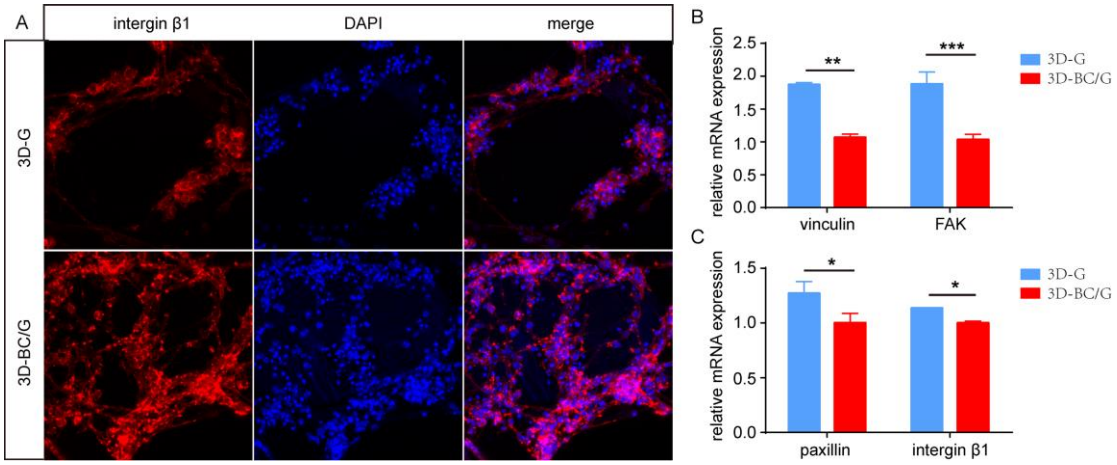
A
intergin β1
DAPI
merge
3D-G
3D-BC/G
B
relative mRNA expression
2.5
2.0
1.5
1.0
0.5
0.0
**
***
vinculin
FAK
3D-G
3D-BC/G
C
relative mRNA expression
1.5
1.0
0.5
0.0
*
*
paxillin
intergin β1
3D-G
3D-BC/G

Figure 4

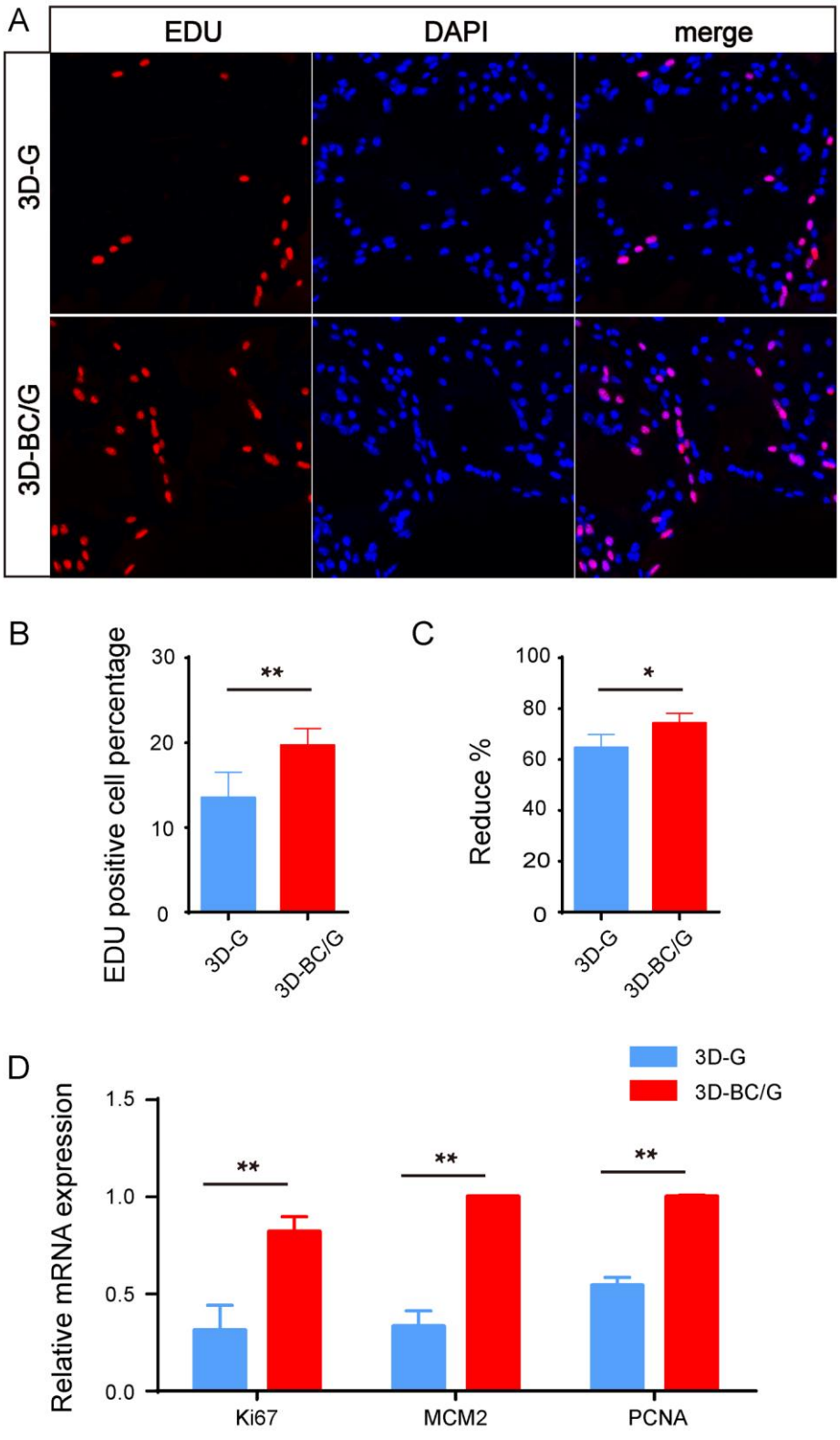
A
EDU
DAPI
merge
3D-G
3D-BC/G
B
EDU positive cell percentage
30
20
10
0
**
3D-G
3D-BC/G
C
Reduce %
100
80
60
40
20
0
*
3D-G
3D-BC/G
D
Relative mRNA expression
1.5
1.0
0.5
0.0
**
**
**
3D-G
3D-BC/G
Ki67
MCM2
PCNA

900 Figure 5

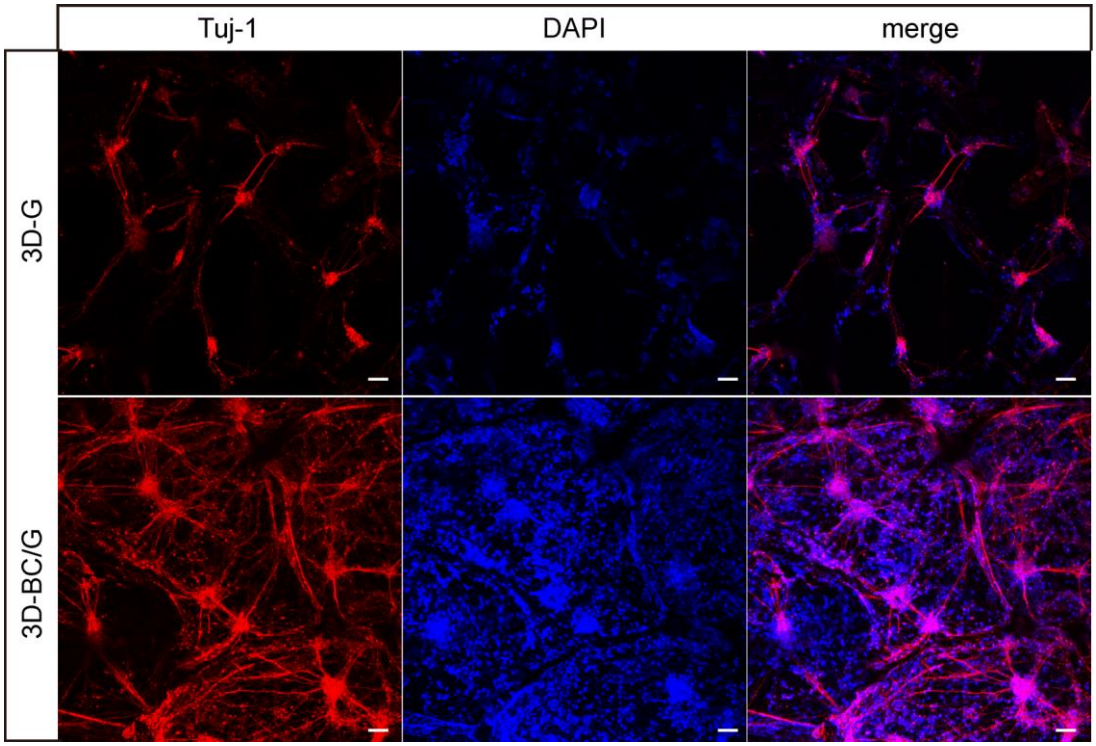

901

902

903 Figure 6

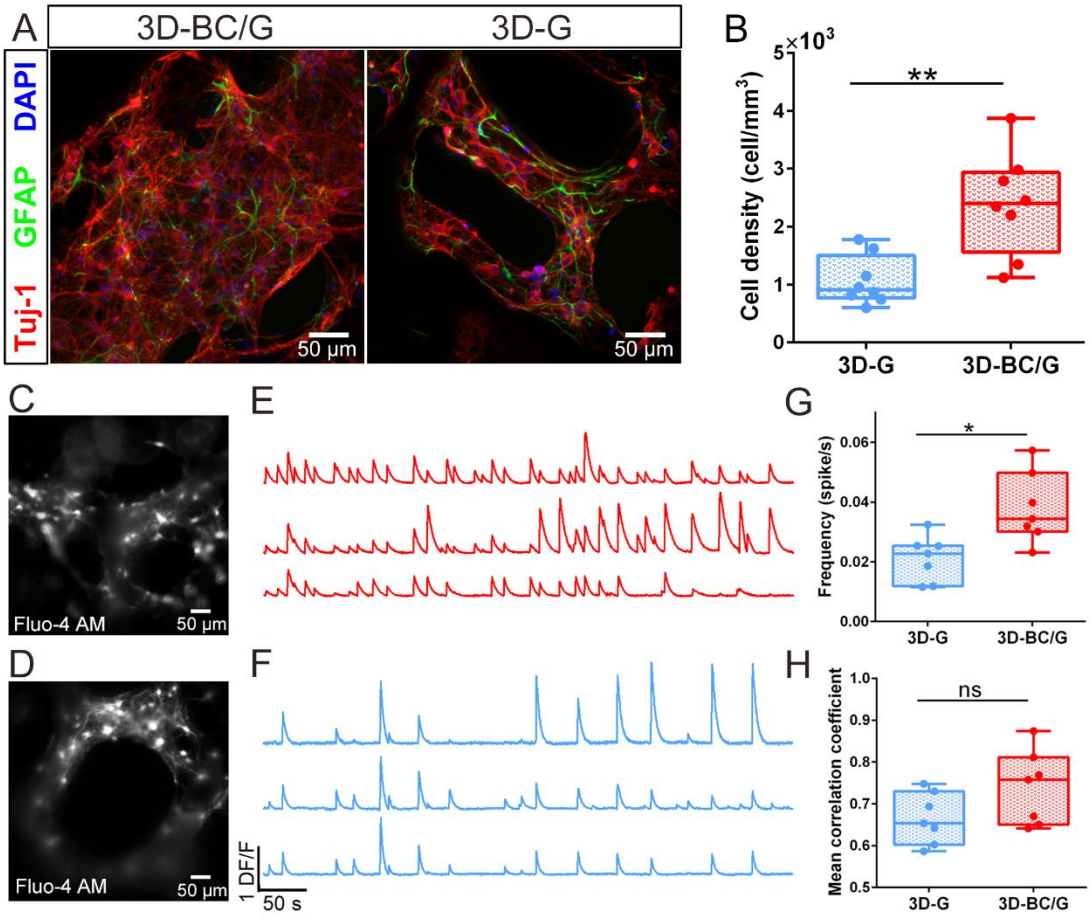

904

905

Figure 7.

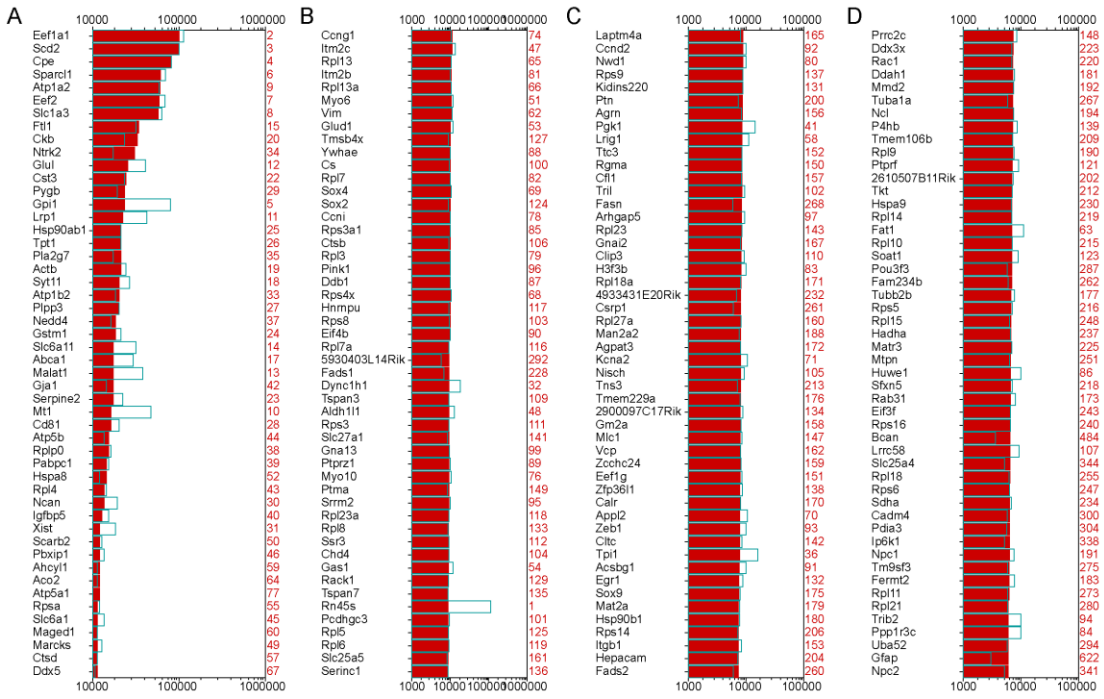
A
10000 100000 1000000
Eef1a1 2
Scd2 3
Cpe 4
Sparcl1 6
Atp1a2 9
Eef2 7
Slc1a3 8
Ftl1 15
Ckb 20
Ntrk2 34
Glul 12
Cst3 22
Pygb 29
Gpi1 5
Lrp1 11
Hsp90ab1 25
Tpt1 26
Pla2g7 35
Actb 19
Syt11 18
Atp1b2 33
Plpp3 27
Nedd4 37
Gstm1 24
Slc6a11 14
Abca1 17
Malat1 13
Gja1 42
Serpine2 23
Mt1 10
Cd81 28
Atp5b 44
Rplp0 38
Pabpc1 39
Hspa8 52
Rpl4 43
Ncan 30
Igfbp5 40
Xist 31
Scarb2 50
Pbxip1 46
Ahcyl1 59
Aco2 64
Atp5a1 77
Rpsa 55
Slc6a1 45
Maged1 60
Marcks 49
Ctsd 57
Ddx5 67
10000 100000 1000000
B
1000 10000 100000 1000000
Ccng1 74
Itm2c 47
Rpl13 65
Itm2b 81
Rpl13a 66
Myo6 51
Vim 62
Glud1 53
Tmsb4x 127
Ywhae 88
Cs 100
Rpl7 82
Sox4 69
Sox2 124
Ccni 78
Rps3a1 85
Ctsb 106
Rpl3 79
Pink1 96
Ddb1 87
Rps4x 68
Hnrnpu 117
Rps8 103
Eif4b 90
Rpl7a 116
5930403L14Rik 292
Fads1 228
Dync1h1 32
Tspan3 109
Aldh1l1 48
Rps3 111
Slc27a1 141
Gna13 99
Ptprz1 89
Myo10 76
Ptma 149
Srrm2 95
Rpl23a 118
Rpl8 133
Ssr3 112
Chd4 104
Gas1 54
Rack1 129
Tspan7 135
Rn45s 1
Pcdhgc3 101
Rpl5 125
Rpl6 119
Slc25a5 161
Serinc1 136
1000 10000 100000 1000000
C
1000 10000 100000
Laptm4a 165
Ccnd2 92
Nwd1 80
Rps9 137
Kidins220 131
Ptn 200
Agrn 156
Pgk1 41
Lrig1 58
Ttc3 152
Rgma 150
Cfl1 157
Tril 102
Fasn 268
Arhgap5 97
Rpl23 143
Gnai2 167
Clip3 110
H3f3b 83
Rpl18a 171
4933431E20Rik 232
Csrp1 261
Rpl27a 160
Man2a2 188
Agpat3 172
Kcna2 71
Nisch 105
Tns3 213
Tmem229a 176
2900097C17Rik 134
Gm2a 158
Mlc1 147
Vcp 162
Zcchc24 159
Eef1g 151
Zfp36l1 138
Calr 170
Appl2 70
Zeb1 93
Cltc 142
Tpi1 36
Acsbg1 91
Egr1 132
Sox9 175
Mat2a 179
Hsp90b1 180
Rps14 206
Itgb1 153
Hepacam 204
Fads2 260
1000 10000 100000
D
1000 10000 100000
Prrc2c 148
Ddx3x 223
Rac1 220
Ddah1 181
Mmd2 192
Tuba1a 267
Ncl 194
P4hb 139
Tmem106b 209
Rpl9 190
Ptprf 121
2610507B11Rik 202
Tkt 212
Hspa9 230
Rpl14 219
Fat1 63
Rpl10 215
Soat1 123
Pou3f3 287
Fam234b 262
Tubb2b 177
Rps5 216
Rpl15 248
Hadha 237
Matr3 225
Mtpn 251
Huwe1 86
Sfxn5 218
Rab31 173
Eif3f 243
Rps16 240
Bcan 484
Lrrc58 107
Slc25a4 344
Rpl18 255
Rps6 247
Sdha 234
Cadm4 300
Pdia3 304
Ip6k1 338
Npc1 191
Tm9sf3 275
Fermt2 183
Rpl11 273
Rpl21 280
Trib2 94
Ppp1r3c 84
Uba52 294
Gfap 622
Npc2 341
1000 10000 100000

Figure 8.

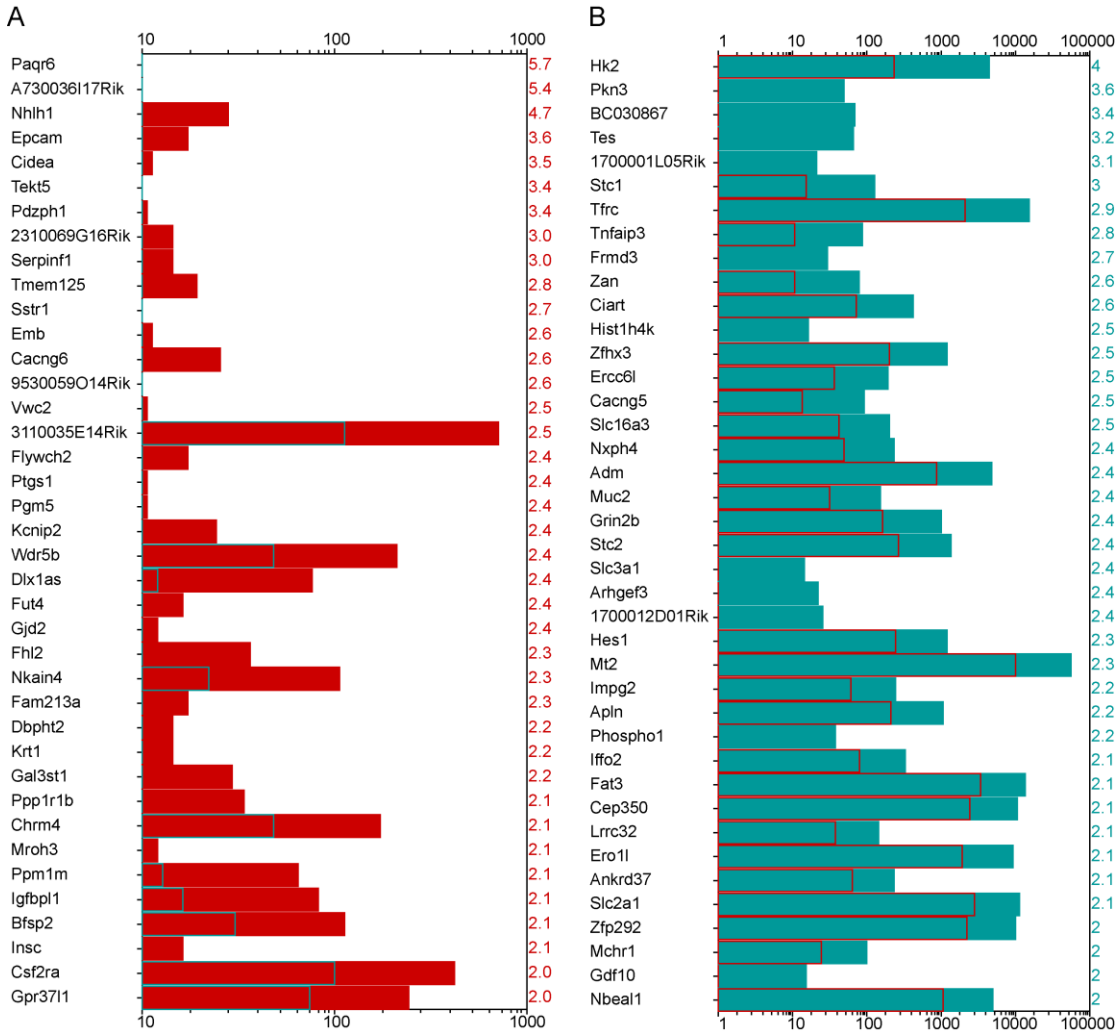
A
10
100
1000
Paqr6 5.7
A730036I17Rik 5.4
Nhlh1 4.7
Epcam 3.6
Cidea 3.5
Tekt5 3.4
Pdzph1 3.4
2310069G16Rik 3.0
Serpinf1 3.0
Tmem125 2.8
Sstr1 2.7
Emb 2.6
Cacng6 2.6
9530059O14Rik 2.6
Vwc2 2.5
3110035E14Rik 2.5
Flywch2 2.4
Ptgs1 2.4
Pgm5 2.4
Kcnip2 2.4
Wdr5b 2.4
Dlx1as 2.4
Fut4 2.4
Gjd2 2.4
Fhl2 2.3
Nkain4 2.3
Fam213a 2.3
Dbpht2 2.2
Krt1 2.2
Gal3st1 2.2
Ppp1r1b 2.1
Chrm4 2.1
Mroh3 2.1
Ppm1m 2.1
Igfbpl1 2.1
Bfsp2 2.1
Insc 2.1
Csf2ra 2.0
Gpr37l1 2.0
10
100
1000
B
1
10
100
1000
10000
100000
Hk2 4
Pkn3 3.6
BC030867 3.4
Tes 3.2
1700001L05Rik 3.1
Stc1 3
Tfrc 2.9
Tnfaip3 2.8
Frmd3 2.7
Zan 2.6
Ciart 2.6
Hist1h4k 2.5
Zfhx3 2.5
Ercc6l 2.5
Cacng5 2.5
Slc16a3 2.5
Nxph4 2.4
Adm 2.4
Muc2 2.4
Grin2b 2.4
Stc2 2.4
Slc3a1 2.4
Arhgef3 2.4
1700012D01Rik 2.4
Hes1 2.3
Mt2 2.3
Impg2 2.2
Apln 2.2
Phospho1 2.2
Iffo2 2.1
Fat3 2.1
Cep350 2.1
Lrrc32 2.1
Ero1l 2.1
Ankrd37 2.1
Slc2a1 2.1
Zfp292 2
Mchr1 2
Gdf10 2
Nbeal1 2
1
10
100
1000
10000
100000

912 Figure 9.

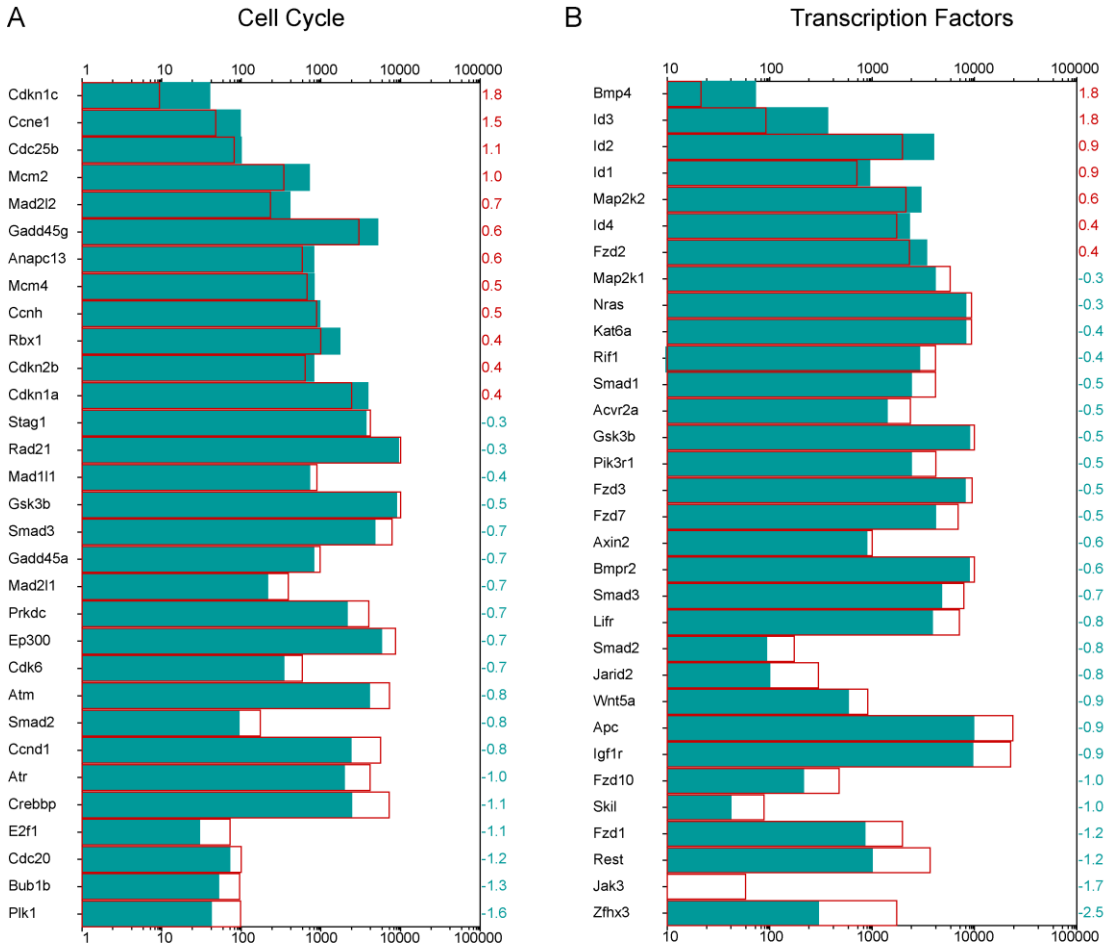

913

914

Figure 10.

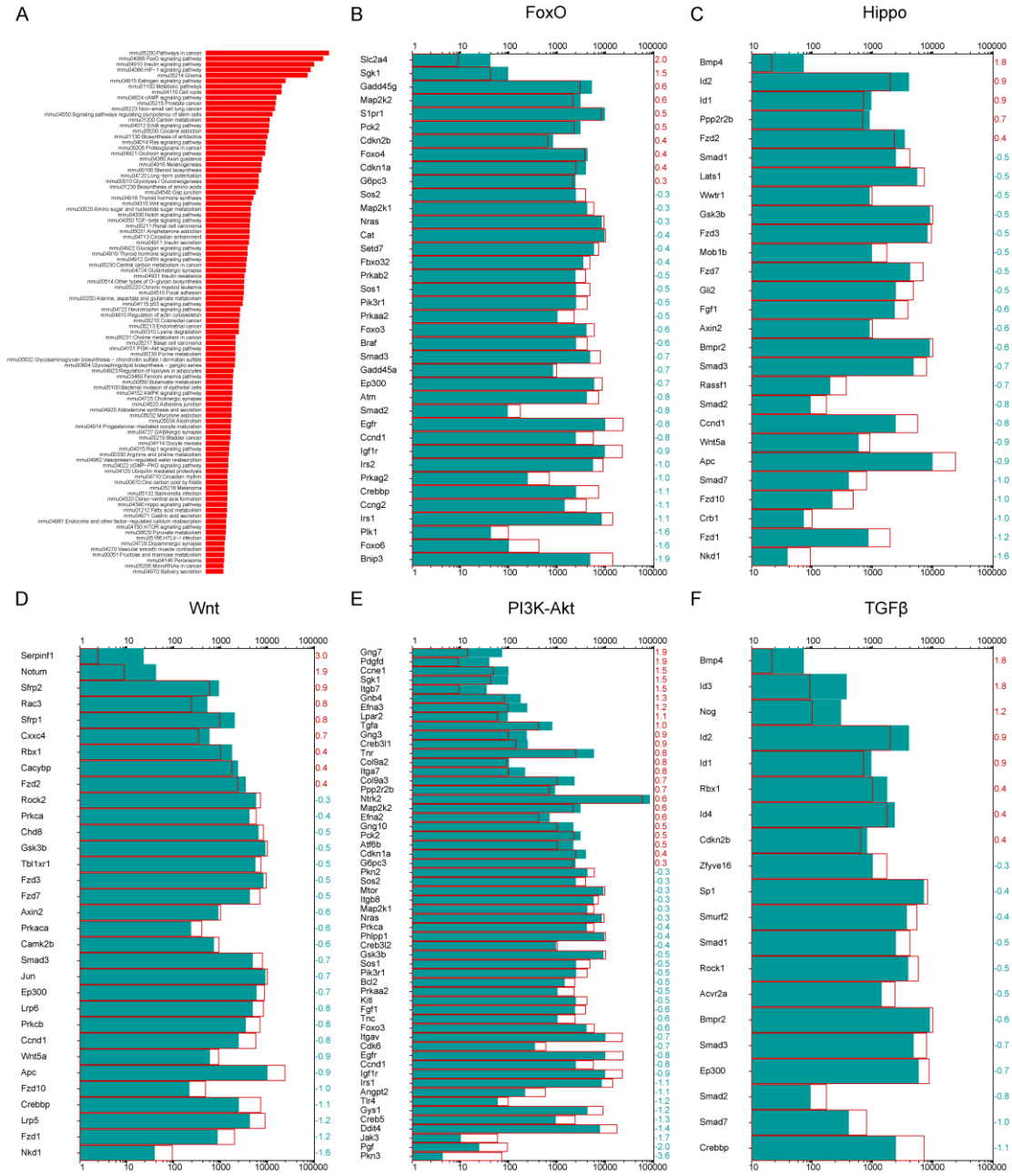

3.4 Precisely Controllable Hybrid Graphene Scaffold Reveals Size Effects on Differentiation of Neural Progenitor Cells in Mimicking Neural Network

Xun Ma, Miao Xiao, Ying Hao, Guosheng Cheng*

Carbon 145 (2019) 90–99

Contents lists available at ScienceDirect

Carbon

journal homepage: www.elsevier.com/locate/carbon

Precisely controllable hybrid graphene scaffold reveals size effects on differentiation of neural progenitor cells in mimicking neural network

Xun Ma [a, b], Miao Xiao [b, c], Ying Hao [b], Guosheng Cheng [a, b, *]

[a] School of Nano Technology and Nano Bionics, University of Science and Technology of China, Hefei, Anhui, 230026, China
[b] CAS Key Laboratory of Nano-Bio Interface, Suzhou Institute of Nano-Tech and Nano-Bionics, Chinese Academy of Sciences, 398 Ruoshui Road, Suzhou Industrial Park, Jiangsu, 215123, China
[c] Neurobiology Sector, International School for Advanced Studies (SISSA), via Bonomea, 265, 34136, Trieste, Italy

ARTICLE INFO

Article history:
Received 25 September 2018
Received in revised form
31 December 2018
Accepted 2 January 2019
Available online 3 January 2019

ABSTRACT

Well-connected neural network in three-dimensional (3D) scaffolds is essential to replicate the neural connections in vivo. The large spacing size in scaffolds enabling cellular entrance through the pores and sufficient neurites across large spacings addresses a "catch-22" problem. Here, this study presents a conductive, interconnected and free-standing 3D hybrid graphene (3D-HG) scaffold with excellent biocompatibility and precise structural controllability. The unique design of two-dimensional graphene film in 3D-HG facilitated the differentiated neural progenitor cells (NPCs) to bridge the spacings between skeletons and promoted the formation of neural networks. Furthermore, skeleton sizes in 3D graphene scaffold have significant impact on the differentiation behaviors of NPCs. This strategy would favor the simulation of neural tissues and expand the use of graphene in neural tissue engineering, providing a powerful tool to explore the physical effects on cell behaviors.

1. Introduction

Transplantation of neural stem/progenitor cells has been demonstrated as a revolutionary and viable therapeutic technology in achieving a significant functional recovery for treating neurodegenerative diseases [1]. Three-dimensional (3D) scaffolds, which more realistically provide a sufficient platform to support the cell growth and recapitulate the in vivo conditions, have been developed to effectively address the common limitations in transplantation including poor cell survival and insufficient integration [2]. Meanwhile, with respect to the significance of adequate differentiation of transplanted cells into neurons in establishing their effective connections with surrounding tissues [3], there is currently a great deal of interest on the direct neuronal differentiation of stem cells using various 3D scaffolds for potential therapy of neurodegenerative diseases [4,5].

Besides, electrical activity plays a crucial role in early neuronal development and migration [6,7], electrical stimulation has been proved to regulate the differentiation and maturity of neural stem/progenitor cells [8]. Thus a strategy to fabricate an ideal scaffold for neural stem/progenitor cells is utilizing conductive materials to induce cell behaviors in response to the electrical stimulation [9]. Fortunately, with the development of material science, a variety of 3D conductive neural scaffolds have emerged, such as synthetic polypyrrole scaffold [10], carbon materials-based scaffold [11,12] and composite scaffold [13]. Among these scaffolds, conductive and biocompatible graphene scaffolds have sparked a growing interest in biomedicine [14–17] owing to their unique characteristics of promoting neurite sprouting [18] and the differentiation of neural stem/progenitor cells into neurons [19], as well as enhancing electrical signaling in neural networks [20,21]. In addition, exciting progress has been made in exploring the biodegradability of graphene for its in vivo applications [22–24].

Cellular networks are intricately and densely interconnected in brain, where neural cells are connected to form functional circuits through their synapses [25]. However, neural cells in 3D culture tended to grow along the skeletons in 3D scaffolds [23] and hardly bridge the spacings between skeletons [17]. Similar finding was also reported on the effect of two-dimensional (2D) topography on neural behaviors [26]. Typically, it has been found that the non-adhesive spacings with the width over 12 μm hampered the neurons to cross [27], while less than 4% of the neurons could cross the obstacles with the height over 22 μm [28]. The existing of spacings in 3D graphene scaffolds without crossed cells led to the restriction of mimicking the in vivo neural network. Nevertheless, the

* Corresponding author. School of Nano Technology and Nano Bionics, University of Science and Technology of China, Hefei, Anhui, 230026, China.
E-mail address: gscheng2006@sinano.ac.cn (G. Cheng).

https://doi.org/10.1016/j.carbon.2019.01.006
0008-6223/

sufficient spacing size in neural cell scaffolds allows cells to efficiently enter into the scaffold, providing the critical supports for cell migration and proliferation, hence the spacings between skeletons in scaffold are supposed to larger than the diameter of cell soma. To achieve a 3D scaffold for neural cells to cross the large spacings and better simulate the natural central nervous system environment, 2D substrate was considered to combine with 3D graphene scaffolds to support the cell-crossing. Though it has been reported that the substrate with adhesive tracks supported neurons to form neurite bridges across plateaus on polydimethylsiloxane (PDMS) grooved substrate [29], the solid substrate would hinder the communication between cells in scaffold and external cells, whereas 2D graphene film offers penetrable platform because of its fragility.

Inspired by the aforesaid significances, we herein report an integrated 3D hybrid graphene (3D-HG) consisting of 3D controllable graphene skeletons and 2D graphene film as neural stem/progenitor cells scaffolds. The conductive 3D-HG not only retains the advantages of graphene material, but also provides support for neurite bridges across spacings due to the existence of 2D graphene film in it. In addition, the excellent structural controllability of 3D-HG offers the convenience for investigating size effects of graphene scaffold on neural cell behaviors. The fabricated 3D-HG scaffold provides new opportunities to extend the uses of graphene materials in biomedicine and can be served as a candidate for potential therapeutics of neurodegenerative diseases.

2. Experimental

2.1. Fabrication of the hybrid Cu/Ni templates

A 200 nm thick layer of PMMA was first spin-coated on a silicon dioxide wafer, followed by a 150 nm thick Cu film was magnetron-sputtered on PMMA via FHR sputter system (FHR Anlagenbau GmbH, Germany). Then, a 10 μm thick AZ-4620 photoresist layer was spin-coated on the Cu film and prebaked at 180 °C for 3 min. MA6/BA6 aligner (Suss Microtech, Germany) was utilized to expose the line patterns under feature sizes, using a hard mode with the exposure time set as 45 s. Afterwards, the Ni skeletons were formed on the Cu film via Ni deposition in electroplating bath exerted with a pulse power under steady current mode of 300 mA, 0.5 kHz. The Ni skeletons were then peeled off from the silicon dioxide wafer by soaking it in acetone for 12 h, followed by etching the Cu film in Ion Beam Etcher (KYKY TECHNOLOGY, China). Finally, two layers of Ni skeleton were arranged on a 25 μm thick copper foil, pressed and annealed at 700 °C for 3 min in a muffle furnace (TM-0912P, China) to bond the three layers together. After naturally cooling down to room temperature, the hybrid Cu/Ni templates with specific sizes and spacings were obtained.

2.2. Fabrication of the 3D-HG

The 3D hybrid graphene (3D-HG) was synthesized according to the reported CVD method [30] with the as-prepared hybrid Cu/Ni templates as a catalyst. The template was tightly pressed against two quartz plates and heated up to 950 °C in a horizontal tube furnace (Thermcraft, USA) under Ar (200 sccm) and H_2 (100 sccm) atmospheres, followed by annealing for 10 min to clean their surfaces and eliminate the thin surface oxide layers under Ar (100 sccm) and H_2 (200 sccm) atmospheres. Next, 10 sccm of CH_4 was introduced into the reaction tube at an ambient pressure under Ar (200 sccm) and H_2 (100 sccm) atmospheres, after 5 min of reaction-gas mixture flow, samples were cooled down to the room temperature. For comparison, 3D graphene foam (3D-GF) grown on commercial Ni foams (Alantum Advanced Technology Materials, China) and 3D controllable graphene (3D-CG) grown on controllable Ni templates [31] were prepared under the same CVD conditions. Different from 3D-GF and 3D-CG, the 3D-HG samples were then floated on the surface of the $FeCl_3$ (1 M) solution for 10 min, followed by wiping the graphene on the bottom of the copper. Afterwards, samples were submerged into the $FeCl_3$ (1 M) solution for 48 h to chemically etch Ni skeletons and Cu foil. Finally, samples were sequentially rinsed with 1, 0.1, 0.01 M HCl solutions and deionized water, followed by progressive dehydration in graded ethanol and lyophilized for the final sample.

2.3. Material characterizations

The morphologies and elemental analysis of the samples were characterized by scanning electron microscopy (SEM) equipped with EDS (Quanta 400 FEG, FEI, USA). The crystallinity and number of the layer presented within graphene were tested by Raman spectrometer (LamRAMHR800, HORIBA, France) from 36 selected points and TEM (Tecnai G2 F20 S-Twin, FEI, USA) from 4 samples, respectively. For TEM examination, samples were sonicated in ethanol solution for 2 h and then dropped onto a copper grid, the edges of some graphene fragments were rolled up, allowing for a cross-sectional view to count the number of graphene layers. The electrical conductivity of the 3D-HG was evaluated by measuring the sheet resistance using four-point probe technique.

2.4. Cell culture

Cell extraction and cell culture were performed as previously reported [32]. Mice (C57BL/6J) were purchased from CAVENS LAB ANIMAL, China. All animal experiments were conducted following to the protocols approved by the Animal Ethics Committee of the Chinese Academy of Sciences. The cortices of E13.5 mouse embryos were dissected under stereomicroscope, followed by dissociating using fire-polished Pasteur pipettes, single-cell suspension was collected after centrifugation and cultured in proliferative medium containing NeuroCult Basal Medium with 10% NeuroCult Proliferation Supplement (StemCell Technologies, Canada), 20 ng/mL Human Recombinant EGF and 10 ng/mL FGF (Thermo Scientific, USA). After sterilized by using 75% alcohol, the 3D graphene samples were sequentially coated with hydrophilic Poly-L-ornithine (100 μg/mL, Sigma, 37 °C, incubated for 2 h) and Laminin (10 μg/mL, Sigma, 37 °C, incubated for 4 h) according to a previous procedure [20]. The neurospheres were disassociated into cells by accutase digestion (StemCell Technologies) and seeded in pre-treated 3D graphene scaffolds. After seeding, cultures were maintained at 37 °C in humidified atmospheres containing 5% CO_2 in an incubator (Thermo Forma, USA). During the culture, half of the cell culture medium was changed every 3 days. For proliferation study, NPCs were seeded at a density of 10^6 cell/mL, and continued to culture in proliferative medium. For differentiation study, NPCs were seeded at a density of 5×10^6 cell/mL, after 1 day of proliferation, differentiation of NPCs was induced by exchanging the proliferative medium with medium containing NeuroCult Basal Medium (StemCell Technologies), 2% B27 supplement (Thermo Scientific) and 2 mM L-glutamine (Thermo Scientific). NPCs between passage 2 and 5 were used in cell experiments.

2.5. Immunofluorescence

At certain days of 3D culturing (7 days for Nestin, GFAP and Tuj-1 staining, 14 days for MAP-2 and Syniapsin-1 staining), cells were washed twice with PBS, fixed in 4% paraformaldehyde for 15 min, permeabilized with 0.1% Triton X-100 in PBS for 10 min and blocked in 1% BSA for 90 min. Primary antibodies solutions including Nestin

(1:500, Abcam, USA), GFAP (1:700, Cell Signaling Technology, USA), Tuj-1 (1:700, Abcam, USA), MAP-2 (1:1000, Sigma, USA) and Synapsin-1 (1:1000, Cell Signaling Technology, USA), were incubated with samples overnight at 4 °C. After that, Alexa-conjugated secondary antibodies (1:1000, Abcam, USA) were added for 45 min incubation, followed by DAPI (2 μg/mL, Beyotime Biotechnology, China) staining for 15 min. Images were collected using confocal laser scanning microscope (CLSM, FV3000, OLYMPUS, Japan).

2.6. EdU/DAPI staining

As a thymidine analog, EdU (5-ethynyl-2'-deoxyuridine) can be incorporated into DNA during active DNA synthesis, cells with incorporated EdU can be thought of as proliferating cells. According to the instructions from the EdU Labelling/Detection Kit (C10310-3, Ribobio, China), NPCs were seeded in the 3D-HG with different skeleton sizes and cultured in proliferative medium for 7 days. NPCs/3D-HG samples were then cultured in proliferative medium containing 10 μM EdU for another 24 h with the following of cleaning, cell fixation and permeabilization. Subsequently, samples were incubated with 1 × Apollo reaction buffer for 30 min in dark, washed by PBS and then added with DAPI solution (2 μg/mL, Beyotime Biotechnology). CLSM was utilized for Image acquisition.

2.7. WST-1 assay

WST-1 (4-[3-(4-Iodophenyl)-2-(4-nitrophenyl)-2H-5-tetrazolio]-1,3-benzene disulfonate) can be reduced by the dehydrogenases in the metabolically active cells and produce a water-soluble formazan dye to indicate the number of viable cells. According to the manufacturer from the WST-1 kit (C0036, Beyotime Biotechnology), NPCs/3D-HG samples after 7-day proliferation were then cultured in the proliferative medium containing WST-1 reagent for another 4 h. The optical density (OD) was read in a Multilabel Reader (PerkinElmer 2030 Multilabel Reader VICTOR X4, PerkinElmer Inc., USA) at 450 nm.

2.8. Live/dead staining

Live and dead cells were stained by Calcein-AM and Propidium Iodide (PI), respectively. Calcein-AM is a cell-permeant nonfluorescent dye that can be converted to green-fluorescent calcein in live cells, while PI is a red-fluorescent counterstain of which the fluorescence can undergo a 20- to 30- fold enhancement once enter cells with damaged membranes and binds to DNA. After cultured in proliferative medium for 7 days, samples were cultured in the proliferative medium containing 0.1 μM Calcein-AM (Thermo Scientific) and 1 μg/mL PI (Beyotime Biotechnology) in dark for another 30 min and observed under CLSM after PBS washing. Cell viability was quantified as the percentages of live (green) cells out of the sum of live (green) and dead (red) cells.

2.9. SEM observation of NPCs

After 7 days culturing in differentiation medium, cells were washed twice with PBS and fixed with 2.5% glutaraldehyde for 2 h at 4 °C, followed by postfixation in 1% osmium tetroxide for 30 min at 4 °C and progressive dehydration in graded ethanol. Afterwards, samples were lyophilized and coated with 15 nm thick gold layer using sputter coater (Emitech K550, Italy). Cell morphologies were visualized by SEM (Quanta 400 FEG, FEI, USA).

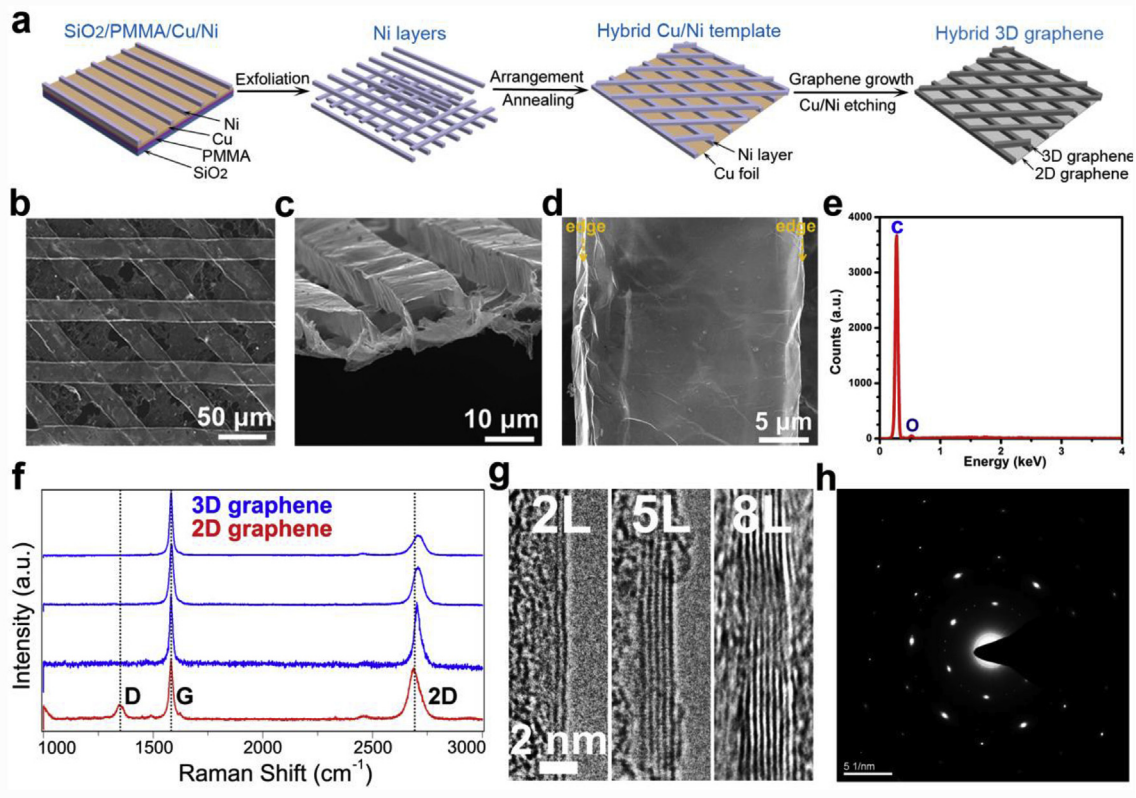

Fig. 1. Fabrication and characterization of 3D-HG. **(a)** Schematic illustration of the procedure used to fabricate the 3D-HG via the combination of micro-fabrication approach and CVD method. **(b)** SEM image of the surface of 3D-HG. **(c)** SEM image of the cross-section of 3D-HG. **(d)** High-magnification SEM image of a typical skeleton in 3D-HG. **(e)** EDS spectra of 3D-HG. **(f)** Typical Raman spectra acquired on the 3D-HG surface at different positions. **(g)** TEM images on the wall edges of the 3D-HG. **(h)** Selected area electron diffraction pattern of 3D-HG. (A colour version of this figure can be viewed online.)

2.10. Electrical stimulation & calcium imaging

To achieve electrophysiological measurements on the communication between NPCs and 3D-HG, we designed a special equipment (Fig. 2b) with 3D-HG as electrode. Specifically, a strip of extra 2D graphene was adhered on the corner of a glass slide (24 mm × 24 mm × 0.17 mm). Template supporting 3D-HG was mounted on slides with one corner connected to the end of 2D graphene, while a plastic pipe surrounding was placed for immobilization using DOW CORNING 3140 RTV COATING (USA). After removal of template by etching, the other end of 2D graphene was connected to the anode by silver paste, while a gold wire penetrated the lid was used for the connection with the cathode.

For calcium imaging, Fluo-4 AM dye, a membrane-permeable dye exhibiting increasing fluorescence intensity when binding with free calcium ion (Ca^{2+}), was used to stain the NPCs cultured in 3D-HG to monitor the changes of intracellular Ca^{2+} concentrations in the process of 100 mV pulse electrical stimulation to 3D-HG. After 3 days of proliferation, NPCs/3D-HG samples were incubated in Hanks' Balanced Salt Solution (HBSS) containing 3 μM Fluo-4 AM (Thermo Scientific) and 0.1% Pluronic F-127 (Thermo Scientific) in dark for 30 min. Then, samples were washed with HBSS, and immersed in NeuroCult Basal Medium in dark for another 30 min, followed by washing with HBSS. The input stimulation was applied by a function generator (JDS6600, JUNTEK, China). Time-lapse calcium level in live NPCs was imaged under fluorescence microscopy (Eclipse Ti–U, Nikon, Japan) using a 20 × objective (Ex 465–495 nm, Em 512–558 nm).

2.11. Real-Time quantitative PCR

The RNA isolation, reverse transcription and PCR analysis were performed following the manufacturer's instructions. Specifically, after certain days (7 days for Tuj-1 expression, 14 days for Synapsin-1 expression) culturing in differentiation medium, total RNA was extracted using TRIzol reagent (15596026, Thermo Scientific). cDNA was synthesized from total RNA using a First Strand cDNA Synthesis Kit (K1622, Thermo Scientific). Real-time PCR reactions were performed using PowerUp SYBR Green Master Mix (A25742, Thermo Scientific) and run on 7500 Real-Time PCR system (Applied Biosystems). The $2^{-\Delta\Delta Ct}$ method was employed to analyze the relative mRNA expression. β-Actin was used as an endogenous control. Primers were as follows: Synapsin-1 (forward: CAGGGTCAAGGCCGCCAGTC, reverse: CACATCCTGGCTGGGTTTCTG). Tuj-1 (forward: TGGACAGTGTTCGGTCTGG, reverse: CCTCCGTATAGTGCCCTTTGG). β-actin (forward: TACAGCTTCACCACCACAGC, reverse: AAGGAAGGCTGGAAAAGAGC).

2.12. Western blot assay

Western blots were performed as previously described [32]. Briefly, after NPCs were cultured in scaffolds for 14 days in differentiation medium, protein was extracted using RIPA Lysis Buffer (Beyotime Biotechnology). The collected proteins were boiled and separated by 12% SDS-PAGE gel, and transferred to PVDF membrane (Millipore). The membrane were blocked for 2 h at room temperature and incubated with primary antibodies to β-actin (Beyotime Biotechnology), Synapsin-1 (Cell signaling Technology) at 4 °C overnight. Then, the membranes were incubated with HRP-conjugated secondary antibodies (Beyotime Biotechnology) for 2 h at room temperature. The membranes were washed and reacted with the ECL western blot substrate (Thermo Scientific). The β-actin was used as an endogenous control. The images were captured using a Luminescent Image Analyzer LAS-4000 (Fuji Film).

2.13. Statistical analyses

Each experiment was repeated three times and at least three replicates were performed in each repetition. The cells were re-prepared in each repetition. The number and fluorescence intensities of cells in scaffolds were quantified using ImageJ software based on 9 different images. Analyses were performed using GraphPad Prism software (v5). Comparison between two groups was made using student's t-test while comparison among three groups was made using one-way ANOVA with a post hoc test. Data were expressed as mean ± S.E.M. The significance levels were set at $^{*}p < 0.05$, $^{**}p < 0.01$ and $^{***}p < 0.001$.

3. Results and discussion

3.1. Fabrication and characterization of 3D-HG

The unique 3D-HG was designed by the combination of approaches of growing 3D graphene structure on Ni skeleton [33] and growing 2D graphene film on Cu foil [30]. Thus, novel hybrid Cu/Ni template was designed for the fabrication of 3D-HG. The fabrication procedure of 3D-HG is presented in Fig. 1a. First, 10 μm thick monolayer Ni templates with designed skeleton sizes and spacings were prepared by micro/nano-fabrication facilities according to our

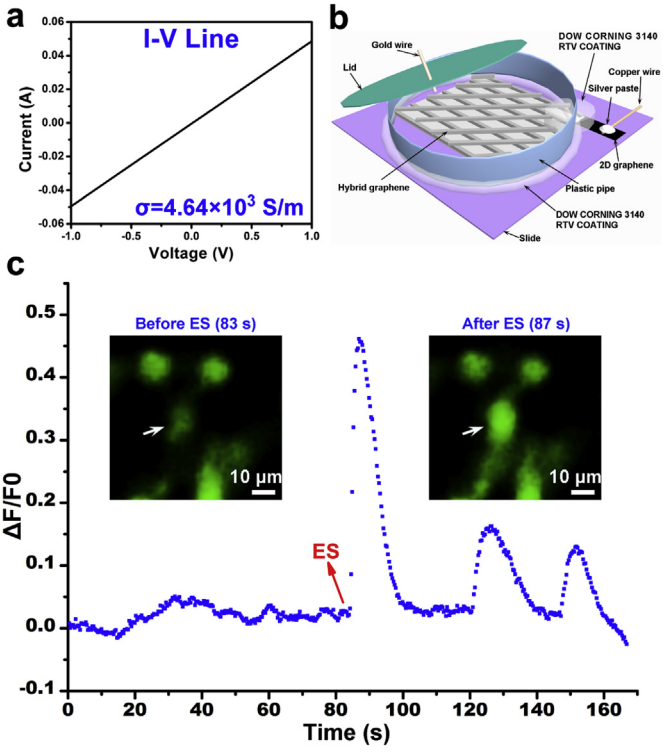

Fig. 2. Conductivity of 3D-HG and electrical stimulation of the NPCs in 3D-HG. (a) Room temperature I-V curve of the 3D-HG measured by four-probe method. **(b)** Schematic of the electrical stimulation equipment, copper wire was used to connect the anode while gold wire was used to connect to the cathode. Electrical signals applied on 2D graphene was transferred to 3D-HG to stimulate cells cultured in the 3D-HG. **(c)** The fluorescence images show the NPCs pre-incubated with Fluo-4 AM dye in 3D-HG before (left) and after (right) electrical stimulation. The cell pointed by the arrow exhibited a significant fluorescence enhancement after stimulation. The curve plots the relative fluorescence intensity change ($\triangle$F/F0) of the arrow-pointed cell in the fluorescence images versus the stimulation time period, where the F0 represents the average fluorescence intensity of the previous 50 images, while $\triangle$F is difference of F (the fluorescence intensity at measured time point) and F0. "ES" represents the stimulation time point at ~84 s. (A colour version of this figure can be viewed online.)

previous report [31]. In the second step, two monolayer Ni templates and a Cu foil were annealed at certain angles to form controllable hybrid Cu/Ni templates. Then, graphene was grown on the hybrid Cu/Ni templates by chemical vapor deposition (CVD). The final monolith of 3D hybrid graphene (3D-HG) containing 3D skeletons and 2D film was successfully achieved after the removal of Cu and Ni by chemical etching. This free-standing 3D-HG exhibited the intact shape and stability in aqueous solution (Fig. S1a). After dried by lyophilization, 3D-HG maintained flexible, allowing for bending under external force (Fig. S1b and Fig. S2).

The structures and morphologies of 3D-HG were observed by SEM. SEM observation at low-magnification (Fig. 1b) indicates the uniform skeleton size, spacing and shape, which can be efficiently controlled by defining the photolithography mask in the process of templates preparation [31]. A flat layer at the bottom of the 3D-HG was ascribed to graphene film with defective structure due to its fragility. In addition, SEM observation at high-magnification (Fig. 1c) shows the cross-section structures of 3D-HG, further confirming the combined structures of 3D hollow scaffold and 2D film. Importantly, the height of 3D-HG was less than the critical height (22 μm) that hinders neurite crossing [28]. High magnification SEM image (Fig. 1d) shows the ripples and wrinkles formed on 3D-HG caused by different thermal expansion coefficients of templates and graphene [33]. Great densities of the ripples and wrinkles were found on the edges. Elemental analysis by energy dispersive spectroscopy (EDS) reveals the dominant carbon composition of 3D-HG, as shown in Fig. 1e, very tiny oxygen signal was probably induced by water during the wet Cu/Ni etching [33].

The 514 nm Raman spectra acquired at different positions on the 3D-HG (Fig. 1f) display few-layer graphene features by identifying three characteristic peaks referred to the literature [34,35]: the disorder-induced D-band at ~1350 cm^{-1}, the G band at ~1580 cm^{-1} generated from the E_{2g} vibrational mode of sp_2 carbon, the 2D band at ~2700 cm^{-1} contributed by the scattering of phonons at the zone boundary. The Raman spectra measured on 3D hollow graphene skeletons show a strongly suppressed D band, demonstrating the high quality of entire graphene skeletons in 3D-HG. A clear D band indicates the defects of 2D graphene film on the bottom of 3D-HG. Meanwhile, the Raman spectra reveal the different number of graphene layers in various domains on hollow graphene skeletons owing to the polycrystalline nature of the Ni scaffold [33]. Consistent with Raman results, high-resolution TEM images (Fig. 1g) provide further evidence of few-layer graphene sheets (less than 10) for 3D-HG structures.

Furthermore, a hexagonal pattern of six-fold symmetry of the carbon atoms arrangement was found from selected area electron diffraction pattern of 3D-HG (Fig. 1h), well-defined diffraction spots instead of ring patterns can be observed at different positions, implying the nature of high-quality crystallinity of 3D-HG. Overall, these results suggest that 3D-HG is a pure graphene scaffold with regular macro-structures, complex surface micro-topologies and innovative architectures.

3.2. Biocompatibility of 3D-HG

To serve as cell-scaffolds, the biocompatibility of novel 3D-HG is crucial. The cytotoxicity of 3D-HG was evaluated by Calcein-AM and PI staining assay with the commonly used 3D-GF [4,23,36] as comparison (Fig. S3a and Fig. S3b). 96.2 ± 1.0% of NPCs cultured in 3D-HG in proliferation medium were viable at day 7, demonstrating the excellent biocompatibility of 3D-HG. On the other hand, to assess cellular stemness, nestin (a protein marker of neural stem/progenitor cells) was used to stain the NPCs cultured in 3D-HG after 7 days, while nuclei were stained with DAPI. According to Fig. S3c and Fig. S3d, 97.0 ± 0.4% of NPCs were immunopositive for nestin shown in green, indicating that NPCs proliferated well in 3D-HG

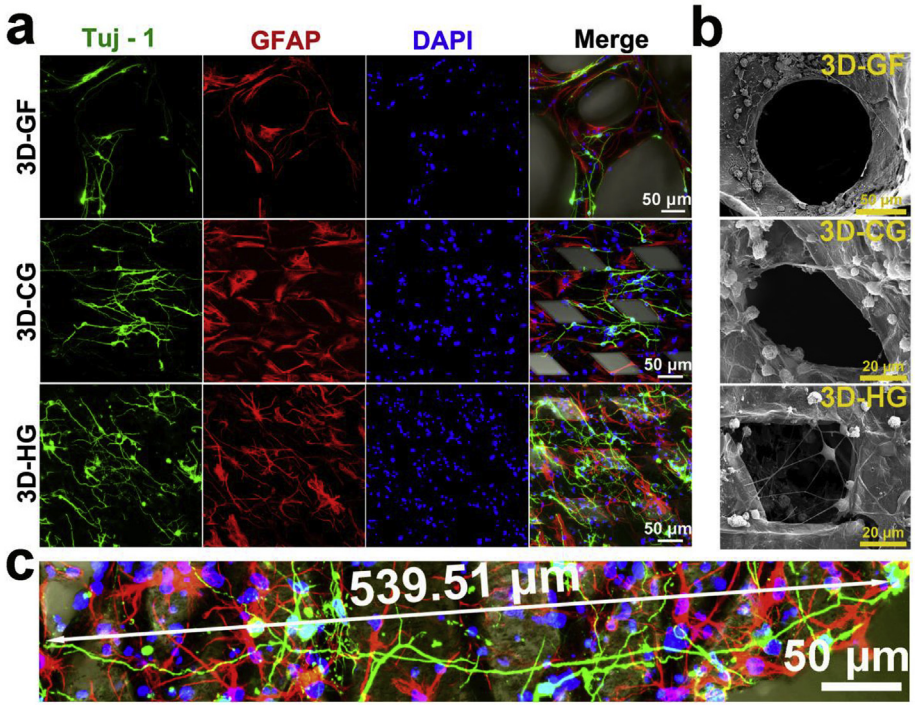

Fig. 3. The images of NPCs in 3D-HG after 7-day differentiation. **(a)** Immunofluorescence images of NPCs in 3D graphene scaffolds after 7-day differentiation, stained against neuron marker Tuj-1 (green), astrocyte marker GFAP (red), nuclei marker DAPI (blue), and merge images containing the bright field. The scaffolds from top to bottom are 3D-GF, 3D-CG, 3D-HG, respectively. **(b)** Corresponding SEM micrographs of NPCs after 7-day differentiation in 3D-GF, 3D-CG and 3D-HG, respectively. **(c)** Immunofluorescence image of one NPC in 3D-HG after 7-day differentiation across eight spacings, stained against Tuj-1 (green), GFAP (red) and DAPI (blue). (A colour version of this figure can be viewed online.)

while maintaining their stemness.

3.3. Electrical stimulation

Considering that the combination of electrical stimulation and stem cell therapy is an appealing strategy for promoting brain repair [37,38], we measured the electrical conductivity of 3D-HG as 4.64×10^3 S/m (Fig. 2a), which far exceeds the average conductance of the brain (0.33 S/m) [39]. Next, we designed a cell electrostimulation device using 3D-HG as electrode (Fig. 2b) to explore its ability of inducing NPCs behaviors in response to electrical stimulation. After 3 days of proliferation, the Ca^{2+} transients of NPCs in 3D-HG electrode were detected before and after the 100 mV electrical stimulation (square wave, 10 Hz, 60 s duration) on 3D-HG. Real-time system for monitoring intracellular Ca^{2+} fluorescence captured 3 images per second, reaching a total of 500 images during ~167 s. Electrical stimulation was applied to the 3D-HG at the moment of capturing the 250th image (~84th second). Fig. 2c expresses that the intracellular Ca^{2+} concentration of a silent NPC in 3D-HG was increased immediately in response to the electrical signal. The silent NPC was triggered towards a regular intracellular Ca^{2+} concentration changes after the electrical stimulation. More supportive images can be observed in Fig. S4. These results implicate the potential of 3D-HG being a commendable transplanted cell scaffold, and the ability of stimulating surrounding tissue to achieve therapeutic effects after transplantation.

3.4. The formation of mimetic neural network across the spacings in 3D-HG

To investigate the differentiation behavior of NPCs in 3D-HG and explore the formation of the neural network across large spacings in 3D-HG. 3D-HG with skeleton width of 50 μm and spacing width of 50 μm (50 μm/50 μm) was selected for the culture of NPCs. Meanwhile, 50 μm/50 μm 3D-CG and 3D-GF were used as comparisons. Both 3D-HG and 3D-CG have very similar size and shape due to the precision of lithography, while 3D-GF possess random sizes ranging from 50 to 100 μm lacking of precisely controllable skeleton size and porosity. Interestingly, we found some differentiated NPCs grown in 3D-HG crossed the spacings between

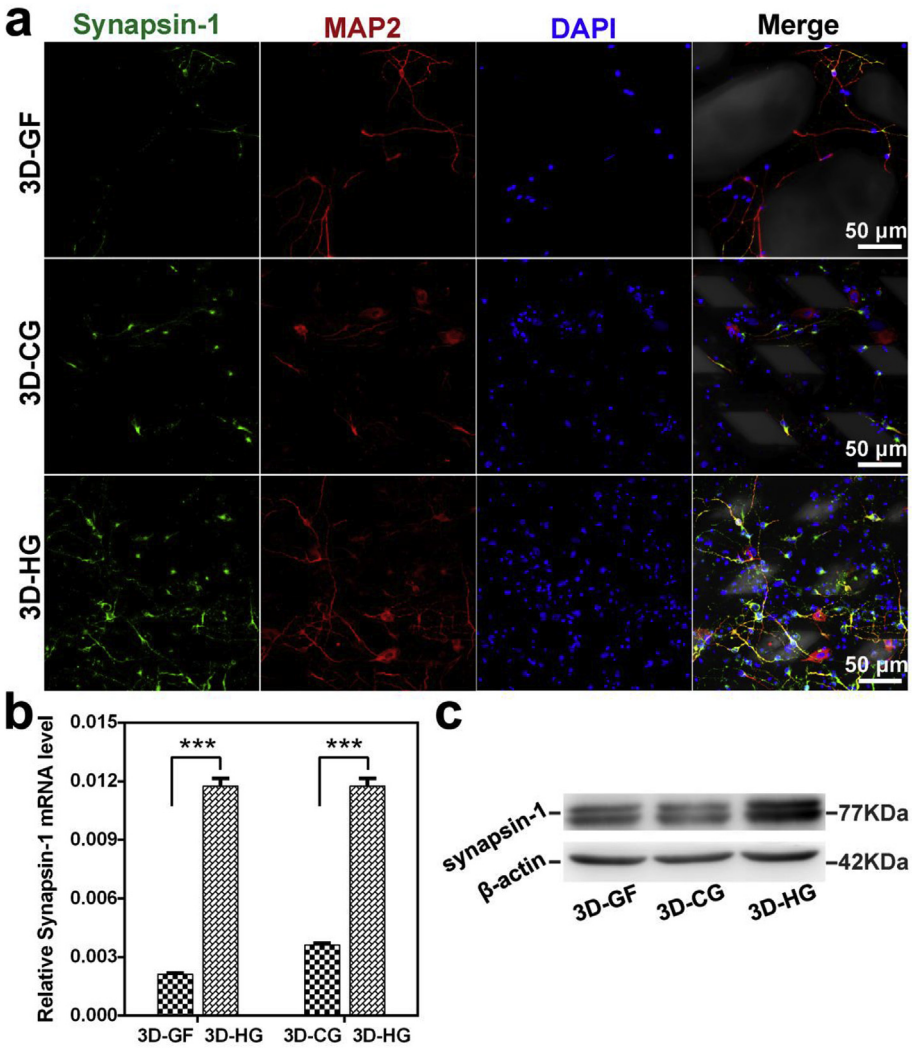

Fig. 4. Immunofluorescence images and the expression of synapsin-1 of NPCs in different graphene scaffolds after 14-day differentiation. (**a**) Immunofluorescence images of NPCs in 3D graphene scaffolds after 14-day differentiation, stained against synaptic marker Synapsin-1 (green), neuronal marker MAP-2 (red), nuclear marker DAPI (blue), and merge images containing the bright field. The scaffolds from top to bottom are 3D-GF, 3D-CG, 3D-HG, respectively. Gene **(b)** and protein **(c)** levels of Synapsin-1 were analyzed. Statistical analyses performed with one-way ANOVA and a Dunnett test, ***$p < 0.001$, error bars are presented as the means ± S.E.M. (A colour version of this figure can be viewed online.)

skeletons in 3D-HG at day 2 (Fig. S5). After 7 days of differentiation, NPCs cultured in 3D graphene scaffolds were stained by Tuj-1 (neuron marker), GFAP (astrocyte marker), DAPI (nuclei marker), respectively. From CLSM images (Fig. 3a), many neurites in the 3D-HG bridged the 50 μm spacings between skeletons and formed neural network structures, whereas most differentiated NPCs localized on skeletons and failed to cross the spacings in 3D-GF and 3D-CG, not mention to cross over two or more spacings in 3D-GF and 3D-CG. The average number of neurites across spacings per neuron in 3D-HG is significantly higher than that of 3D-GF and 3D-CG, as presented in Fig. S6. For 3D-HG, crossed neurites could extend and span multiple spacings to contact with each other (Fig. 3c).

Additionally, in agreement with CLSM results, SEM images verified that a lot of suspended neurite bridges across the spacing formed in 3D-HG while little neurite bridges formed in 3D-GF and 3D-CG (Fig. 3b). The neural network extending both along the skeletons and across the spacings would more realistically mimic the natural central nervous system environment compared with the neural network extending mainly along the skeletons, and acquire more reciprocal interaction with the recipient tissue for transplantation applications.

A desirable neural network comprises a plurality of neurons that are interconnected by synapses, allowing electrochemical signals to exchange and process within the network [40]. Therefore, it is intriguing to verify the presence of synaptic connection between differentiated NPCs in 3D-HG. After 14 days of differentiation, NPCs cultured in graphene scaffolds were stained with synapsin-1 (synaptic marker), MAP-2 (neuronal marker) and DAPI (Fig. 4a). The synapsin-1 immunofluorescence appeared between the differentiated NPCs, together with the MAP-2 expression, confirm that the NPCs differentiated into neural networks. Notably, the expression of synaptic protein in 3D-HG is more intensive than that in 3D-GF and 3D-CG (Fig. 4a and Fig. S7a). The changing of synapse formation was further validated by measuring the expression of synapsin-1 mRNA by qPCR (Fig. 4b) and synapsin-1 protein by Western blot analysis (Fig. 4c), respectively. Fig. S7b shows the corresponding quantitative analysis of Western blot. As expected, the mRNA and protein expression level of synapsin-1 were significantly higher in NPCs cultured in 3D-HG. Collectively, the 3D-HG promoted the formation of neural networks due to the unique design of 2D graphene film in it.

An ideal 3D cell scaffold for implantation should enable cells in scaffold to communicate with the cells in recipient tissues. To determine if the 2D graphene film at the bottom of 3D-HG impedes the contact of cells in scaffold with external cells, as illustrated in Fig. S8, NPCs were seeded in 3D-HG (5×10^6 cells/mL) and on glass slide (4×10^4 cells/cm^2) separately, then cultured together with 3D-HG on top of glass slide. After 7 days of differentiation, the cross-section of 3D-HG on glass slide was visualized via SEM. We can find that several neurites (or astrocyte processes) penetrated 2D graphene film and connected to the cells on the slide below (Fig. 5). Specifically, Fig. 5a clearly shows that neurites (or astrocyte processes) penetrated the 2D graphene film, while Fig. 5b and c reveal that the extended neurites (or astrocyte processes) from the 3D-HG and the cells on glass slide at the bottom can establish good connections. The results indicate that the defective flat 2D graphene film in the 3D-HG not only provides the support for the prolongation of neurites, but also renders cells permeable to external environments.

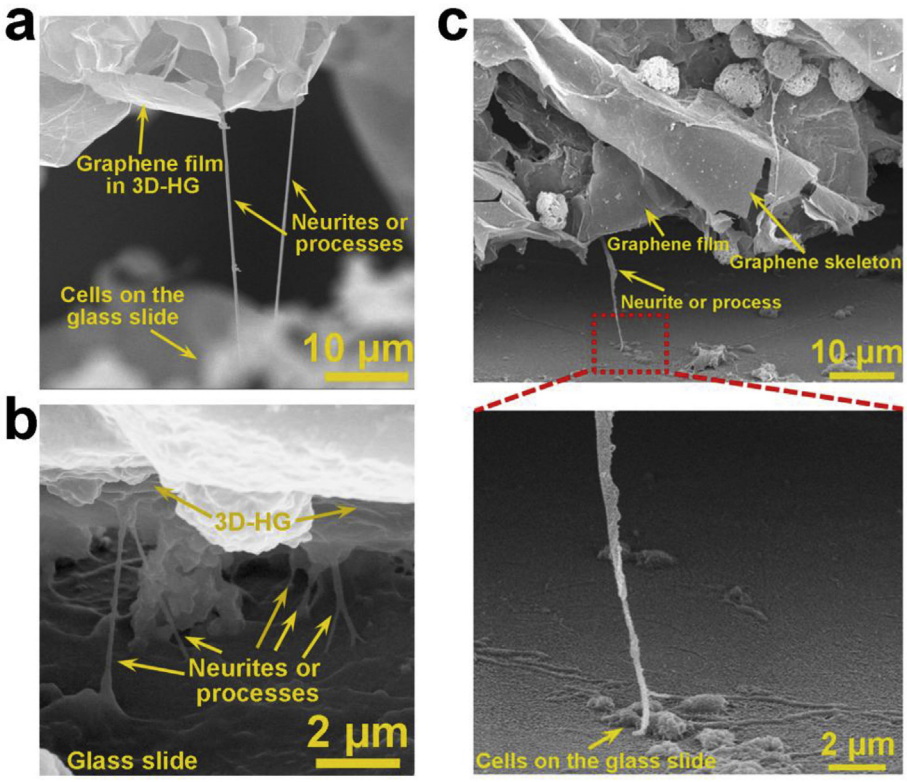

Fig. 5. SEM images of NPCs in 3D-HG penetrated the 2D graphene film after 7-day differentiation. (a) Neurites (or astrocyte processes) could penetrate the 2D graphene film. **(b)** The extended neurites (or astrocyte processes) from the upper 3D-HG connected to the differentiated NPCs on the glass slide at the bottom. **(c)** One neurite (or astrocyte process) from the 3D-HG was well connected to the cells on the glass slide. (A colour version of this figure can be viewed online.)

3.5. The effects of graphene skeleton sizes on the behaviors of NPCs

Notably, the skeleton widths of PDMS have a great impact on the neural stem/progenitor cells behaviors [41,42]. Discovering the size effect of 3D scaffold on cell behaviors utilizing a scaffold with precisely controllable skeleton size and porosity is essential to conciliate neuronal cell development. Therefore, it is important to investigate the size effect of conductive graphene skeletons on NPCs behaviors. Considering the sufficient area for NPCs attachment, we designed 3D-HG with various skeleton sizes larger than the size of NPC (9.9 ± 0.2 μm, measured by means of an objective micrometer, Fig. S9). 3D-HG was designed with sizes listed as follows: 10 μm skeleton with 50 μm spacing (10 μm/50 μm), 20 μm skeleton with 50 μm spacing (20 μm/50 μm), 50 μm skeleton with 50 μm spacing (50 μm/50 μm). After 7 days in proliferation culture, the proliferation of NPCs in different 3D-HG was examined by measuring the ratio of EdU-positive cells (Fig. S10a). Statistical analysis for the percentages of EdU-positive cells in Supplementary Fig. S10b reveals no significant difference among the 3D-HG with different skeleton widths, demonstrating that the graphene skeleton width do not affect cell proliferation when exceeding the cell sizes. The WST-1 cell proliferation assay further confirms this result (Fig. S10c).

However, the graphene skeleton widths greatly influenced the differentiation behaviors of NPCs, primarily on neuronal differentiation rate (Fig. 6a). The percentages of Tuj-1 immunoreactive cells

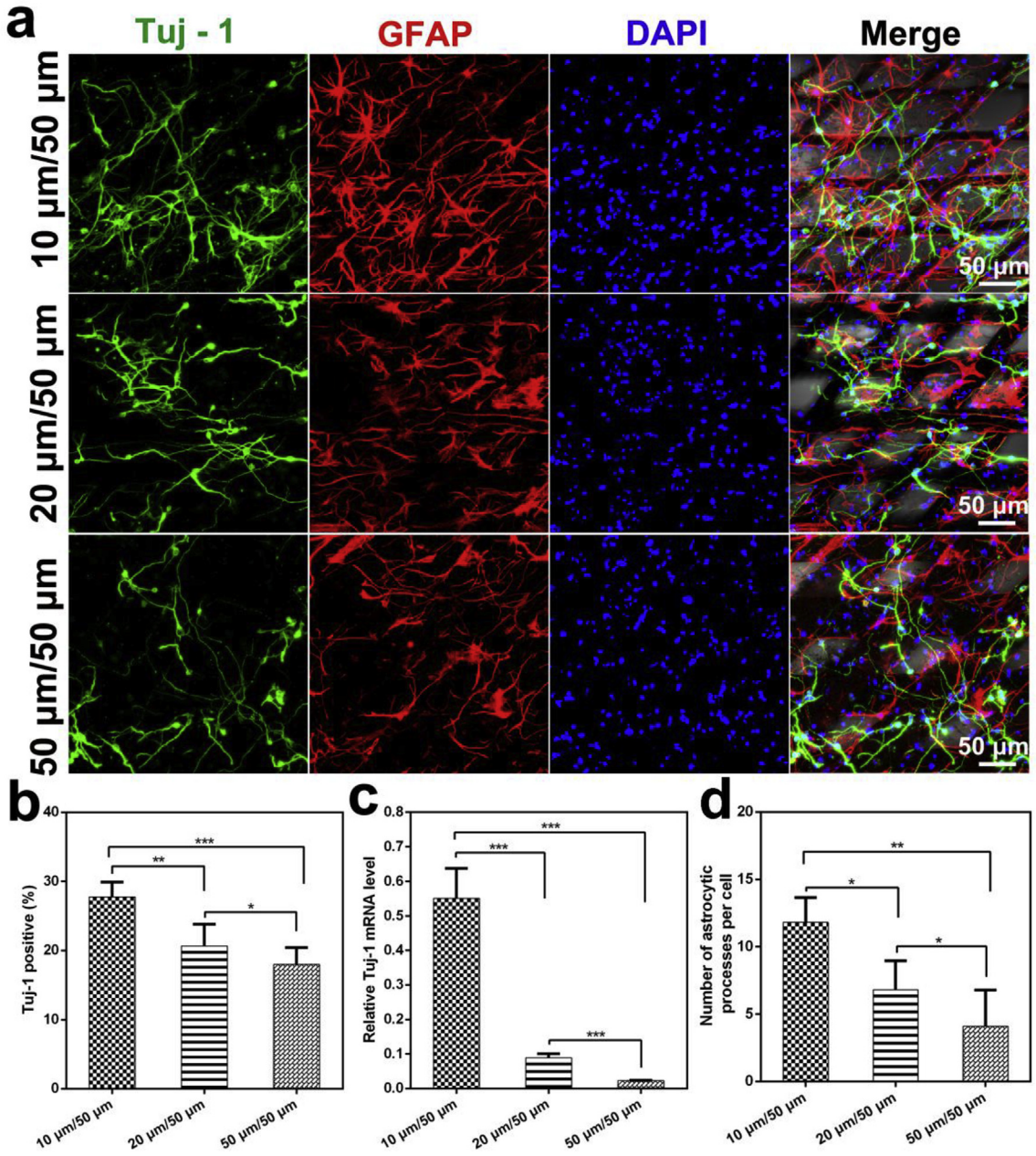

Fig. 6. The differentiated NPCs in the 3D-HG with various skeleton width. (a) Immunofluorescence staining of NPCs in 3D-HG with spacing width of 50 μm after 7-day differentiation, stained against neuron marker Tuj-1 (green), astrocyte marker GFAP (red), nuclei marker DAPI (blue), and merge image containing the bright field. The skeleton widths from top to bottom are 10 μm, 20 μm, 50 μm, respectively. **(b)** Percentage of Tuj-1-positive cells in (a). **(c)** The relative mRNA expression of Tuj-1 in NPCs in the 3D-HG with different skeleton widths after 7-day differentiation. **(d)** Number of astrocytic processes per cell in (a). Statistical analyses performed with one-way ANOVA and a Tukey test, $^{***}p < 0.001$, $^{**}p < 0.01$, $^{*}p < 0.05$, error bars are presented as the means ± S.E.M. (A colour version of this figure can be viewed online.)

reduced with the increasing skeleton width (27.7 ± 2.2% in 10 μm/50 μm 3D-HG, 20.6 ± 1.0% in 20 μm/50 μm 3D-HG, 18.0 ± 0.8% in 50 μm/50 μm 3D-HG, Fig. 6b), indicating that NPCs preferred to neuronal differentiation on narrower graphene skeleton. Neuronal differentiation rate changing was revalidated by measuring the expression of Tuj-1 mRNA. As expected, the mRNA expression levels of Tuj-1 was significantly higher in NPCs cultured on thinner skeletons (Fig. 6c). The size change did not cause a significant difference in the differentiation rate of the astrocytes (Fig. S11), but affected the number of astrocytic processes per cell. As observed, narrower skeletons increased the number of astrocytic processes per cell (Fig. 6d). Our observation might be ascribed to the stiffness changes of the scaffolds caused by the skeletons width changes [43]. As seen in Fig. S12, narrower skeleton width led to the decrease of the elastic modulus. It has been documented that softer substrate prefers to neuronal differentiation of neural stem/progenitor cells [42]. Meanwhile, the higher density of neurons differentiated from NPCs can increase the direct contact between astrocytes and neuronal processes, further increasing the complexity of astrocytes morphology [44]. Besides, the unique surface microstructure of graphene materials [45] may affect the differentiation behaviors of NPCs. We present the evidence of the ripples and wrinkles with nanometer-scale width and micrometer-scale length on the surface (Fig. 1d), while the nano-size lines have been reported to direct the differentiation of stem cells into neuronal lineage [46,47]. The skeletons in 3D-HG have hollow cuboids-like structure with the square or rectangle cross sections (Fig. 1c). Dense ripples and wrinkles present on the surface near the edge of square or rectangle, while the center of skeletons is relatively smooth (Fig. 1d). As the width of the skeleton decreases, the ratio of the surface area near the edge to the total surface area increases. Therefore, the higher density of ripples and wrinkles on 3D-HG with smaller width increases the promotion of NPCs differentiation into neurons. In addition, it is noteworthy of the formation of neural network across the spacings in all 3D-HG with different skeleton widths (Fig. 6a). Further, spacings, angles and layer thickness can be controlled for the geometry effect on cell behaviors by modulating UV lithography masks and Ni plating in our future studies.

4. Conclusion

In summary, we successfully developed an integrated 3D-HG consisting of 3D controllable graphene skeleton and 2D graphene film via the combination of micro-fabrication strategy and CVD. The free-standing 3D-HG exhibits excellent conductivity and biocompatibility. NPCs cultured in 3D-HG can efficiently respond to the 100 mV pulse electrical stimulation applied to 3D-HG. The differentiated NPCs in 3D-HG are capable of bridging the large spacings to form extensive neural networks, penetrating the bottom graphene film and interconnecting with the external cells, promoting the formation of neural networks. Of further importance and novelty, lithography technique was applied to precisely control the sizes of structures to obtain 3D-HG with various skeleton widths. Interestingly, width of graphene skeletons did not significantly affect the proliferation of NPCs when exceeding the cell sizes, but had impact on NPCs differentiation into neurons. Therefore, this intriguing 3D-HG not only expands the applications of graphene in neural tissue engineering but also provides a powerful tool for exploring the physical effects on cell behaviors.

Supplementary data

Photographs of 3D-HG; Resistance variation of 3D-HG/PDMS composite with different bending radius; Biocompatibility of 3D-HG; Ca^{2+} transients of NPCs in 3D-HG before and after the 100 mV electrical stimulation; Schematic illustration of the procedure designed to visualize the contact of cells in 3D-HG and cells on glass; Proliferation state of NPCs in 3D-HG with different skeleton widths; Young's moduli of different 3D-HG.

Acknowledgements

This work was supported by the Key Research and Development Program of Jiangsu Province (BE2017665) and National Key Basic Research Program of China (973 Program grant no. 2014CB965003). The authors are grateful for the professional services of Platforms of Characterization & Test and Nanofabrication Facility at Suzhou Institute of Nano-Tech and Nano-Bionics, Chinese Academy of Sciences. We are also thankful to Ziyun Jiang and Lingyan Yang for their guidance in cell extraction experiment.

Appendix A. Supplementary data

Supplementary data to this article can be found online at https://doi.org/10.1016/j.carbon.2019.01.006.

References

[1] G. Martino, S. Pluchino, The therapeutic potential of neural stem cells, Nat. Rev. Neurosci. 7 (2006) 395.
[2] K.I. Park, Y.D. Teng, E.Y. Snyder, The injured brain interacts reciprocally with neural stem cells supported by scaffolds to reconstitute lost tissue, Nat. Biotechnol. 20 (2002) 1111–1117.
[3] T.C. Burns, G.K. Steinberg, Stem cells and stroke: opportunities, challenges and strategies, Expert Opin. Biol. Ther. 11 (2011) 447–461.
[4] N. Tasnim, V. Thakur, M. Chattopadhyay, B. Joddar, The efficacy of graphene foams for culturing mesenchymal stem cells and their differentiation into dopaminergic neurons, Stem Cell. Int. 2018 (2018) 12.
[5] Y. Niu, X. Chen, D. Yao, G. Peng, H. Liu, Y. Fan, Enhancing neural differentiation of induced pluripotent stem cells by conductive graphene/silk fibroin films, J. Biomed. Mater. Res. A. 106 (2018) 2973–2983.
[6] N.C. Spitzer, Electrical activity in early neuronal development, Nature 444 (2006) 707–712.
[7] L. Li, Y.H. El-Hayek, B. Liu, Y. Chen, E. Gomez, X. Wu, et al., Direct-current electrical field guides neuronal stem/progenitor cell migration, Stem Cell. 26 (2008) 2193–2200.
[8] Y.J. Huang, H.C. Wu, N.H. Tai, T.W. Wang, Carbon nanotube rope with electrical stimulation promotes the differentiation and maturity of neural stem cells, Small 8 (2012) 2869–2877.
[9] Z.Q. Feng, T. Wang, B. Zhao, J. Li, L. Jin, Soft graphene nanofibers designed for the acceleration of nerve growth and development, Adv. Mater. 27 (2015) 6462–6468.
[10] P.M. George, T.M. Bliss, T. Hua, A. Lee, B. Oh, A. Levinson, et al., Electrical preconditioning of stem cells with a conductive polymer scaffold enhances stroke recovery, Biomaterials 142 (2017) 31–40.
[11] P. Gupta, S. Sharan, P. Roy, D. Lahiri, Aligned carbon nanotube reinforced polymeric scaffolds with electrical cues for neural tissue regeneration, Carbon 95 (2015) 715–724.
[12] O. Akhavan, E. Ghaderi, S.A. Shirazian, R. Rahighi, Rolled graphene oxide foams as three-dimensional scaffolds for growth of neural fibers using electrical stimulation of stem cells, Carbon 97 (2016) 71–77.
[13] S. Shrestha, B.K. Shrestha, J.I. Kim, S. Won Ko, C.H. Park, C.S. Kim, Electrodeless coating polypyrrole on chitosan grafted polyurethane with functionalized multiwall carbon nanotubes electrospun scaffold for nerve tissue engineering, Carbon 136 (2018) 430–443.
[14] C. Martín, S. Merino, J.M. González-Domínguez, R. Rauti, L. Ballerini, M. Prato, et al., Graphene improves the biocompatibility of polyacrylamide hydrogels: 3D polymeric scaffolds for neuronal growth, Sci. Rep. 7 (2017) 10942.
[15] Z. Zhang, L.H. Klausen, M. Chen, M. Dong, Electroactive scaffolds for neurogenesis and myogenesis: graphene-based nanomaterials, Small 14 (2018) 1801983.
[16] W.C. Kenry, K.P. Lee, Loh, C.T. Lim, When stem cells meet graphene: opportunities and challenges in regenerative medicine, Biomaterials 155 (2018) 236–250.
[17] Q. Song, Z. Jiang, N. Li, P. Liu, L. Liu, M. Tang, et al., Anti-inflammatory effects of three-dimensional graphene foams cultured with microglial cells, Biomaterials 35 (2014) 6930–6940.
[18] N. Li, X. Zhang, Q. Song, R. Su, Q. Zhang, T. Kong, et al., The promotion of neurite sprouting and outgrowth of mouse hippocampal cells in culture by graphene substrates, Biomaterials 32 (2011) 9374–9382.
[19] S.Y. Park, J. Park, S.H. Sim, M.G. Sung, K.S. Kim, B.H. Hong, et al., Enhanced

differentiation of human neural stem cells into neurons on graphene, Adv. Mater. 23 (2011) H263–H267.
[20] M. Tang, Q. Song, N. Li, Z. Jiang, R. Huang, G. Cheng, Enhancement of electrical signaling in neural networks on graphene films, Biomaterials 34 (2013) 6402–6411.
[21] N.P. Pampaloni, M. Lottner, M. Giugliano, A. Matruglio, F. D'Amico, M. Prato, et al., Single-layer graphene modulates neuronal communication and augments membrane ion currents, Nat. Nanotechnol. 13 (2018) 755–764.
[22] M. Chen, X. Qin, G. Zeng, Biodegradation of carbon nanotubes, graphene, and their derivatives, Trends Biotechnol. 35 (2017) 836–846.
[23] M. Loeblein, G. Perry, S.H. Tsang, W. Xiao, D. Collard, P. Coquet, et al., Three-dimensional graphene: a biocompatible and biodegradable scaffold with enhanced oxygenation, Adv. Healthc. Mater. 5 (2016) 1177–1191.
[24] Y. Li, L. Feng, X. Shi, X. Wang, Y. Yang, K. Yang, et al., Surface coating-dependent cytotoxicity and degradation of graphene derivatives: towards the design of non-toxic, degradable nano-graphene, Small 10 (2014) 1544–1554.
[25] K. Watanabe, D. Kamiya, A. Nishiyama, T. Katayama, S. Nozaki, H. Kawasaki, et al., Directed differentiation of telencephalic precursors from embryonic stem cells, Nat. Neurosci. 8 (2005) 288.
[26] K. Kolind, K.W. Leong, F. Besenbacher, M. Foss, Guidance of stem cell fate on 2D patterned surfaces, Biomaterials 33 (2012) 6626–6633.
[27] P. Clark, S. Britland, P. Connolly, Growth cone guidance and neuron morphology on micropatterned laminin surfaces, J. Cell Sci. 105 (1993) 203–212.
[28] N. Li, A. Folch, Integration of topographical and biochemical cues by axons during growth on microfabricated 3-D substrates, Exp. Cell Res. 311 (2005) 307–316.
[29] J.S. Goldner, J.M. Bruder, G. Li, D. Gazzola, D. Hoffman-Kim, Neurite bridging across micropatterned grooves, Biomaterials 27 (2006) 460–472.
[30] X. Li, W. Cai, J. An, S. Kim, J. Nah, D. Yang, et al., Large-area synthesis of high-quality and uniform graphene films on copper foils, Science 324 (2009) 1312–1314.
[31] M. Xiao, T. Kong, W. Wang, Q. Song, D. Zhang, Q. Ma, et al., Interconnected graphene networks with uniform geometry for flexible conductors, Adv. Funct. Mater. 25 (2015) 6165–6172.
[32] H. Niu, R. Gou, Q. Xu, D. Duan, Recombinant insulin-like growth factor binding protein-4 inhibits proliferation and promotes differentiation of neural progenitor cells, Neurosci. Lett. 642 (2017) 71–76.
[33] Z. Chen, W. Ren, L. Gao, B. Liu, S. Pei, H.-M. Cheng, Three-dimensional flexible and conductive interconnected graphene networks grown by chemical vapour deposition, Nat. Mater. 10 (2011) 424.
[34] A.C. Ferrari, J.C. Meyer, V. Scardaci, C. Casiraghi, M. Lazzeri, F. Mauri, et al., Raman spectrum of graphene and graphene layers, Phys. Rev. Lett. 97 (2006) 187401.
[35] L.M. Malard, M.A. Pimenta, G. Dresselhaus, M.S. Dresselhaus, Raman spectroscopy in graphene, Phys. Rep. 473 (2009) 51–87.
[36] T. Zhang, N. Li, K. Li, R. Gao, W. Gu, C. Wu, et al., Enhanced proliferation and osteogenic differentiation of human mesenchymal stem cells on bio-mineralized three-dimensional graphene foams, Carbon 105 (2016) 233–243.
[37] Y. Huang, Y. Li, J. Chen, H. Zhou, S. Tan, Electrical stimulation elicits neural stem cells activation: new perspectives in CNS repair, Front. Hum. Neurosci. 9 (2015), 586-586.
[38] W. Zhu, T. Ye, S.-J. Lee, H. Cui, S. Miao, X. Zhou, et al., Enhanced neural stem cell functions in conductive annealed carbon nanofibrous scaffolds with electrical stimulation, Nanomed-nanotechnol. 14 (2018) 2485–2494.
[39] B.N. Cuffin, D. Cohen, K. Yunokuchi, R. Maniewski, C. Purcell, G.R. Cosgrove, et al., Tests of EEG localization accuracy using implanted sources in the human brain, Ann. Neurol. 29 (1991) 132–138.
[40] F.W. Hopf, J. Waters, S. Mehta, S.J. Smith, Stability and plasticity of developing synapses in hippocampal neuronal cultures, J. Neurosci. 22 (2002) 775–781.
[41] A. Béduer, C. Vieu, F. Arnauduc, J.-C. Sol, I. Loubinoux, L. Vaysse, Engineering of adult human neural stem cells differentiation through surface micropatterning, Biomaterials 33 (2012) 504–514.
[42] F. Guilak, D.M. Cohen, B.T. Estes, J.M. Gimble, W. Liedtke, C.S. Chen, Control of stem cell fate by physical interactions with the extracellular matrix, Cell Stem Cell 5 (2009) 17–26.
[43] D.E. Discher, P. Janmey, Y.-l. Wang, Tissue cells feel and respond to the stiffness of their substrate, Science 310 (2005) 1139.
[44] J.A. Stogsdill, J. Ramirez, D. Liu, Y.H. Kim, K.T. Baldwin, E. Enustun, et al., Astrocytic neuroligins control astrocyte morphogenesis and synaptogenesis, Nature 551 (2017) 192.
[45] S.J. Chae, F. Güneş, K.K. Kim, E.S. Kim, G.H. Han, S.M. Kim, et al., Synthesis of large-area graphene layers on poly-nickel substrate by chemical vapor deposition: wrinkle formation, Adv. Mater. 21 (2009) 2328–2333.
[46] F. Pan, M. Zhang, G. Wu, Y. Lai, B. Greber, H.R. Schöler, et al., Topographic effect on human induced pluripotent stem cells differentiation towards neuronal lineage, Biomaterials 34 (2013) 8131–8139.
[47] K. Yang, H. Jung, H.-R. Lee, J.S. Lee, S.R. Kim, K.Y. Song, et al., Multiscale, hierarchically patterned topography for directing human neural stem cells into functional neurons, ACS Nano 8 (2014) 7809–7822.

Supplementary data

Precisely Controllable Hybrid Graphene Scaffold Reveals Size Effects on Differentiation of Neural Progenitor Cells in Mimicking Neural Network

Xun Ma[a,b], Miao Xiao[b,c], Ying Hao[b], Guosheng Cheng[a,b,*]

[a] School of Nano Technology and Nano Bionics, University of Science and Technology of China, Hefei, Anhui 230026, China.

[b] CAS Key Laboratory of Nano-Bio Interface, Suzhou Institute of Nano-Tech and Nano-Bionics, Chinese Academy of Sciences, 398 Ruoshui Road, Suzhou Industrial Park, Jiangsu 215123, China.

[c] Neurobiology Sector, International School for Advanced Studies (SISSA), via Bonomea, 265, 34136 Trieste, Italy.

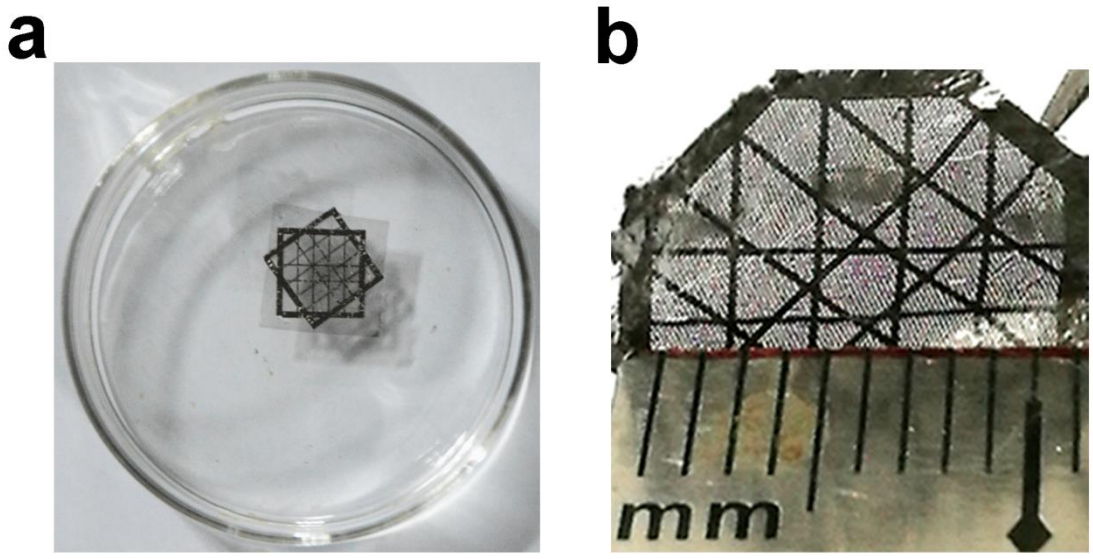

Figure S1. Characterizations of 3D-HG. **(a)** Photograph of a piece of 3D-HG floating on DI water in a dish with the diameter of 6 cm. **(b)** Photograph of a piece of 3D-HG bending with one half under the ruler and the other half tilted by a tweezer (upper right corner).

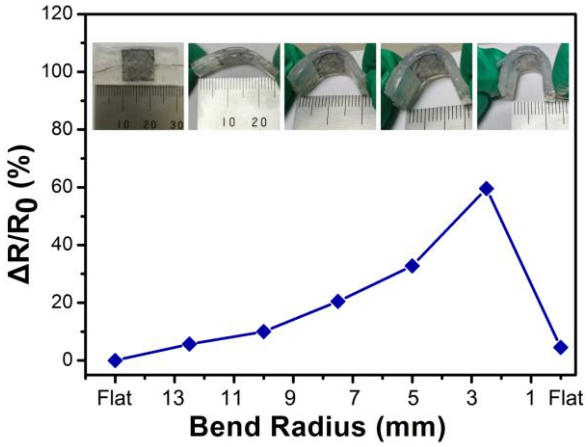

Figure S2. Resistance variation of 3D-HG/ PDMS composite with different bending radius. To assess the conductivity of 3D-HG under different degrees of bending, 3D-HG/Polydimethylsiloxane (PDMS) composites was fabricated by infiltration of PDMS into 3D-HG according to the reported method[1, 2]. The 3D-HG/PDMS composites show good flexibility and stability without breaking at different bend radius. The electrical conductivity can recover after straightening.

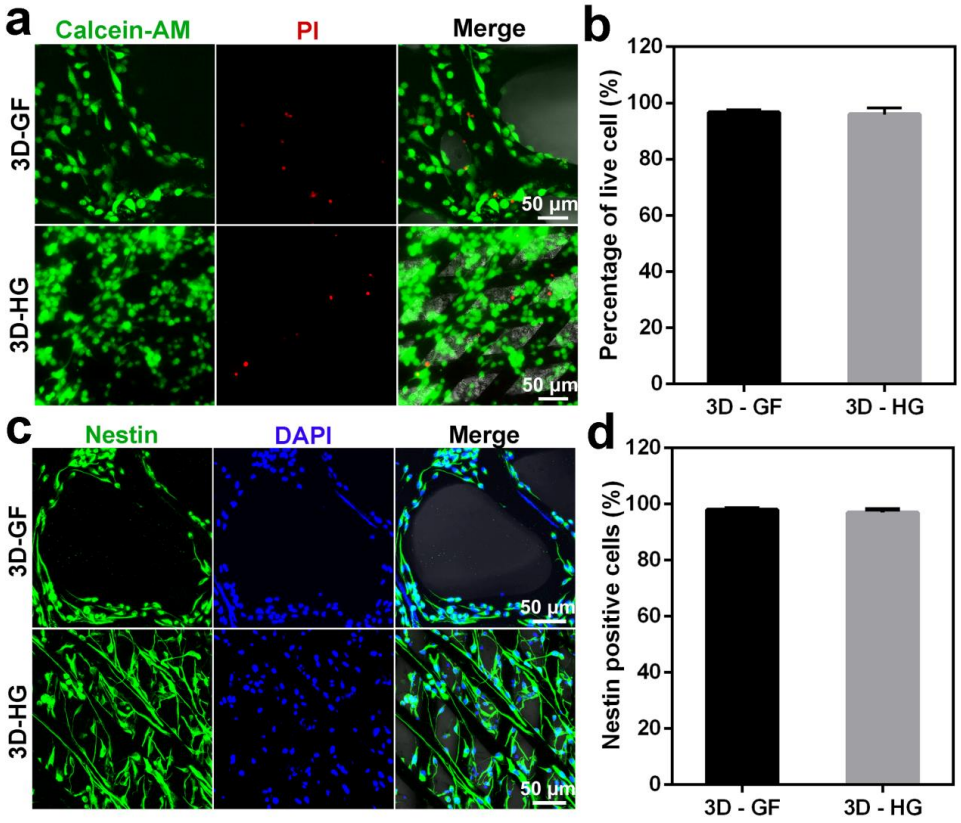

Figure S3. Biocompatibility of 3D-HG. **(a)** Cell viability of NPCs in 3D-HG and 3D-GF after 7 days of culture as determined by live/dead assay, live cells and dead cells are stained with Calcein-AM (green) and PI (red), respectively. **(b)** Percentage of live cells in (a). **(c)** Immunofluorescence images of nestin (green) and nuclei stained with DAPI (blue) in NPCs after 7 days of culture, showing the stemness retention of NPCs in 3D-HG and 3D-GF. **(d)** Percentage of Nestin-positive cells in (c). The merge images containing the bright field. Statistical analyses performed with student's t-test indicate no significant difference, the experiment was repeated three times, the error bars are presented as the means ± S.E.M.

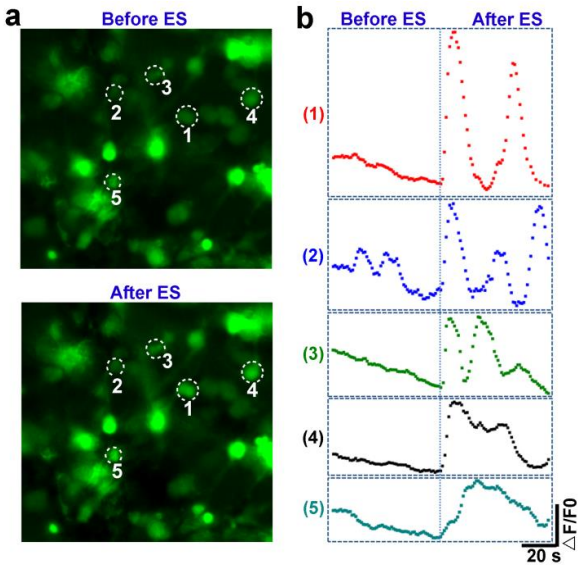

Figure S4. The Ca^{2+} transients of NPCs in 3D-HG before and after the 100 mV electrical stimulation. Five cells with obvious changes in Ca^{2+} transients before and after electrical stimulation was selected to plot $_{\triangle}F/F0$ curves respectively. The cells simultaneously underwent rapid changes in Ca^{2+} transients after electrical stimulation, while one cell (curve 2) underwent spontaneous activity before electrical stimulation.

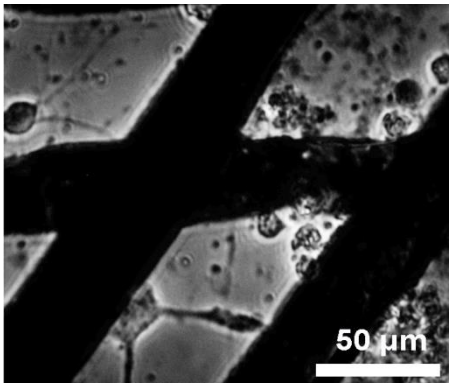

Figure S5. A typical image of the NPCs grown in 3D-HG across the spacing in 3D-HG after 1 day of differentiation. The image was captured by an inverse research microscope (Eclipse TS100, Nikon, Japan) under a 40× objective.

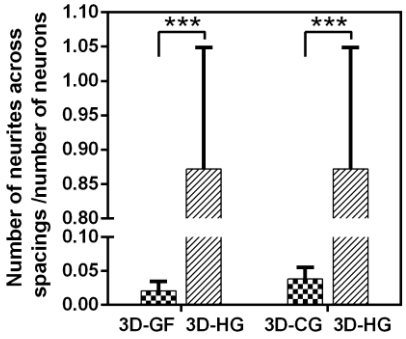

Figure S6. The quantification of the average number of neurites across spacings per neuron in 3D-GF, 3D-CG and 3D-HG based on a total of 9 images of three pieces of each material. Statistical analysis was performed with one-way ANOVA and a Dunnett test, ***$p < 0.001$, error bars are presented as the means ± S.E.M.

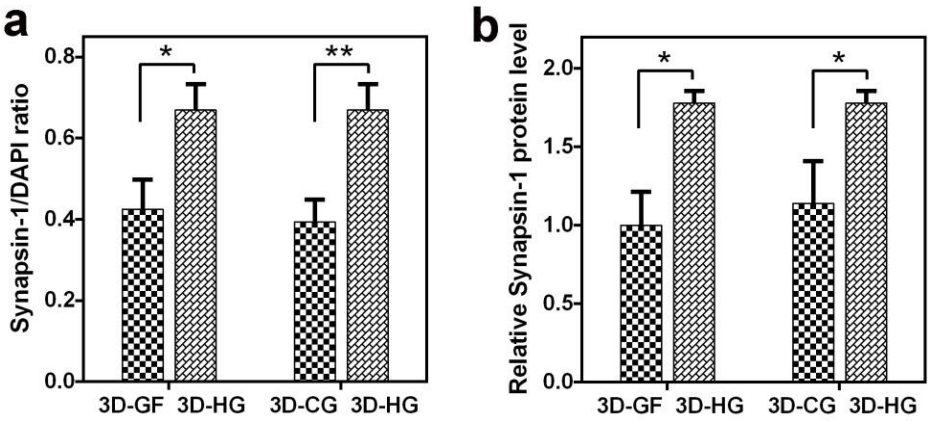

Figure S7. Quantification of the expression of synapsin-1 of NPCs in different graphene scaffolds after 14-day differentiation. **(a)** Mean fluorescent intensity of synapsin-1 immunostaining measured in arbitrary units. **(b)** The quantitative analysis of Western blot. Data is shown as mean ± SEM; one-way ANOVA and a Dunnett test; *$p < 0.05$, **$p < 0.01$.

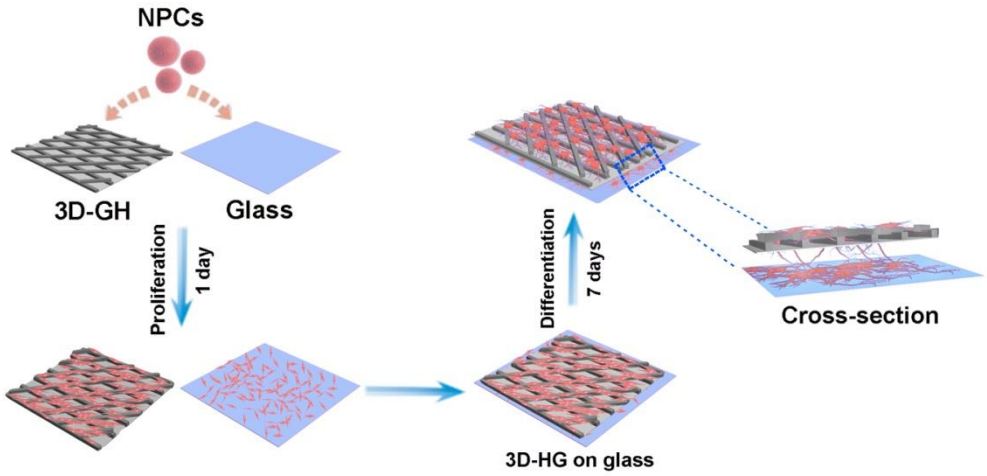

Figure S8. Schematic illustration of the procedure designed to visualize the contact of cells in 3D-HG and cells on glass.

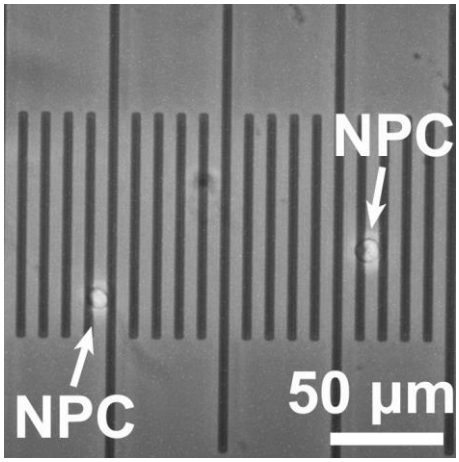

Figure S9. A typical image of NPCs on objective micrometer (Divisions = 10 μm.) obtained by an inverse research microscope (Eclipse TS100, Nikon, Japan). The average diameter of NPCs is 9.94 ± 0.18 μm (average ± S.E.M, n =100 cells).

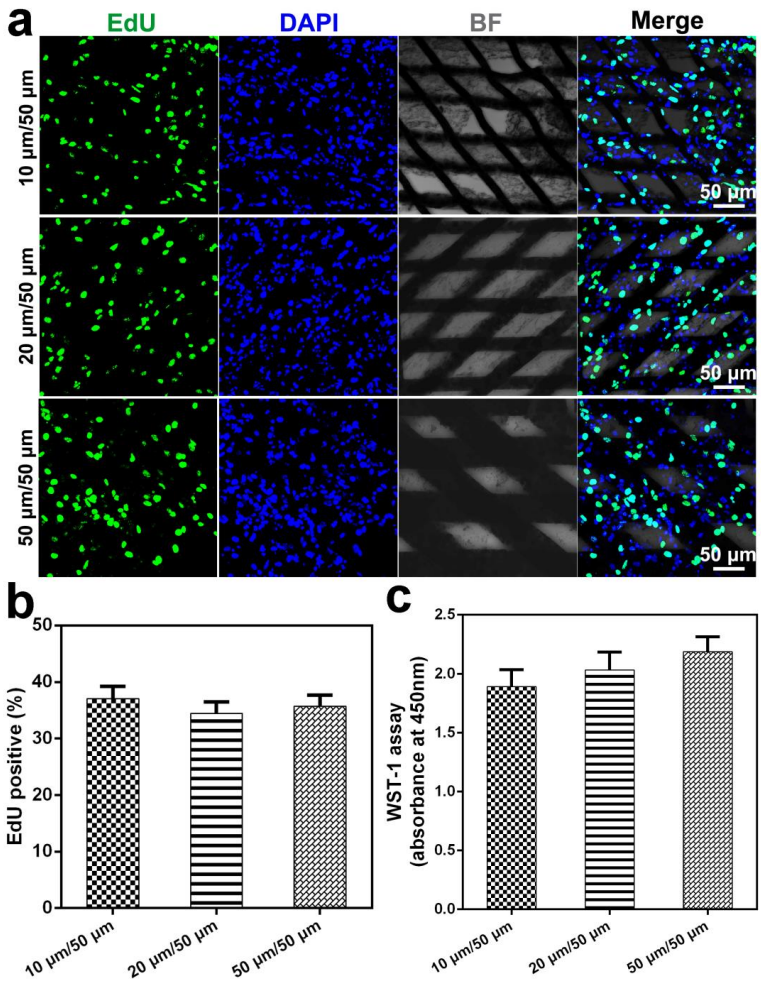

Figure S10. Proliferation state of NPCs in 3D-HG with different skeleton widths after 7 days of culture. **(a)** From left to right: the proliferating NPCs indicated by EdU-positive cells (green); all nuclei are counterstained with DAPI (blue); the bright field images of 3D-HG with different skeleton widths; merged images. **(b)** Percentage of EdU-positive cells in (a). **(c)** Effect of graphene skeleton widths on cell proliferation investigated by the WST-1 assay. Statistical analyses performed with one-way ANOVA and a Turkey test indicate no significant difference, error bars are presented as the means ± S.E.M.

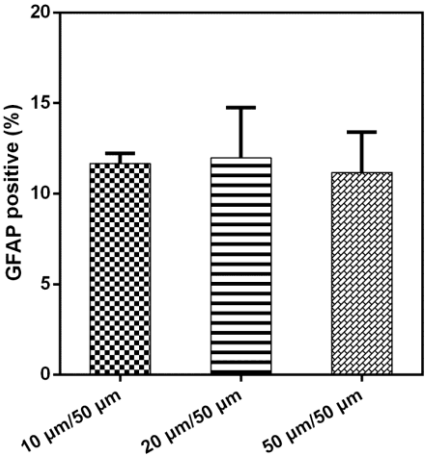

Figure S11. Percentage of GFAP-positive cells in Figure 6a. Statistical analyses performed with one-way ANOVA and a Turkey test indicate no significant difference, error bars are presented as the means ± S.E.M.

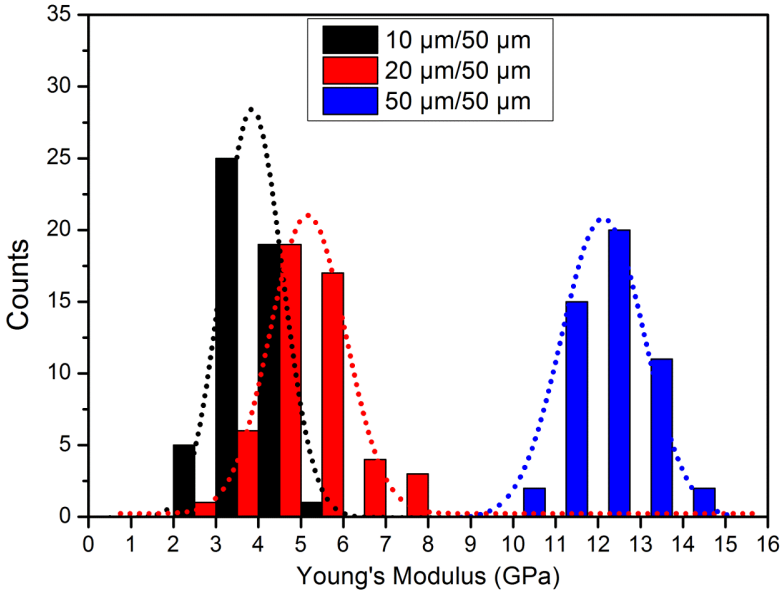

Figure S12. Histogram of elastic stiffness. Dashed line in plot represent Gaussian fits to data. Atomic force microscopy (AFM, Dimension Icon, Bruker Corporation, Germany) in tapping mode was utilized to detect the elastic modulus of 3D-HG with different skeleton widths[3]. The estimated Young's moduli were obtained using Nanoscope Analysis (v 1.90) under DMT model. Young's modulus values obtained from random 50 sections for each scaffold were used to plot Gaussian distribution curves.

References

[1] Z. Chen, C. Xu, C. Ma, W. Ren, H.-M. Cheng, Lightweight and Flexible Graphene Foam Composites for High-Performance Electromagnetic Interference Shielding, Adv. Mater. 25 (2013) 1296-1300.

[2] Z. Chen, W. Ren, L. Gao, B. Liu, S. Pei, H.-M. Cheng, Three-dimensional flexible and conductive interconnected graphene networks grown by chemical vapour deposition, Nat. Mater. 10 (2011) 424.

[3] L. Changgu, W. Xiaoding, J.W. Kysar, H. James, Measurement of the elastic properties and intrinsic strength of monolayer graphene, Science 32 (2008) 385-388.

Conclusion and Future Perspectives

In summary, the researches during my PhD aimed to construct more physiologically relevant microenvironments *in vitro* to mimic the complex of brain connections and develop feasible physical cues on the regulation of neuronal network to meet the customized applications in neural tissue engineering. Firstly, I have fabricated a 3D monolithic porous GCNT web with fully geometric, mechanical and electrical interconnectivity by *in situ* CVD growth of interconnected CNT web into the GF pores. The 3D GCNT web provides a novel biomaterial to construct a 3D cortex-like network which responds to dense neuronal network and functional activity closer to the *in vivo* conditions. The cortex-like network allows to study brain connectivity and neuronal dysfunction and, further, to construct an ideal glioma infiltration model to map the 3D overall invasion, which could be an additional and more visible technology for preclinical therapeutic approaches screening. Therefore, our system is not only a novel platform for live cell imaging achievement but also a new route towards the findings of improved methods to eradicate tumours without affecting the host's cells. On the other hand, there are also some limitations in this work. We presented "cortex-like" in the published paper but "cortex-like" didn't mean that we have built a cortex model having six layers for different functions. It meant dense neuronal network and functional activity closer to the *in vivo* conditions. Indeed, it is really a huge and difficult program to build a six layers cortex *in vitro* and for sure our work is far away from this goal. For the formation of brain organoid and understanding the neural processing, we need much more efforts not only from researchers in the field of materials and neurobiology but also biochemistry, mathematics and computer.

The fully interconnected 3D GCNT web provides a hierarchical microarchitecture that support for cell growth and nano interface between neurons and CNTs. To further explore the modification of 3D graphene foam, my collaborators and I fabricated three-dimensional bacterial cellulose-graphene foam (3D-BC/G), which was prepared via *in situ* bacterial cellulose interfacial polymerization on the skeleton surface of porous

graphene foam. The addition of bacterial cellulose into graphene foams have the ability to remarkably enhance the biocompatibility, proliferation, differentiation and formation of neural network differentiated from neural stem cells. Moreover, primary cortical neurons cultured on 3D-BC/G formed an intensely-active neuronal network with higher network activity than that formed on 3D graphene foam.

One of the primary goals of neural tissue engineering is to guide neurite growth in a desired direction, therefore, to pattern the alignment of the neuronal growth and network formation is highly valued.[86] We investigated the ordered growth of neurons and alignment of neuronal network formation on the support of graphene in 3D for the first time. The fabricated 3D-OG with the pore size of 20 μm, the skeleton width of 20 μm and the 90° orientation angles of building blocks presented high neuronal culture compatibility, where neurons and glia grew along the skeleton geometry and formed functional network. Compared to standard neuronal culture on coverslip, 3D-OG structure didn't affect the relative abundance of neurons and glial cells but induced astrocytes exhibiting much more in vivo like morphologies. Moreover, many more bipolar neurons were found on 3D-OG scaffolds because of the ordered graphene skeleton. We also found that neurons were more active on 3D-OG scaffolds and cellular communication occurred along the graphene skeleton over a long distance.

All together, these results indicated that graphene and CNT scaffolds possessed high biocompatibility for neural culture. They could support the neurons to form a dense neuronal network and promote the electrical activity of neuronal network. By positive regulation of the structures to fabricate heterostructures with micro support of graphene foam and nano interface of CNT and bacterial cellulose, we further improved the properties of graphene and CNT scaffolds to reconstruct *in vitro* neuron connections closer to *in vivo* microenvironment. Thus, they can be not only applied to build *in vitro* models better mimicking physiological and pathological conditions but also used for the screening of drugs against a variety of diseases. We carried out the study of glioma infiltration in the 3D cortex-like network constructed by 3D GCNT webs, which presented an ideal tool to study 3D biological processes *in vitro* representing a pivotal

step towards precise and personalized medicine. Future developments already in process include the analysis of the 3D motion of malignant glioma from patients in our model and the comparison of ECM secreted by different kinds of malignant glioma cells. The application of 3D GCNT web in cancer model construction also represents an important step towards precise and personalized medicine. Indeed, it is possible to derive cortical cells from the stem cells of a patient and to screen drugs that can block the infiltration of brain cancer cells obtained from the same patient. Moreover, 3D ordered graphene structures provided geometrical cues in neurons, leading to directional neurite outgrowth and consequently increasing neuronal network connections, which leads to significant process in designing scaffold−tissue interfaces and ultimately the development of customized neuro-prosthetics in tissue engineering and regenerative medicine. To further regulate the behaviours of neurons *in vitro*, we plan to develop more physical cues on the 3D culture platforms to achieve direct electrical stimulation or even magnetoelectrical, photoelectrical, thermoelectrical stimulations so that neuronal cultures could be non-contact-manipulated.

Reference

1. Watanabe, K.; Kamiya, D.; Nishiyama, A.; Katayama, T.; Nozaki, S.; Kawasaki, H.; Watanabe, Y.; Mizuseki, K.; Sasai, Y., Directed differentiation of telencephalic precursors from embryonic stem cells. *Nature neuroscience* **2005,** *8* (3), 288.

2. Derby, B., Printing and Prototyping of Tissues and Scaffolds. *Science* **2012,** *338* (6109), 921-926.

3. Biswal, B. B.; Mennes, M.; Zuo, X. N.; Gohel, S.; Kelly, C.; Smith, S. M.; Beckmann, C. F.; Adelstein, J. S.; Buckner, R. L.; Colcombe, S.; Dogonowski, A. M.; Ernst, M.; Fair, D.; Hampson, M.; Hoptman, M. J.; Hyde, J. S.; Kiviniemi, V. J.; Kotter, R.; Li, S. J.; Lin, C. P.; Lowe, M. J.; Mackay, C.; Madden, D. J.; Madsen, K. H.; Margulies, D. S.; Mayberg, H. S.; McMahon, K.; Monk, C. S.; Mostofsky, S. H.; Nagel, B. J.; Pekar, J. J.; Peltier, S. J.; Petersen, S. E.; Riedl, V.; Rombouts, S. A. R. B.; Rypma, B.; Schlaggar, B. L.; Schmidt, S.; Seidler, R. D.; Siegle, G. J.; Sorg, C.; Teng, G. J.; Veijola, J.; Villringer, A.; Walter, M.; Wang, L. H.; Weng, X. C.; Whitfield-Gabrieli, S.; Williamson, P.; Windischberger, C.; Zang, Y. F.; Zhang, H. Y.; Castellanos, F. X.; Milham, M. P., Toward discovery science of human brain function. *P Natl Acad Sci USA* **2010,** *107* (10), 4734-4739.

4. Griffith, L. G.; Swartz, M. A., Capturing complex 3D tissue physiology in vitro. *Nat Rev Mol Cell Bio* **2006,** *7* (3), 211-224.

5. (a) Tang-Schomer, M. D.; White, J. D.; Tien, L. W.; Schmitt, L. I.; Valentin, T. M.; Graziano, D. J.; Hopkins, A. M.; Omenetto, F. G.; Haydon, P. G.; Kaplan, D. L., Bioengineered functional brain-like cortical tissue. *Proceedings of the National Academy of Sciences* **2014,** *111* (38), 13811-13816; (b) Ulloa Severino, F. P.; Ban, J.; Song, Q.; Tang, M.; Bianconi, G.; Cheng, G.; Torre, V., The role of dimensionality in neuronal network dynamics. *Sci Rep* **2016,** *6*, 29640; (c) Usmani, S.; Aurand, E. R.; Medelin, M.; Fabbro, A.; Scaini, D.; Laishram, J.; Rosselli, F. B.; Ansuini, A.; Zoccolan, D.; Scarselli, M., 3D meshes of carbon nanotubes guide functional reconnection of segregated spinal explants. *Science advances* **2016,** *2* (7), e1600087; (d) Soman, P.; Kelber, J. A.; Lee, J. W.; Wright, T. N.; Vecchio, K. S.; Klemke, R. L.; Chen, S., Cancer cell migration within 3D layer-by-layer microfabricated photocrosslinked PEG scaffolds with tunable stiffness. *Biomaterials* **2012,** *33* (29), 7064-7070.

6. Serrano, M. C.; Nardecchia, S.; Garcia-Rama, C.; Ferrer, M. L.; Collazos-Castro, J. E.; del Monte, F.; Gutierrez, M. C., Chondroitin sulphate-based 3D scaffolds containing MWCNTs for nervous tissue repair. *Biomaterials* **2014,** *35* (5), 1543-1551.

7. Zhou, X.; Nowicki, M.; Cui, H. T.; Zhu, W.; Fang, X. Q.; Miao, S. D.; Lee, S. J.; Keidar, M.; Zhang, L. J. G., 3D bioprinted graphene oxide-incorporated matrix for promoting chondrogenic differentiation of human bone marrow mesenchymal stem cells. *Carbon* **2017,** *116*, 615-624.

8. Li, N.; Zhang, Q.; Gao, S.; Song, Q.; Huang, R.; Wang, L.; Liu, L. W.; Dai, J. W.; Tang, M. L.; Cheng, G. S., Three-dimensional graphene foam as a biocompatible and conductive scaffold for neural stem cells. *Scientific Reports* **2013,** *3*.

9. Dhandayuthapani, B.; Yoshida, Y.; Maekawa, T.; Kumar, D. S., Polymeric Scaffolds in Tissue Engineering Application: A Review. *Int J Polym Sci* **2011**.

10. Lee, S. J.; Esworthy, T.; Stake, S.; Miao, S.; Zuo, Y. Y.; Harris, B. T.; Zhang, L. G., Advances in 3D Bioprinting for Neural Tissue Engineering. *Adv. Biosyst.* **2018,** *2* (4), 18.

11. Canales, A.; Jia, X.; Froriep, U. P.; Koppes, R. A.; Tringides, C. M.; Selvidge, J.; Lu, C.; Hou, C.; Wei, L.; Fink, Y.; Anikeeva, P., Multifunctional fibers for simultaneous optical, electrical and chemical

interrogation of neural circuits in vivo. *Nat Biotech* **2015,** *33* (3), 277-284.
12. Bazargani, N.; Attwell, D., Astrocyte calcium signaling: the third wave. *Nat Neurosci* **2016,** *19* (2), 182-9.
13. Huang, G. Y.; Li, F.; Zhao, X.; Ma, Y. F.; Li, Y. H.; Lin, M.; Jin, G. R.; Lu, T. J.; Genin, G. M.; Xu, F., Functional and Biomimetic Materials for Engineering of the Three-Dimensional Cell Microenvironment. *Chem. Rev.* **2017,** *117* (20), 12764-12850.
14. Naderi, H.; Matin, M. M.; Bahrami, A. R., Review paper: Critical Issues in Tissue Engineering: Biomaterials, Cell Sources, Angiogenesis, and Drug Delivery Systems. *Journal of Biomaterials Applications* **2011,** *26* (4), 383-417.
15. Baharvand, H.; Hashemi, S. M.; Kazemi Ashtian, S.; Farrokhi, A., Differentiation of human embryonic stem cells into hepatocytes in 2D and 3D culture systems in vitro. *International Journal of Developmental Biology* **2006,** *50* (7), 645-652.
16. Murphy, A. R.; Laslett, A.; O'Brien, C. M.; Cameron, N. R., Scaffolds for 3D in vitro culture of neural lineage cells. *Acta biomaterialia* **2017**.
17. (a) Xiao, M.; Kong, T.; Wang, W.; Song, Q.; Zhang, D.; Ma, Q.; Cheng, G., Interconnected Graphene Networks with Uniform Geometry for Flexible Conductors. *Advanced Functional Materials* **2015,** *25* (39), 6165-6172; (b) Alessandri, K.; Feyeux, M.; Gurchenkov, B.; Delgado, C.; Trushko, A.; Krause, K.-H.; Vignjevic, D.; Nassoy, P.; Roux, A., A 3D printed microfluidic device for production of functionalized hydrogel microcapsules for culture and differentiation of human Neuronal Stem Cells (hNSC). *Lab on a Chip* **2016,** *16* (9), 1593-1604; (c) Elsayed, M.; Merkel, O. M., Nanoimprinting of topographical and 3D cell culture scaffolds. *Nanomedicine* **2014,** *9* (2), 349-366.
18. Langer, R.; Vacanti, J. P., TISSUE ENGINEERING. *Science* **1993,** *260* (5110), 920-926.
19. Benya, P. D.; Shaffer, J. D., DEDIFFERENTIATED CHONDROCYTES REEXPRESS THE DIFFERENTIATED COLLAGEN PHENOTYPE WHEN CULTURED IN AGAROSE GELS. *Cell* **1982,** *30* (1), 215-224.
20. (a) Lee, E. Y. H.; Parry, G.; Bissell, M. J., MODULATION OF SECRETED PROTEINS OF MOUSE MAMMARY EPITHELIAL-CELLS BY THE COLLAGENOUS SUBSTRATA. *Journal of Cell Biology* **1984,** *98* (1), 146-155; (b) Petersen, O. W.; Ronnovjessen, L.; Howlett, A. R.; Bissell, M. J., INTERACTION WITH BASEMENT-MEMBRANE SERVES TO RAPIDLY DISTINGUISH GROWTH AND DIFFERENTIATION PATTERN OF NORMAL AND MALIGNANT HUMAN BREAST EPITHELIAL-CELLS. *Proceedings of the National Academy of Sciences of the United States of America* **1992,** *89* (19), 9064-9068.
21. Baker, B. M.; Chen, C. S., Deconstructing the third dimension - how 3D culture microenvironments alter cellular cues. *Journal of Cell Science* **2012,** *125* (13), 3015-3024.
22. Justice, B. A.; Badr, N. A.; Felder, R. A., 3D cell culture opens new dimensions in cell-based assays. *Drug Discovery Today* **2009,** *14* (1-2), 102-107.
23. (a) Sun, T.; Jackson, S.; Haycock, J. W.; MacNeil, S., Culture of skin cells in 3D rather than 2D improves their ability to survive exposure to cytotoxic agents. *Journal of Biotechnology* **2006,** *122* (3), 372-381; (b) Reininger-Mack, A.; Thielecke, H.; Robitzki, A. A., 3D-biohybrid systems: applications in drug screening. *Trends in Biotechnology* **2002,** *20* (2), 56-61; (c) Huh, D.; Hamilton, G. A.; Ingber, D. E., From 3D cell culture to organs-on-chips. *Trends in Cell Biology* **2011,** *21* (12), 745-754.
24. Breslin, S.; O'Driscoll, L., Three-dimensional cell culture: the missing link in drug discovery. *Drug Discovery Today* **2013,** *18* (5-6), 240-249.
25. Yang, N.; Ng, Y. H.; Pang, Z. P. P.; Sudhof, T. C.; Wernig, M., Induced Neuronal Cells: How to

Make and Define a Neuron. *Cell Stem Cell* **2011,** *9* (6), 517-525.

26. Lancaster, M. A.; Renner, M.; Martin, C. A.; Wenzel, D.; Bicknell, L. S.; Hurles, M. E.; Homfray, T.; Penninger, J. M.; Jackson, A. P.; Knoblich, J. A., Cerebral organoids model human brain development and microcephaly. *Nature* **2013,** *501* (7467), 373-+.

27. Lee, S.-J.; Zhu, W.; Nowicki, M.; Lee, G.; Heo, D. N.; Kim, J.; Zuo, Y. Y.; Zhang, L. G., 3D printing nano conductive multi-walled carbon nanotube scaffolds for nerve regeneration. *Journal of Neural Engineering* **2018,** *15* (1), 016018.

28. Usmani, S.; Aurand, E. R.; Medelin, M.; Fabbro, A.; Scaini, D.; Laishram, J.; Rosselli, F. B.; Ansuini, A.; Zoccolan, D.; Scarselli, M.; De Crescenzi, M.; Bosi, S.; Prato, M.; Ballerini, L., 3D meshes of carbon nanotubes guide functional reconnection of segregated spinal explants. *Science Advances* **2016,** *2* (7).

29. Hong, J. K.; Madihally, S. V., Next Generation of Electrosprayed Fibers for Tissue Regeneration. *Tissue Engineering Part B-Reviews* **2011,** *17* (2), 125-142.

30. Okamoto, K.; Ishikawa, T.; Abe, R.; Ishikawa, D.; Kobayashi, C.; Mizunuma, M.; Norimoto, H.; Matsuki, N.; Ikegaya, Y., Ex vivo cultured neuronal networks emit in vivo-like spontaneous activity. *J Physiol Sci* **2014,** *64* (6), 421-431.

31. Sasai, Y., Next-Generation Regenerative Medicine: Organogenesis from Stem Cells in 3D Culture. *Cell Stem Cell* **2013,** *12* (5), 520-530.

32. Huang, H.; Ding, Y.; Sun, X. S.; Nguyen, T. A., Peptide Hydrogelation and Cell Encapsulation for 3D Culture of MCF-7 Breast Cancer Cells. *Plos One* **2013,** *8* (3).

33. Tibbitt, M. W.; Anseth, K. S., Hydrogels as Extracellular Matrix Mimics for 3D Cell Culture. *Biotechnology and Bioengineering* **2009,** *103* (4), 655-663.

34. Lantoine, J.; Grevesse, T.; Villers, A.; Delhaye, G.; Mestdagh, C.; Versaevel, M.; Mohammed, D.; Bruyere, C.; Alaimo, L.; Lacour, S. P.; Ris, L.; Gabriele, S., Matrix stiffness modulates formation and activity of neuronal networks of controlled architectures. *Biomaterials* **2016,** *89*, 14-24.

35. Qi, L.; Li, N.; Huang, R.; Song, Q.; Wang, L.; Zhang, Q.; Su, R.; Kong, T.; Tang, M.; Cheng, G., The effects of topographical patterns and sizes on neural stem cell behavior. *PloS one* **2013,** *8* (3), e59022.

36. Chen, W.; Villa-Diaz, L. G.; Sun, Y.; Weng, S.; Kim, J. K.; Lam, R. H. W.; Han, L.; Fan, R.; Krebsbach, P. H.; Fu, J., Nanotopography Influences Adhesion, Spreading, and Self-Renewal of Human Embryonic Stem Cells. *Acs Nano* **2012,** *6* (5), 4094-4103.

37. Park, S. Y.; Park, J.; Sim, S. H.; Sung, M. G.; Kim, K. S.; Hong, B. H.; Hong, S., Enhanced Differentiation of Human Neural Stem Cells into Neurons on Graphene. *Advanced Materials* **2011,** *23* (36), H263-+.

38. Lee, W. C.; Lim, C. H. Y. X.; Shi, H.; Tang, L. A. L.; Wang, Y.; Lim, C. T.; Loh, K. P., Origin of Enhanced Stem Cell Growth and Differentiation on Graphene and Graphene Oxide. *Acs Nano* **2011,** *5* (9), 7334-7341.

39. Khaitan, D.; Chandna, S.; Arya, M. B.; Dwarakanath, B. S., Establishment and characterization of multicellular spheroids from a human glioma cell line; Implications for tumor therapy. *Journal of Translational Medicine* **2006,** *4*.

40. Lin, R.-Z.; Chang, H.-Y., Recent advances in three-dimensional multicellular spheroid culture for biomedical research. *Biotechnology Journal* **2008,** *3* (9-10), 1172-1184.

41. Becerra-Bayona, S.; Guiza-Arguello, V.; Qu, X.; Munoz-Pinto, D. J.; Hahn, M. S., Influence of select extracellular matrix proteins on mesenchymal stem cell osteogenic commitment in three-dimensional contexts. *Acta Biomaterialia* **2012,** *8* (12), 4397-4404.

42. Szot, C. S.; Buchanan, C. F.; Freeman, J. W.; Rylander, M. N., 3D in vitro bioengineered tumors based on collagen I hydrogels. *Biomaterials* **2011,** *32* (31), 7905-7912.
43. Albrecht, C.; Helmreich, M.; Tichy, B.; Marlovits, S.; Plasenzotti, R.; Egerbacher, M.; Haeusler, G., Impact of 3D-culture on the expression of differentiation markers and hormone receptors in growth plate chondrocytes as compared to articular chondrocytes. *International Journal of Molecular Medicine* **2009,** *23* (3), 347-355.
44. Rose, J. C.; De Laporte, L., Hierarchical Design of Tissue Regenerative Constructs. *Adv. Healthc. Mater.* **2018,** *7* (6), 31.
45. Dutta, R. C.; Dutta, A. K., Cell-interactive 3D-scaffold; advances and applications. *Biotechnology Advances* **2009,** *27* (4), 334-339.
46. Lee, J.; Cuddihy, M. J.; Kotov, N. A., Three-dimensional cell culture matrices: State of the art. *Tissue Engineering Part B-Reviews* **2008,** *14* (1), 61-86.
47. (a) Chimene, D.; Lennox, K. K.; Kaunas, R. R.; Gaharwar, A. K., Advanced Bioinks for 3D Printing: A Materials Science Perspective. *Ann. Biomed. Eng.* **2016,** *44* (6), 2090-2102; (b) Pati, F.; Ha, D. H.; Jang, J.; Han, H. H.; Rhie, J. W.; Cho, D. W., Biomimetic 3D tissue printing for soft tissue regeneration. *Biomaterials* **2015,** *62*, 164-175.
48. (a) Binan, L.; Ajji, A.; De Crescenzo, G.; Jolicoeur, M., Approaches for Neural Tissue Regeneration. *Stem Cell Rev. Rep.* **2014,** *10* (1), 44-59; (b) Ghasemi-Mobarakeh, L.; Prabhakaran, M. P.; Morshed, M.; Nasr-Esfahani, M. H.; Baharvand, H.; Kiani, S.; Al-Deyab, S.; Ramakrishna, S., Application of conductive polymers, scaffolds and electrical stimulation for nerve tissue engineering. *J. Tissue Eng. Regen. Med.* **2011,** *5* (4), E17-E35.
49. Ray, A.; Slama, Z. M.; Morford, R. K.; Madden, S. A.; Provenzano, P. P., Enhanced Directional Migration of Cancer Stem Cells in 3D Aligned Collagen Matrices. *Biophys J* **2017,** *112* (5), 1023-1036.
50. Mu, Y.; Wu, F.; Lu, Y. R.; Wei, L. M.; Yuan, W. E., Progress of electrospun fibers as nerve conduits for neural tissue repair. *Nanomedicine-Uk* **2014,** *9* (12), 1869-1883.
51. Egeblad, M.; Rasch, M. G.; Weaver, V. M., Dynamic interplay between the collagen scaffold and tumor evolution. *Current Opinion in Cell Biology* **2010,** *22* (5), 697-706.
52. Cross, V. L.; Zheng, Y.; Choi, N. W.; Verbridge, S. S.; Sutermaster, B. A.; Bonassar, L. J.; Fischbach, C.; Stroock, A. D., Dense type I collagen matrices that support cellular remodeling and microfabrication for studies of tumor angiogenesis and vasculogenesis in vitro. *Biomaterials* **2010,** *31* (33), 8596-8607.
53. Winter, C. C.; Katiyar, K. S.; Hernandez, N. S.; Song, Y. J.; Struzyna, L. A.; Harris, J. P.; Cullen, D. K., Transplantable living scaffolds comprised of micro-tissue engineered aligned astrocyte networks to facilitate central nervous system regeneration. *Acta Biomaterialia* **2016,** *38*, 44-58.
54. Kleinman, H. K.; Martin, G. R., Matrigel: Basement membrane matrix with biological activity. *Seminars in Cancer Biology* **2005,** *15* (5), 378-386.
55. Lancaster, M. A.; Renner, M.; Martin, C.-A.; Wenzel, D.; Bicknell, L. S.; Hurles, M. E.; Homfray, T.; Penninger, J. M.; Jackson, A. P.; Knoblich, J. A., Cerebral organoids model human brain development and microcephaly. *Nature* **2013,** *501* (7467), 373-+.
56. Koutsopoulos, S.; Zhang, S., Long-term three-dimensional neural tissue cultures in functionalized self-assembling peptide hydrogels, Matrigel and Collagen I. *Acta Biomaterialia* **2013,** *9* (2), 5162-5169.
57. Li, X.; Liu, X.; Josey, B.; Chou, C. J.; Tan, Y.; Zhang, N.; Wen, X., Short Laminin Peptide for Improved Neural Stem Cell Growth. *Stem Cells Translational Medicine* **2014,** *3* (5), 662-670.
58. Tedesco, M. T.; Di Lisa, D.; Massobrio, P.; Colistra, N.; Pesce, M.; Catelani, T.; Dellacasa, E.; Raiteri, R.; Martinoia, S.; Pastorino, L., Soft chitosan microbeads scaffold for 3D functional neuronal

networks. *Biomaterials* **2018,** *156*, 159-171.
59. (a) Nagaoka, M.; Si-Tayeb, K.; Akaike, T.; Duncan, S. A., Culture of human pluripotent stem cells using completely defined conditions on a recombinant E-cadherin substratum. *Bmc Developmental Biology* **2010,** *10*; (b) Meng, Q.; Tao, C.; Qiu, Z.; Akaike, T.; Cui, F.; Wang, X., A hybrid substratum for primary hepatocyte culture that enhances hepatic functionality with low serum dependency. *International Journal of Nanomedicine* **2015,** *10*, 2313-2323.
60. Shao, Y.; Sang, J.; Fu, J., On human pluripotent stem cell control: The rise of 3D bioengineering and mechanobiology. *Biomaterials* **2015,** *52*, 26-43.
61. El-Sherbiny, I. M.; Yacoub, M. H., Hydrogel scaffolds for tissue engineering: Progress and challenges. *Global cardiology science & practice* **2013,** *2013* (3), 316-42.
62. Zhu, J.; Marchant, R. E., Design properties of hydrogel tissue-engineering scaffolds. *Expert Review of Medical Devices* **2011,** *8* (5), 607-626.
63. Mahoney, M. J.; Anseth, K. S., Three-dimensional growth and function of neural tissue in degradable polyethylene glycol hydrogels. *Biomaterials* **2006,** *27* (10), 2265-2274.
64. Yang, F.; Xu, C. Y.; Kotaki, M.; Wang, S.; Ramakrishna, S., Characterization of neural stem cells on electrospun poly(L-lactic acid) nanofibrous scaffold. *Journal of Biomaterials Science-Polymer Edition* **2004,** *15* (12), 1483-1497.
65. Xu, X.-Y.; Li, X.-T.; Peng, S.-W.; Xiao, J.-F.; Liu, C.; Fang, G.; Chen, K. C.; Chen, G.-Q., The behaviour of neural stem cells on polyhydroxyalkanoate nanofiber scaffolds. *Biomaterials* **2010,** *31* (14), 3967-3975.
66. Zhang, Z.-N.; Freitas, B. C.; Qian, H.; Lux, J.; Acab, A.; Trujillo, C. A.; Herai, R. H.; Viet Anh Nguyen, H.; Wen, J. H.; Joshi-Barr, S.; Karpiak, J. V.; Engler, A. J.; Fu, X.-D.; Muotri, A. R.; Almutairi, A., Layered hydrogels accelerate iPSC-derived neuronal maturation and reveal migration defects caused by MeCP2 dysfunction. *Proceedings of the National Academy of Sciences of the United States of America* **2016,** *113* (12), 3185-3190.
67. Sisi, L.; Francesco Paolo Ulloa, S.; Jelena, B.; Li, W.; Giulietta, P.; Vincent, T.; Yong, C., Improved neuron culture using scaffolds made of three-dimensional PDMS micro-lattices. *Biomedical Materials* **2018,** *13* (3), 034105.
68. Zhu, B.; Luo, S.-C.; Zhao, H.; Lin, H.-A.; Sekine, J.; Nakao, A.; Chen, C.; Yamashita, Y.; Yu, H.-h., Large enhancement in neurite outgrowth on a cell membrane-mimicking conducting polymer. *Nat. Commun.* **2014,** *5*, 4523.
69. Tang, Y.; Ulloa Severino, F. P.; Iseppon, F.; Torre, V.; Chen, Y., Patch method for culture of primary hippocampal neurons. *Microelectronic Engineering* **2017,** *175*, 61-66.
70. Fattahi, P.; Yang, G.; Kim, G.; Abidian, M. R., A Review of Organic and Inorganic Biomaterials for Neural Interfaces. *Adv. Mater.* **2014,** *26* (12), 1846-1885.
71. Zhou, X.; Nowicki, M.; Cui, H.; Zhu, W.; Fang, X.; Miao, S.; Lee, S. J.; Keidar, M.; Zhang, L. G., 3D bioprinted graphene oxide-incorporated matrix for promoting chondrogenic differentiation of human bone marrow mesenchymal stem cells. *Carbon* **2017,** *116*, 615-624.
72. Lovat, V.; Pantarotto, D.; Lagostena, L.; Cacciari, B.; Grandolfo, M.; Righi, M.; Spalluto, G.; Prato, M.; Ballerini, L., Carbon nanotube substrates boost neuronal electrical signaling. *Nano Letters* **2005,** *5* (6), 1107-1110.
73. Malarkey, E. B.; Fisher, K. A.; Bekyarova, E.; Liu, W.; Haddon, R. C.; Parpura, V., Conductive Single-Walled Carbon Nanotube Substrates Modulate Neuronal Growth. *Nano Lett* **2009,** *9* (1), 264-268.
74. Bosi, S.; Rauti, R.; Laishram, J.; Turco, A.; Lonardoni, D.; Nieus, T.; Prato, M.; Scaini, D.; Ballerini,

L., From 2D to 3D: novel nanostructured scaffolds to investigate signalling in reconstructed neuronal networks. *Scientific reports* **2015,** *5*, 9562.

75. Rago, I.; Rauti, R.; Bevilacqua, M.; Calaresu, I.; Pozzato, A.; Cibinel, M.; Dalmiglio, M.; Tavagnacco, C.; Goldoni, A.; Scaini, D., Carbon Nanotubes, Directly Grown on Supporting Surfaces, Improve Neuronal Activity in Hippocampal Neuronal Networks. *Adv. Biosyst.* **2019,** *3* (5), 13.

76. Bareket, L.; Waiskopf, N.; Rand, D.; Lubin, G.; David-Pur, M.; Ben-Dov, J.; Roy, S.; Eleftheriou, C.; Sernagor, E.; Cheshnovsky, O.; Banin, U.; Hanein, Y., Semiconductor Nanorod-Carbon Nanotube Biomimetic Films for Wire-Free Photostimulation of Blind Retinas. *Nano Letters* **2014,** *14* (11), 6685-6692.

77. Eleftheriou, C. G.; Zimmermann, J. B.; Kjeldsen, H. D.; David-Pur, M.; Hanein, Y.; Sernagor, E., Carbon nanotube electrodes for retinal implants: A study of structural and functional integration over time. *Biomaterials* **2017,** *112*, 108-121.

78. Teradal, N. L.; Jelinek, R., Carbon Nanomaterials in Biological Studies and Biomedicine. *Adv. Healthc. Mater.* **2017,** *6* (17), 36.

79. Akhavan, O.; Ghaderi, E.; Shirazian, S. A.; Rahighi, R., Rolled graphene oxide foams as three-dimensional scaffolds for growth of neural fibers using electrical stimulation of stem cells. *Carbon* **2016,** *97*, 71-77.

80. Severino, F. P. U.; Ban, J.; Song, Q.; Tang, M.; Bianconi, G.; Cheng, G.; Torre, V., The role of dimensionality in neuronal network dynamics. *Scientific reports* **2016,** *6*, 29640.

81. Shin, S. R.; Shin, C.; Memic, A.; Shadmehr, S.; Miscuglio, M.; Jung, H. Y.; Jung, S. M.; Bae, H.; Khademhosseini, A.; Tang, X. S.; Dokmeci, M. R., Aligned carbon nanotube-based flexible gel substrates for engineering bio-hybrid tissue actuators. *Adv Funct Mater* **2015,** *25* (28), 4486-4495.

82. Ren, J.; Xu, Q.; Chen, X.; Li, W.; Guo, K.; Zhao, Y.; Wang, Q.; Zhang, Z.; Peng, H.; Li, Y. G., Superaligned Carbon Nanotubes Guide Oriented Cell Growth and Promote Electrophysiological Homogeneity for Synthetic Cardiac Tissues. *Advanced materials* **2017,** *29* (44).

83. (a) Shin, S. R.; Jung, S. M.; Zalabany, M.; Kim, K.; Zorlutuna, P.; Kim, S. B.; Nikkhah, M.; Khabiry, M.; Azize, M.; Kong, J.; Wan, K. T.; Palacios, T.; Dokmeci, M. R.; Bae, H.; Tang, X. W.; Khademhosseini, A., Carbon-Nanotube-Embedded Hydrogel Sheets for Engineering Cardiac Constructs and Bioactuators. *Acs Nano* **2013,** *7* (3), 2369-2380; (b) Aurand, E. R.; Usmani, S.; Medelin, M.; Scaini, D.; Bosi, S.; Rosselli, F. B.; Donato, S.; Tromba, G.; Prato, M.; Ballerini, L., Nanostructures to Engineer 3D Neural-Interfaces: Directing Axonal Navigation toward Successful Bridging of Spinal Segments. *Advanced Functional Materials* **2018,** *28* (12), 1700550.

84. Schutt, F.; Signetti, S.; Kruger, H.; Roder, S.; Smazna, D.; Kaps, S.; Gorb, S. N.; Mishra, Y. K.; Pugno, N. M.; Adelung, R., Hierarchical self-entangled carbon nanotube tube networks. *Nature communications* **2017,** *8* (1), 1215.

85. Kato-Negishi, M.; Onoe, H.; Ito, A.; Takeuchi, S., Rod-Shaped Neural Units for Aligned 3D Neural Network Connection. *Advanced healthcare materials* **2017,** *6* (15).

86. Marcus, M.; Baranes, K.; Park, M.; Choi, I. S.; Kang, K.; Shefi, O., Interactions of Neurons with Physical Environments. *Adv. Healthc. Mater.* **2017,** *6* (15), 19.